NASA TECHNICAL
MEMORANDUM

NASA TM X-64690
August 1972

NASA TM X-64690

CHEMICAL PROPULSION RESEARCH AT MSFC

RESEARCH ACHIEVEMENTS REVIEW

VOLUME IV REPORT NO. 6

SCIENCE AND ENGINEERING DIRECTORATE
GEORGE C. MARSHALL SPACE FLIGHT CENTER
MARSHALL SPACE FLIGHT CENTER, ALABAMA

GEORGE C. MARSHALL SPACE FLIGHT CENTER

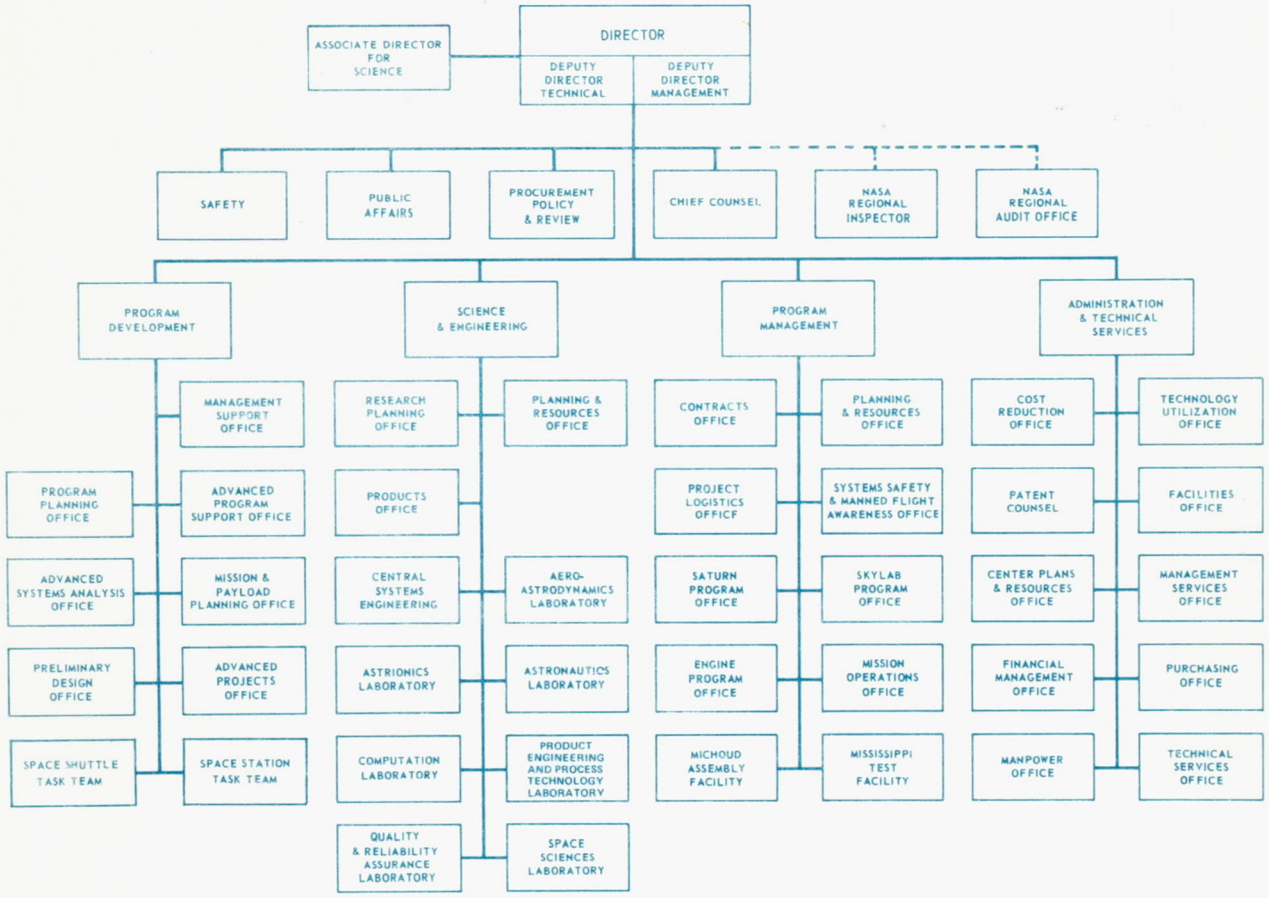

RESEARCH ACHIEVEMENTS REVIEWS COVER THE FOLLOWING FIELDS OF RESEARCH

- Radiation Physics
- Thermophysics
- Chemical Propulsion
- Cryogenic Technology
- Electronics
- Control Systems
- Materials
- Manufacturing
- Ground Testing
- Quality Assurance and Checkout
- Terrestrial and Space Environment
- Aerodynamics
- Instrumentation
- Power Systems
- Guidance Concepts
- Astrodynamics
- Advanced Tracking Systems
- Communication Systems
- Structures
- Mathematics and Computation
- Advanced Propulsion
- Lunar and Meteoroid Physics

PREFACE

The Research Achievements Reviews document research accomplished by the laboratories of Marshall Space Flight Center. Each review covers one or two fields of research and attempts to present the results in a form readily usable by specialists, system engineers, and program managers.

Reviews of this fourth series are designated Volume IV and will span the period from May 1970 through May 1972.

In accordance with NASA policy the International System of Units (SI Units), as defined in NASA SP-7012, is used in this publication.

The papers in this report were presented August 5, 1971

William G. Johnson
Director
Research Planning Office

Page intentionally left blank

CONTENTS.....

SOME CHEMICAL PROPULSION TECHNOLOGY HIGHLIGHTS

LIST OF ILLUSTRATIONS

HIGH SPEED SHAFT SEALS FOR ROCKET ENGINE TURBOPUMPS

CONTENTS (Continued).....

LIST OF TABLES

LIST OF ILLUSTRATIONS

CONTENTS (Continued).....

TWO-PHASE PUMPING OF CRYOGENIC PROPELLANTS

By H. P. Stinson and L. A. Gross

LIST OF ILLUSTRATIONS

CONTENTS (Continued).....

LIQUID ROCKET COMBUSTION STABILITY

LIST OF TABLES

LIST OF ILLUSTRATIONS

ROCKET COMBUSTION INSTABILITY SUPPRESSION WITH CAVITY RESONATORS

By R. H. Counts

LIST OF ILLUSTRATIONS

PULSE PERFORMANCE ANALYSIS FOR SMALL HYPERGOLIC PROPELLANT ROCKET ENGINES

By Gerald W. Smith

CONTENTS (Continued).....

LIST OF TABLES

LIST OF ILLUSTRATIONS

ENGINEERING ADVANCES IN AEROSPIKE ROCKET ENGINES

By Rex Bailey

CONTENTS (Continued).....

LIST OF TABLES

LIST OF ILLUSTRATIONS

CONTENTS (Continued).....

PERFORMANCE ANALYSIS OF AEROSPIKE ROCKET ENGINES

By Klaus W. Gross

LIST OF ILLUSTRATIONS

CONTENTS (Continued).....

EXTENDIBLE ROCKET NOZZLE DEVELOPMENT

LIST OF ILLUSTRATIONS

CRYOGEN FLOW CONTROL COMPONENTS FOR ROCKET PROPULSION SYSTEMS

By J. H. Potter

LIST OF ILLUSTRATIONS

CONTENTS (Concluded).....

SOME CHEMICAL PROPULSION TECHNOLOGY HIGHLIGHTS

By

Hans G. Paul

Chemical propulsion has played and is playing an important role at Marshall Space Flight Center. During past years MSFC has been involved in the development of a number of rocket engines and total propulsion systems for the various Saturn stages and earlier for Army missiles. More recently, this organization has been assigned the responsibility for developing the Space Shuttle main propulsion rocket engines and the Space Shuttle booster propulsion system.

All chemical propulsion technology efforts at MSFC are aimed at improving our capabilities, so that future propulsion systems can perform more demanding tasks, be less complex, have longer service life, and can be developed, produced, and operated at lower cost.

The Chemical Propulsion Research Achievements Review held in 1967 dealt with improved fluid connectors, main seal technology for vent valves, various fluid mechanics topics, the high pressure Bell engine and the aerospike engine, and the J-2X engineering program. In the present review the detailed discussions of advances in the fields of turbomachinery, rocket combustion, performance, engine systems, and fluid flow components represent only a portion of a number of research achievements. The following list gives the title and contract number of additional technology efforts along with significant accomplishments:

1. Titanium Pump Impeller with Diffusion-Bonded Shroud, NAS8-20761 — Shrouded impellers offer advantages in high pressure pumps; on impellers with an integral shroud, the optimum shape of fluid passages is often not obtainable since accessibility is restricted to the machining tool. Diffusion-bonding of the shroud after machining optimum fluid passage permits improved pump efficiencies.

2. Thermodynamic Improvements in LH_2 Turbopumps, NAS8-20324 — A thermal insulation coating that adheres to internal pump surfaces allows reduced chill times and chillant flow during pump start.

3. Advanced Injector Concepts Investigation, NAS8-21052 — An injector has been developed by brazing a stack of thin platelets with etched-in flow passages; hydrogen entering as a warm gas vaporizes liquid oxygen which, when injected as a gas, permits wide-range throttling and prevents low frequency combustion instability.

4. Minimum Pressure Loss in Duct Systems, NAS8-21133 — Analytical tools are provided for assessing and avoiding flow-induced vibrations that cause fatigue failures in flexible lines.

5. Cryofluid Flow Oscillations in Heat Exchangers, NAS8-11422/21014/21045 — Analytical methods are given for estimating relative stability as a function of geometry and fluid parameters to avoid thermally driven flow oscillations.

6. Design Criteria for Zero-Leakage Fluid Connectors, NAS8-4012/24387 — Updated analyses and design methods for high quality, flight-type fluid connectors and a fluid connector handbook have been established.

7. MSFC Swaged Collar Tube Connector, NAS8-20572 — Tube connector sizes from 0.635 to 3.175 cm (0.25 to 1.25 in.) are nearing qualification completion; their weight is considerably reduced, and leakage rates have been reduced to 1×10^{-6} cm^3/s (Figs. 1 and 2).

8. Resupply, Maintenance, Repair (RMR) Studies, NAS8-26194/26196 — Presented are preliminary design solutions based on RMR concepts that promise reliable, long life subsystem operation in orbit with less redundancy or overdesign through crew involvement.

9. Space Shuttle High and Low Pressure Auxiliary Propulsion System Studies, NAS8-26248/26249 — Areas where new technology is needed such as reduced response times and extended life for various components are identified.

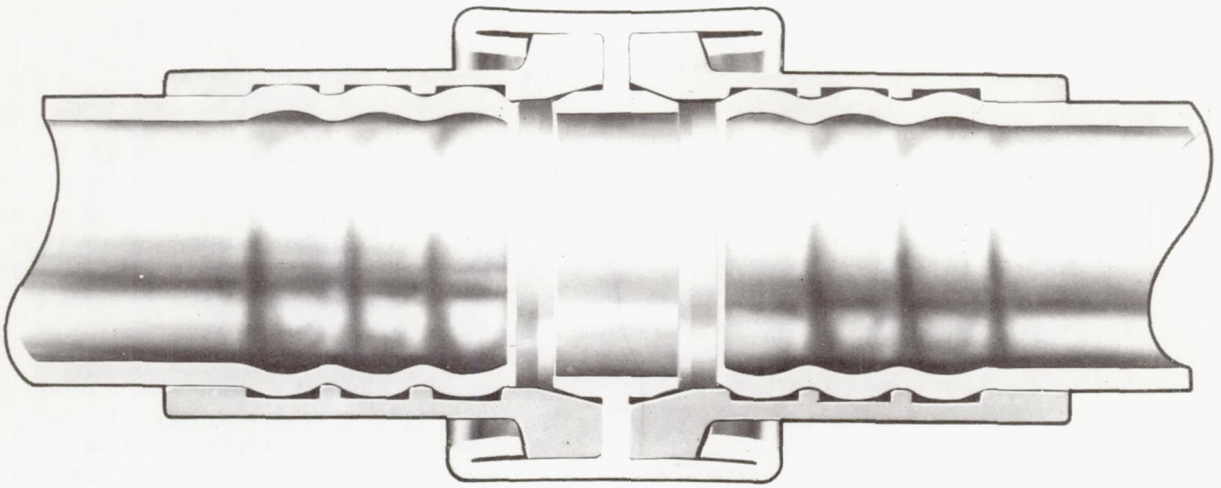

Figure 1. MSFC swaged collar tube connector.

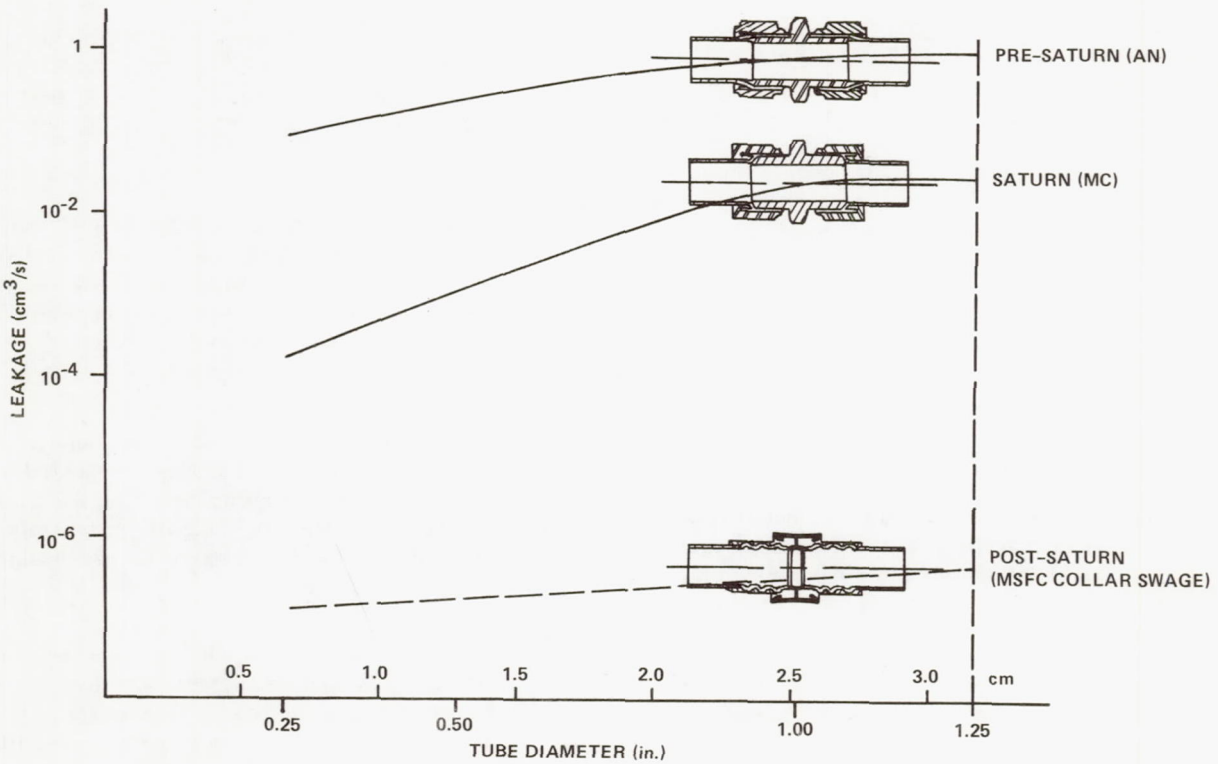

Figure 2. Tube connector leak rates.

Next, some examples are given on how chemical propulsion technology advanced during past years.

Over a number of years technology programs investigated the influences of various pump inducer design parameters on cavitation. As a result of this technology support, the suction performance of inducers in liquid oxygen and liquid hydrogen pumps improved by about a factor of two, as can be seen in Figure 3, which in historical order shows the suction specific speed,

$$N_{ss} = N \cdot Q^{1/2}/(NPSH)^{3/4} \quad ,$$

of the cryopropellant pumps for the A-7, S-3D, H-1, RL-10, J-2, and F-1 rocket engines. Increased suction specific speeds permit pumps to run at lower inlet pressures, lower tank pressures, and higher shaft speeds with the result that pump, tank wall, and pressurant weight can be saved. The development of the Space Shuttle will benefit from these technology advances.

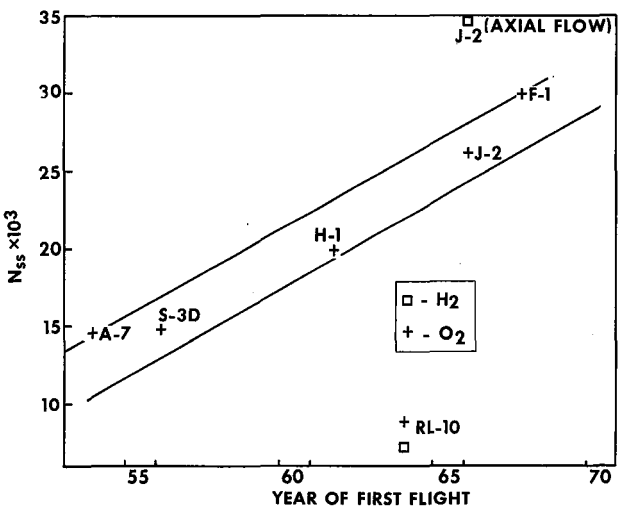

Figure 3. Suction specific speed history.

The growth of impeller tip speeds in cryopropellant pumps of rocket engines is indicated relative to time in Figure 4. The tip speed of LH_2 pumps improved from around 244 m/s (800 ft/s) on the RL-10 and J-2 to 793 m/s (2600 ft/s) on the 350-K technology pump or by a factor of more than three; tip speeds of oxygen pumps advanced from 61 m/s (200 ft/s) on the RL-10 to 290 m/s (950 ft/s) on the 350-K technology pump or by a factor of more than four and one-half. Increased tip speeds have become a reality because technology programs have provided improved high strength alloys, improved manufacturing techniques, and bearings running in cryopropellants at increased Dn values.*

High pump impeller tip speeds are advantageous if low density fluids such as LH_2 have to be discharged at pressures of several thousand N/cm^2 as required by the Space Shuttle main propulsion engines. The combination of increased impeller tip speed and shaft speeds helps shrink the pump envelope and contributes to keeping the Shuttle booster base area, which must accommodate a large number of rocket engines, as compact as possible.

An important area of chemical propulsion technology is thrust chamber cooling. Progress made in this field is evident from Figure 5 which shows throat heat fluxes of the regeneratively cooled thrust chambers of the RL-10, J-2, J-2S and a technology-supported prototype chamber; the design point of the future Shuttle main engine is also indicated. It can be seen that the capability of handling heat fluxes encountered in cryorocket combustion chambers increased during the past decade by a factor greater than ten. The relatively modest maximum heat flux in combustion chambers of current jet engines is shown for comparison.

Again technology programs proved the propulsively efficient regenerative cooling method feasible for heat fluxes up to 16 342 W/cm^2 (100 $Btu/in.^2$-s); also, this technology achievement is greatly aiding the Shuttle main engine development. A further step to be taken here consists of providing extended thrust chamber life under high heat fluxes.

In Figure 6 an attempt is made to compare dry engine weight per unit vacuum thrust of existing and planned H_2-O_2 rocket engines as a function of engine exit area per unit vacuum thrust. Low values of engine exit area correspond to high values of chamber pressure; the upper curve includes the weight for accessories. It can be concluded that rocket engines taking advantage of technology achievements such as higher suction specific speeds, higher impeller tip speeds, and higher chamber pressures offer weight advantages and considerable envelope advantages. By taking the RL-10, the first LH_2-LO_2 rocket engine, as a basis of comparison, it can be

* Dn = bearing diameter (in millimeters) times shaft revolution per minute.

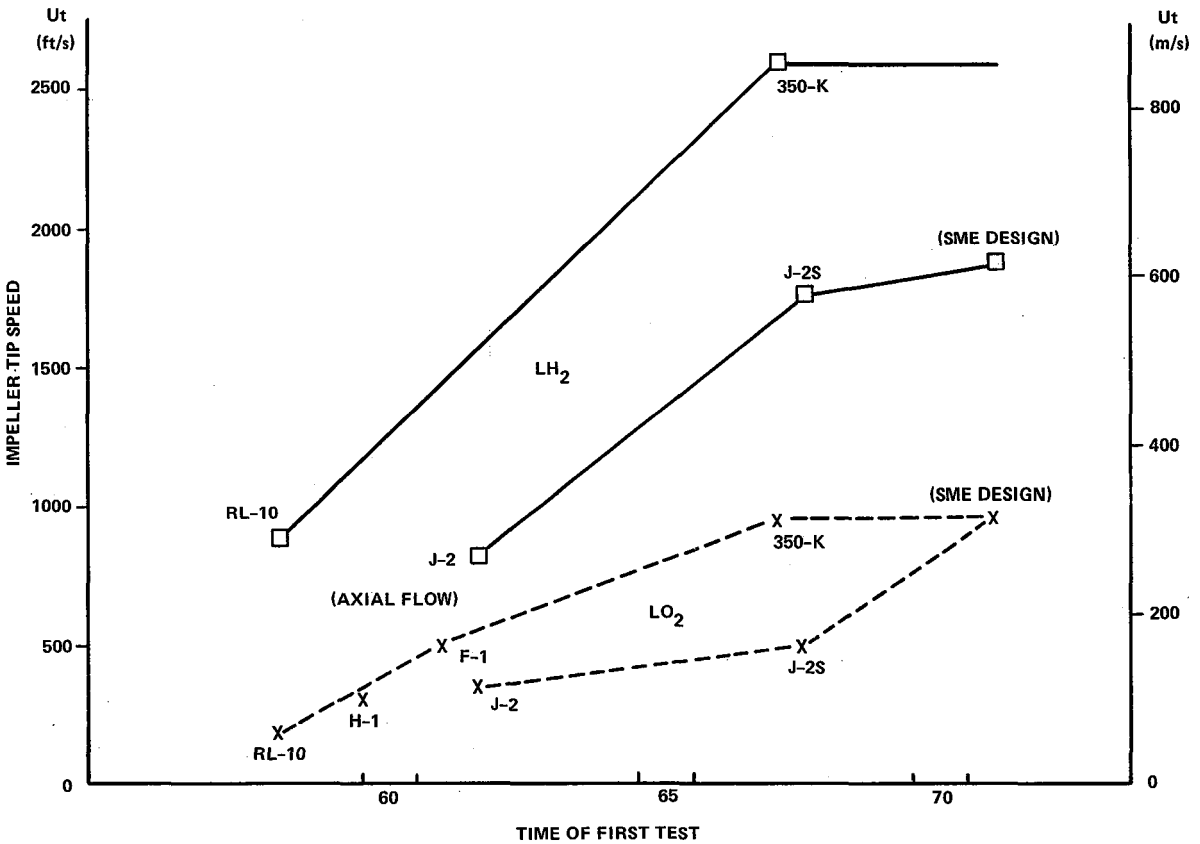

Figure 4. Impeller tip speed growth of rocket engine hydrogen-oxygen pumps from 1958 through 1970.

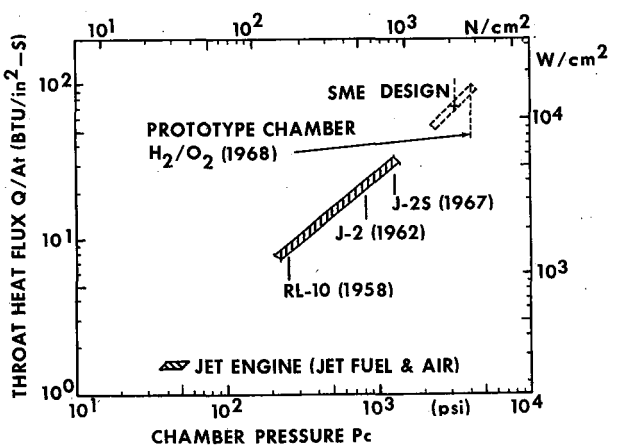

Figure 5. Throat heat flux versus chamber pressure for LH_2-LO_2 rocket engines.

seen in Figure 6 that the engine exit area of the J-2S is reduced by 75 percent and that of the future Shuttle booster main engine (left dashed line rectangle) is reduced by approximately 90 percent, whereas the

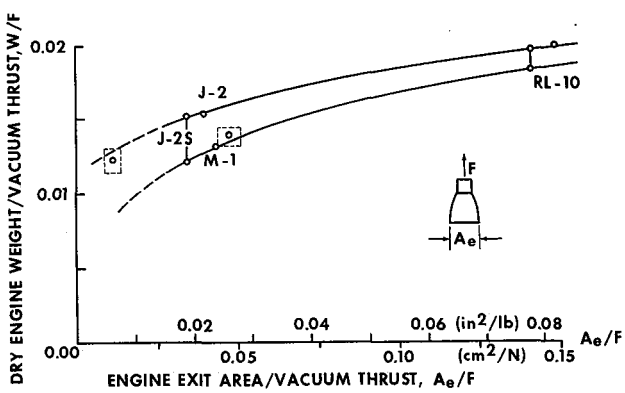

Figure 6. LH_2-LO_2 rocket engine weight versus nozzle exit area per unit vacuum thrust.

engine weight reductions amount to 20 and approximately 30 percent, respectively.

One more area of endeavor vital to chemical propulsion technology concerns the conservation of cryopropellants. Hydrogen evaporation losses in percent per day are plotted in relation to storage volume in Figure 7. The points designated 9 represent the hydrogen loss of the S-IVB stage on the ground and in orbit, and point 15 represents that of a flight-type LH_2 tank recently tested at MSFC. The storage performance of this tank equals an order of magnitude improvement of two based on equal storage volume and, for comparison, excels the high-quality-insulated railroad tank car, point 1.

Technology programs of past years provided more efficient insulation materials, improved analysis, improved instrumentation, improved design of key elements for cryopropellant storage systems, improved manufacturing and assembly methods, and in doing so made respectable achievements possible.

The following advances should also be mentioned here:

- Dynamic Stability of Rocket Engine Injectors
- Tankhead Engine Start (RL-10, F-1, J-2X)
- Main Chamber Tapoff Turbine Drive (H-IX, J-2X)
- Propellant-Lubricated, High Speed Bearings
- High Pressure Cryopropellant Pumps
- Rocket Engines with Fuel-Free Exhaust (RL-10, SSME)
- POGO Suppression, Elimination (S-IC, S-II)
- Man-Rated Propulsion Systems
- Improved Reliability Performance

However, in spite of an impressive number of achievements, chemical propulsion technology cannot rest on laurels. In the past, chemical propulsion

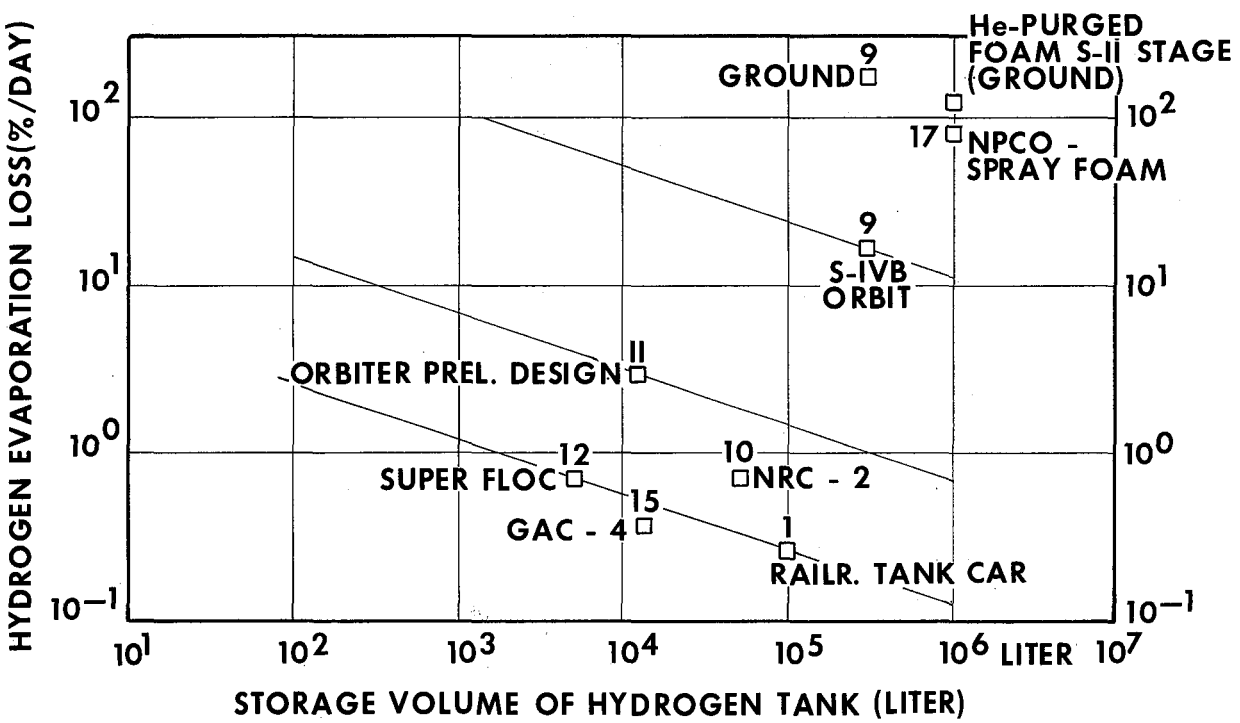

Figure 7. Daily evaporation loss of liquid hydrogen storage tanks.

technology efforts had to satisfy such objectives as high performance, low inert mass, and safe, simple operation. Future objectives are more demanding and tougher to meet; as indicated in Figure 8, additional requirements of long operational life, reuse, low cost, and compatibility with crew, passengers, and ecology must also be satisfied. In this regard, the remaining decade will offer even greater challenges for our chemical propulsion technology activities.

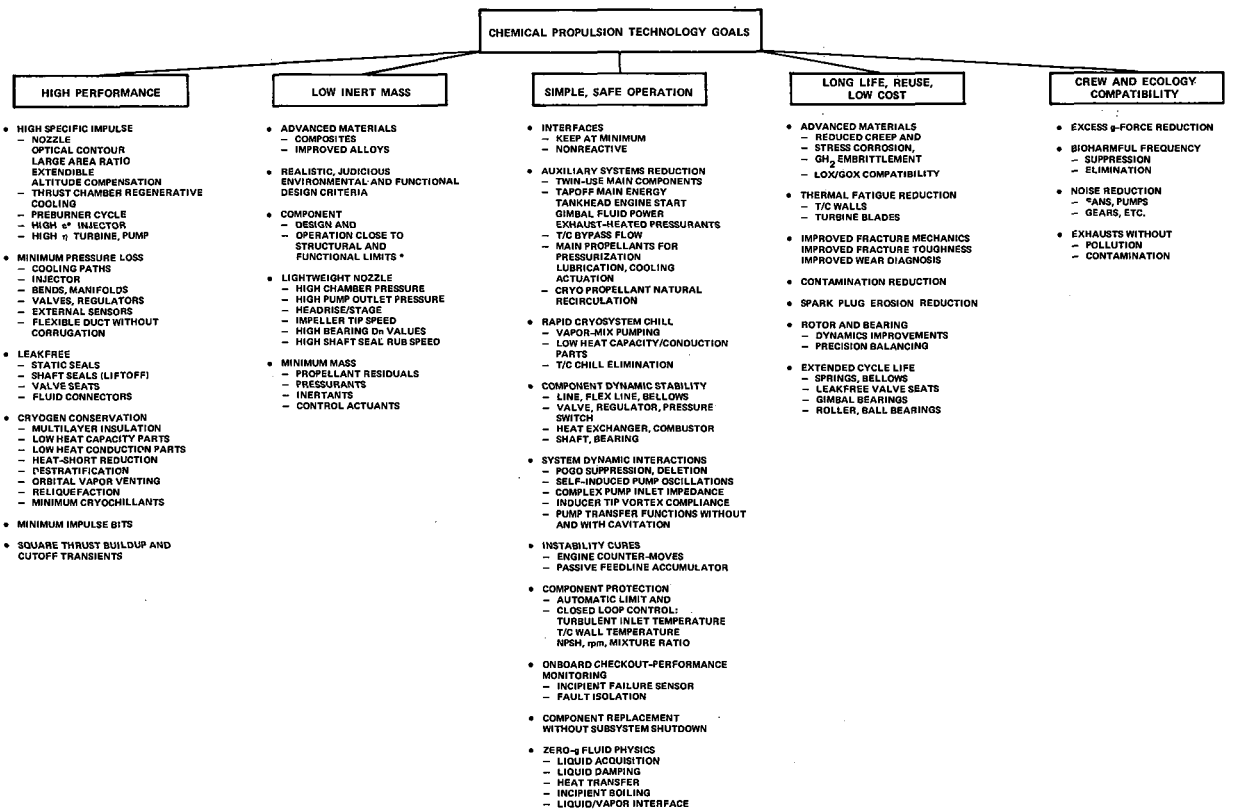

Figure 8. Future objectives of chemical propulsion technology.

HIGH SPEED SHAFT SEALS FOR ROCKET ENGINE TURBOPUMPS

By

F. D. Pitsenberger

SUMMARY

Many concepts for the design of the secondary, internal seal of the turbopump dynamic shaft seal have been studied; the bellows design was selected as the most satisfactory to achieve lower leakage, greater reliability, and longer life for both cryogenic and high temperature service. The bellows was known to have an instability problem when subjected to fluid pressure oscillations or turbopump shaft vibrations. A study of bellows damping methods was completed and piston damping, orifice damping, and particle damping were experimentally evaluated. The particle damped bellows seal was determined to have the greatest potential for improved operation in the variable environment encountered during the operating cycles of rocket engine turbomachinery. This seal was further tested in a simulated turbopump environment with very satisfactory results.

The primary sealing face of the dynamic shaft seal was experimentally evaluated to determine the factors affecting leakage during coast or standby periods when the turbopump shaft is not rotating. It is customary to predict this oxidizer or fuel leakage by testing the seal prior to flight with an inert gas such as helium. However, it has not been possible to determine a true correlation between the inert gas and cryogenic oxidizer or fuel. A model seal and a production seal were tested under simulated conditions, and it was determined that a true correlation can be empirically determined if the seal is designed to minimize thermal distortion.

INTRODUCTION

The shaft seals used in rocket engine turbopumps have been plagued with serious problems of static and dynamic leakage, dynamic instability, and catastrophic failures that in some instances have resulted in destruction of the turbopump and severe damage to the engine. The continued advancement of turbomachinery has required the development of new seal technology to cope with the extremes of temperature, speed, pressure, and extended life.

The present turbopump shaft seals are really two seals in one. The seal that is called the primary seal consists of the seal face (nosepiece) that is held against a rotating shaft mating ring and must seal across a high speed rubbing surface (Figs. 1 and 2). This primary seal must be free to move axially to follow any axial movement of the shaft and mating ring and to allow for manufacturing tolerances of the shaft and mating ring. The secondary seal is internal to the seal assembly and prevents internal leakage through the seal while allowing the primary seal to move with the movements of the mating ring. Figure 1 shows a typical lip type secondary seal with coil springs holding the primary seal against its mating ring. Figure 2 shows a bellows seal design in which the bellows acts both as a secondary seal to prevent internal leakage through the seal and also as the spring force to hold the primary seal against the mating ring. Both of these seal designs are currently being used. However, the lip seal has the problems of cracking of the thin lip material and contamination damaging the lip, while the bellows seal has the problems of cracking of the bellows because of vibration and leakage past the primary seal because of

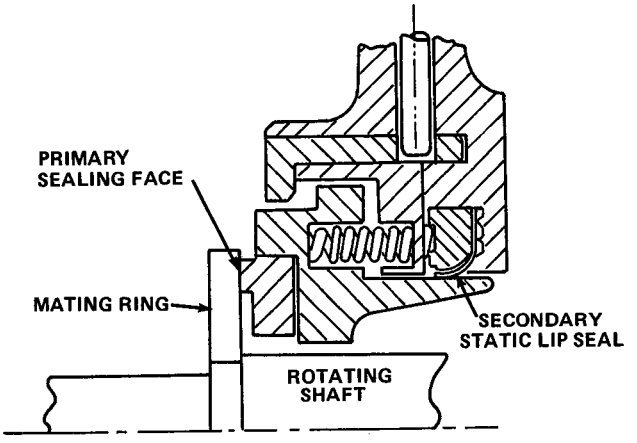

Figure 1. Standard lip seal.

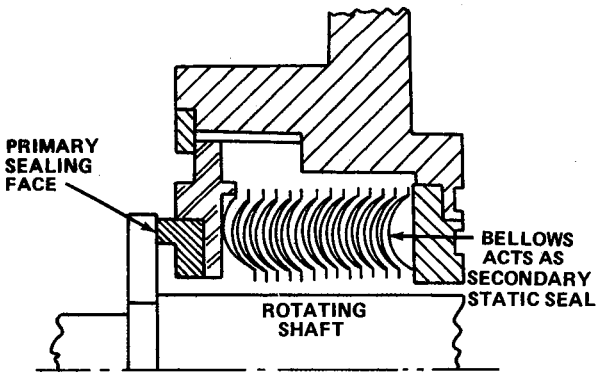

Figure 2. Standard bellows seal.

instability of the bellows, thus allowing the primary seal to bounce off the mating ring.

The study reported on herein was in two phases. The objective of phase I was to study the secondary seal to achieve lower leakage, greater reliability, and longer life under more severe operating conditions of greater speeds and higher pressures. The objective of phase II was to study the primary seal to improve the techniques of predicting leakage and determine the causes of leakage under static conditions during standby and coast periods of flight when the turbopump shaft is not rotating. The study of the primary seal during dynamic conditions was beyond the scope of work of this program. Therefore, a contract was initiated with North American Rockwell Corporation, Rocketdyne Division to accomplish this study.

PHASE I SECONDARY SEAL

Concepts Investigated

A review of all sealing concepts was conducted, and 18 concepts evolved as possible methods. A thorough analysis of these concepts determined that the bellows seal design was the most promising if the problems of cracking and instability of the bellows could be resolved by an improved method of damping. A conventional method of damping the unstable motion of bellows is by frictional devices, usually spring loaded, contacting the bellows convolutions and/or the bellows carrier. Although this method is effective, the amount of damping is not easily controlled and damper material and contacting surfaces are subject to wear. In addition, if the input vibration becomes large, a higher frictional load is then necessary for adequate control. Simultaneously, this higher load increases energy input and the potential for ignition of exposed propellants. An analytical study of all damping methods indicated that the three most logical approaches were piston damping, orifice damping, and particle damping. These three methods were selected for detail design and testing to verify the analytical conclusions and to determine the optimum method for use in a turbopump, cryogenic environment.

The piston damped bellows seal (Fig. 3) employs a viscous method of controlling induced vibratory motion of the bellows and consists of a piston ring that is contained in the housing and maintains a close clearance with the sealing face retainer outer diameter which acts as the piston. The fluid being sealed fills the cavity surrounding the bellows outside diameter behind the piston ring, and any axial movement of the seal face changes the volume of this cavity forcing fluid through the small clearance between the piston ring and piston thus damping excessive vibration or axial movement of the seal face. Initial computer studies describing damping characteristics

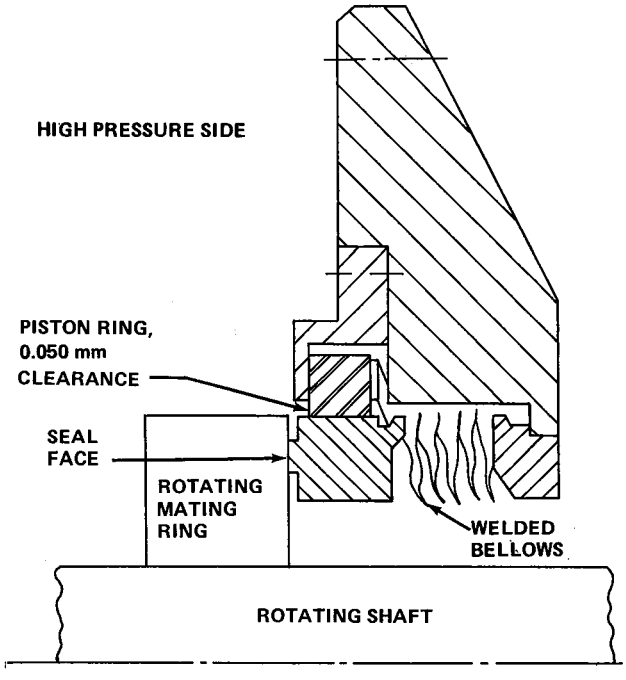

Figure 3. Piston damped bellows seal.

in terms of displacement versus time response showed a definite reduction in amplitude when the radial piston clearance was reduced from 0.250 to 0.050 mm (0.010 to 0.002 in.).

The orifice damped bellows seal (Fig. 4) also utilizes viscous friction to absorb imposed axial vibration. The design consists of two cavities formed by two pairs of radially stacked welded bellows and separated by an orifice plate. The end fitting of one pair of bellows supports the primary sealing surface, and the end fitting on the other bellows closes the system. Both cavities are filled with a fluid suitable to the temperature environment. As the seal face is subjected to axial movements, the damping fluid contained in the bellows cavity is forced through the orifices creating viscous forces to absorb input energy. The rear bellows cavity or compensator assembly accumulates the volume of fluid forced through the orifices and also acts to increase or decrease the total volume caused by a fluid temperature/density change. To obtain significant damping, a fluid with the high density associated with liquids must be used. Analog computer calculations indicated that little damping is obtained with a gaseous medium at the relatively small displacements of this seal. This seal design is more suited to high temperature applications because the damping fluid is contained and sealed in the bellows cavity. For the purpose of this study, liquid metal sodium-potassium (NaK) was used.

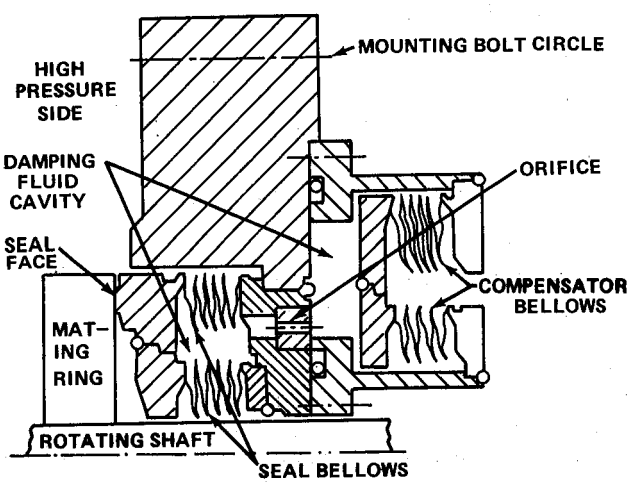

Figure 4. Orifice damped bellows seal.

The particle damped bellows seal (Fig. 5) incorporates a number of containers attached rigidly to the seal face. When these containers are filled to near capacity with very small spherical particles, the particles react to vibration inputs by absorbing displacement energy through inertia and friction of the particle masses acting on the inside surface of the containers.

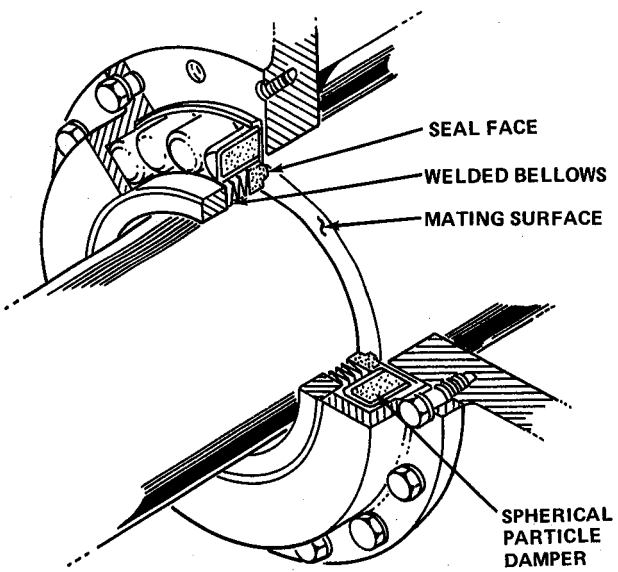

Figure 5. Particle damped bellows seal.

Test Program

The three seal designs were not designed for a specific turbopump application or for rotational tests. However, requirements and operational criteria were based on conditions consistent with advanced turbomachinery. The nonrotating tests accomplished with each seal are discussed in the following.

Static leakage and proof pressure tests were conducted at pressures up to 2.58×10^6 N/m^2 (375 psi) to verify mechanical integrity and design requirements. A leakage test across the seal face as well as a mass spectrometer check for porous weld beads were made also.

Total face load tests were conducted to measure the effective seal face unit loading as a result of the

combined bellows spring load and hydraulic loading. These tests were conducted using an Instron machine that allows a dynamic measure of the seal face loads by controlling the shaft movement and simultaneously recording the load exerted on the load cell. The test equipment is shown schematically in Figure 6 and the test setup is shown in Figure 7. The operational characteristics determined through total load tests are as follows:

1. Spring force of the bellows through the desired operating range.

2. Effective hydraulic area.

3. The change of the bellows effective diameter caused by deformation of the bellows plates when varying the operational pressure.

4. The change of seal face unit loading with respect to a change in compressed length or a change in pressure.

5. Seal leakage to test the adequacy of the pressure balance.

Fluid pressure cycling tests were conducted to measure the ability of the bellows to withstand pressure pulses up to 6.89×10^5 N/m^2 (100 psi) amplitude at 3, 10, 20, and 30 Hz. Seal leakage was measured during the tests.

Mechanical cycling and recovery rate tests were conducted to monitor the seal integrity when exposed to mating ring axial displacements of ±0.375 to ±0.750 mm (0.015 to 0.030 in.) at 16 to 100 Hz in liquid nitrogen and gaseous nitrogen. These tests were used to determine the capability of the seal face to follow the mating ring. The tester had the capability to maintain cryogenic temperatures as well as high temperatures to 811° K (1000° F) while pressurized to 1.72×10^6 N/m^2 (250 psi).

Vibration tests were conducted to record the frequency of all resonant points observed in a 2-g peak-to-peak sweep from 15 to 2000 Hz in the axial axis of the seal without the sealing face in contact with a mating ring. Each seal was also subjected to its major resonant frequency for 10 min in the axial axis at a 12-g level below 500 Hz and at a 30-g level above 500 Hz. The test fixture had the capability to operate at cryogenic and 811°K (1000°F) temperatures while pressurized to 1.72×10^6 N/m^2 (250 psi). Seal leakage was monitored as was sealing and mating ring displacement.

All test fixtures were schematically similar to Figure 6 with varying methods of applying hydraulic and mechanical inputs to the seal specimen and mating ring.

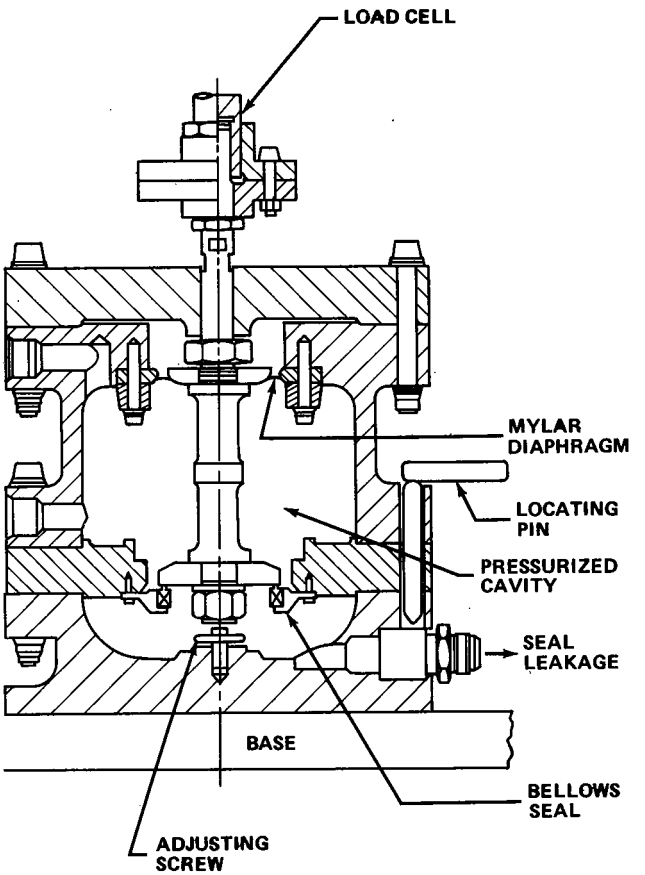

Figure 6. Total face load tester.

Piston Damped Bellows Seal

The piston damped bellows seal final design, shown in Figure 8, was designed with a 9.65-cm (3.8-in.) piston diameter and with radial piston ring clearances of 0.050 mm (0.002 in.), 0.100 mm (0.004 in.), 0.150 mm (0.006 in.), 0.200 mm (0.008 in), and 0.250 mm (0.010 in.). These clearances were maintained constant by three small equally spaced pads on the piston.

Initial computer studies of damping characteristics in terms of displacement versus time response showed a definite reduction in amplitude when the

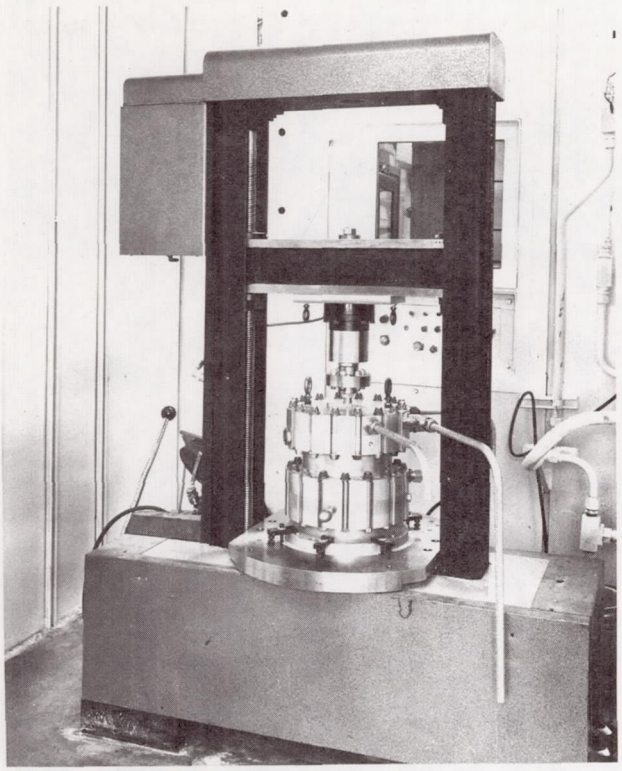

Figure 7. Total load test setup.

piston clearance was reduced from 0.250 to 0.050 mm (0.010 to 0.002 in.). The study also showed that no appreciable damping is obtained in a gas medium with the small axial motion involved, but a damping coefficient of sufficient magnitude is obtained from a liquid medium. A further reduction in clearance below 0.050 mm (0.002 in.) was not considered because it is accompanied by rubbing and will approach the method of frictional damping currently employed by the seal industry.

Four identical seals were manufactured and subjected to an experimental program. One seal was mechanically cycled without a piston ring installed to obtain a comparison and to study the seal performance without damping. The seal was exposed to mating ring mechanical cycling at ±0.175-mm (0.007-in.) amplitude at 100 Hz in liquid nitrogen (LN_2) at 1.72×10^6 N/m^2 (250 psi). After 69 000 cycles, the seal leakage exceeded the range of the flowmeter and the seal was removed from the tester. Inspection revealed the seal to have a failed bellows in the inside diameter weld at the heat-affected zone of the third and eighth convolutions. The seal face apparently did not remain in contact with the mating ring at the 100-Hz cycling rate, as evidenced by fretting between the seal face and mating ring and by comparison of the displacement transducer traces monitoring the axial movement of the seal face and the axial displacement of the tester mating ring. The failed bellows was completely analyzed, and it was determined that the material was metallurgically sound and did not contribute to the failure. A fractograph was taken which indicated that the premature failure was caused by fatigue of the material. This test established that the seal design would not operate satisfactorily under vibrating conditions without some form of bellows damping.

Another seal was installed in the tester with a piston ring which maintained a 0.101-mm (0.004-in.) radial clearance with the piston. It was cycled for a total of one million cycles under the same conditions as the failed seal. The seal face satisfactorily followed the cycling mating ring as evidenced by the low and constant leakage rates and by a comparison of the mating ring and seal face linear displacement transducers. Posttest inspection of the seal revealed the bellows and sealing face to be in perfect condition.

The third seal with the same piston ring clearance was tested at ±0.750-mm (0.030-in.) amplitude at 16 Hz in LN_2 at 1.72×10^6 N/m^2 (250 psi) for one million cycles with effective damping; no damage to the seal occurred.

A series of vibration tests was conducted on the fourth piston damped seal with and without a damping piston ring to observe seal face response at resonance. The seal was installed without a piston ring at the mean operating height in which the bellows was compressed 2.75 mm (0.110 in.). A test housing enclosed the seal to provide a volume for a gaseous nitrogen (GN_2) or LN_2 environment at the bellows outside diameter. Displacement was monitored by two linear transducers, one attached to the bellows carrier and one mounted on the test housing to monitor relative movement.

With no piston installed, tests were run at 2 g and 5 g. A frequency sweep to 2000 Hz showed three points of resonance (606, 1400, and 1800 Hz). Both transducers indicated an identical maximum amplitude of 0.006 mm (0.00025 in.). With a piston installed [0.050-mm (0.002-in.) clearance] the tests were repeated. The results indicated no change in amplitude. The environment was GN_2 heated to 755°K (900°F) and pressurized to 1.38×10^6 N/m^2

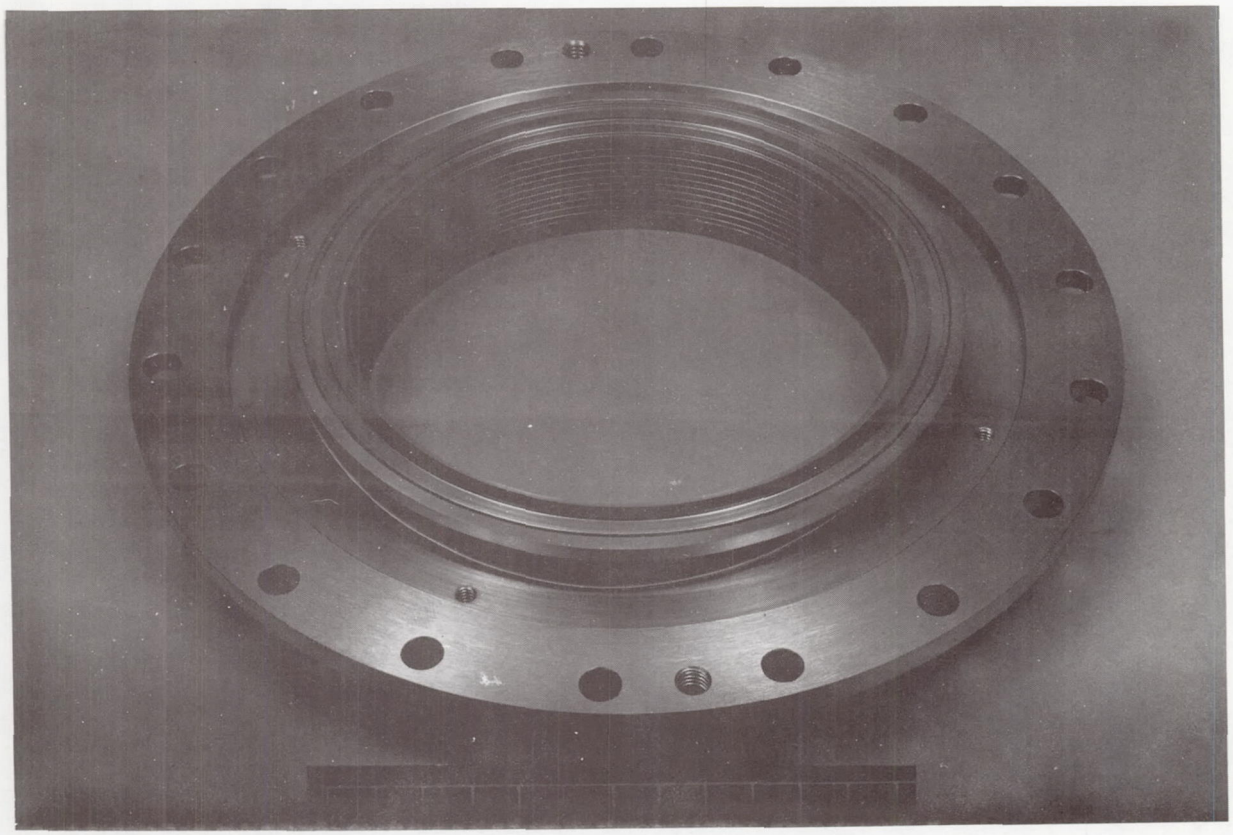

Figure 8. Piston damped seal.

(200 psia). Results of the tests support the previous conclusion that damping will not occur in a gaseous environment at small displacement amplitudes.

To increase the possibility of seal face lift-off, the compression load of the bellows was decreased beyond normal operation. With the bellows compressed 0.250 mm (0.010 in.), the seal was subjected to the same frequency sweep but only the first indication of resonance was considered. The seal was exposed only to normal room atmosphere; at approximately 600 Hz, lift-off occurred with a maximum amplitude of 0.050 mm (0.002 in.). The test was repeated using LN_2 to note any change in amplitude caused by a fluid condition pressurized to 1.38×10^6 N/m^2 (200 psia). The resonant frequency and maximum amplitude decreased by a very small amount under LN_2 environmental conditions, indicating that little damping existed with these small displacements and the fluid used.

Orifice Damped Bellows Seal

The orifice damped bellows seal final design is shown in Figure 9. Computer analysis indicates that damping can be obtained with the orifice system using liquid nitrogen; however, a stable condition of liquid is required during all periods of operation. Sodium potassium, used as the damping medium, is a more predictable fluid especially in a temperature environment of 811°K (1000°F) or greater.

Sodium potassium is a eutectic alloy called NaK-77 (77-percent K and 23-percent Na) and is being used as the damping medium in the orifice damped seals for operation in a 811°K (1000°F) gaseous environment. A review of the presently available hydraulic fluids revealed that they would not be as satisfactory as NaK over the temperature range of interest, 294 to 811°K (70 to 1000°F).

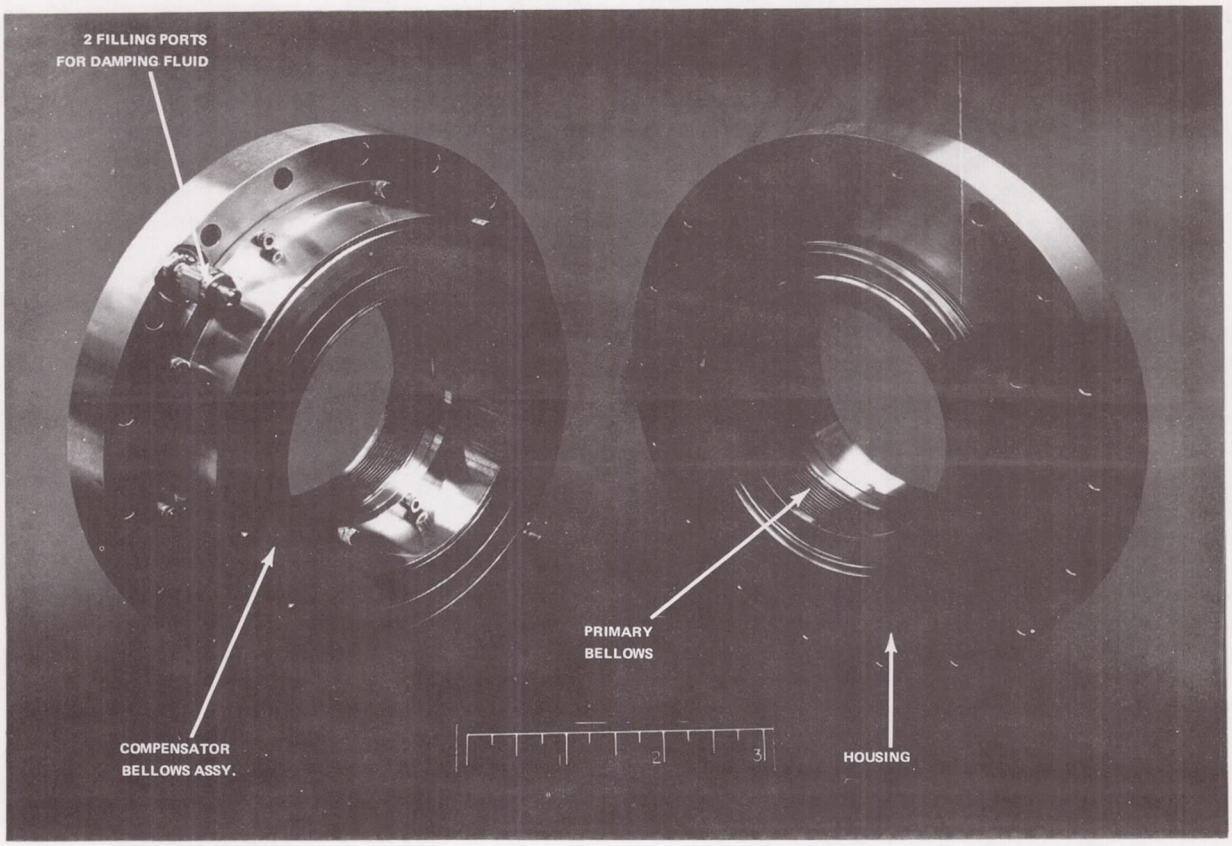

Figure 9. Orifice damped seal.

The properties of interest in this program are a wide operating temperature range, low density, high thermal conductivity, and relatively good chemical stability. NaK-77 has a melting point of 262°K (12°F) and boils at about 1057°K (1443°F) under atmospheric pressure. The density is comparable to that of conventional hydraulic fluids, while its viscosity is somewhat lower than that of water.

Because of the hazards imposed when using NaK, safety precautions are required. The list below shows the response of NaK to certain environments.

1. Water reacts violently with NaK, to form hydrogen gas and the oxides and hydroxides of sodium and potassium. The heat of reaction is great enough to ignite mixtures of hydrogen and oxygen if air is present.

2. Alcohols react mildly with NaK at room temperature and may be used for cleaning under controlled conditions. Reaction is fastest with methyl and ethyl alcohol, and slower with the heavier alcohols such as propyl and butyl. Air must be excluded from the cleaning system.

3. At room temperature bulk NaK open to the air reacts slowly with oxygen to form a surface scum. If spilled, small particles of NaK may ignite spontaneously, particularly with dust and many combustible materials. The ignition temperature for bulk NaK in air is about 478°K (400°F).

4. Carbon tetrachloride reacts violently and explosively with NaK.

5. Trichloroethylene forms highly unstable, dangerously explosive dichloroacetylene.

6. Natural hydrocarbons from refined petroleum oil are inert. Kerosene and white mineral oil are very useful in flushing the system and

excluding air from the surface of NaK in open containers.

7. Carbon dioxide is considered dangerously reactive.

8. Fire extinguishing materials are dry calcium carbonate, dry sand, and dry sodium chloride.

The corrosive attack of NaK on Inconel 750 was considered to be a problem in high temperature testing and required investigation. There are several important modes of attack.

One mode of attack is mass transfer in which elements from one metal in one part of the system are dissolved and reprecipitated in another part of the system. Grain boundaries are also attacked through fingerlike dissolution along the boundaries, uneven surfaces, or as slivers of corrosion product between grains. Dissolution of stringers of inclusions is a mode of attack of particular importance with welded bellows plates. Plate stock rolled in a "dirty" condition or welded without proper cleaning will have soluble inclusions in the bellows plate as well as in the weld bead. NaK will dissolve these stringers and weaken the structural joint. Stress corrosion is also a potential failure mode with the welded bellows seal.

An Inconel 750 TIG welded bellows specimen, manufactured under current state-of-the-art of seal vendor weld specifications, was submerged in NaK for 7 hr at 811°K (1000°F). The bellows specimen was compressed to induce tensile stresses in the bellows. Posttest inspection revealed the bellows to be in satisfactory condition. Mass transfer and stress corrosion cracking were not observed; however, some dissolution did take place along the grain boundaries of the Inconel 600 end fitting. Oxide scale formed during welding in the bead root was dissolved. This attack was confined to the outer surface but does stress the importance of "clean" welds.

The computer program also showed that the orifice size and number of orifices would vary for different frequencies and amplitudes of the mating ring vibrations and also for different hydraulic areas and bellows spring constants of the particular design.

Two orifice damped seals were tested in the mating ring cycling test fixture with ±0.750-mm (0.030-in.) amplitude for one million cycles. One seal was cycled at 30 Hz in 755°K (900°F) GN_2 at 1.72×10^6 N/m^2 (250 psi), and the other seal was cycled at 16 Hz in cryogenic LN_2 at 1.72×10^6 N/m^2 (250 psi). Both seals operated satisfactorily with sufficient damping to cause the seal face to accurately follow the mating ring with very low fluid leakage; no failures occurred.

An orifice damped seal was pressure-cycle tested by imposing oscillating LN_2 pressures on the primary seal bellows with the damping cavity filled with recirculating LN_2. The seal was installed at the mean design bellows compression and remained at that compression unless influenced by the pulsating pressure. The seal cavity was pressurized to 1.38×10^5 N/m^2 (200 psi) and pulsed at $\pm 3.45 \times 10^5$ N/m^2 (50 psi) at 10, 20, and 30 Hz. After about 700 000 cycles, a bellows fatigue failure was experienced. The recirculating LN_2 used as the damping fluid was subject to a volume/density change, which indicates it may be necessary to limit the use of this design to fluids that can be contained and sealed in the damping cavity.

Particle Damped Bellows Seal

Initially, a feasibility study was conducted to determine the damping potential of metal powder. Molybdenum was selected on the basis of availability.

Various sizes of spherical powder were purchased and a simple test model was fabricated. The test model consisted of two aluminum blocks with a series of drilled holes to contain the spherical particles. The blocks were clamped together on a spring beam and mounted to the vibration plate as shown in Figure 10. Two methods of determining the amount of damping were employed: (1) forced vibration and (2) free vibration.

In forced vibration the exciting force was held constant (2-g peak) and the exciting frequency was varied. The damping was determined by measuring the bandwidth of resonance peak at the half-power points in terms of normalized frequency. The formula is as follows:

$$\Delta f \equiv \text{damping} \equiv 3.14\left(\frac{f_2}{f_n} - \frac{f_1}{f_n}\right)$$

where

f_n = resonant frequency,

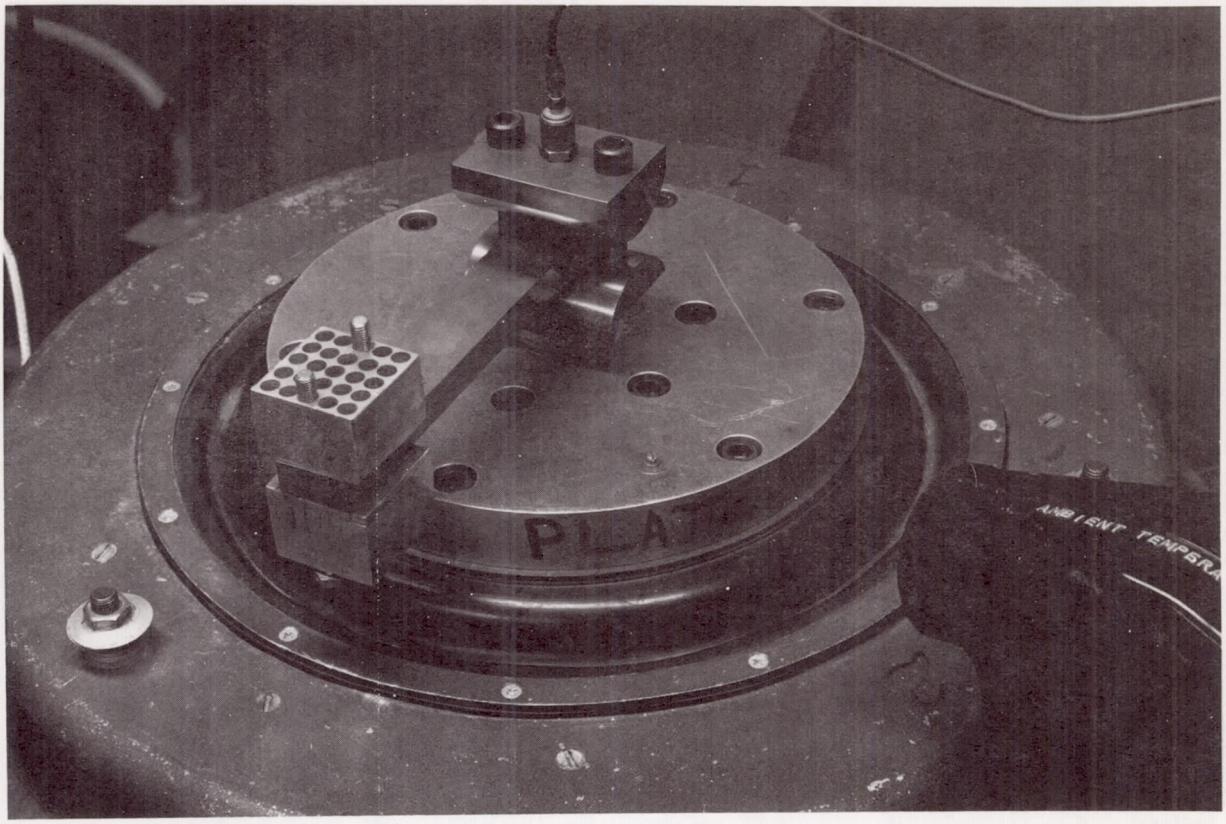

Figure 10. Particle damping test setup.

f_1 = lower half-power frequency,

and

f_2 = upper half-power frequency.

In the free vibration test, one end of the beam was fixed and the other end was deflected and allowed to freely return to its starting reference point. The damping was determined from the rate of decay of oscillation. This method is defined as the logarithmic decrement, and it is the natural logarithm of the ratio of any two successive amplitudes,

$$\Delta \equiv \text{damping} \equiv \ln \frac{X_2}{X_1} \quad ,$$

where

ln = natural logarithm,

X_1 = first cycle amplitude,

and

X_2 = second cycle amplitude.

The forced vibration method of testing was the most successful and reliable. Because of the loss of energy to the beam support, the data from the free vibration method were inconsistent.

In addition to damping, the frequency at resonance and the amplification at resonance were measured and recorded. The amplification is defined as the ratio of the acceleration into the beam to the acceleration out of the beam; i.e.,

$$\text{Amplification} = \frac{G_{out}}{G_{in}} \quad \text{or} \quad \frac{A_o}{A_i} \quad .$$

Tests were run on all six particle sizes with the fixture one-half full and on four particle sizes with the fixture full. There were not enough particles of the 110-μm (0.0043 in.) and 80-μm (0.0031-in.) sizes to fill the fixture. The results of the tests are shown in Table 1.

The results of the tests clearly indicate that the best damping characteristics are obtained with the 50-μm (0.0019-in.) particles. As the particle diameters decreased from 150-μm (0.0059-in.) to 50-μm (0.0019-in.), the resonant frequency decreased, the amplification decreased, and the damping from both the free and the forced vibration increased.

A test was conducted to determine what portion of the damping was caused by the mass of the particles and what portion was caused by the motion of the particles. Two steel masses (equal to the particle mass) were attached to the empty particle holders and the test was conducted in the same manner as the previous tests. The test was repeated with one of the steel masses removed. The results shown in Table 2 indicate that the masses caused the resonant frequency to decrease, the amplification to increase, and the damping to decrease.

Comparing the test results further indicates that damping can be attributed to relative movement of the particles in the container and that a solid mass of particles would have no effective damping.

Damping was next measured with the 50-μm (0.0019-in.) particle size varying the quantity by weight from 50 to 200 g. This was done to determine the effects of different amounts of the same particle size on damping. Figures 11 and 12 show the results of the tests from forced vibration and free vibration. The tabulated results shown in Table 3 indicate that as the number of particles increased, the resonant frequency decreased, the amplification decreased, and the damping increased. The results also show that only a small change in damping occurs from one-half full to full.

TABLE 1. TEST DATA, PARTICLE DAMPING

Particle Size	One-Half Full				Full			
μm (in.)	f_n [a]	A_o/A_i [b]	Δf [c]	Δ [d]	f_n	A_o/A_i	Δf	Δ
150 (0.0059)	165	10.80	0.368	0.288	155	4.51	0.735	0.523
140 (0.0055)	164	11.00	0.282	0.157				
110 (0.0043)	163	8.91	0.325	0.214	143	3.38	1.156	0.521
80 (0.0031)	162	7.36	0.416	0.273				
65 (0.0025)	162	6.49	0.543	0.300	149	3.61	1.081	0.826
50 (0.0019)	159	5.82	0.663	0.434	149	3.87	0.950	0.877
Empty	170	37.80	0.100	0.070				

a. f_n = resonant frequency

b. A_o/A_i = amplification

c. Δf = forced vibration damping

d. Δ = free vibration damping

TABLE 2. TEST DATA, EFFECT OF MASS

Weight, g	Fn, Hz	A_o/A_i	Δf	Δ
91.5	144	59.8	0.054	0.094
185.5	129	50.0	0.074	0.094

A test was also conducted to note any change in effective damping when a given mass of particles is loaded in two different ways. A total of 100 g of the 50-μm (0.0019-in.) size particles were loaded in such a way that all of the holes were one-half full. The forced vibration test was then run, and repeated with the same mass loaded, in which one-half the holes were empty and one-half were full. The results showed that no significant change in resonant frequency, amplification, or damping occurred.

The following general conclusions were drawn:

1. Particle damping is effective on the basis of the test model considered.

2. Damping increases with decreasing particle diameter.

3. Damping increases with increasing quantity of particles within the known limits of the test model considered.

4. Damping is unaffected by how a given mass of particles is loaded in the fixture.

Following the feasibility beam tests, actual seal hardware was fabricated for vibrational, nonrotating testing to establish the most effective level of fill of the particle containers. One piezoelectric accelerometer was bonded to the seal face with its exciting axis parallel to the seal's longitudinal axis. A control accelerometer was installed on the vibration table

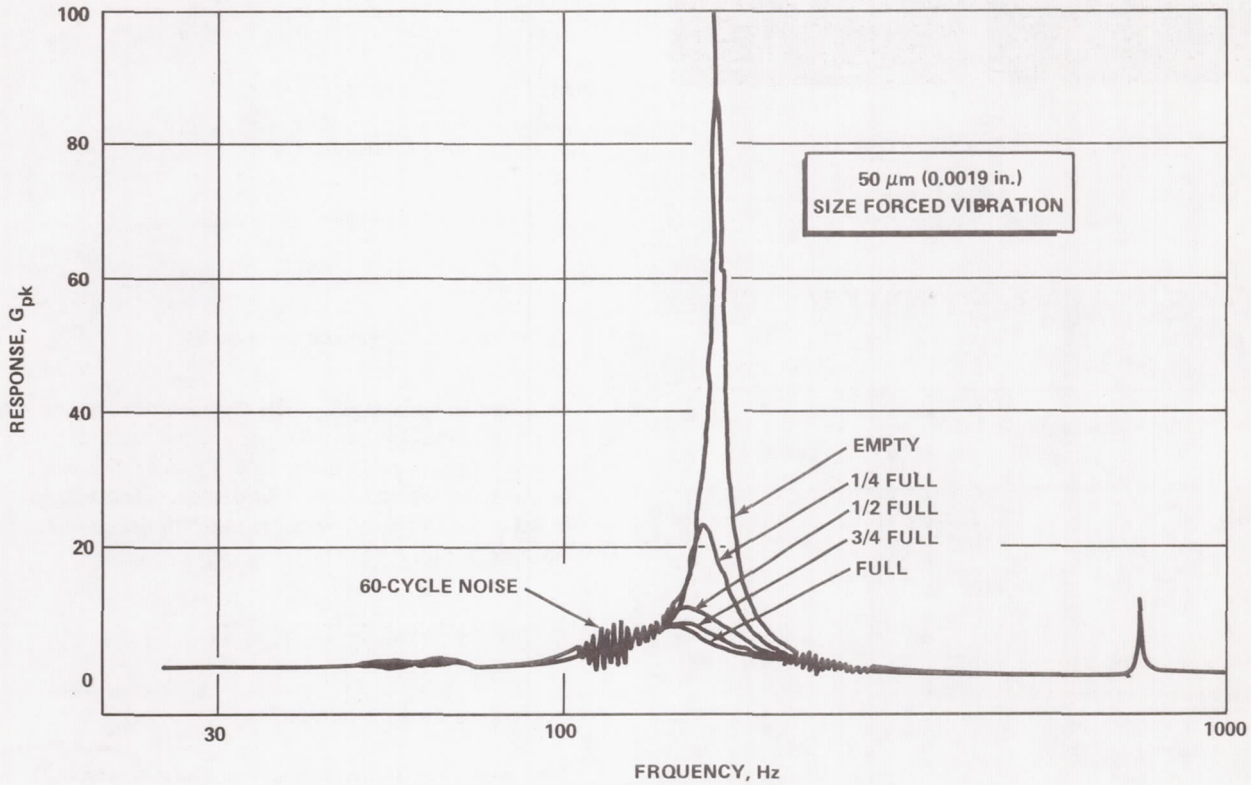

Figure 11. Particle vibration test.

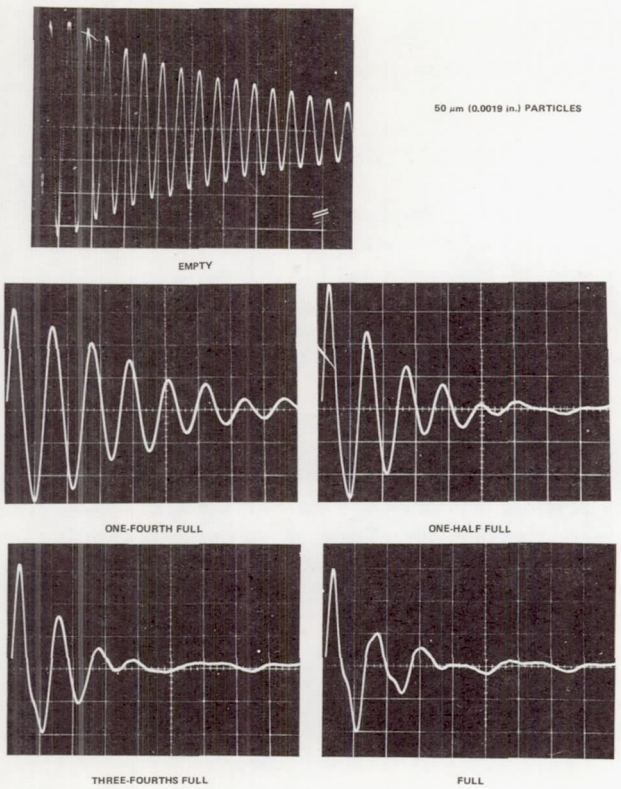

Figure 12. Free vibration test data.

TABLE 3. TEST DATA, EFFECT OF PARTICLE QUANTITY

	Weight, g	f_n, Hz	A_o/A_i	Δf	Δ
Empty	-	172	49.10	-	-
One-Fourth Full	50	162	11.90	0.281	0.211
One-Half Full	100	156	5.60	0.700	0.622
Three-Fourths Full	150	146	4.10	1.086	0.679
Full	200	144	3.99	1.003	1.076

to monitor input excitation. The test setup used is shown in Figure 13. No special environment was used nor was the bellows restrained. The motion of the seal was free axial movement responding to an input acceleration of 0.5 g. The molybdenum particles used to examine the damping effect were chosen based on previous beam tests, which show that particles having a -325 sieve size rating give the best results. This sieve size includes particles of 44-μm (0.0017 in.) and below. The tests were conducted with an exciting force held constant (0.5-g peak) and the frequency varied from 20 Hz to 1 kHz. Relative damping was determined by measuring the bandwidth of the resonant peak at the half-power points in terms of normalized frequency. Figure 14 illustrates the damping measurement.

As the bandwidth increases, relative damping also increases. The formula used to compute relative damping for this case is

$$\Delta f = \text{relative damping} = \pi \left(\frac{f_2}{f_n} - \frac{f_2}{f_n} \right) ,$$

where

f_n = resonant frequency,

f_1 = lower half-power frequency,

and

f_2 = upper half-power frequency.

In addition to damping, the frequency at resonance and the amplification at resonance were measured and recorded. The amplification is defined as the ratio of acceleration into the mass to the acceleration out of the mass and is another term used to define effective damping; i.e.,

$$\text{Amplification} = \frac{G_{out}}{G_{in}} \text{ or } \frac{A_o}{A_i} .$$

Table 4 shows these test results.

The test results for two cases, empty and the most effective, show that a reduction in amplification of 66 percent occurs from empty to three-fourths full.

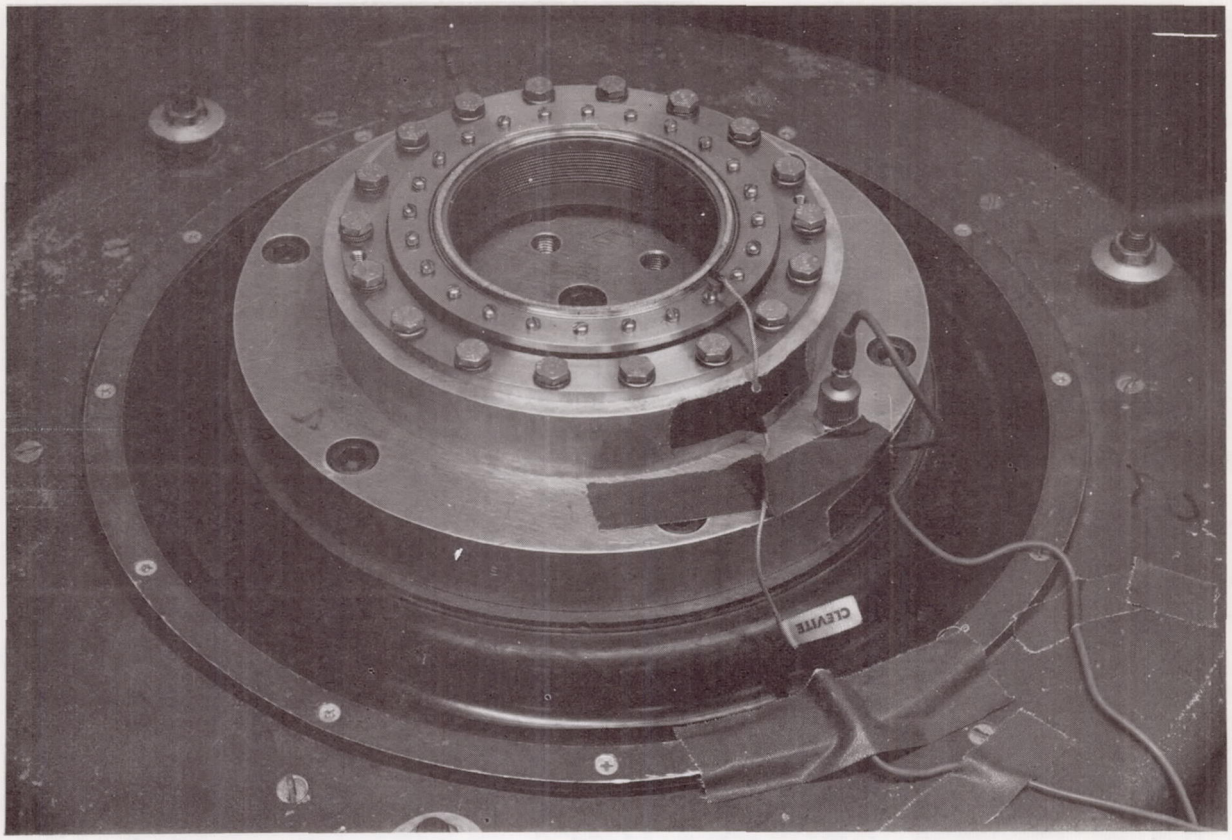

Figure 13. Vibration test setup, particle damping seal.

A series of tests was conducted to establish the amount of damping available with the spring mass system restrained as in actual operation. The bellows was compressed 2.16 mm (0.085 in.) by a disc mounted as an integral part of the vibration table, therefore imposing a constant load on the bellows. Tests were conducted in a frequency sweep range from 30 Hz to 2 kHz at vibration input levels of 1, 5, and 10 g rms with the particle holders both empty and three-fourths full. A short test was also run at three-eighths full to verify the particle holder optimum filling level. The accelerometer data were recorded on log paper plotting the frequency versus bellows response (g rms). As a result of loading the bellows, several points of resonance occurred at different frequencies. Damping could not be defined in terms of the fundamental frequency and the half-power points as was the case in the unrestrained bellows tests; therefore, maximum output response (g rms) was used and damping was

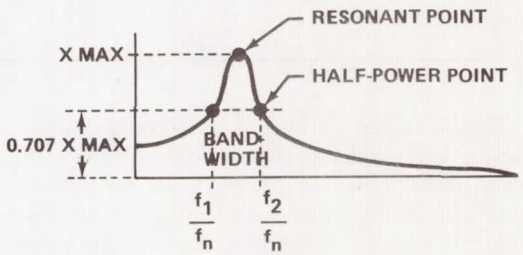

Figure 14. Damping measurement bandwidth.

referred to as the ratio of the two outputs, empty and three-fourths full. Table 5 presents the data for the tests showing damping as

$$\Delta = \text{damping} = \frac{\text{g rms undamped}}{\text{g rms damped}} \text{ with constant input .}$$

TABLE 4. TEST DATA, BELLOWS UNRESTRAINED

Test No.	Capsule Condition	f_1	f_n	f_2	Δf	A_o/A_i	G_{in}	G_{out}
1	Empty	75.5	75.9	76.3	0.033	108	0.5	54
2	One-Fourth Full	71.1	72.5	72.6	0.065	51	0.5	25.5
3	One-Half Full	66.5	67.7	68.3	0.0835	43	0.5	21.5
4	Three-Fourths Full	62.4	63.5	64.5	0.1039	35.2	0.5	17.6
5	Full	60.0	60.6	60.7	0.0364	93	0.5	46.5

TABLE 5. TEST DATA, BELLOWS RESTRAINED

Input, G_{in}	Maximum Response, G_{out}	Frequency at Maximum Response	Damping, Δ	Particles
1	28	1173	7.4	0
1	3.8	906		Three-Fourths Full
5	72	1039	2.08	0
5	34.8	1065		Three-Fourths Full
10	118	1021	2.2	0
10	53	1066		Three-Fourths Full

Based on the results of the vibration tests, a dynamic test model seal was designed for a liquid oxygen (lox) turbopump application for rotating tests up to 20 000 rpm and 98 m/sec (320 ft/sec) rubbing velocity. The configuration was based on the nonrotating model used for vibration testing, and five seals were procured. The same bellows configuration that was used in the nonrotating seal was used in the dynamic seal.

Three types of tests were scheduled; lox dynamic tests, dry dynamic tests, and dry vibration tests. The objective of the dynamic tests was to obtain partial seal face behavior characteristics associated with carbon face wear and seal leakage, with and without the damping device employed. Three tests were planned from which conclusions based on wear and leakage measurements were drawn. To aggravate the seal operating conditions, the seal was installed with a misalignment of 0.127 mm (0.005 in.) relative to the rotating mating ring. The mating ring was installed with an indicated axial runout of 0.050 mm (0.002 in.), which tilted the ring and provided a wobbling effect. The test environment was specified as pressurized liquid oxygen at pressures up to 1.72×10^6 N/m^2 (250 psig) with a shaft speed of 20 000 rpm.

A series of tests in lox with and without particles in the containers was conducted. The tests without particles resulted in severe mating ring and seal face wear and excessive leakage. The tests with particles in the containers showed the seal was sufficiently damped to achieve longer life and negligible leakage.

Figure 15 shows a typical comparison of these data.

A series of rotating tests was conducted to visually observe seal movement characteristics. The series was documented by high speed photography at speeds up to 20 000 rpm. Both the undamped and damped cases were observed. The tests consisted of installing the seal alternately at the same bellows compression of 2.43 mm (0.095 in.), which provided a spring load of 9.1 kg (20 lb). Both seals were of the type used in the first series of tests and there were no modifications to increase bellows spring rate. Initially, alignment of the undamped seal was set up with a mating ring axial runout of 0.100 mm (0.004 in.) to produce a wobbling effect. A pressurized environment was not used, reducing the carbon wear potential from hydraulic loading and readily permitting high speed camera access.

The first test, conducted without particles at 20 000 rpm, resulted in severe vibration and noise level; therefore, the induced wobbling effect was reduced by changing to a maximum axial runout of 0.025 mm (0.001 in.). The second test indicated improvement, but substantial bellows and seal movement was apparent. At a film speed of 500 frames/sec, a nutating action of the seal face and bellows was recorded, which indicated the type response when undamped. The nutating was determined to be 112.5 Hz. At a shaft speed of 20 000 rpm (333 Hz), the ratio of shaft speed to nutating frequency is 3:1.

Tests conducted with the same seal using particle damping showed no visible indication of nutating action at 20 000 rpm or less and produced no discernible noise levels. Review of the film verified the results obtained from vibration tests and simulated turbopump tests; i.e., the stable effect obtained with the use of particle damping.

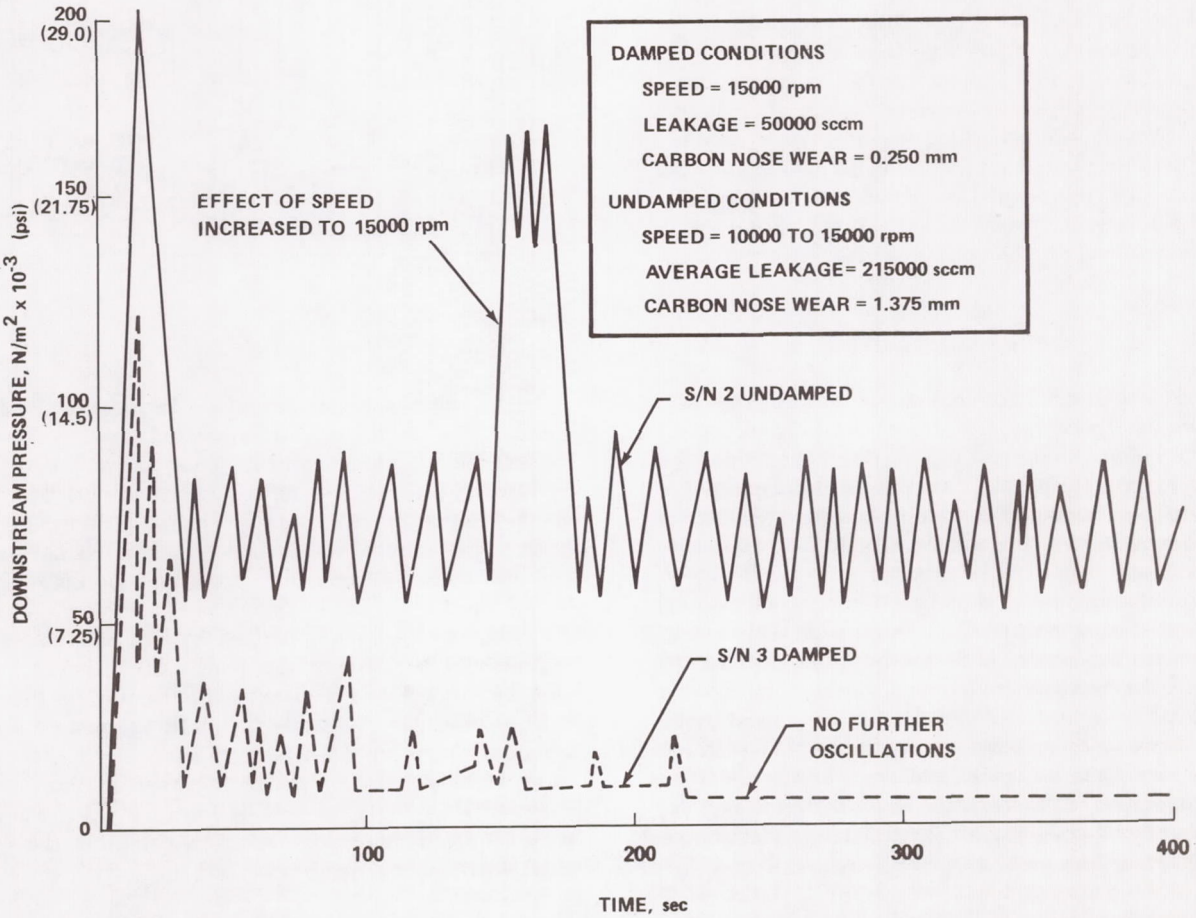

Figure 15. Particle damped rotating seal test.

PHASE II PRIMARY SEAL FACE LEAKAGE DURING STATIC CONDITIONS

The current method employed to determine turbopump shaft seal leakage during static conditions in-flight is to flow gaseous helium (GHe) during static ground testing and predict from the results what the static flight leakage will be. Recent experience with production turbopumps for pumping liquid hydrogen (LH_2) has indicated the lack of sufficient knowledge to extrapolate from the leakage data for GHe to the of LH_2. The relationships that exist between the parameters that govern static seal leakage are not completely understood, nor are all the flow governing parameters known. The objectives of this program were: (1) to establish the relationships between GHe and LH_2 static leakage, (2) to evaluate methods of improving the technique of predicting seal leakage, and (3) to determine the causes of face seal static leakage.

Ambient temperature GHe and LH_2 were used because one of the program objectives was to correlate the flow from one fluid to the other. GHe at 33°K (-400°F) was used to determine the temperature influence between it and the ambient GHe. Water was used to give a reference for the LH_2 data because it was thought the LH_2 would change to a two-phase fluid when passing through the seal, and the water would remain a liquid and therefore could be used to correlate with the LH_2.

Seal Tester Design

The tester design chosen for the program is shown in Figure 16. The features of the tester include a quartz optical flat mating ring, which was used to indicate parallelism during buildup and for viewing the leakage flow during testing. An alternate steel mating ring was also available. The model carbon seal support was constructed of Invar to reduce the amount of thermal distortion of the carbon seals to a minimum. Also, the model seals were fastened to the Invar sufficiently far removed from the sealing nose to further reduce the amount of thermal distortion. The deformation caused by the fasteners will decrease with distance. Therefore, the greater the distance is between the fastener and sealing surface, the smaller the distortion is. A comparison between the model and a production seal is shown in Figure 17.

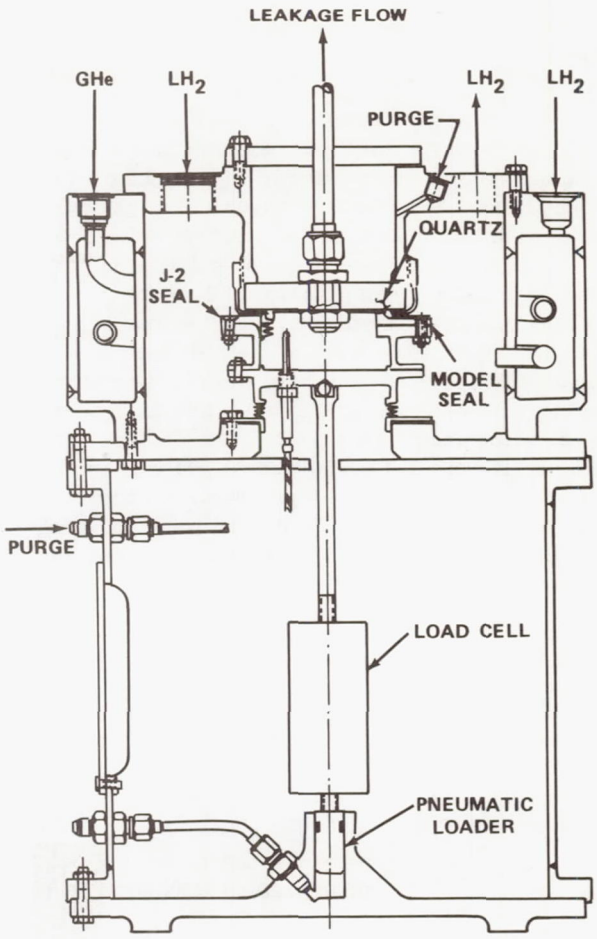

Figure 16. Face seal static leakage tester.

The body assembly contained an inner and outer cavity. The cavity was incorporated to allow flowing GHe at the LH_2 temperature. This was accomplished by flowing LH_2 into the outer cavity and into the cavity above the mating ring, and flowing GHe into the tube in the outer cavity, which acts as a heat exchanger and chills the GHe before it flows into the inner cavity.

The seal load was varied by the pneumatic cylinder located below the load cell. The location of the bellows allowed self-aligning of the seal. However, because the bellows mean effected diameter (MED) was affected by the varying pressure and the differences in the diameters of the seal and bellows, a calibration was required prior to testing to establish the total load on the seal.

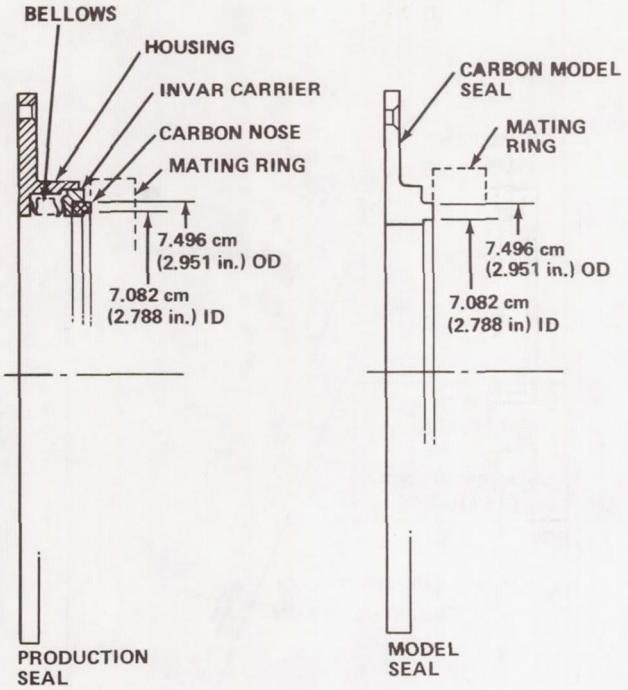

Figure 17. Seal configurations.

The pneumatic cylinder was of commercial design with a 2.85-cm (1.125-in.) bore. The load cell was 0 to 45.4 kg (0 to 100 lb.)

The static seal tester is shown installed in the facility in Figure 18.

Leakage Flow Analysis

Fluid flowing through the sealing face of a seal is described by various theories. The flow regime that exists is determined by either Mach number, Reynolds number, or molecular mean free path length. The lower limit of flow is in the molecular regime. The criterion used to indicate the existence of this regime is to compare the leakage clearance to the molecular mean free path length. The mean free path can be obtained from texts such as Reference 1. When the mean free path length is equal to or greater than the clearance, the flow is molecular. As the leakage gap is increased, relative to the mean free path, the flow enters the transient region. This region is a combination of molecular and laminar. The regime exists until the clearance is about two orders of magnitude greater than the mean free path.

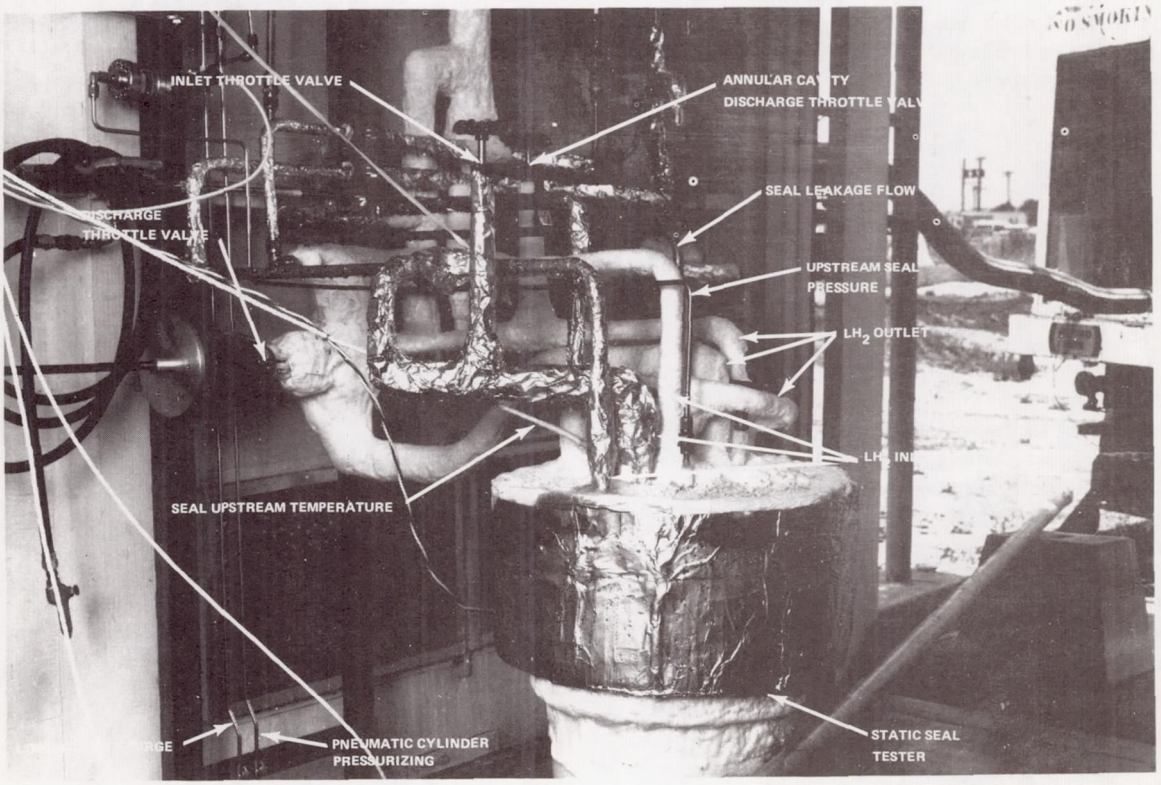

Figure 18. Static seal tester test setup.

Molecular flow is brought about when collisions between the molecules and the channel walls are an appreciable percentage of the total molecular collisions. A more detailed explanation can be found in Reference 2. Increasing the leakage clearance to the point where molecular collisions with the wall are no longer a sizable percentage of the total number will cause the flow to be laminar. The upper boundary of laminar flow is defined by a given value of Reynolds number, which in this case is about 500. By increasing the Reynolds number above this point sufficiently, the beginning of the turbulent flow range will be encountered. The flow regimes above this will not be considered here. The various flow regimes can be thought of as being brought about, other things being equal, by changing the leakage clearances. Flow regimes above turbulent would require clearances much larger than those encountered in face seals. Average clearances on the order of 2.5×10^{-4} to 2.5×10^{-5} mm (10^{-5} to 10^{-6} in.) were expected and were confirmed by test results. The seal clearance is caused by surface asperities. Waviness of relatively long wavelength as compared to the asperities could also be a factor. Surface finish measurements rarely indicate waviness. The flow regimes are shown diagramatically in Figure 19.

A method of locating the flow regimes for the various fluids is to calculate the mean free path and compare this to the "channel" dimension. Mean free path = $L = 1/\pi n\sigma^2$, where

$$\sigma^2 = \frac{mc}{3\pi\mu}$$

and

$$c = \sqrt{\frac{3kT}{m}} \quad ,$$

where k is equal to the universal gas constant divided by Avogadro's number, T is the temperature, and m is the molecular mass.

At standard conditions and GHe,

$n = 3 \times 10^{19}$ atoms/cm^3

$k = 1.37 \times 10^{-23}$ J/atom°K ,

and

$\mu = 1.92 \times 10^{-4}$ g/cm sec .

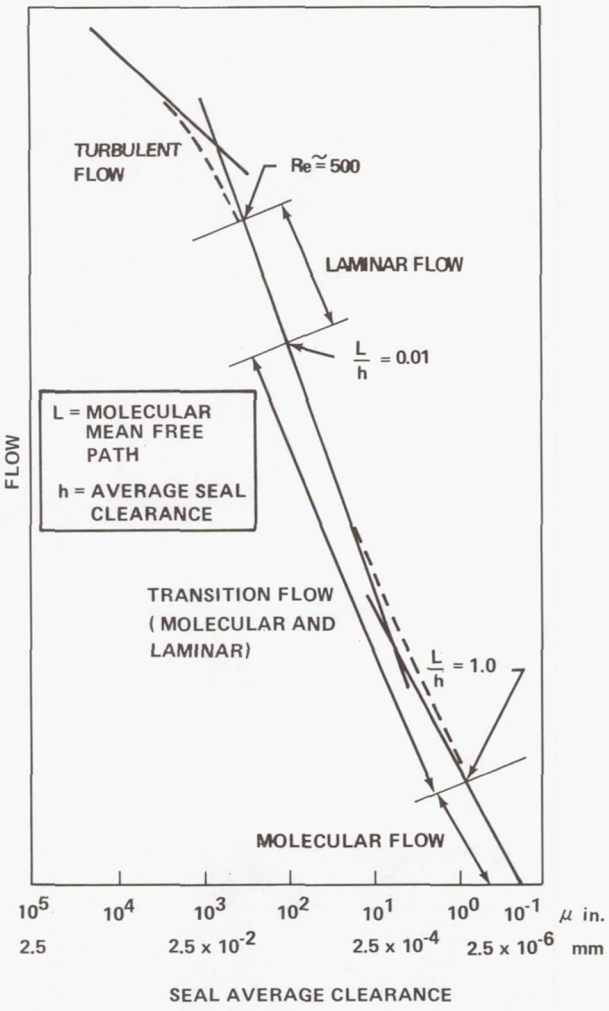

Figure 19. Flow regimes.

For GHe,

$m = 4 \times 1.66 \times 10^{-24}$ g .

At 33°K (-400° F) and GHe,

$n = 10^{21}$ atoms/cm^3

and

$\mu = 4.14 \times 10^{-5}$ g/cm sec .

At 20°K (-423° F) and LH_2,

$n = 142 \times 10^{17}$ atoms/cm^3 ,

$m = 3.32 \times 10^{-24}$ g ,

and

$$\mu = 1.23 \times 10^{-6} \text{ g/cm sec} \quad .$$

With the above conditions, the mean free paths for the respective fluids are:

Fluid	Mean Free Path	Expected Clearance
294°K (70°F) GHe	2×10^{-4} mm (0.8×10^{-5} in.)	2.5×10^{-4} mm (10^{-5} in.)
33°K (-400°F) GHe	4×10^{-6} mm (1.6×10^{-7} in.)	2.5×10^{-4} mm (10^{-5} in.)
LH_2	1.5×10^{-7} mm (0.6×10^{-8} in.)	2.5×10^{-4} mm (10^{-5} in.)

Test Results and Discussion

Testing was conducted while flowing ambient temperature GHe, 33°K (-400°F) GHe, LH_2, and water. These fluids were flowed through static carbon face seals at various pressures and various values of seal nose apparent stress (face loads).

The test results are presented as h/L versus load at constant pressures. This parameter is a function of seal geometry only and is not dependent on the test fluid. For this reason this parameter should correlate the data with the various fluids if a theory can be obtained that describes the flow while flowing each of the fluids. Plotting versus load will also indicate the dependence of the leakage parameter on load.

Figure 20 presents the data for the model seal with the 200-μmm (8-μin.) rms surface finish, and Figure 21 presents the data for the 2500-μmm (100-μin.) rms surface finish. Previous calculations indicated the ambient and 33°K (-400°F) GHe leakage would be in the transition flow regime. The mean free path calculation indicates the ambient GHe flow would be toward the molecular end of the transition regime, and the 33°K (-400°F) GHe would be toward the laminar. The same type of calculation indicated the LH_2 leakage would be either laminar or in the transition regime. However, this was based on flowing GH_2 instead of LH_2. The reason for this will be discussed later. A calculation for water was not performed, because in a liquid the mean free path is sufficiently short to ensure laminar flow under the conditions encountered in this test program.

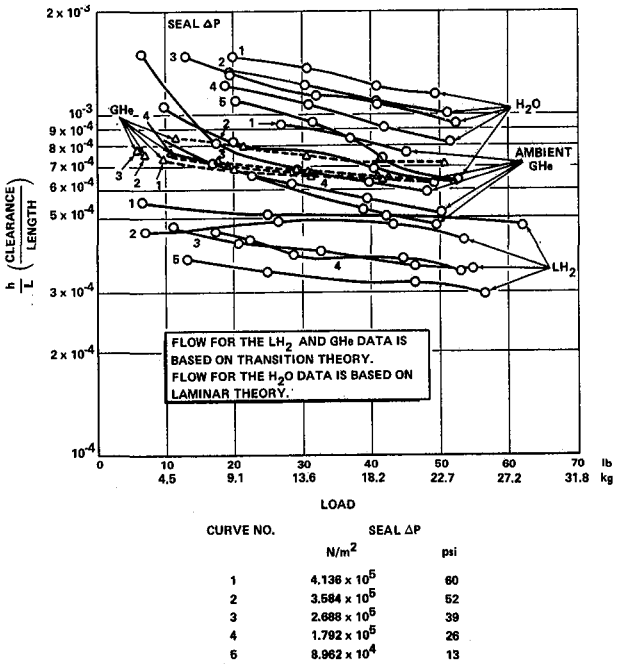

CURVE NO.	SEAL ΔP N/m^2	psi
1	4.136×10^5	60
2	3.584×10^5	52
3	2.688×10^5	39
4	1.792×10^5	26
5	8.962×10^4	13

Figure 20. Leakage parameter dependency on seal load and ΔP for a 25.4-cm (10-in.) circumference carbon static seal with a 200-μmm (8-μin.) rms surface finish.

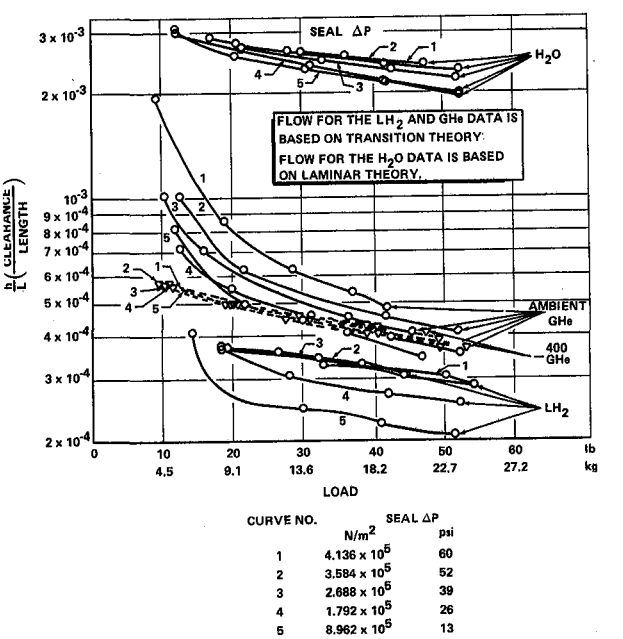

CURVE NO.	SEAL ΔP N/m^2	psi
1	4.136×10^5	60
2	3.584×10^5	52
3	2.688×10^5	39
4	1.792×10^5	26
5	8.962×10^5	13

Figure 21. Leakage parameter dependency on seal load and ΔP for a 25.4-cm (10-in.) circumference carbon static seal with a 2500-μmm (100-μin.) rms surface finish.

The LH_2 test results presented in Figure 20 are based on transition flow theory because this theory correlated the data better than the other theories that were tried. This figure was generated by solving the transition flow equation for h/L using test data and plotting lines of constant pressure. During the LH_2 portion of the test program, an optical flat that allowed observation of the leakage was installed. A rather large amount of boiling upstream of the seal was observed, indicating that the majority of leakage fluid was GH_2 and not LH_2. If some liquid entered with the gas, it would traverse the seal with very little change in quality. This would result in a higher flow than if the flow were almost all gas. Figures 20 and 21 indicate that this is not the case; therefore, it is concluded that GH_2 was flowing and not LH_2. Taking into account the care taken to reduce heat leaks by insulating, and the observed results [that of boiling even at 4.136×10^5 N/m^2 (60 psig)], it seems very reasonable to assume that the primary production seal leakage during a turbopump run will also be GH_2 and not LH_2. This may even occur during static leakage in the turbopump; i.e., when the turbine is at ambient temperature.

The spread encountered in the ambient GHe, LH_2, and water data in Figures 20 and 21 is not completely explainable. The isobars for a given fluid being separated from one another indicates that the flow theory does not exactly describe the flow, possibly because of plastic deflection of the seal. By changing the order of the equation, the isobars are made to converge. This method can be used to correlate the ambient GHe and the LH_2 data and obtain a much closer correlation than is possible by following the transition flow theory. The results obtained by this method are shown for the seal with the 200-μmm (8-μin.) finish in Figure 22 and for the seal with the 2500-μmm (100-μin.) finish in Figure 23. The isobars were made to converge by raising the flow term in the transition flow equation for the GHe data to the 0.4 power.

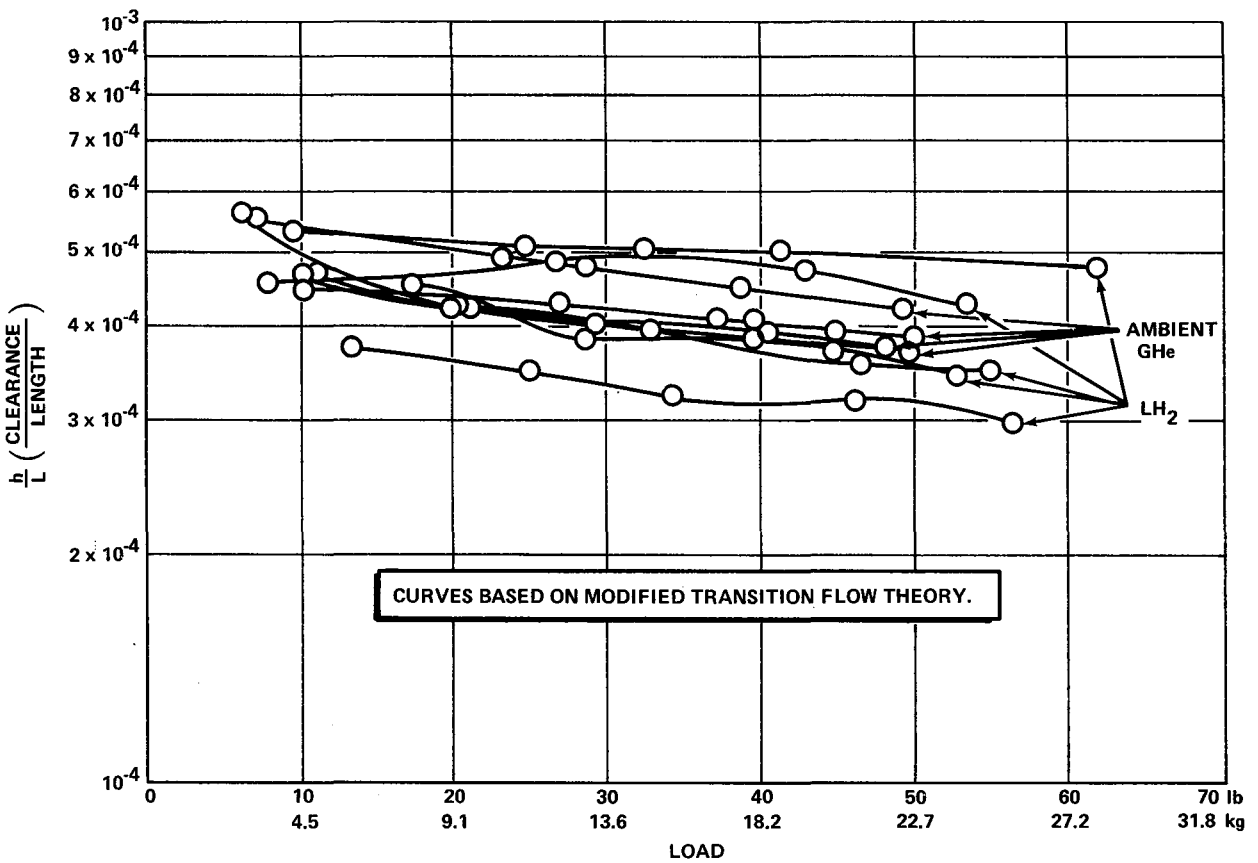

Figure 22. Correlations between ambient GHe and LH_2 seal leakage for a seal surface finish of 200 μmm (8 μin.).

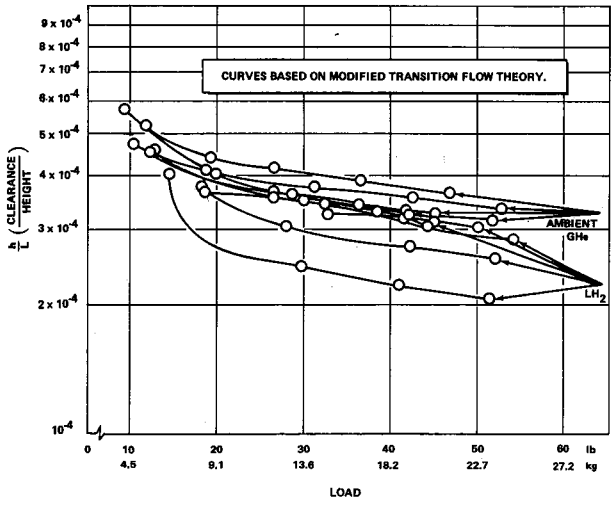

Figure 23. Correlations between ambient GHe and LH_2 seal leakage for a seal surface finish of 2500 μmm (100 μin.).

The above method holds for the two model seals as shown and would therefore be expected to apply to the production seal. During LH_2 testing with the production seal, the leakage was at least two orders of magnitude larger than with the model seals. The flow with GHe was about the same for the production and model seals. Therefore, with the production seal, the higher LH_2 leakage indicated that correlation between GHe and LH_2 would not be possible with the method employed in this program, as long as the model seal data correlated. These results indicate the geometric parameter h/L is changing. To obtain a correlation with this occurring would require a method such as that of statistical correlation. However, this would require a large number of data points, which was beyond the scope of this program.

This lack of correlation between the LH_2 and GHe data for the production seal was caused by thermal distortion. The carbon nose was held by an Invar carrier. The carbon was lapped flat at ambient temperature, and then, when it was chilled to the LH_2 temperature, the difference in contraction between the carbon and Invar distorted the carbon, and thus the flow path. No way of predicting this distortion has been found. The model seals were designed to minimize thermal distortion, as pointed out earlier in this report; therefore, data correlation over a large temperature difference was successful with these seals.

The water data did not agree as closely as expected. Figures 20 and 21 indicate the lack of agreement between the water data and the GHe and LH_2 data. The water data were obtained to compare with the LH_2 data. Originally it was thought that when leaking LH_2, it would enter the seal as a liquid and change on the way through the seal to a two-phase fluid. The water data would be used as a reference to correlate the LH_2 data because it remains a single-phase fluid. When it was determined that the LH_2 enters as a gas, the water data were no longer of primary interest and a better correlation was not pursued.

Returning to Figures 22 and 23 and calculating the flow expected in LH_2 from the ambient GHe data at a load of 5.44 kg (12 lb) results in the following: for the 200-μmm (8-μin.) seal, the GHe data indicate that the LH_2 flow will be 0.807 cm^3/sec. This is the liquid flow; the gas flow would be larger by the density ratio. The test data for LH_2 indicate a flow of 1.12 cm^3/sec. The 2500-μmm (100-μin.) seal gas data predict an LH_2 flow of 0.496 cm^3/sec as compared to the actual LH_2 test data of 0.297 cm^3/sec. These results indicate that good correlation was achieved. However, as discussed before, the results cannot be applied to the present configuration of the production fuel seal.

A quartz optical flat was used as a mating ring in an attempt to view LH_2 as it was leaking past the seal. Visual observation indicated boiling upstream of the seal was taking place, but no fluid could be seen leaking through the seal. Motion pictures were also taken with a telephoto lens. The results obtained from the films were the same as those obtained from direct observations. These results, and the results based on flow theory presented earlier, indicate the leaking fluid was GHe and not LH_2. The boiling upstream of the seal was caused by heat leaks, thus causing the leaking fluid to be a gas.

Flow Theory

Molecular flow is brought about when the channel dimension is the same order as the mean free path of the gas molecule. The derivation of the equation for this regime is due initially to Knudsen [3] and was obtained from Reference 4.

Knudsen begins with the assumption that the number of molecules striking 1 cm^2 of surface per

second is $1/4\ N\bar{c}$, where $\bar{c}$ is the average velocity of the molecules. If there are N molecules per cubic-centimeter, the number dN, where d is the derivative, with velocity components between c and c + dc is given by the Maxwell distribution law as

$$dN = \frac{4N}{\alpha^3 \sqrt{\pi}}\ c^2\ e^{\frac{c^2}{-\alpha^2}}\ dc \quad .$$

The terms are defined in Reference 4, where α is the most probable speed and e is the base of the natural log. The number of these molecules that strike 1 cm^2 of surface per second is then 1/4 cdN. The molecules that have a component of velocity of translation w parallel to the wall on striking are absorbed and remitted equally in all directions. The momentum given the wall by these dN molecules is 1/4 cm wdN. Since w is the component of the velocity of the gas molecules parallel to the wall, w may be written as Kc, where K is a constant of proportionality. This expresses w as a fractional part of c, the molecular velocity, and ascribes the Maxwell distribution to the components w in this manner. The momentum transfer is $1/4\ Kc^2\ wdN$. The momentum B given the wall by molecules of all velocity is therefore given by

$$B = 1/4\ NK\ \frac{4}{\sqrt{\pi}}\ m \int \frac{c^4}{\alpha^3}\ e^{\frac{c^2}{-\alpha^2}}\ dc = 1/4\ NK\ m\ 3/2\ \alpha^2 .$$

Substituting $\bar{c}$ for α, where $\bar{c} = 2\alpha/\sqrt{\pi}$, results in

$$B = \frac{3\pi}{32}\ NmKc^{-2} \quad .$$

As $\bar{c}$ is $\Sigma c/N$,

$$K\bar{c} = \Sigma\ \frac{Kc}{N} = \frac{\Sigma w}{N} = V \quad .$$

This V is the geometric mean of the velocity of all molecules. It is therefore the velocity of the mass of gas down the channel, and the momentum $B = 3\pi/32\ Nm\bar{c}V$, which assumes V constant across the channel.

Consider a flow channel of rectangular dimensions with dL the element of length, b the width, and A its area. In dt sec, this channel receives an amount of momentum given by $3\pi/32\ Nm\bar{c}VbdLdt$. Setting $Nm = \rho$, the density of the gas, and expressing $\bar{c}$ in terms of the pressure P, from the relation $P = \pi/8\ N\ mc^{-2}$, the above quantity becomes $3/8\ \sqrt{\pi/2}\ \rho \sqrt{\rho/\rho}\ VbdLdt$. If it is assumed that the wall dbL gets the whole momentum that results from the pressure drop $-(dP/dL)\ dL$, one obtains the relation between the momentum transfer, $-A(dP/dL)\ dLdt$ in the time dt due to the pressure difference across the area A, and the momentum transfer to the wall as

$$3/8 \sqrt{\frac{\pi}{2}}\ \rho \sqrt{\frac{P}{\rho}}\ Vb = -A\frac{dP}{dL} \quad .$$

For G the mass flow $G = AV$; therefore

$$G = -8/3 \sqrt{\frac{2}{\pi}} \sqrt{\frac{\rho}{P}}\ \frac{A^2}{b}\ \frac{dP}{dL} \quad .$$

If the ratio $\rho/P = \rho_1$,

$$G = 8/3 \sqrt{\frac{2}{\pi}} \sqrt{\rho_1}\ \frac{A^2}{b}\ \frac{dP}{dL}$$

and $Q_t = G/\rho_1$; then

$$Q_t = -8/3 \sqrt{\frac{2}{\pi}} \sqrt{\frac{1}{\rho_1}}\ \frac{A^2}{b}\ \frac{dP}{dL} \quad .$$

Therefore

$$Q_t\ \frac{b}{A^2}\ dL = -8/3 \sqrt{\frac{2}{\pi}}\ \frac{dP}{\sqrt{\rho_1}} \quad .$$

If the area is bh, where h is the channel height and the pressures are P_1 and P_2 $(P_1 > P_2)$,

$$Q_t = \frac{1}{\sqrt{\rho_1}}\ \frac{(P_1 - P_2)}{3/8 \sqrt{\frac{\pi}{2}} \int \frac{b}{(bh)^2}\ dL} \quad .$$

Therefore,

$$Q_t = 8/3 \sqrt{\frac{2}{\pi}} \frac{(P_1 - P_2)\, bh^2}{\sqrt{\rho_1}\, L} \quad .$$

This, therefore, describes the flow in the molecular flow regime. In the laminal regime the derivation is from Reference 5. The equation for an element of fluid in static equilibrium can be written as

$$2Pby - (P - dP)\, 2by - 2\, Tbdx = 0 \quad ,$$

where T is the shear defined by Newton's law of viscous flow $T = -\mu\, du/dy$, where u is the velocity of a particle at a distance y from the center of the passage and μ is the viscosity. Combining these two equations,

$$du = \frac{y}{\mu}\, dy\, \frac{dP}{dx} \quad .$$

Integrating with limits of $y = h/2$ and $u = 0$,

$$u = \left(\frac{h^2}{8} - \frac{y^2}{2}\right) \frac{1}{\mu} \frac{dP}{dx} \quad .$$

The area of flow is 2by for an increment of flow dQ; therefore,

$$dQ = \frac{2by}{\mu} \left(\frac{h^2}{8} - \frac{y^2}{2}\right) \frac{dP}{dx} \quad .$$

Integrating the flow over the entire flow area, putting in limits, and adding a minus sign because dP/dx is negative in the direction of flow,

$$Q = \frac{bh^3}{12\mu} \frac{dP}{dx} \quad .$$

If $\rho g Q = w$,

$$w = -\frac{\rho g bh^3}{12\mu} \frac{dP}{dx} \quad ,$$

and $P/\rho = RT$, the perfect gas law; thus,

$$w = -\frac{gbh^3\, P}{24\mu\, RT} \frac{dP}{dx} \quad .$$

Integrating from P_1 to P_2 and 0 to L yields

$$w = -\frac{gbh^3}{24\mu\, RTL} \left(P_1^2 - P_2^2\right) \quad .$$

The region between the molecular and laminar is known as the transition region. In this region both laminar and molecular flow effects are in operation. The method used to describe this flow regime is the direct addition of the two flow theories. The result is

$$w = 8/3 \sqrt{\frac{2}{\pi}} \frac{bh^2 \left(P_1 - P_2\right)}{\rho L \sqrt{\rho_1}} + \frac{bh^3 \left(P_1^2 - P_2^2\right) g}{24\mu\, LRT\rho} \quad .$$

CONCLUSIONS

Phase I

Based on test data the piston damped and orifice damped bellows seal designs would work successfully for constant pump conditions and environment. However, they both utilize a viscous friction method of controlling induced vibratory motion, and the orifice size and piston clearance must be varied with different frequencies and amplitudes as well as with different viscosities of the damping fluid. They also provide no damping in a gas environment or for very small seal face displacements. It was concluded that these two designs were not a great improvement over current designs unless they were in a predetermined constant environment.

The particle damped seal would be a more satisfactory design. Sufficient damping was achieved in all environments and the design is not affected by changing frequencies and amplitudes. The design is very simple and there are no wearing parts with no contamination or fire risk when in the proximity of propellants. This seal will achieve the initial objectives of lower leakage, greater reliability, and longer life.

Phase II

GHe data were used to predict LH_2 leakage through static carbon face seals. A leakage

parameter, which is a function of seal geometry only, was obtained from transition flow theory and was used to correlate between fluids that fall in this flow regime. Using this theory, the leakage flow could be defined even when fluid physical properties were changed.

The ability to predict LH_2 leakage from GHe test data was demonstrated. This was achieved by modifying the transition flow equation empirically. Leakage flow dependence on seal pressure drop was best defined for the 33°K (-400°F) GHe data and to a lesser extent for the ambient GHe and LH_2 data.

The influence of seal load on leakage was demonstrated. As would be expected, the leakage decreases as load is increased. The relationship between flow and load is nearly linear.

Leakage flow was shown to decrease as seal surface finish increased from 200 μmm (8 μin.) rms to 2500 μmm (100 μin.) rms, thus indicating the asperities or serrations offered more resistance to flow.

REFERENCES

1. Hirschfelder, J.O.; Curtiss, C.F.; and Bird, R.B.: Molecular Theory of Gases and Liquids. John Wiley and Sons, Inc., New York, 1954.

2. Duschman, S.; and Lafferty, J.: Scientific Foundations of Vacuum Technique. John Wiley and Sons, Inc., New York, 1962.

3. Knudsen, M.: Ann. Physik, vol. 28, no. 75, 1909, p. 999; vol. 35, 1911, p. 389.

4. Lobe, L.: Kinetic Theory of Gases. McGraw-Hill Book Company, New York and London, 1934.

5. Grinnel, S.K.: Flow of a Compressible Fluid in a Thin Passage. ASME 55-SA-13, May 1956.

BIBLIOGRAPHY

Allen, C.M.; Bell, J.C.; et al.: Rotating-Shaft Helium Seal Investigation. Battelle Memorial Inst., Columbus, Ohio, NP-11243 Contract DA-44-099-eng-3375, August 25, 1959.

Batch, B.A.; Goldring, B.A.; and Winney, P.E.: An Instrument for Measuring the Main Surface Profile on Seal Faces. Journal of Scientific Instruments, vol. 1, series 2, 1968.

Bauer, P.: Investigation of Leakage and Sealing Parameters. IIT Research Institute, Technical Report AFRPL-TR-65-153, August 1965.

Bell, K.J.; et al.: Flow Through Annular Orifices. Trans. ASME, vol. 79, April 1957, pp. 593-601.

Crego, D.F.: Centrifugal Compressors: Seals and Sealing Systems. Petroleum Refinery, vol. 7, no. 34, Jan. 1955, pp. 143-6; Petroleum Engineer, vol. 28, Feb. 1956, pp. C17-22.

Davies, M.G.: The Generation of Lift by Surface Roughness in Radial Face Seals. Int. Conf. on Fluid Sealing, Paper E-4, British Hydrodymechanics Research Association, April 17-19, 1961.

Dawson, L.J.: Development and Design of Mechanical Seals for Centrifugal Pumps. Ingersoll-Rand, 1950.

Dawson, P.: Investigation of Cavitation in Lubricating Films Supporting Small Loads. Proc. Conf. On Lubrication and Wear, Paper 49, Instn. Mech. Engrg., London, Oct. 1-3, 1957, pp. 93-99.

BIBLIOGRAPHY (Continued)

Dega, R. L.: Recent Advances in Lip Seal Technology. National Conference Industrial Hydraulics, October 1960, pp. 154-63.

Denny, D. F.: Some Measurements of Fluid Pressures Between Plane Parallel Thrust Surfaces and Special Reference to Radial Fact Seals. Wear, vol. 4, no. 1, 1961, pp. 64-83.

Findlay, J. A.: Cavitation in Mechanical Face Seals. ASME, 67-WA/LUB-20.

Gaibel, E.; and Lyman, F. A.: A Theoretical Investigation of Leakage Through Rotary Shaft Seal. Report 850489, U.S. Naval Eng. Experiment Sta., Annapolis, Nov. 28, 1961.

Gresham, W. A., Jr.; et al.: Review of the Literature on Two-Phase (Gas-Liquid) Fluid Flow in Pipes. Engineering Experiment Station of the Georgia Institute of Technology, WADS-TR 55-422, June 1955, Contract AF33(616)2660, AD 95752.

Grinnel, S.K.: Flow of a Compressible Fluid in a Thin Passage. ASME 55-SA-13, May 1957.

Hamilton, D. B.; Walowit, J. A.; and Allen, C. M.: A Theory of Lubrication by Microirregularities. Journal of Basic Engineering, Trans. ASME, series D, vol. 88, no. 1, March 1966, pp. 177-185.

Huhn, D.: Theory of Fluid Sealing. Int. Conf. On Fluid Sealing, Paper D2, April 17-19, 1961.

Hydrogen Handbook, A Compilation of Properties, Handling and Testing Procedures, Compatibility with Materials and Behavior at Low Temperatures. Arthur D. Little, Inc., under Contract with Parker Aircraft Co., AFFTC TR60-19, Contract AF33(616)6710, AD 242285, April 1960.

Jackobsson, B.; and Floberg, L.: The Finite Journal Bearing, Considering Vaporization. Trans. of Chalmers University of Tech., No. 190, 1957, Gothenburg, Sweden, Report No. 3 from the Institute of Machine Elements.

Kearton, W. J.: Flow of Air Through Radial Labyrinth Glands. Inst. of Mech. Engrg., Proceedings, vol. 169, no. 30, 1955, pp. 539-52.

King, A. L.: Bibliography on Fluid Sealing. BIB-1, British Hydrodynamics Research Association, South Road, Temple Fields, Harlow, Essex, England, May 1962.

Mayer, E.: Leakage and Wear in Mechanical Seals. Machine Design, vol. 32, March 3, 1960, pp. 106-13.

McCray, C. R.: Radial Positive-Contact Seals. Machine Design, The Seals Book, Jan. 19, 1961, pp. 9-14.

Miller, E. E.; et al.: Physical Theory for Capillary Flow Phenomena. Journal of Applied Physics, vol. 27, 1956, pp. 324-32.

Miyakawa, Y.: Influence of Surface Roughness on Boundary Friction. Journal of the American Society of Lubrication Engineers, May 1965.

Nau, B. S.; and Turnbull, D. E.: Some Effects of Elastic Deformation on the Characteristics of Balanced Radial Face Seals. Int. Conf. on Fluid Sealing, Paper D3, British Hydromechanics Research Assn., Harlow, Essex, England, April 17-19, 1961.

Nau, B. S.: Cavitation in Thin Films. The British Hydrodynamic Research Association, TN832, Nov. 1964.

BIBLIOGRAPHY (Concluded)

Rudinger, G.: Nonsteady Discharge of Subcritical Flow. ASME, Paper 60-WA-152 for Meeting Number 1960.

Stair, W.K.: Bibliography on Dynamic Shaft Seals. Preliminary Issue, University of Tennessee, Engineering Experiment Station, May 1962.

Study of Dynamic and Static Seals for Liquid Rocket Engines, General Electric Company, NASA Contract No. NAS7-102, Final Report Vols. 1 and 2, February 25, 1963.

Summers-Smith, D.: Laboratory Investigation of the Performance of a Radial Face Seal. Int. Conf. on Fluid Sealing, Paper D1, British Hydromechanics Research Assn., Harlow, Essex, England, April 17-19, 1961.

Tao, L.N.; and Donovan, W.: Through-Flow in Concentric and Eccentric Annuli of Fine Clearance With and Without Relative Motion of Boundaries. Trans. ASME, vol. 77, 1955, pp. 1291-1301.

The Physical and Thermodynamic Properties of Helium. Whittaker Controls, Los Angeles, Calif., September 1960.

Tolansky, S.: Surface Microtopography. Internal Science and Technology, vol. 9, September 1962, pp. 32-9.

Vermes, G.: Fluid Mechanics Approach to Labyrinth Seal Leakage Problem. Trans. ASME, series A, Journal of Engineering for Power, vol. 83, April 1961, pp. 161-9.

Wilkinson, S.C.W.: Mechanical Seal Design. Engineering Materials and Design, vol. 5, Aug.-Sept. 1962, pp. 572-576, 664-667.

Zabriskie, W.; et al.: Labyrinth Seal Leakage Analysis. Trans. ASME, series D, Journal of Basic Engineering, vol. 81, September 1959, pp. 326-6.

TWO-PHASE PUMPING OF CRYOGENIC PROPELLANTS

By

H. P. Stinson and L. A. Gross

SUMMARY

Two-phase cryogenic propellant pumping techniques developed during the past 5 years are discussed herein. During this period the theory of two-phase pumping of hydrogen has been developed into an operational technique that can result in significant benefits to space vehicle propulsion systems. Using two-phase pumping techniques, zero LH_2 tank net positive suction head (NPSH) has been demonstrated on turbopump and rocket engine firings, and limited experimental results have shown that two-phase pumping of liquid oxygen is feasible. Design techniques have been developed for improving the two-phase pumping capability of inducers.

INTRODUCTION

Historically, rocket engine pump net positive suction heads have been driven progressively lower to exploit the vehicle performance gains available through the use of lightweight, low pressure propellant tanks and the reduced tank pressurization system requirements. It is ultimately desired to store cryogenic propellants at their vapor pressure in appropriately designed low pressure tanks and eliminate the need for engine prestart pressurization systems. To do this, it is necessary that the propellant pumps be designed to operate at the condition in which the propellant vapor pressure and the pump inlet pressure are equal and two-phase propellant (liquid and gas) exists at the inlet. The recent efforts to develop a two-phase pumping capability for cryogenic pumps are described herein.

The capability of the propellant pump to operate at a low NPSH is based upon the ability of the inlet section of the pump (usually an inducer) to operate partially cavitated without an appreciable performance loss. Performance loss is measured by the degradation of the pump-developed head as the NPSH is lowered. An NPSH greater than the minimum value must be supplied to achieve satisfactory engine operation.

It is well known [1, 2] that fluids experience a degree of subcooling because of vaporization during cavitation. The amount of subcooling is dependent upon the thermodynamic properties of the fluid and is typically termed the vapor pressure depression or thermodynamic suppression head (TSH). At conditions near the liquid critical pressure, the TSH available can become significant. The NPSH that must be supplied to the pump is considered to be composed of the total pressure above vapor pressure at the pump inlet plus the TSH available. With liquids such as ambient water, the TSH available is insignificant. With ambient pressure cryogenic propellants, however, a substantial TSH is available. Under certain circumstances the total NPSH required by the pump can be supplied by the TSH; the pressure at the inlet to the pump will be equal to the vapor pressure, and the regime of two-phase pumping is entered.

The B-factor concept for analyzing thermodynamic effects of cavitation as introduced by Stahl and Stepanoff [1] has been refined and correlated with cavitating venturi data for several liquids by Gelder, Ruggeri, and Moore [3]. Moore [4] applied these methods to pump cavitation performance but pointed out that their method did not apply if a vapor-liquid existed in the inlet line to the pump.

A quasi-static vaporization model to calculate B-factor and a table presentation of B-factors for common liquids were developed by Hord and Voth [5]. The use of these techniques predicted the inception point for two-phase pumping; however, they gave no clue as to pump performance once the two-phase regime had been entered.

TWO-PHASE PUMPING EXPERIMENTS

Meng and Connelly [6] performed a series of experiments in which the inlet line of an LH_2 pump inducer was heated to produce nonequilibrium vapor-liquid during operation. It was found that significant amounts of vapor (15 percent by volume) could be ingested without adversly affecting the pump

performance. Furthermore, it was shown that the pump inducer in two-phase operation performed essentially the same as for single-phase operation when the inlet flow coefficient was corrected for the presence of vapor. Since the performance as measured by the head produced did not drop, it was concluded that the vapor was collapsed in the inducer passages. Suction performance, when corrected for flow coefficient, remained essentially unchanged and led to the conclusion that the available TSH was unaffected by the two-phase fluid. The vapor-liquid combination was thus pumped as a homogeneous mixture in which the previously discussed thermodynamic improvements apply. The vapor was collapsed internal to the inducer.

After Meng and Connelly demonstrated the feasibility of pumping two-phase hydrogen, a number of pump test programs were conducted to evaluate the two-phase pumping capability of various pumps by exploiting the thermodynamic effects of cavitation. A program was conducted by Rocketdyne [7] to determine the vapor handling capability of the J-2 hydrogen pump. Hydrogen at several bulk temperatures was pumped from a facility run tank into a catch tank with a screen placed in the suction duct to provide sufficient pressure drop to obtain two-phase flow at the inlet to the pump. A point immediately upstream from the screen was used as the reference point to establish the liquid hydrogen fluid properties. A constant enthalpy expansion was assumed between the reference station and the pump inlet. Using the enthalpy determined by pressure and and temperature measurements at the reference station and the pressure measured at the pump inlet, the quality of the hydrogen at the pump inlet was determined. Typical test results using this method of calculation are presented in Figure 1a [7]. It can be seen that the pump was capable of operating with 20 percent vapor by volume at the inlet at this particular flow and speed. It was concluded from this program that the J-2 hydrogen pump had sufficient vapor handling capability to allow zero tank NPSH operation in the S-IVB stage at hydrogen bulk temperatures above approximately 23.9°K.

At approximately the same time the J-2 pump testing was being conducted, two efforts were initiated by the Lewis Research Center in support of the nuclear propulsion system to investigate two-phase hydrogen pumping. The first of these programs [8] was similar to the J-2 hydrogen pump program in that the two-phase pumping capability of an existing pump, the MK-25 LH_2 pump, was exploited by elevating the hydrogen temperature. Rocketdyne again placed a screen in the suction system to provide sufficient pressure drop to obtain two-phase hydrogen at the pump inlet, and the data reduction technique of assuming a constant enthalpy process between the reference station and the pump inlet was employed. A typical set of data from this program is presented in Figure 1b [8]. The ability to meet the suction performance requirements imposed by the nuclear propulsion system was successfully demonstrated in this test program. An Aerojet program [9] differed from the Rocketdyne program in two respects; (1) a low-speed inducer was used to obtain low NPSH operation and (2) the zero tank NPSH mode of operation was investigated. The twin-spool turbopump consisted of a high speed turbopump with a low speed inducer driven by a coaxial shaft. The vapor handling capability of the twin-spool pump was sufficient to allow satisfactory pump operation with a two-phase mixture in the propellant tank (zero tank NPSH). This demonstration of zero tank NPSH operation provided a base for using this mode of operation with a flight-configuration feed system. A typical set of data from this program showing pump performance as a function of tank NPSH is presented in Figure 1c [9].

Based upon the information obtained from these pump test programs, an in-house program was initiated at the Marshall Space Flight Center to demonstrate the zero tank NPSH mode of operation using a flight propulsion system. This program was conducted in two phases; J-2 hydrogen pump tests and J-2 engine tests. The S-IVB stage suction system was employed for the pump tests. Cavitation tests were conducted at hydrogen bulk temperatures from 21.7 to 25.0°K at flows and speeds equivalent to the J-2 engine operating at mixture ratios of 4.5 and 5.0. A typical set of data from these tests is presented in Figure 1d. Note that in Figure 1d two curves are presented for the 23.9 and 25°K data. These curves represent the two methods used to calculate the vapor fraction at the pump inlet after the tank saturation condition was reached. The curve having the lowest vapor handling capability for a given temperature assumes the hydrogen in the tank remains saturated liquid as the tank pressure is lowered. The curve having the greatest vapor handling capability assumes a constant enthalpy expansion in the tank as the tank pressure is lowered. It is not known which of these methods most closely approximates the actual process; however, the actual vapor volume at the pump inlet should be within the limits shown. From these tests it was concluded that the J-2 hydrogen pump had sufficient vapor handling capability to allow zero tank NPSH operation in the S-IVB stage at hydrogen bulk temperatures above 23.3°K.

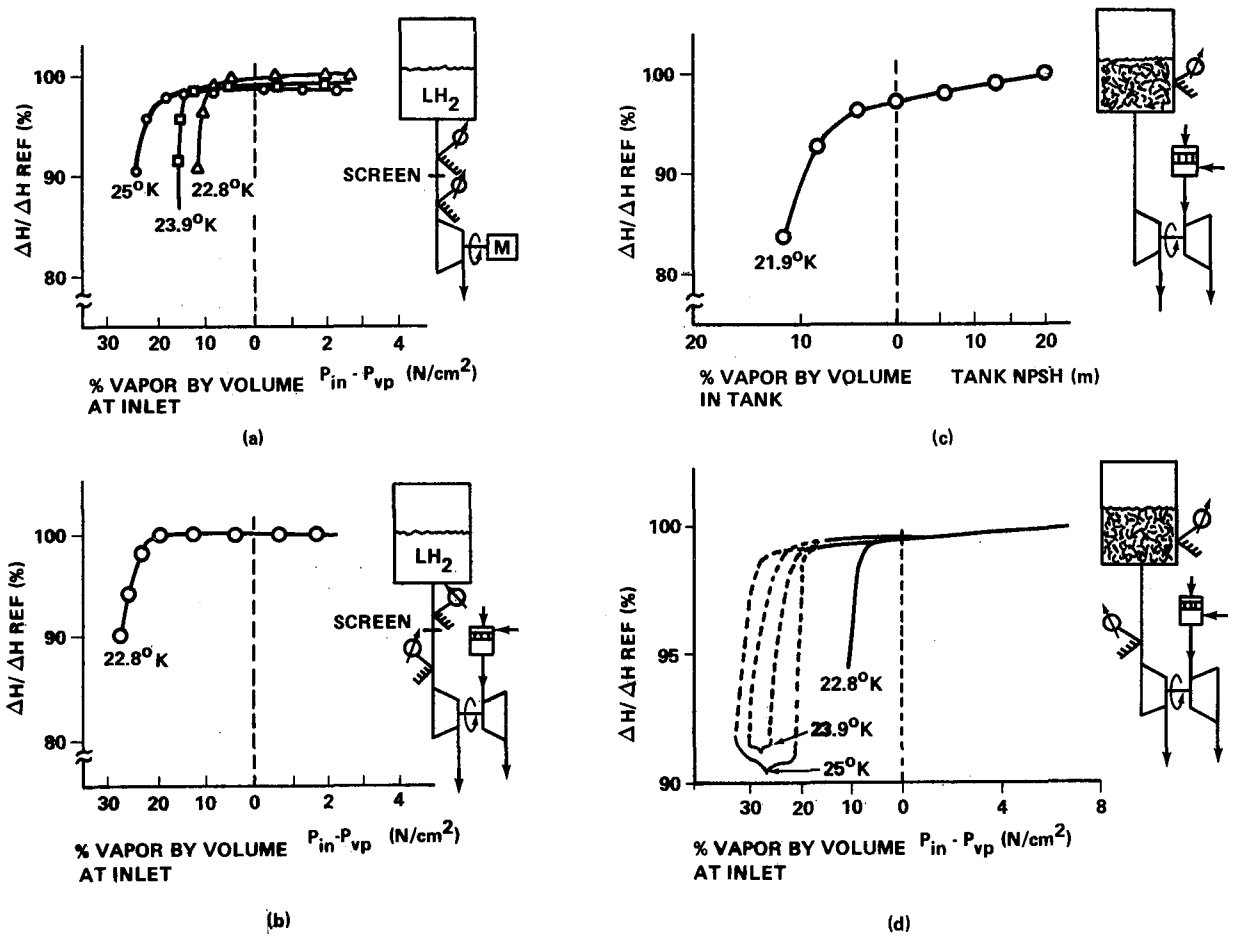

Figure 1. Hydrogen two-phase pumping.

Start transient tests were also conducted with zero tank NPSH during the pump test program. The pump was thoroughly chilled prior to start. Eight successful starts were obtained during the program. Two tests were terminated by the pump overspeed cutoff prior to attaining mainstage operation. These overspeed cutoffs were caused by a large volume of vapor being introduced into the pump by a dead-end section of pipe in the suction system. This large vapor volume was evident on all the tests. However, by slowing the start transient and insulating the dead-end section of ducting, the volume was minimized sufficiently to allow satisfactory starts. Although these transients did not simulate the J-2 engine transients, the conditions were more severe than those imposed by the engine. Typical pump starts are compared to a J-2 transient in Figure 2. It was concluded from these tests that the pump had sufficient vapor handling capability to allow the J-2 engine to start and operate with zero tank NPSH in the S-IVB stage and that propulsion systems designed for zero tank NPSH must avoid feed system dead ends.

The engine test program was conducted at the S-IVB battleship test facility at MSFC. This facility completely simulated the S-IVB stage. The steady-state tests were conducted by allowing the propellant to heat until the desired hydrogen bulk temperature was obtained. The tank was then pressurized to 5.5 N/cm^2 above the vapor pressure and the test was initiated. After steady-state operation was obtained, the tank pressure was lowered until the saturation condition in the tank was reached. Once the zero tank NPSH condition was reached, the tank pressure was held constant for approximately 15 s of operation. Pump and engine performance data from two of the tests are presented in Figure 3. Note that at the lower temperature a significant loss in pump performance was experienced; however, with the warmer hydrogen, no appreciable performance loss occurred.

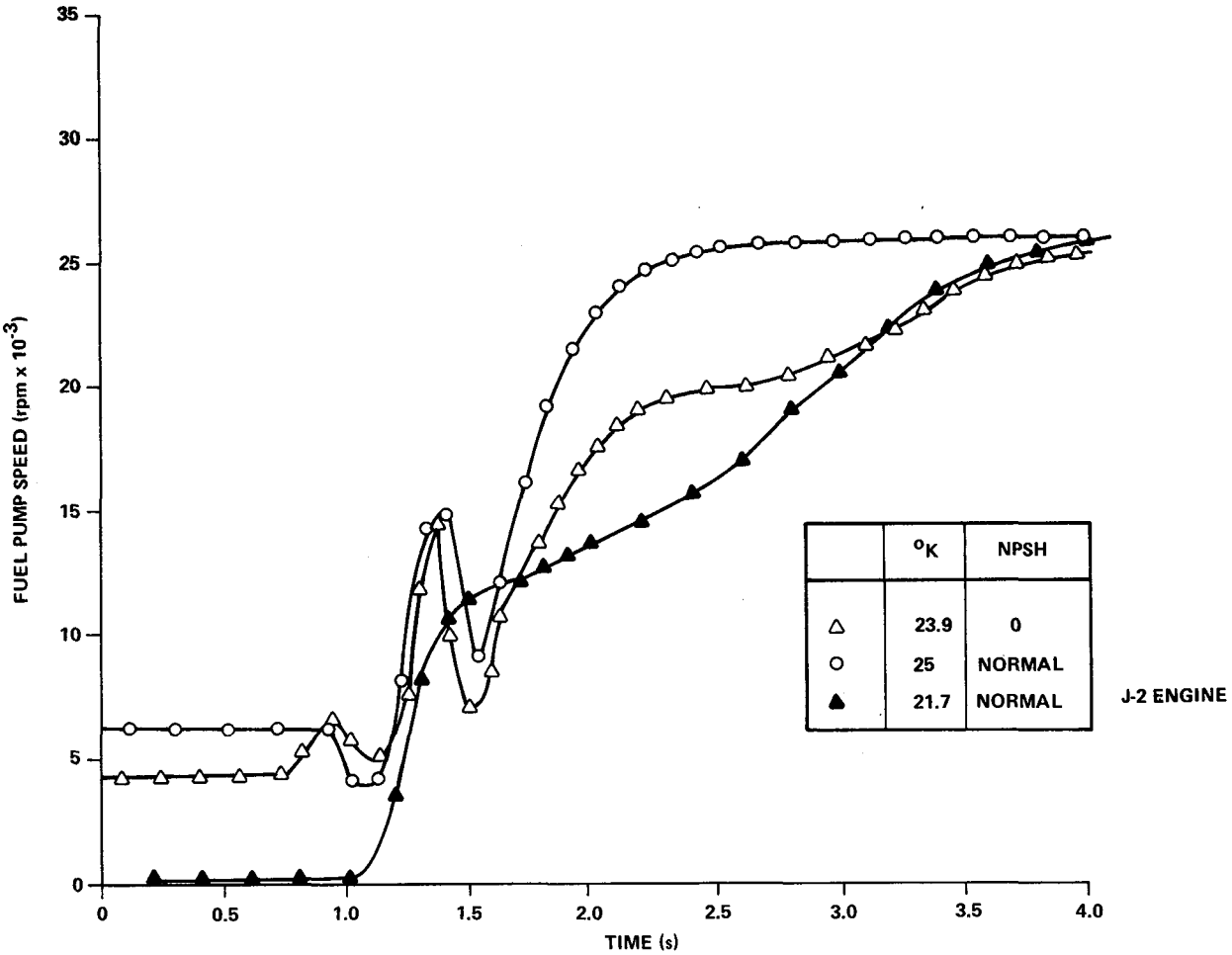

Figure 2. Start tests.

These same characteristics are reflected in the corresponding engine chamber pressures.

The normal J-2 engine/S-IVB start sequence was used during the transient tests. With saturated hydrogen in the tank (zero tank NPSH), the stage recirculation system was used to chill the pump. Transient data from a test with high NPSH and one with zero tank NPSH are presented in Figure 4. No significant changes can be noted as a result of starting with zero tank NPSH.

These pump and engine test programs have demonstrated the feasibility of the zero tank NPSH operating mode with hydrogen. This capability has not, however, been demonstrated with oxygen. To gain experience pumping two-phase oxygen, a program was conducted at the Marshall Center using the J-2 oxygen pump and the S-IVB oxidizer feed system. Cavitation tests were conducted at oxygen bulk temperatures between 95.5 and 100.1°K. The initial tests were conducted at flows and speeds equivalent to the J-2 engine operating at mixture ratios of 4.5 and 5.0. At these high flows and speeds the pump was not capable of handling any vapor. The pump's suction performance did, however, improve as the oxygen bulk temperature was increased. Pump performance data for the tests conducted at the 4.5 mixture ratio condition are presented in Figure 5.

Following this initial oxygen pump test series, the pump flow and speed were reduced to one-half of rated conditions and the test program was repeated. At these lower flows and speeds, two-phase pumping was obtained on all the tests. Data for one of the pump operating conditions are presented in Figure 6. Again, the improved suction

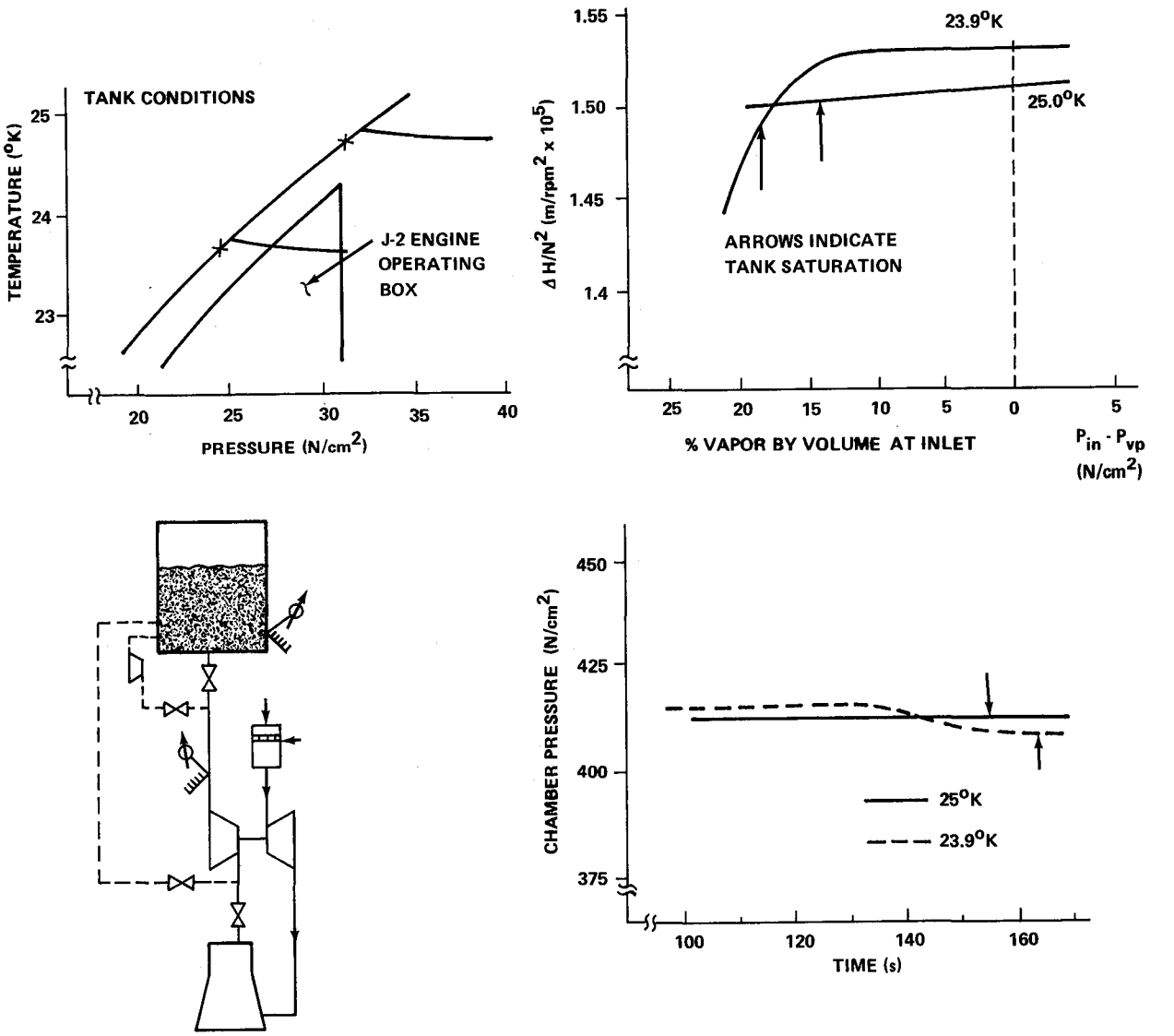

Figure 3. J-2 engine testing, zero LH_2 tank NPSH.

performance with increasing propellant temperature is noted. These tests have demonstrated the feasibility of pumping two-phase oxygen.

DESIGN OF TWO-PHASE INDUCERS

The two-phase pumping discussed thus far has been performed with existing pumps by exploiting the thermodynamic effects of cavitation at elevated propellant bulk temperatures. This has resulted in tests being conducted at tank pressures significantly above the pressure of normal boiling point propellants. Although zero tank NPSH operation at these high tank pressures could allow vehicle improvements by eliminating repressurization systems and relaxing operational constraints, it does defeat the objective of minimizing tank weight. Therefore, to obtain the objective of minimum tank weight (tank weight dependent only on structural requirements), it is necessary to design inducers specifically for two-phase operation that will allow zero tank NPSH operation at or very near the normal boiling point.

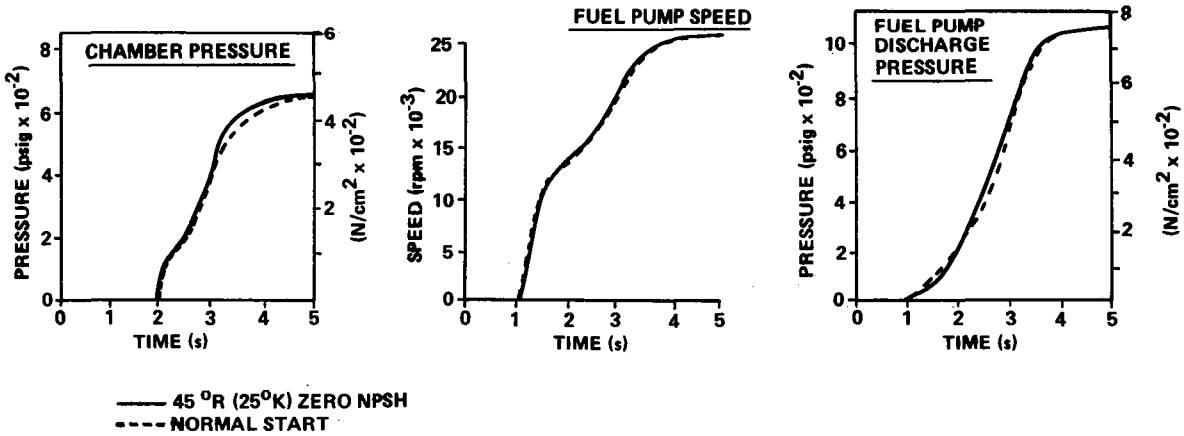

Figure 4. J-2 engine transients.

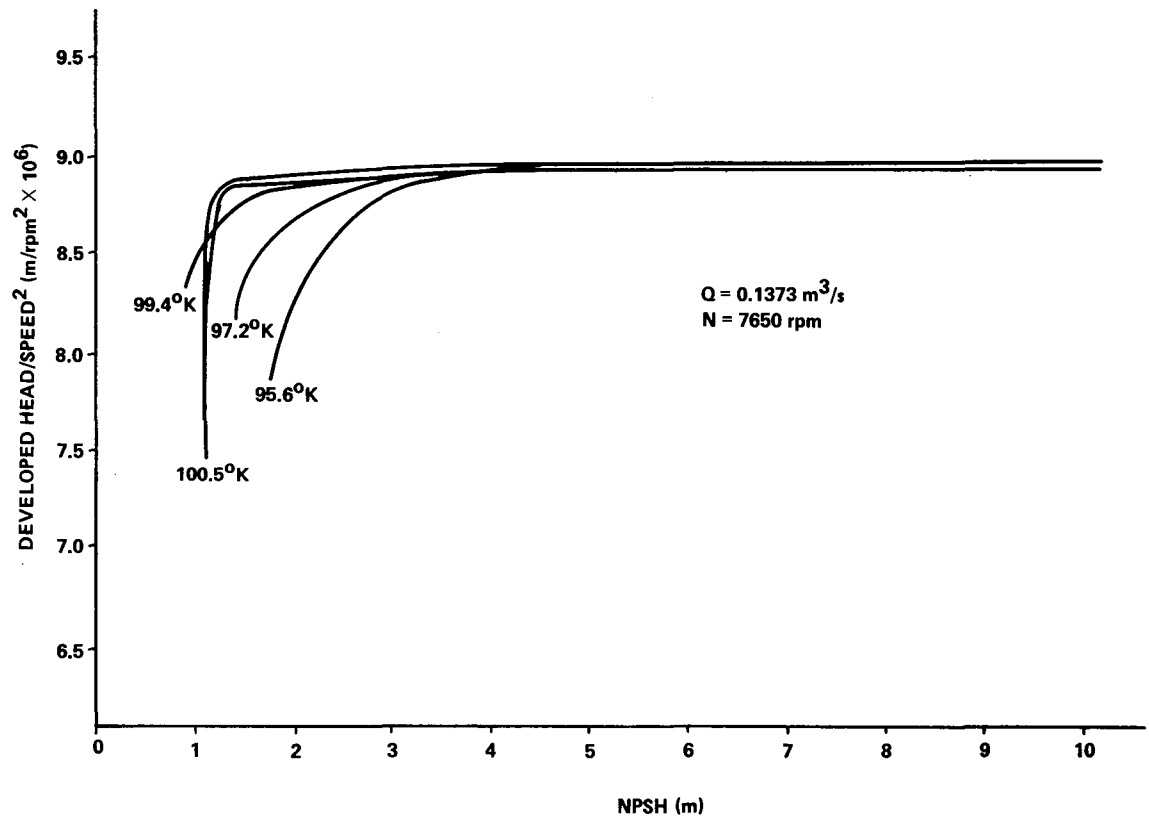

Figure 5. J-2 oxygen pump.

Bissell, Wong, and Winstead [10] developed a theory for head breakdown of pump inducers operating in the two-phase regime based upon the acoustic characteristics of the two-phase fluid entering the inducer. It was well known that two-phase mixtures exhibit a very significant decrease in acoustic velocity from both the all-liquid or all-gas regimes. It was theorized that the head breakdown resulted from choking either in inducer channels or in the inlet annulus (Fig. 7). As the amount of vapor at

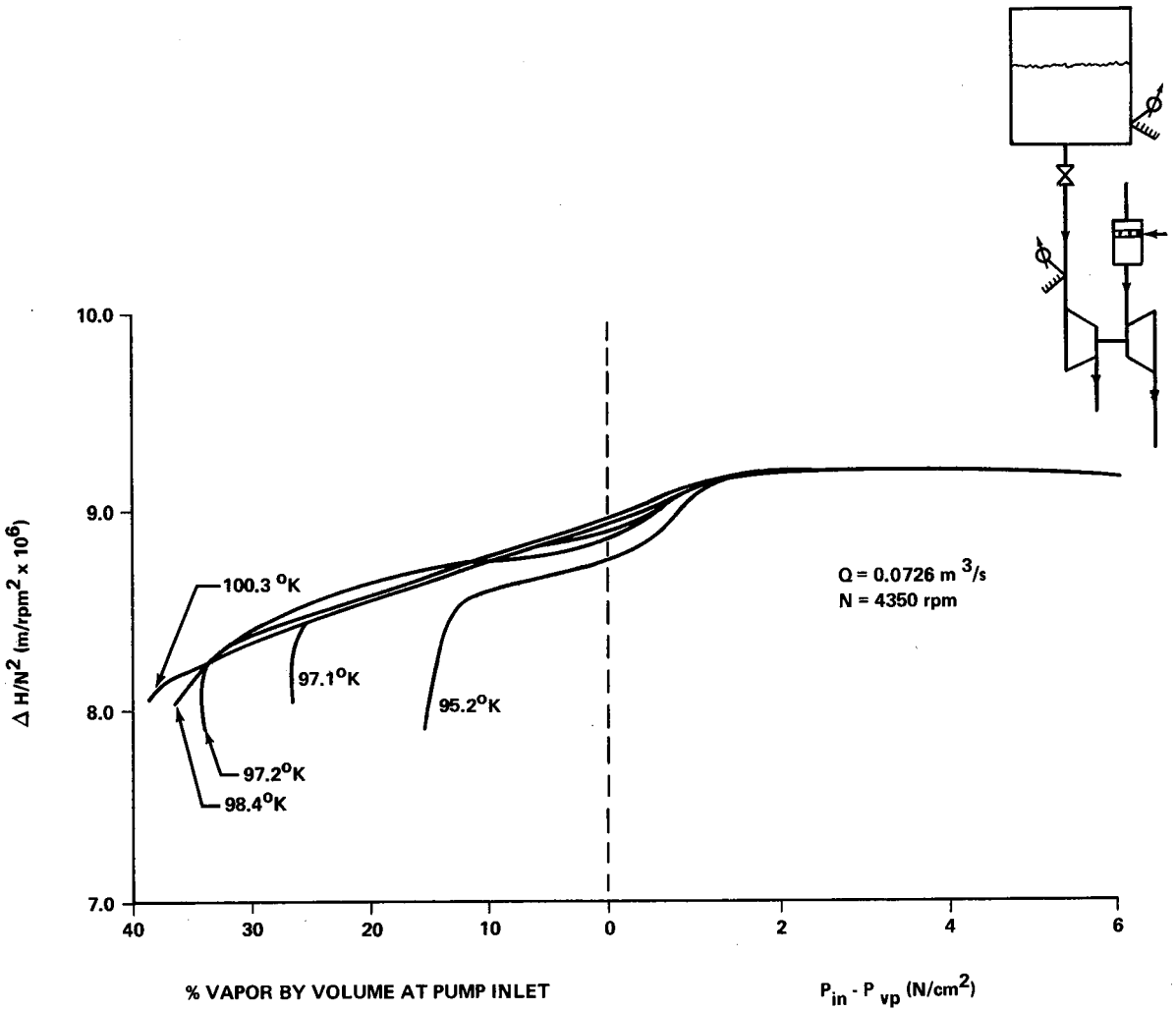

Figure 6. J-2 oxygen pump tests.

the inlet increased at constant mass flow, the relative flow area immediately upstream of the inducer eventually became greater than the relative flow area in the inducer channel. If the relative velocity was equal to or greater than the acoustic velocity of the two-phase mixture, choking occurred. By correlating two-phase inducer data [8] with assumed flow processes in the inlet line and the inducer channels, it was found that an equilibrium two-phase mixture process best matched the data for the inlet line analysis, and a constant quality, perfect gas analysis with weak oblique shocking at the blade channel inlet best matched the data for channel analysis.

From this analysis, criteria for design of inducers for two-phase operation were established. The two-phase inducer should be designed for high incidence to blade angle ratios (i/b) to forestall choking in the inducer channels and for low mass flow rates to inducer frontal area ($\dot{\omega}$/A) to preclude choking in the inlet annulus.

Using these design criteria a two-phase inducer was designed, fabricated, and tested in a J-2 hydrogen pump. The results of these tests compared to the analytical predictions for three hydrogen bulk temperatures are presented in Figure 8 [11]. From this figure, it can be seen that very good agreement

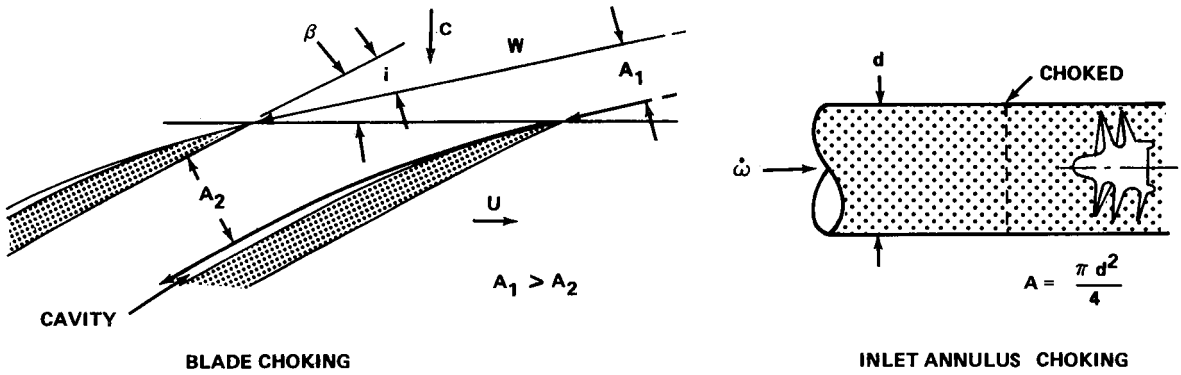

- 2 ϕ FLOW ANALYSIS
  - INLET LINE EQUILIBRIUM
  - CONSTANT QUALITY, PERFECT GAS, WEAK OBLIQUE SHOCK
- 2 ϕ DESIGN CRITERIA
  - HIGH i/β
  - LOW $\dot{\omega}/A$

Figure 7. Two-phase head breakdown.

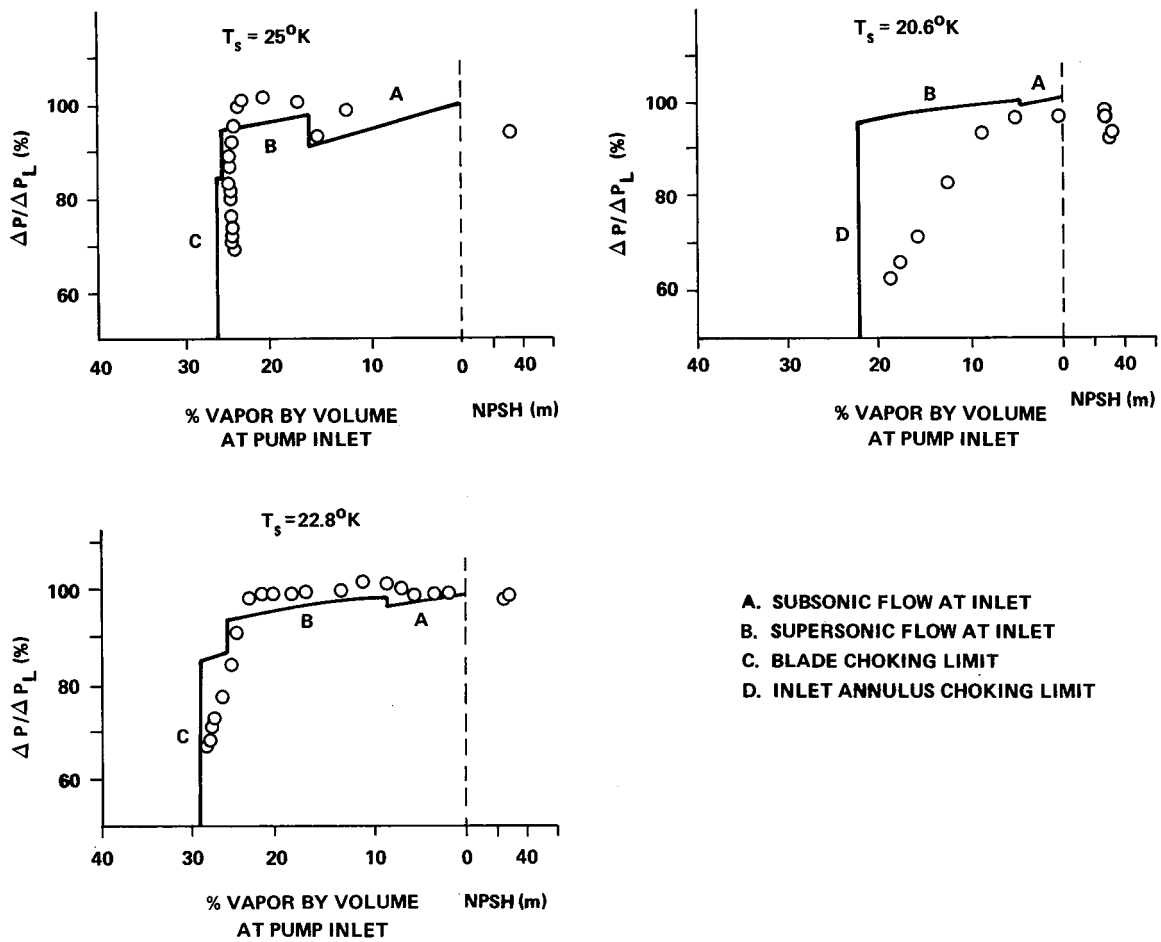

Figure 8. Comparison of analytical and experimental data.

was obtained between the theory and data. The largest discrepancy exists for the lower temperature hydrogen ($T_s = 20.6°K$) where the data show an earlier and a much more gradual loss in performance than was predicted. Excellent agreement with test data was obtained at the higher hydrogen temperatures. In addition to obtaining good agreement between theory and test, a significant improvement in the pump's vapor handling capability was obtained. A comparison of the two-phase inducer's performance to the standard J-2 inducer is presented in Figure 9 [11]. The two-phase inducer had a greatly improved vapor handling capability at the lower hydrogen temperatures. At approximately 22° K the standard inducer has zero vapor handling capacity, whereas the two-phase inducer had the capability to handle 25 percent vapor by volume. This increased vapor pumping capability at low hydrogen temperatures would allow zero tank NPSH operation at saturation pressures very near the normal boiling point for hydrogen. Therefore, with inducers designed specifically for two-phase operation, the full potential of zero tank NPSH operation can be utilized.

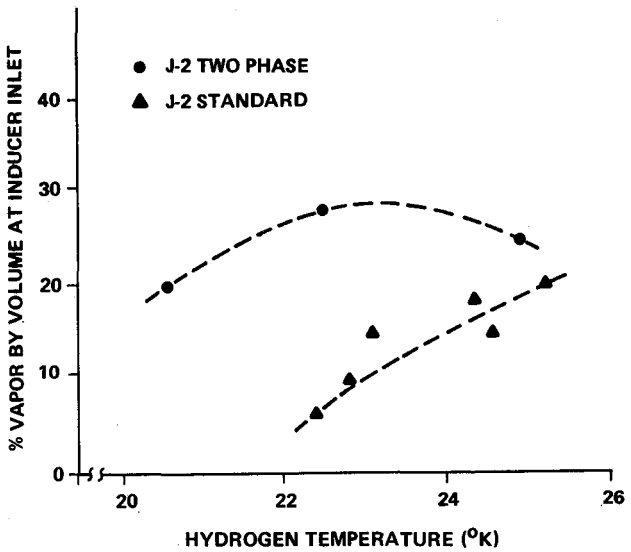

Figure 9. Comparison of two-phase performance.

CONCLUSIONS

Utilizing the thermodynamic effects of cavitation, it is possible to pump two-phase hydrogen with a number of pumps at their normal operating flows and speeds. The zero tank NPSH mode of operation has been demonstrated in hydrogen pump test facilities and during the operation of a complete propulsion system. An inducer has been designed, fabricated, and tested that will allow zero tank NPSH operation very near normal boiling point hydrogen. These test programs and the analytical effort have developed zero tank NPSH with hydrogen to a realistic operating mode.

The feasibility of pumping two-phase oxygen has been demonstrated. However, additional work is required before an operational capability can be attained. Attaining an operational capability with oxygen will be much more difficult than with hydrogen because of differences in the thermodynamic properties of the two fluids.

REFERENCES

1. Stahl, H.A.; and Stepanoff, A.J.: Thermodynamic Aspects of Cavitation in Centrifugal Pumps. Trans. ASME, vol. 78, no. 8, Nov. 1956, pp. 1691-1693.

2. Saleman, Victor: Cavitation and NPSH Requirements of Various Liquids. ASME, Journal of Basic Engineering, vol. 81, no. 2, June 1959, pp. 167-180.

3. Gelder, Thomas F.; Ruggeri, Robert S.; and Moore, Royce D.: Cavitation Similarity Considerations Based on Measured Pressure and Temperature Depressions in Cavitated Regions of Freon 114. NASA TN D-3509, July 1966.

4. Moore, Royce D.: Prediction of Pump Cavitation Performance. Fluid Mechanics and Design of Turbomachinery Symposium, Pennsylvania State University, August 31-September 2, 1970.

REFERENCES (Concluded)

5. Hord, J.; and Voth, R. O.: Tabulated Values of Cavitation B-Factor for Helium, H_2, N_2, F_2, O_2, Refrigerant 114, and H_2O. National Bureau of Standards Technical Note 397, February 1971.

6. Meng, Phillip R.; and Connelly, Robert E.: Investigation of Effects of Simulated Nuclear Radiation Heating on Inducer Performance in Liquid Hydrogen. NASA TM X-1359, February 1971.

7. J-2X Experimental Engine Program for the Period 1 January 1967 to 31 December 1967. Final Report, Rocketdyne Report R-7344, April 4, 1968.

8. Suction Performance of the Mark 25 Liquid Hydrogen Pump. Rocketdyne Report BCI 68-105.

9. Bair, E. K.; et al.: Investigation of Twin-Spool Turbopump Performance. NASA CR-72540, September 1969.

10. Bissell, W. R.; Wong, G. S.; and Winstead, T. W.: An Analysis of Two-Phase Flow in LH_2 Pumps for O_2/H_2 Rocket Engines. AIAA 5th Propulsion Joint Specialist Conference, Colorado Springs, Colorado, June 9-13, 1969.

11. King, J. A.: Two Phase Hydrogen Pump Inducers. Proceedings of Space Transportation System Propulsion Technology Conference, vol. 1, April 6-7, 1971.

LIQUID ROCKET COMBUSTION STABILITY

By

R. J. Richmond

The impetus for the stability work described herein was the realization in the early 1960's that future liquid rocket engines would operate at high chamber pressure [2068 N/cm^2 (3000 psi) versus 689 N/cm^2 (1000 psi) for the then current engines] with liquid hydrogen and liquid oxygen propellants. Combustion instability was a problem that plagued the development of the then current engines; therefore, in laying the groundwork for a new generation of engines, information was needed as to whether the higher operating pressures would worsen this problem. Thus, in 1962 a program was initiated at Aerojet General to explore the combustion instability problem at high chamber pressure with liquid hydrogen and liquid oxygen propellants. The analysis used was the time lag theory of combustion instability developed by Professor Crocco at Princeton University in the late 1950's. Crocco's theory postulates that the instantaneous change in the burning rate or energy release rate is proportional to the chamber pressure fluctuation to some power, n, which is called the interaction index. Thus,

$$R' \propto P_c'^{n} ,$$

where R' is the burning rate change, P_c' is the chamber pressure fluctuation, and n is the interaction index.

Immediately after injection into the chamber, the propellants undergo heating, atomization, vaporization, and finally chemical reaction. The time from injection to completion of energy release is called the total time lag, τ_T. This total time lag depends on the burning rate. The chamber pressure fluctuations cause the burning rate to vary, producing a change in the total time lag. This change in the total time lag is called the sensitive time lag τ. Thus, the sensitive time lag is the lag that develops between the pressure fluctuations and the burning rate fluctuations.

The total time lag, therefore, is composed of two portions; the first portion, which is not dependent on pressure, is called the insensitive time lag and the second portion, which is dependent on pressure, is called the sensitive time lag. This is depicted in Figure 1. Crocco, therefore, was able to characterize the combustion by two parameters, n and τ, without dealing with the physical and chemical processes mentioned above. The conservative equations containing the burning rate term were solved for the neutral stability boundaries in terms of n and τ. The neutral stability boundaries separate the stable zones from the unstable zones on the n, τ plane.

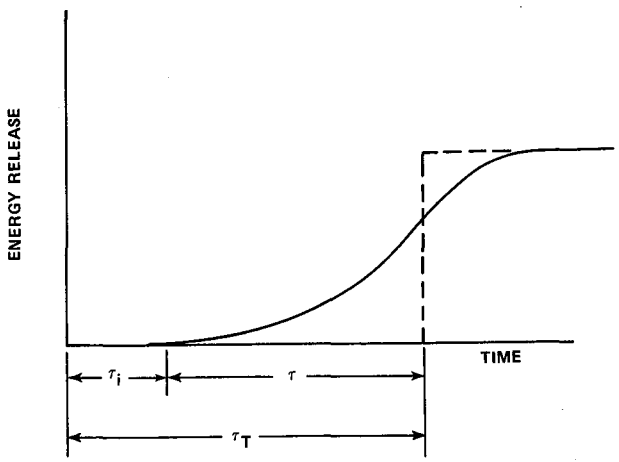

Figure 1. Energy release versus time for unmixed bipropellants.

To determine the effect of chamber pressure on combustion stability, a series of tests was conducted using a 20.3-cm (8.0-in.) diameter chamber of two lengths, 31.8 cm (12.5 in.) and 66.0 cm (26.0 in.). Three distinctly different injectors were used: the first, which is called a conventional injector, is a like-on-like impinging fuel doublet with an oxidizer showerhead; the second, which is called a coaxial injector, is a showerhead oxidizer surrounded by an annulus of fuel;

and the third, which is called a pentad injector, consists of four streams of oxidizer impinging on one stream of fuel. These elements are shown in Figure 2.

The neutral stability boundaries for the conventional injector together with the experimental results are shown in Figure 3. Note that the theoretical effect of increased chamber pressure tends to raise the neutral stability limits slightly for the tangential modes, which is a stabilizing effect, and lower them for the longitudinal modes, which is a destabilizing effect. The neutral stability boundaries are a strong function of the chamber and nozzle

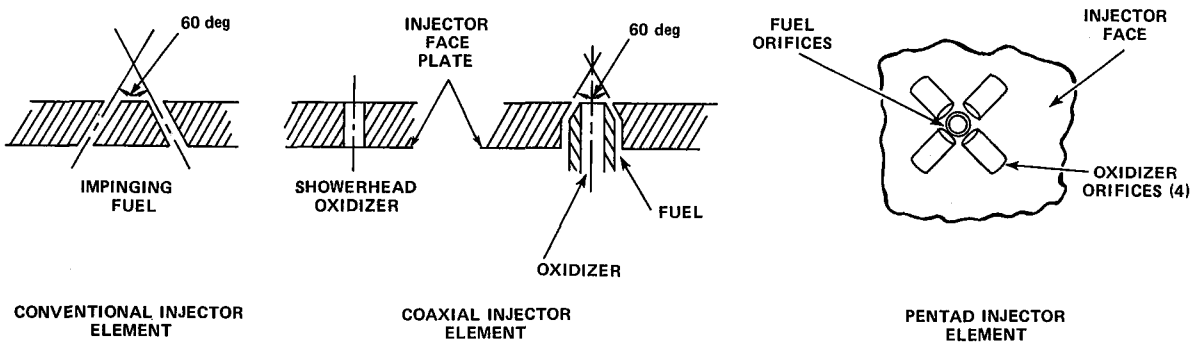

Figure 2. Injector elements tested.

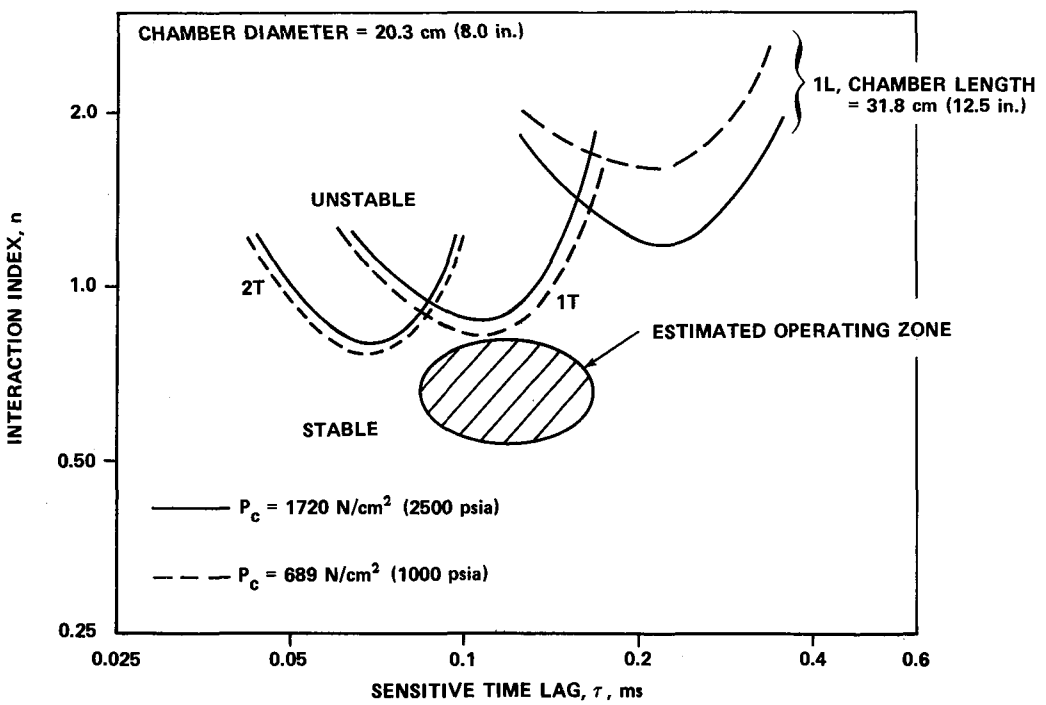

EXPERIMENTAL RESULTS, CONVENTIONAL INJECTOR

CHAMBER LENGTH	CHAMBER PRESSURE	MIXTURE RATIO	STABILITY
31.6 cm (12.5 in.)	1760 N/cm^2 (2555 psia)	6.5	1T
66.0 (26.0)	600 (870)	6.8	1T
66.0 (26.0)	766 (1110)	6.3	1T
66.0 (26.0)	1530 (2218)	4.2	1T

Figure 3. Stability limits and n, τ operating zone for a 20.3-cm (8.0-in.) conventional injector.

geometry and a weak function of the combustion distribution produced by the injector. Thus, for practical purposes, the chamber geometry dictates the stability boundaries and the injector element dictates the operating point.

In this study the chamber pressure was varied by changing the throat area of the nozzle while maintaining a constant flow rate. Thus, the large effect of pressure on the first longitudinal mode is really a result of a nozzle geometry change to effect the pressure change. The tangential modes are not as sensitive to nozzle geometry as the longitudinal modes.

The experimental results, displayed in Figure 3, show that the first tangential mode of instability was obtained in all four tests regardless of chamber pressure. Thus, chamber pressure had no effect on the occurrence of tangential instability for the conventional injector. Since the instability had to be artificially triggered by a chamber pressure pulse, the normal n, τ operating zone for the injector was estimated to be as shown in the figure, which is in a stable area of the plot.

The neutral stability boundaries and the experimental results for the coaxial injector are shown in Figure 4. In addition to the chamber pressure effects discussed in Figure 3, Figure 4 also shows the theoretical effect of chamber length on the first longitudinal mode. The sensitive time lag at the minimum n value can be thought of as being equal to one-half the period of a sinusoidal oscillation. Thus,

$$\tau = 1/2P = \frac{1}{2f} \quad , \tag{1}$$

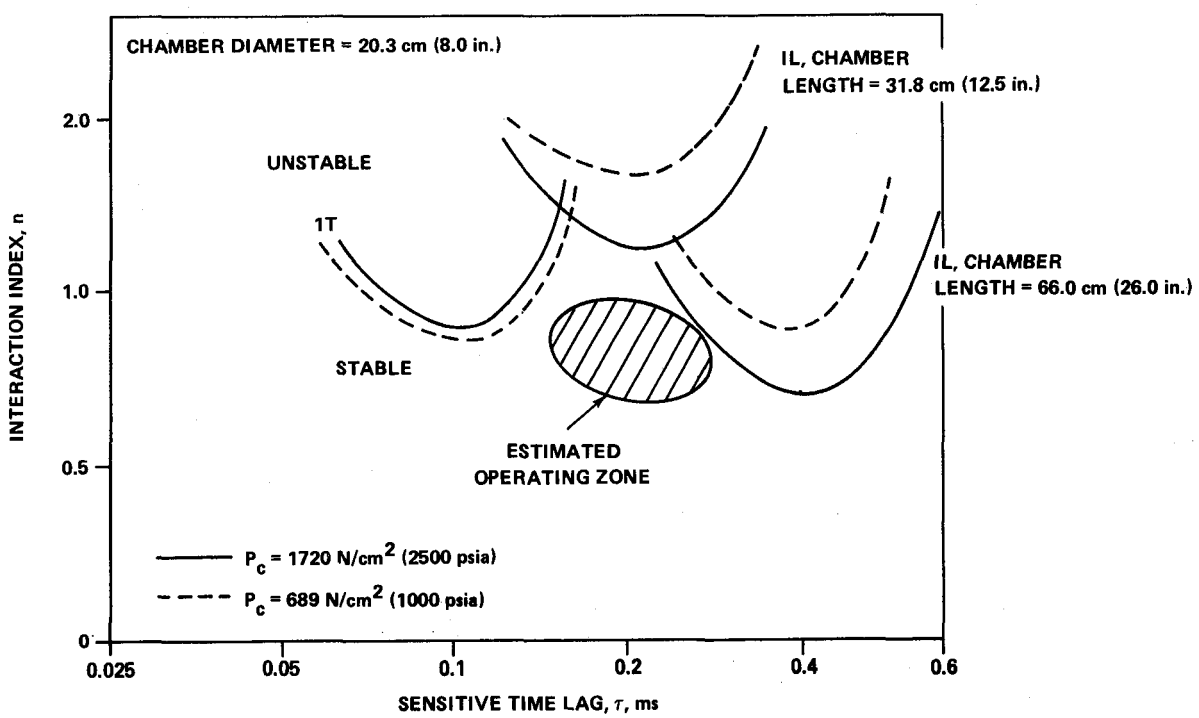

EXPERIMENTAL RESULTS, COAXIAL INJECTOR

CHAMBER LENGTH		CHAMBER PRESSURE		MIXTURE RATIO	STABILITY
31.8 cm	(12.5 in.)	1610 N/cm^2	(2345 psia)	5.7	STABLE
66.0	(26.0)	700	(1020)	4.3	STABLE
66.0	(26.0)	935	(1360)	4.3	STABLE
66.0	(26.0)	1600	(2325)	3.2	IL
66.0	(26.0)	1710	(2495)	6.3	IL

Figure 4. Stability limits and n, τ operating zone for a 20.3-cm (8.0-in.) coaxial injector.

where

τ is the sensitive time lag,

P is the period,

and

f is the frequency.

The frequency of the tangential and longitudinal modes is obtained from a solution of the wave equation in cylindrical coordinates. For the longitudinal modes, the solution is

$$f = \frac{mC_o}{2L} \quad , \tag{2}$$

where

f is the frequency,

m is the mode number, 1 for 1L, 2 for 2L, etc.,

C_o is the speed of sound,

and

L is the chamber length.

By combining equations (1) and (2),

$$\tau = \frac{L}{mC} \quad . \tag{3}$$

Thus, it can be seen that as the chamber length is increased, the value of the sensitive time lag at the minimum value of interaction index is increased.

A similar analysis applies for the tangential modes. In this case the solution of the wave equation is

$$f = \frac{S_{\nu\eta} C_o}{\pi D} \quad , \tag{4}$$

where

f is the frequency,

$S_{\nu\eta}$ is the transverse mode coefficient,

C_o is the speed of sound,

and

D is the chamber diameter.

By combining equations (1) and (4),

$$\tau = \frac{\pi D}{2S_{\nu\eta} C_o} \quad . \tag{5}$$

Thus, for the tangential modes the value of the sensitive time lag at the minimum value of the interaction index is increased as the chamber diameter is increased. Referring to Figure 4, it is seen from the experimental data that the system was stable except for the tests where the 66.0-cm (26.0-in.) chamber was used at about 1720 N/cm^2 (2500 psia) chamber pressure. Therefore, it is evident that increased chamber pressure can have a destabilizing effect on the longitudinal modes. Since the instabilities were artificially triggered, the estimated operating zone for the coaxial injector is as shown in Figure 4.

The neutral stability boundaries and the experimental results for the pentad injector are shown in Figure 5. The experimental results show that the system was stable for both chamber lengths and for both regimes of chamber pressure [689 N/cm^2 (1000 psia) and 1720 N/cm^2 (2500 psia)]. Since the system was stable, the operating zone for the pentad injector was more difficult to estimate. Thus, the estimated operating zone shown in Figure 5 is rather broad. No conclusion could be reached regarding the effect of chamber pressure on combustion stability with the pentad injector.

A second phase of the program was established for the purpose of verifying that the n, τ operating zone of a particular injector element is a characteristic of that element regardless of the geometry of the particular combustor with which it is used. The method of demonstrating this was to move the theoretical neutral stability boundaries on the n, τ plane by varying the geometry of the combustor, while using the exact same injector elements as were used in the previous work. Thus, if a new combustor were used that had a neutral stability boundary for a different mode of instability falling over the established n, τ operating zone for the particular injector element and if tests showed that this new mode of instability occurred, then the postulated outcome could be proved. Since experience had shown that tangential modes are a more severe problem than longitudinal modes in real engines, it was decided to

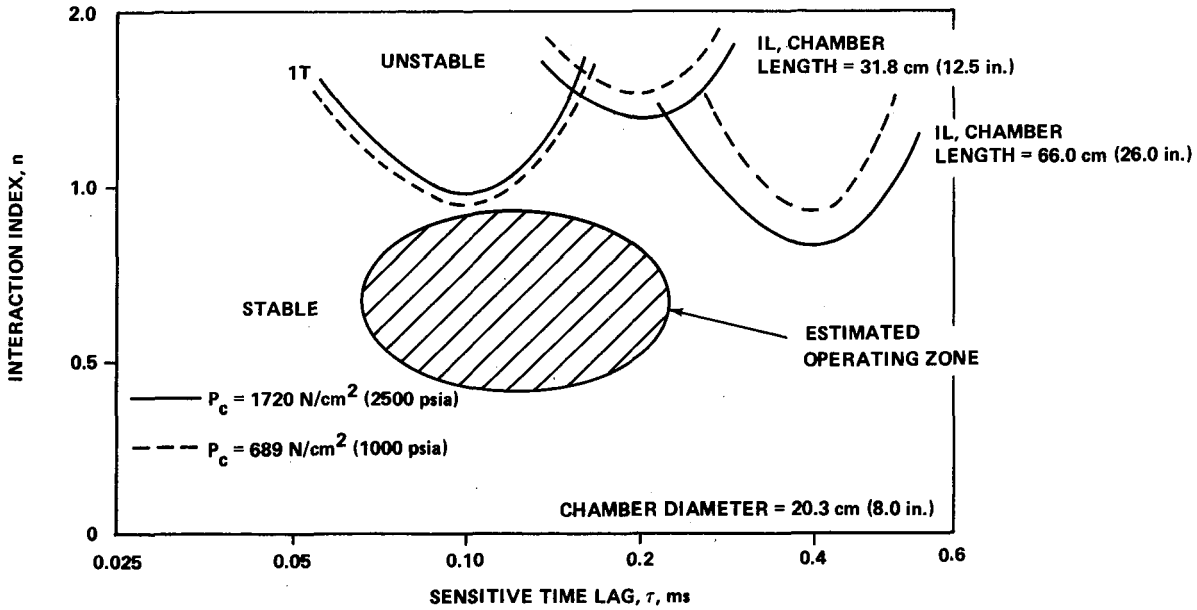

EXPERIMENTAL RESULTS PENTAD INJECTOR

CHAMBER LENGTH	CHAMBER PRESSURE	MIXTURE RATIO	STABILITY
31.8 cm (12.5 in.)	1485 N/cm^2 (2141 psia)	8.3	STABLE
66.0 (26.0)	710 (1036)	5.2	STABLE
66.0 (26.0)	1040 (1515)	5.7	STABLE
66.0 (26.0)	1670 (2415)	5.4	STABLE

Figure 5. Stability limits and n, τ operating zone for a 20.3-cm (8.0-in.) pentad injector.

vary the combustor geometry by changing diameter rather than length. A new combustor, 35.6 cm (14.0 in.) in diameter, was built and tested with injectors composed of the same elements as were used with the earlier 20.3-cm (8.0-in.) diameter combustor.

The neutral stability boundaries for this 35.6-cm (14.0-in.) diameter combustor together with the n, τ operating zone predicted for the conventional injector from the earlier 20.3-cm (8.0-in.) combustor work are shown in Figure 6. Since the effect of chamber pressure on the tangential modes has already been shown to be small, the boundaries are shown only for 1720 N/cm^2 (2500 psia) chamber pressure. The location of the n, τ operating zone predicts that this combustor would be unstable in the first and second tangential modes. The experimental results show that both these modes were encountered. The second tangential mode was encountered spontaneously and the first tangential mode was obtained by pulsing, as would be expected from the location of the n, τ operating zone relative to the neutral stability boundaries.

The neutral stability boundaries together with the n, τ operating zone predicted for the coaxial injector from the earlier 20.3-cm (8.0-in.) diameter work are shown in Figure 7. The location of the n, τ operating zone predicts that this combustor would be unstable in the first tangential mode, and could be unstable in the first longitudinal mode and in the combined first tangential-second longitudinal mode. Experimentally, the first tangential and the combined first tangential-second longitudinal modes were encountered. The first tangential-second longitudinal mode was encountered spontaneously and the first tangential mode was obtained by pulsing. This suggests that the n, τ operating zone be modified slightly by shifting it to the left where it would intersect the first tangential-second longitudinal stability boundary. Reasonably good agreement between the experimental results and predictions was obtained.

The neutral stability boundaries together with the n, τ operating zone predicted for the pentad injector from the earlier 20.3-cm (8.0-in.) diameter work are shown in Figure 8. The location of

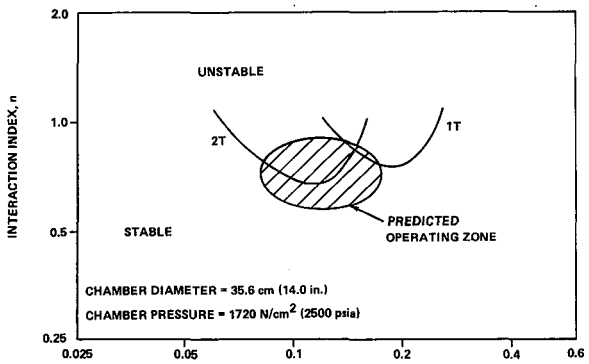

EXPERIMENTAL RESULTS, CONVENTIONAL INJECTOR

CHAMBER LENGTH	CHAMBER PRESSURE	MIXTURE RATIO	STABILITY
20.3 cm (8.0 in.)	630 N/cm² (920 psia)	5.78	1T
20.3 (8.0)	1610 (2340)	4.05	2T
61.0 (24.0)	1730 (2510)	5.50	1T

Figure 6. Stability limits and n, τ operating zone for a 35.6-cm (14.0-in.) conventional injector.

the n, τ operating zone indicates that the most likely instability modes the combustor could encounter would be the first and second tangential modes. Experimentally, the first tangential mode was encountered with the 35.6-cm (14.0-in.) diameter combustor. The predicted n, τ operating zone was very broad initially because instability was not encountered when the pentad was tested in the 20.3-cm (8.0-in.) diameter combustor. The results from the 35.6-cm (14.0-in.) diameter tests suggest that this zone is not as broad as shown in Figure 8 and should be modified by moving the extreme left side of the boundary to a τ value of approximately 0.13. The sensitive time lag for this injector element is probably about 0.2 ms, which explains why the first tangential mode was encountered in the 35.6-cm (14.0-in.) diameter combustor but not in the 20.3-cm (8.0-in.) diameter combustor.

The results of these two series of tests with the 20.3-cm (8.0-in.) and 35.6-cm (14.0-in.) diameter

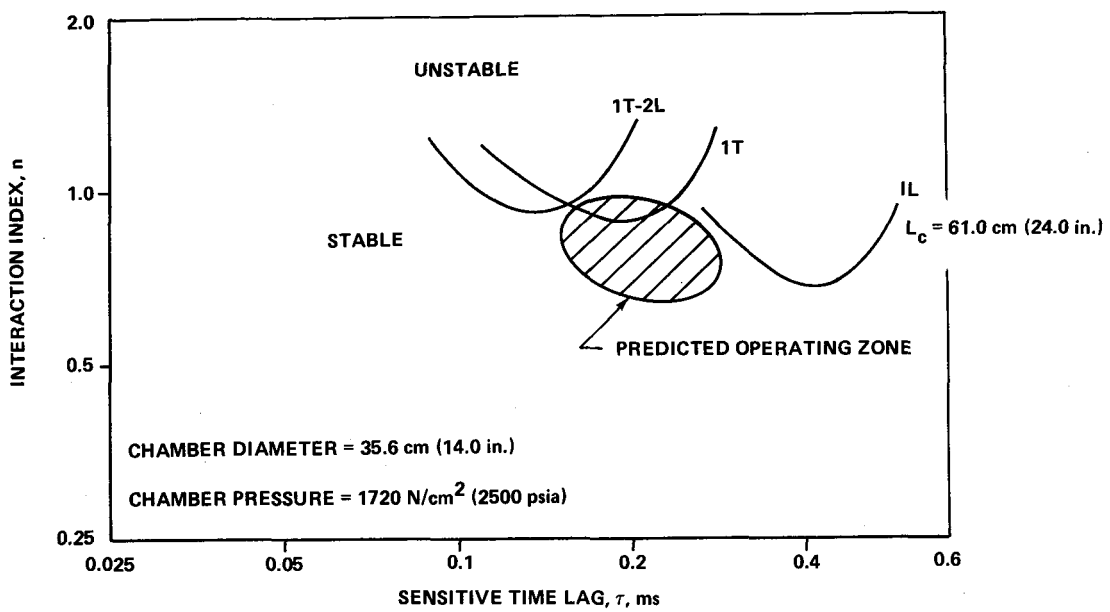

EXPERIMENTAL RESULTS COAXIAL INJECTOR

CHAMBER LENGTH	CHAMBER PRESSURE	MIXTURE RATIO	STABILITY
61.0 cm (24.0 in.)	660 N/cm² (960 psia)	6.28	STABLE
61.0 (24.0)	1400 (2045)	3.09	1T AND COMBINED 1T-2L
61.0 (24.0)	1600 (2320)	5.57	COMBINED 1T-2L

Figure 7. Stability limits and n, τ operating zone for a 35.6-cm (14.0-in.) coaxial injector.

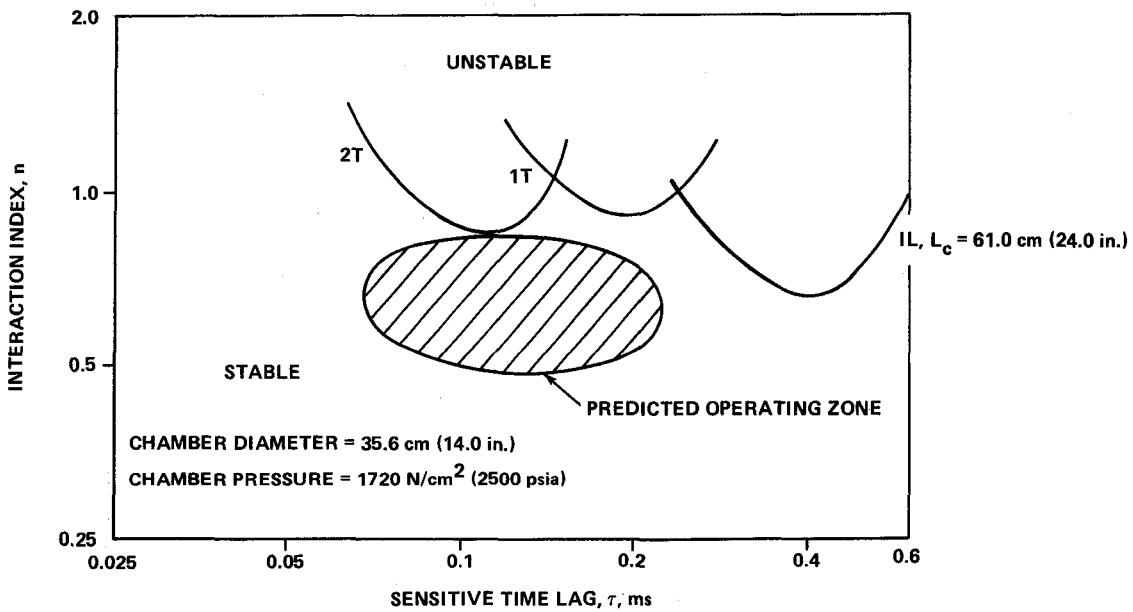

EXPERIMENTAL RESULTS PENTAD INJECTOR

CHAMBER LENGTH	CHAMBER PRESSURE	MIXTURE RATIO	STABILITY
61.0 cm (24.0 in.)	660 N/cm^2 (960 psia)	5.72	1T
61.0 (24.0)	1650 (2400)	5.03	1T

Figure 8. Stability limits and n, τ operating zone for a 35.6-cm (14.0-in.) pentad injector.

combustors showed that the n, τ operating zone for an injector element could be deduced from test data with acceptable accuracy and that this operating zone remains essentially fixed for a particular element.

Once it was established that the operating zone for a particular injector element is a characteristic of that element, a third phase of the program was established to determine the influence of injector element design variables such as orifice diameter, velocity ratio, chamber pressure, and chamber Mach number on the n, τ operating zone. The coaxial injector element was selected for this work because it is the most widely used element for hydrogen-oxygen rockets. Four variations of the coaxial injector element were built and tested. The critical dimensions along with the test conditions are shown in Table 1. The first three were tested in the 35.6-cm (14.0-in.) diameter chamber and the fourth was tested in an annular chamber with an outside diameter of 27.9 cm (11.0 in.) and an inside diameter of 14.3 cm (5.64 in.). A total of 34 tests was conducted with these injectors.

The stability data from these tests were correlated along with data from other programs that used coaxial injector elements. The correlating equations that resulted are shown in Figure 9. For chamber pressures below the critical pressure of the most volatile propellant (oxygen in this case), the sensitive time lag is a weak function of the oxidizer orifice diameter, chamber Mach number, and chamber pressure. It is a strong function of the propellant injection velocity ratio and the impingement angle. Thus, the sensitive time lag is influenced to a small degree by factors other than injector variables, but the major influence is due to the velocity ratio and the impingement angle. When chamber pressure is equal to or greater than the critical pressure of the most volatile propellant, it has no effect on the sensitive time lag. This is represented by the second correlating equation. These equations are also plotted in Figure 9. The variation of the F parameter in the correlating equations with velocity ratio and impingement angle is shown in Figure 10. This correlation was also made from the test results.

TABLE 1. COAXIAL INJECTOR ELEMENT CHARACTERISTICS

Injector	1	2	3	4
No. of Elements	54	54	108	54
Oxidizer Orifice Diameter, cm (in.)	0.584 (0.230)	0.650 (0.256)	0.430 (0.169)	0.568 (0.224)
Fuel Annulus Width, cm (in.)	0.084 (0.033)	0.087 (0.034)	0.038 (0.015)	0.071 (0.028)
Injection Area Ratio, F/O	0.984	0.748	1.02	0.943
Propellant Impingement Angle, deg	30	30	30	30

Test Conditions	
Variable	Range
$\dot{P}_c$	689 to 1720 N/cm^2 (1000 to 2500 psia)
O/F	3 to 10
VR	2 to 12
M_c	0 to 0.16
Injector Density	14 to 210 g/s-cm^2 (0.2 to 3.0 lb/s-in.^{2})

A similar attempt to correlate the interaction index with the injector variables showed that it is a very weak function of the oxidizer orifice diameter. For practical purposes it has a constant mean value of approximately 0.6. Thus, for the coaxial element some control of the sensitive time lag is possible by design of the element, but the interaction index cannot be controlled by design.

In summary, the program investigated three specific areas pertaining to combustion instability with hydrogen-oxygen propellants. The first was a determination of the influence of chamber pressure on combustion stability. It was concluded that increased chamber pressure has no discernible influence on the tangential modes but can have a degrading effect on the longitudinal modes. The strong effect of pressure noted here for the longitudinal modes would not necessarily hold for a real rocket engine. The reason for this is that the chamber pressure was increased by replacing the nozzle with one of a smaller throat diameter. Since the diameter of the cylindrical portion of the combustor was unchanged, a geometry change occurred that provided a better reflecting surface for longitudinal waves. In an actual engine the contraction ratio of the combustor would be reduced correspondingly, thus minimizing the reflecting surface.

The second part of the investigation was designed to demonstrate whether or not a specific injector element could be characterized by a specific range of sensitive time lag and interaction index; it was concluded that it could be. With this information it was possible to proceed to the third part of the investigation which was an attempt to correlate injector design variables and operating conditions with the sensitive time lag and interaction index.

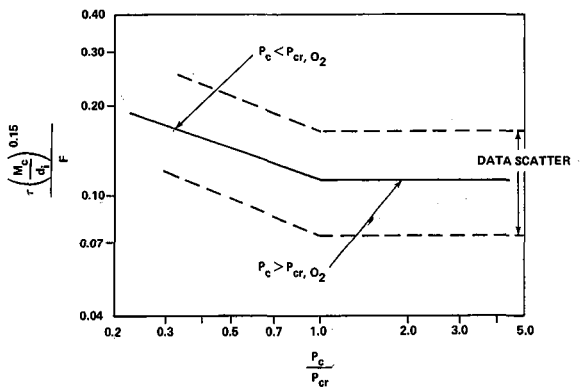

$\tau = 0.11 (d_i/M_c)^{0.15} (P_c/P_{cr})^{-1/3} F$ $(P_c \leq P_{cr})$

$\tau = 0.11 (d_i/M_c)^{0.15} F$ $(P_c > P_{cr})$

WHERE:

- τ = TIME LAG, ms
- d_i = INJECTION ORIFICE DIAMETER (LEAST VOLATILE PROPELLANT), in.
- P_{cr} = CRITICAL PRESSURE (LEAST VOLATILE PROPELLANT)
- P_c = CHAMBER PRESSURE
- M_c = CHAMBER MACH NUMBER
- VR = VELOCITY RATIO
- ϕ = PROPELLANT IMPINGEMENT ANGLE
- F = FUNCTION OF VELOCITY RATIO AND IMPINGEMENT ANGLE

Figure 9. Correlating equations.

Correlating equations were obtained for the sensitive time lag using the coaxial injector element. The interaction index was found to be insensitive to these variables and to have a mean value of approximately 0.6.

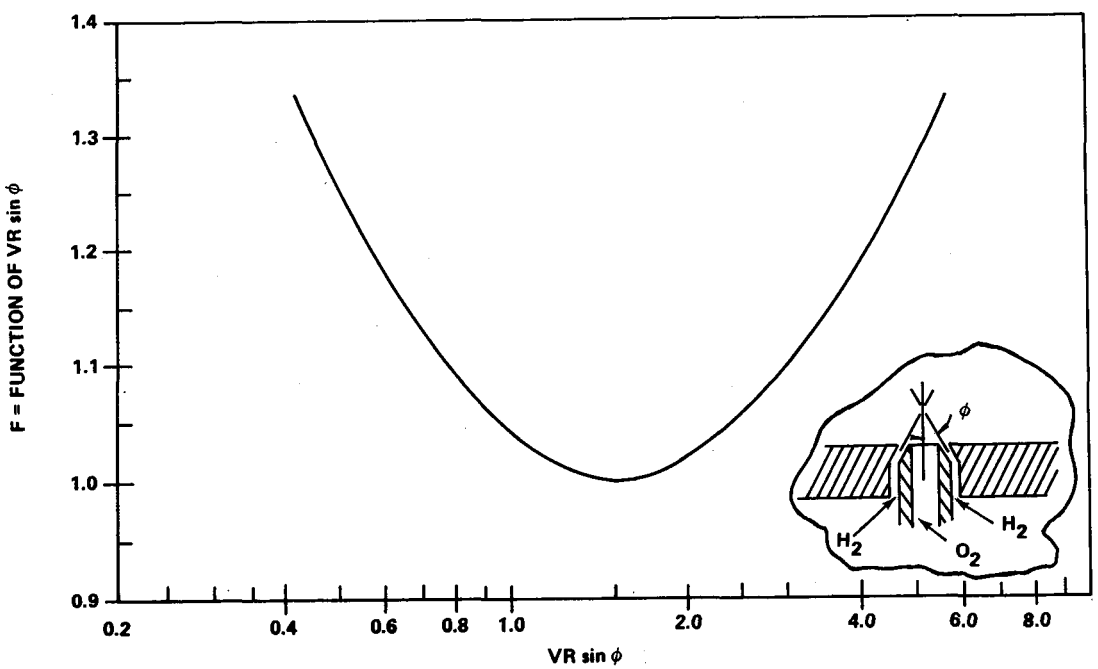

Figure 10. Function of VR sin ϕ versus VR sin ϕ.

BIBLIOGRAPHY

An Experimental Investigation of Combustion Stability Characteristics at High Chamber Pressure Final Report, Phase II, Aerojet General Corporation, Report No. 11741/SA6-F, Volume 1, August 25, 1966.

An Experimental Investigation of Combustion Stability Characteristics at High Chamber Pressure. Interim Report, Aerojet General Corporation, Report No. 11741-1, September 5, 1965.

High Chamber Pressure Operation for Launch Vehicle Engine Programs. Final Report, Aerojet General Corporation, Report No. 4008-SA4-F, June 1, 1964.

Stability Characterization of Advanced Injectors. Final Report, Phase 1, Aerojet General Corporation, Report No. 20672-P1F, October 25, 1968.

ROCKET COMBUSTION INSTABILITY SUPPRESSION WITH CAVITY RESONATORS

By

R. H. Counts

SUMMARY

Properly tuned Helmholtz resonator damping devices are an effective method for eliminating high frequency combustion instability in rocket engine thrust chambers. A program was implemented with the objective of extending Helmholtz resonator theory to thrust chamber conditions to establish a standard design procedure. By using systematic cold-flow testing and hot firings, empirical design equations have been formulated. An effort is currently underway to extend the design theory to other types of acoustical damping devices such as quarter-wave tubes and slots.

INTRODUCTION

The phenomenon of combustion instability has plagued all types of high heat-release combustors from industrial furnaces to rocket engines. In general, the problem has been most severe in flight propulsion systems such as turbojets, ramjets, and rocket thrust chambers where weight considerations dictate highly efficient structures. In such applications, pressure, vibration, and heat loads resulting from combustion instability are superimposed on the normal loading and are usually destructive.

In rocket thrust chambers, high frequency combustion instability can be eliminated by reducing the coupling between the oscillations and the driving process or by increasing the damping in the combustion chamber. The former is usually attempted by either modifying the injector or by using injector face baffles. Stabilizing combustion by modifying the injector is a cut-and-try process, and the necessary modifications are often made at the expense of performance. To be effective, baffles must extend well into the propellant mixing and combustion zone, which not only presents a difficult cooling problem but can also cause performance degradation.

Acoustic damping devices increase the damping in combustion chambers and are very effective when properly designed. They are located in the combustion chamber surfaces outside the mixing zones, and thus have no predicted performance loss.

It is the purpose of this paper to discuss the highlights of the work that MSFC has sponsored for developing a design theory for applying acoustical damping devices to thrust chamber instability.

DISCUSSION

The acoustical damping device found to be most effective is an array of Helmholtz resonators. This consists of a perforated wall (liner) separated by a volume of gas from a solid wall, usually the chamber pressure vessel (Figs. 1 and 2). The mass of gas in the liner apertures and the volume of gas in the cavity behind the liner form an oscillatory system that is analogous to a spring-mass system and has the typical frequency response of a damped oscillator. An effective liner may be designed with no detailed knowledge of the mechanism of combustion instability because the only properties of an unstable combustion process that affect the acoustic performance of the liner are the frequency and the amplitude of the oscillations. The acoustic performance is expressed by the absorption coefficient, which is defined as the fraction of incident energy dissipated by the liner. The energy loss in the system results from turbulence and friction on the side walls of the apertures. At low incident wave amplitudes, energy dissipation is predominately caused by viscous losses from the oscillation of the gas in the aperture. At high incident wave amplitudes, turbulence and circulation resulting from high oscillatory velocities control the absorbing characteristics. For design purposes, the absorption coefficient is described for a given medium by specifying the two components, resistance and reactance, of the acoustic wall impedance. The components are functions of the liner geometry, the properties of the gas in the liner apertures, and the

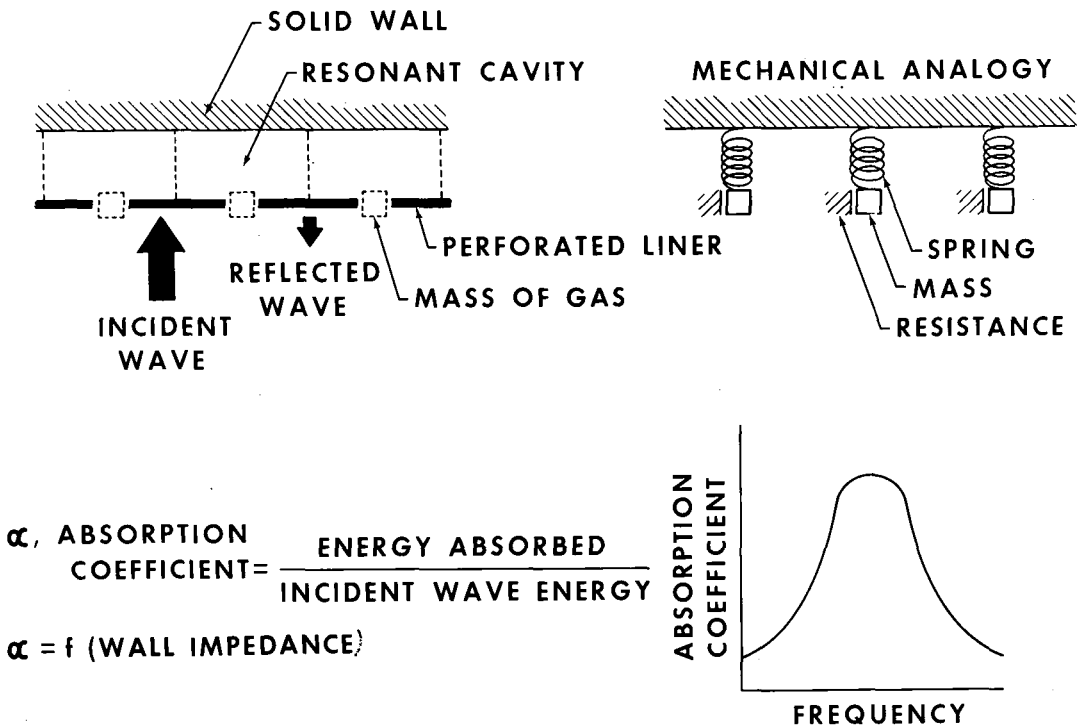

Figure 1. Absorbing liner principles.

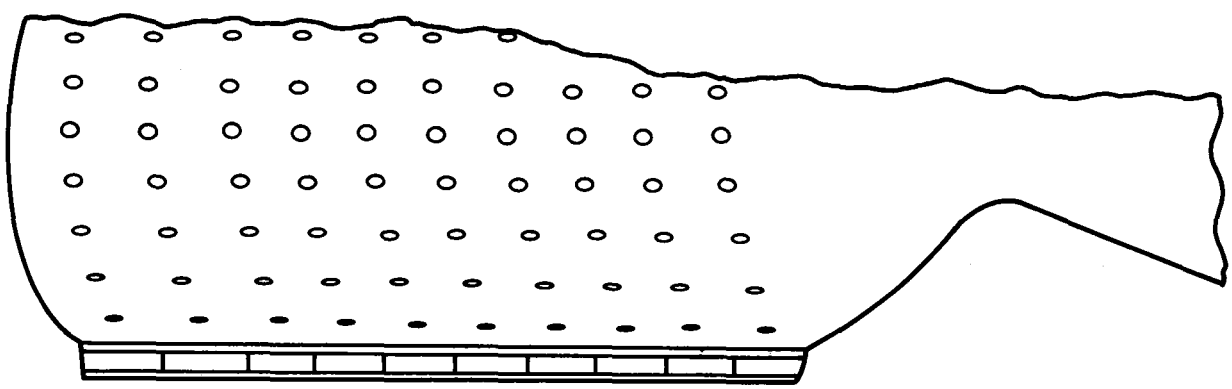

Figure 2. Acoustic liner array.

frequency and amplitude of the pressure oscillations. To obtain good absorption characteristics, liners are designed so that the resonant frequency of the system is near the frequency of the potential combustion instability in the thrust chamber.

As early as 1950, arrays of Helmholtz resonators were used by Pratt and Whitney Aircraft to eliminate high frequency "screech" in airbreathing engine afterburners (Fig. 3). Although the mechanism causing "screech" in afterburners was not and

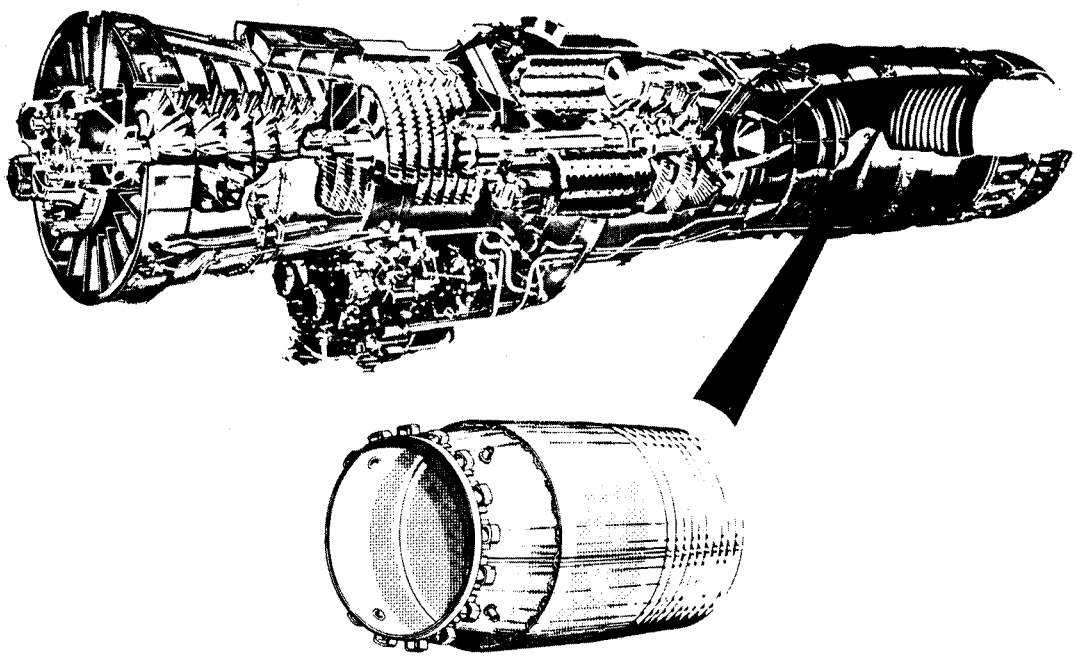

Figure 3. Solution for high frequency combustion instability in afterburners.

is not completely understood, the liners have been completely successful in its damping. In 1963 work sponsored by Marshall Space Flight Center was begun at Pratt and Whitney to adapt resonator theory for rocket engine combustion instability and to develop and demonstrate a theory and design procedure.

The design of resonator arrays for usual acoustical applications is a single and straightforward process; however, many complex factors affect the application of the theory to the design of rocket chamber absorbers. The high gas temperatures, complex flow situations, high pressure amplitudes, gas density stratifications, and other related effects impose serious limitations and uncertainties on the design techniques. A systematic approach to the solution of these problems was taken. The effects of each of the above factors on absorption was quantitatively described and corroborated through impedance tube cold-flow experiments using ambient air and gaseous helium and nitrogen as test media. At strategic intervals, verifications were made with hot-fire testing (Fig. 4).

Some of the areas covered and the results are as follows:

1. Effect of High Oscillation on Absorption

It was quickly determined that with the high oscillation amplitude involved, the resistance term of the linear impedance would be in the nonlinear region. By the use of analytical studies and cold-flow impedance tube testing, empirical design equations were successfully extended to include impedance in the nonlinear range.

2. Liner Location and Length

To answer the question of where and how long a liner must be, hot-fire testing using four quarter-length liners that could be replaced with solid sections was conducted (Fig. 5). Test results indicated that with the tangential instability induced, the first quarter next to the injector was most critical (Fig. 6).

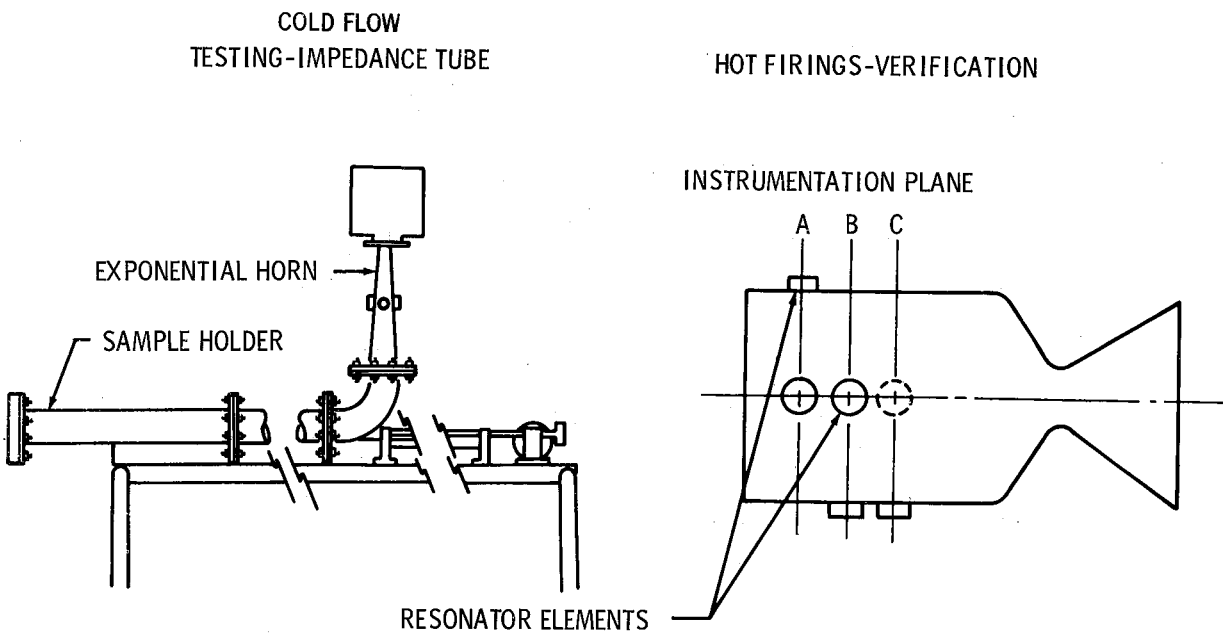

Figure 4. Cold-flow impedance tube testing and hot-fire verification testing.

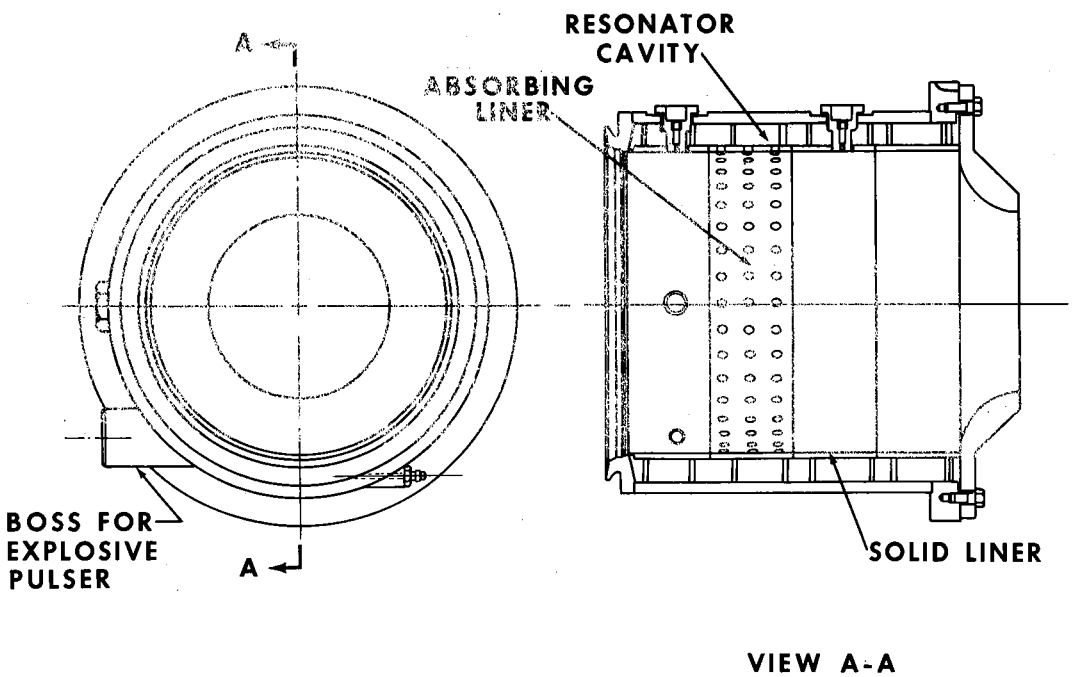

Figure 5. Quarter-length liner in a 15 K uncooled chamber.

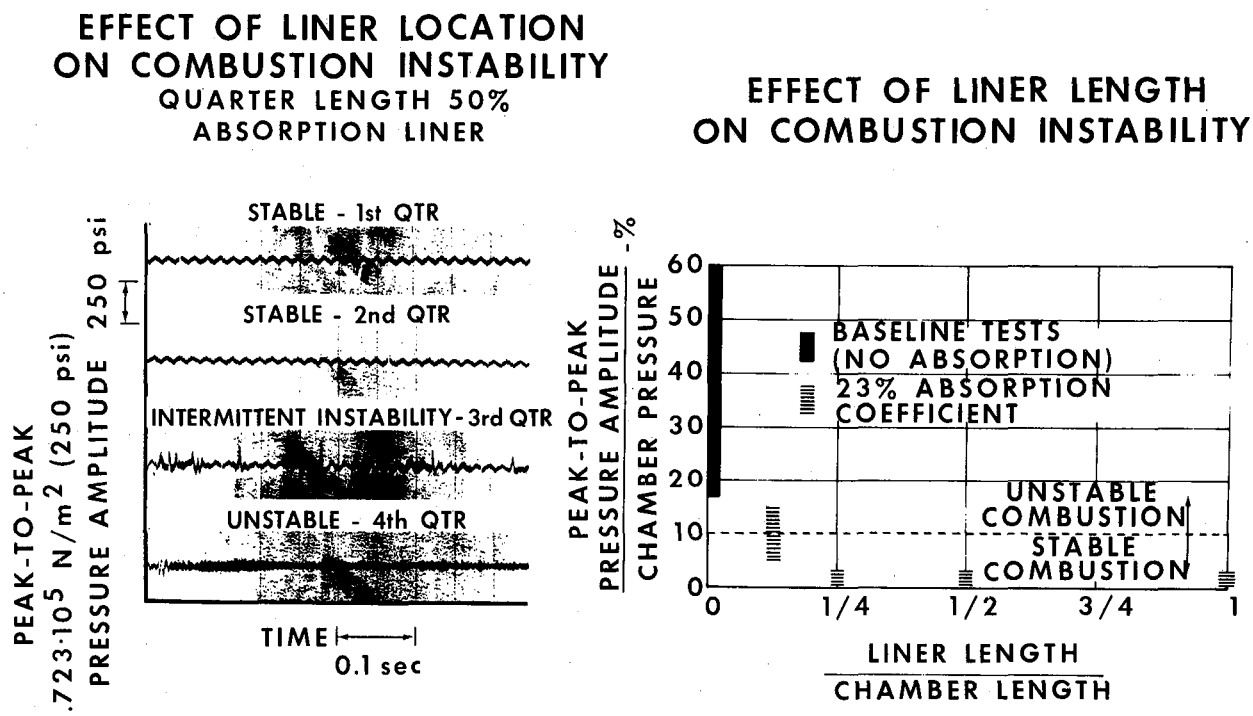

Figure 6. Effect of liner length and location on combustion instability.

3. Effects of Chamber Gas Flows on Liner Performance

Cold-flow testing was conducted with high velocity gas flows both past and/or through liners. The effects were determined, and thus the theory was modified.

4. Improved Liner Absorbing Bandwidth Characteristics

If shifting modes of instability are indicated, a broader bandwidth may be obtained by using an array of resonators tuned to different frequencies (Fig. 7).

5. Final Verification of Improved Liner Design Theory

During the early years of the hot-fire verification testing the instability was damped or it was not damped. No method was available until recently for measuring liner impedance during actual hot-fire testing (Fig. 8). This capability was developed and a final verification was made. The average deviation between the theoretical and experimental absorption was ±11 percent, which is satisfactory for designing absorbing liner arrays for rocket combustion chambers.

It was concluded that although the amount of absorption required to damp instability in all thrust chambers has not been determined, indications are that acoustic arrays are very effective. Because the stability characteristics of every injector-chamber configuration are different, the approach recommended is that liners for new systems be designed for the highest possible absorption.

It was also concluded that resonator damping devices have a wider range of application than was previously thought. In many thrust chamber designs, particularly the high performance regeneratively cooled chambers, the installation of liner arrays is not feasible (Fig. 9). In many instances it is only possible to install single resonators or rows of resonators. In other instances chamber construction lends itself only to the installation of slots or quarter-wave tubes.

An example of this was the single ring acoustic liner that damped the instability in the 445-N (100-lb) thrust C-1 engine. Although this liner was successful, it was discovered that some of the terms in the design theory for determining the absorption coefficient are ambiguous. For this reason an additional effort is in progress to extend the design theory to include nonarray damping devices. This consists of additional analysis and cold-flow testing.

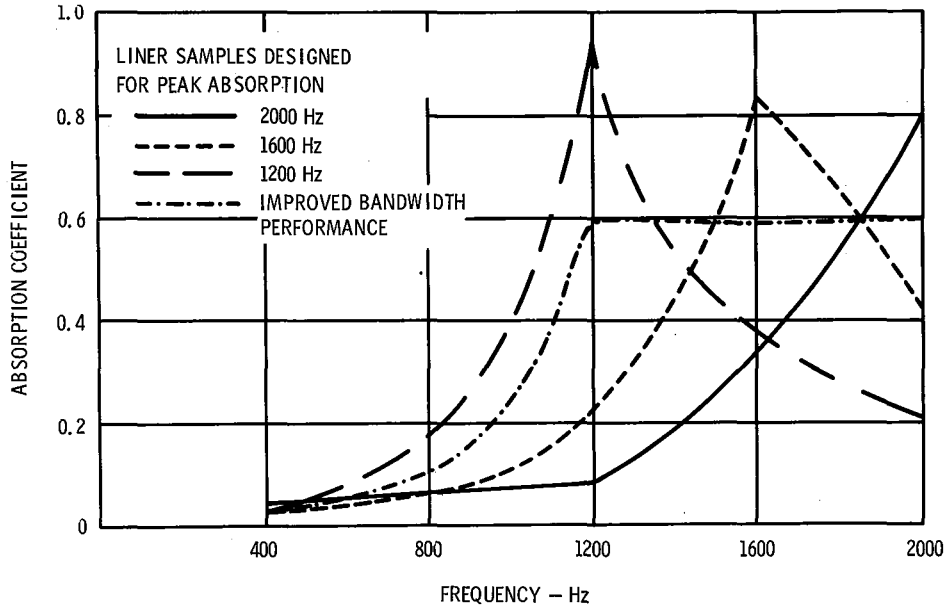

Figure 7. Liner bandwidth characteristics.

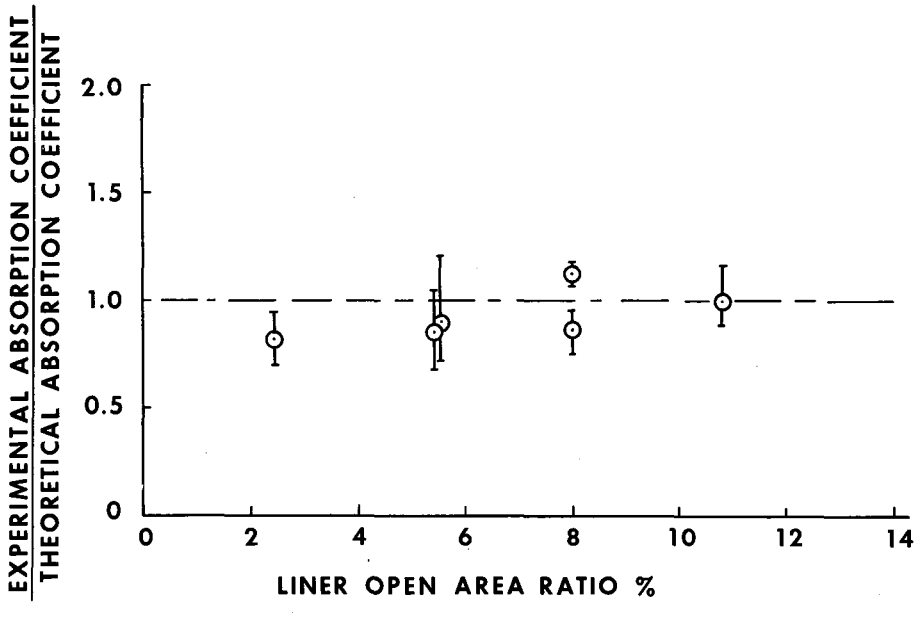

Figure 8. Measurement of liner impedance during hot-fire testing.

The cold-flow testing is being conducted in a reverberation chamber, an apparatus that has a wider range than the impedance tube.

The preliminary design theory has been completed and test data have shown very good agreement (Fig. 10). Additional testing is underway to investigate the dimensional limitation and optimum spacing of resonators.

At the completion of this year's effort, it is felt that the program's objective of developing a theory for the design of acoustical damping devices for damping thrust chamber instability with a wide range of application will be achieved.

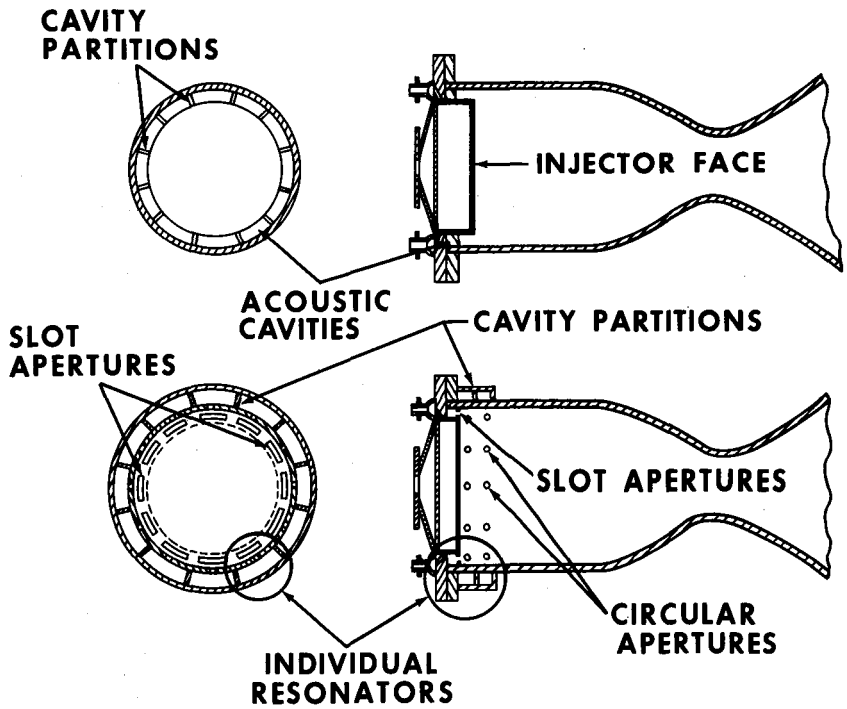

Figure 9. Acoustic cavities and individual resonators used as damping devices — example configurations and locations for rocket chamber installations.

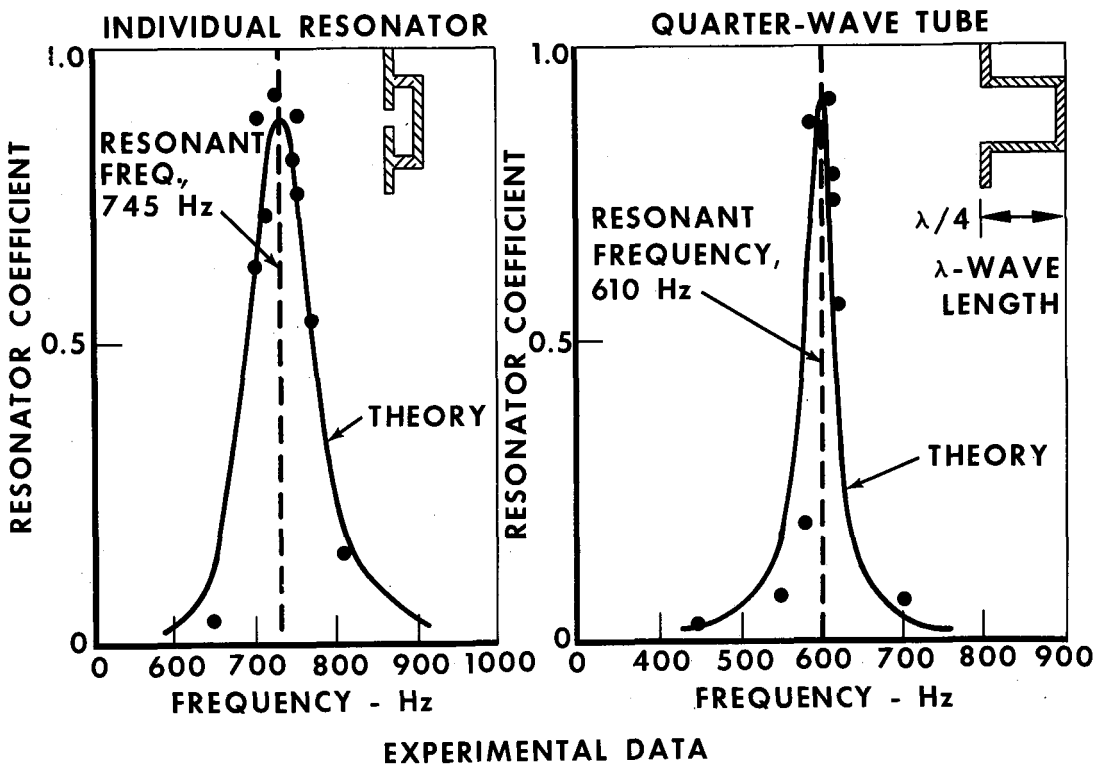

Figure 10. Comparison of experimental results with nonarray design theories.

Page intentionally left blank

PULSE PERFORMANCE ANALYSIS FOR SMALL HYPERGOLIC PROPELLANT ROCKET ENGINES

By

Gerald W. Smith

SUMMARY

Small rocket engine tests were conducted for the purpose of obtaining pulse performance data to aid in preliminary design and evaluation of attitude control systems. Both monopropellant and hypergolic bipropellant engines of thrust levels from 5 to 445 N (1 to 100 lb) were tested. The performance data for the hypergolic propellant rockets are compared with theoretical performance calculated from idealized chamber filling and evacuation characteristics. Electromechanical delays in valve response and heat transfer characteristics were found to cause substantial deviation between theoretical performance and test performance. The theoretical analysis is modified to obtain a semiempirical model for hypergolic propellant rockets which is demonstrated to be reasonably accurate for two different engine configurations over a considerable range of duty cycles.

LIST OF SYMBOLS

Symbol	Meaning
A	cross-sectional area
c_f	engine thrust coefficient
c_p, c_v	specific heat at constant pressure and constant volume, respectively
c^*	characteristic exhaust velocity $\equiv \sqrt{RT_c}/\Gamma$
F	engine thrust
I_{sp}	specific impulse
I_t	total impulse
L^*	engine characteristic length $\equiv V_c/A_t$
M	Mach number
m	mass
P	pressure
R	universal gas constant
t	time
V	volume
u	velocity relative to vehicle
γ	ratio of specific heats $\equiv c_p/c_v$
Γ	$(\gamma)^{1/2}\,[2/(\gamma+1)]^{(\gamma+1)/2(\gamma-1)}$
$(\bar{\ })$	average value
$(\cdot)$	differentiation with respect to time

Subscripts

a	atmospheric condition
c	chamber condition
d	discharge condition
f, o	fuel and oxidizer injected, respectively
p	propellant (fuel plus oxidizer) injected
e, t	nozzle exit and throat, respectively
s	steady-state condition

INTRODUCTION

The direction of the nation's space exploration program toward missions with longer lifetimes, such

as the Apollo, Skylab, and Mars missions, has created very stringent design and operational requirements for launch vehicles and spacecraft subsystems. The attitude control system (ACS) provides rocket impulse for vehicle orientation and orbital or plane maneuvers. In the past, mission requirements for the ACS have been primarily suborbital or satellite oriented, requiring relatively low thrust levels and total impulse (I_t). A typical satellite mission would require total impulses of less than 45 000 N-s (10 000 lbf-s) with a resulting subsystem weight of a few hundred kilograms. For systems of this size, reliability, simplicity, and use of state-of-the-art technology tend to be the major design criteria; performance is of secondary consideration. However, as mission lifetime and required total impulse and system weight increase, more emphasis must be placed on performance as a major design criterion. From the requirement for improved performance, two basic system designs have emerged, a monopropellant design and a bipropellant design.

The monopropellant system utilizes a single propellant, anhydrous hydrazine (N_2H_4) and a catalyst bed that decomposes the propellant. The temperature of decomposition ranges from 1140 to 1260° K (1600 to 1800° F) with a theoretical vacuum specific impulse (I_{sp}) of approximately 260 s. The bipropellant system (Fig. 1) uses two propellants, an oxidizer and a fuel, which are hypergolic. The most commonly used oxidizer is nitrogen tetroxide (N_2O_4), a liquid that is hypergolic with many fuels. Most common among the fuels are the various derivatives of hydrazine, a toxic liquid which is very flammable and ignites spontaneously in contact with N_2O_4. In contrast to the rather low chamber temperature of the monopropellants, the flame temperature of these bipropellants may be as high as 3310° K (5500° F) with a theoretical vacuum specific impulse of approximately 330 s.

The sizing of an attitude control system requires that the engine performance be known for the entire mission duty cycle. Test results have shown that the specific impulse (I_{sp}) varies with the engine duty cycle (Fig. 2). Determining the impulse performance versus duty cycle for a given engine configuration with any degree of accuracy is not a

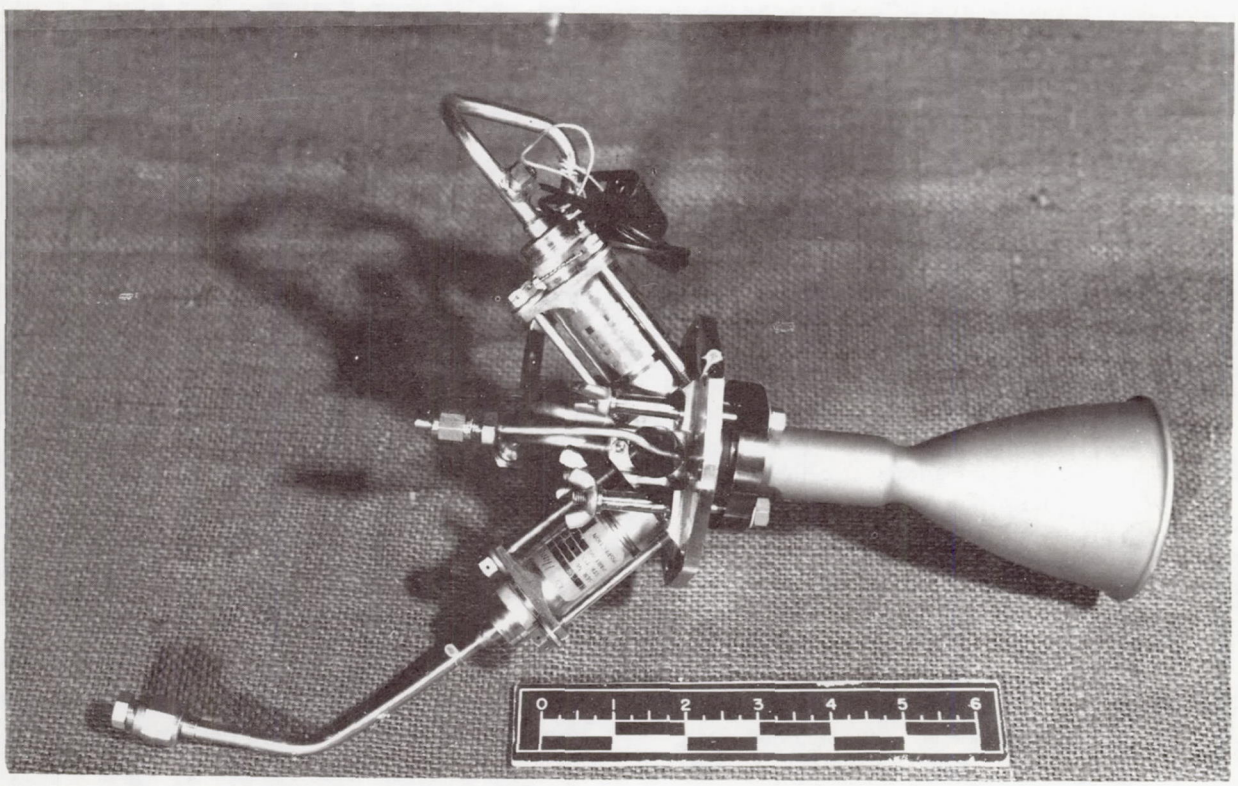

Figure 1. Typical bipropellant attitude control engine, F = 98 N (22 lbf).

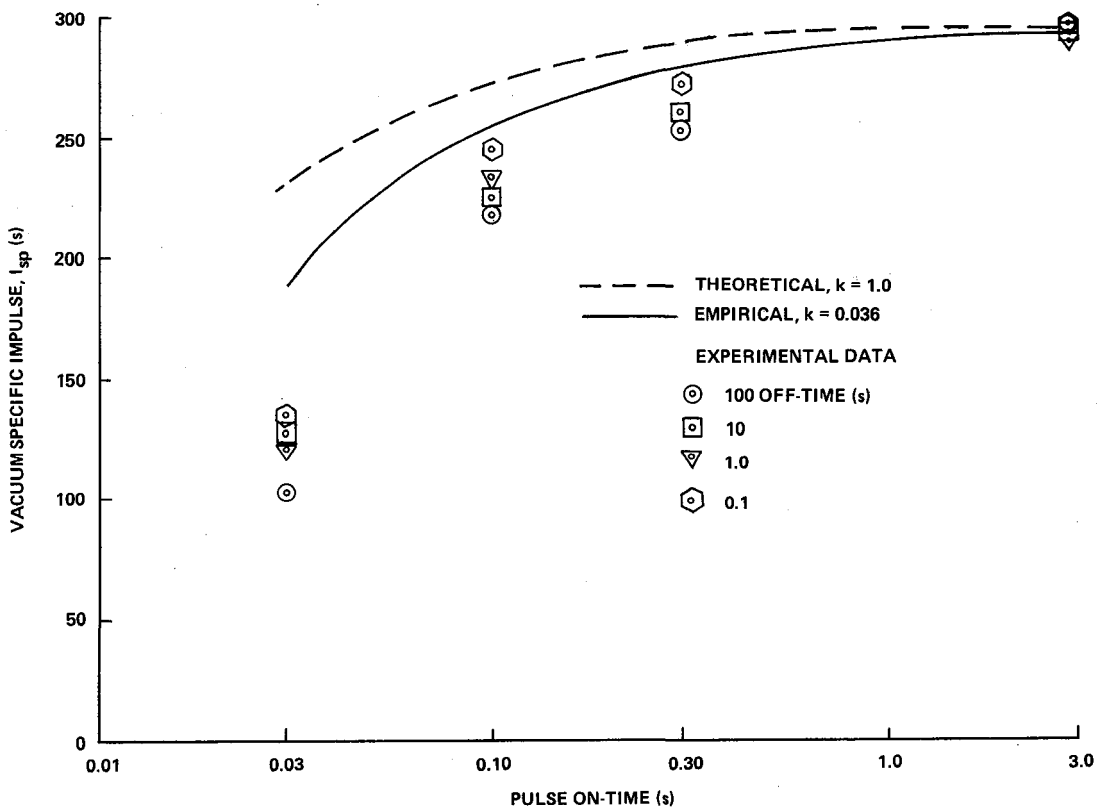

Figure 2. Typical performance of pulsed attitude control engine.

straightforward task and usually requires a test program designed to simulate the mission duty cycle and the engine operating environment. The capability of predicting the engine performance for specific operating conditions within reasonable accuracy limits would therefore be a very useful tool for the system designer.

The analytical determination of the thrust-time curve can be divided into four parts: (1) the pressure history up to the point of ignition, (2) the pressure history during the ignition process, (3) steady-state operation, and (4) the pressure during tailoff. For the case of very short pulses, the thrust trace may be completely transient. An accurate performance model must include all portions of the trace from valve signal initiation through pressure decay. The reaction mechanism and the combustion characteristics of the propellants dictate the pressure and temperature environment within the combustion chamber. The major portion of this investigation and the test data which are used as a basis for the performance model are based on a nitrogen tetroxide (N_2O_4) monomethylhydrazine (MMH) hypergolic propellant combination whose general characteristics are given in Reference 1.

Analytical prediction models exist which predict with reasonable accuracy the performance that can be expected with a fairly comprehensive selection of propellant combinations if the propellant atomization characteristics are known. Several theoretical studies have been made to describe the combustion of liquid sprays under the assumption that propellant vaporization is the rate controlling process [2]. The droplet size and distribution must be known to predict the engine performance. Accurate measurements of the degree of atomization and propellant mixing in an actual rocket engine environment are extremely difficult to achieve, although attempts at such measurements have been made with high speed photography, laboratory or scale model tests, and various gas sampling techniques. Detailed discussions of the interrelations of injector design, atomization, vaporization, and combustion efficiency are given by Lewis, Ingebo, Miesse, Priem, and Penner [2-7]. Analysis of performance of hypergolic propellants is further complicated because reaction may occur in

both liquid and gaseous states. Tests indicate that below certain critical pressure and temperature limits the initial reaction occurs in the liquid phases, whereas for higher pressures and temperatures, normal gas-gas reaction occurs [8, 9]. Release of the propellants into a confined region, such as a combustion chamber, under space vacuum conditions results in a rapid pressure rise, which is due solely to vaporization of the oxidizer. This results in primarily a gaseous phase reaction producing consistent and repeatable start transient characteristics even at very low ambient pressure conditions.

Clearly, ignition delay time and the start transient after ignition are very important factors in determining the impulse developed by an engine during a short pulse. The ignition delay time has been somewhat arbitrarily defined as that time interval required to generate a sufficient quantity of intermediates in the rate controlling reaction step so that product gases near the adiabatic flame temperature are produced [10]. For a N_2H_4-N_2O_4 propellant combination, the rate controlling step is highly exothermic so that the product gases are those generated during this reaction. Because of the high temperatures, subsequent reactions occur very quickly. The suggested kinetics for the reaction is [10]

$$2\ N_2H_4 + N_2O_4 \rightarrow 3\ N_2 + 4\ H_2O \quad , \qquad (1)$$

although there is some evidence that the mechanism of the reaction involves an initial neutralization followed by an oxidation, or

$$N_2H_4 + N_2O_4 \rightarrow 2\ N_2 + 2\ H_2O + O_2 \qquad (2)$$

$$O_2 + N_2H_4 \rightarrow N_2 + 2\ H_2O \quad . \qquad (3)$$

Experimental measurements of ignition delay times using hydrazine-nitric acid mixtures yield results from 0.1 to 3 ms and flame speeds of approximately 61 m/s (200 ft/s) are indicated [11]. For small rocket motors, 7.6 cm (3 in.) in length or diameter, the length of time required for a flame to sweep the chamber is about 1 ms. Once ignition is achieved, the chamber pressure transient depends on the amount of propellant inside the chamber. A model for predicting hypergolic ignition transients in space engines is presented by Seamans [12]. This analysis treats the pressurization of a thrust chamber as a sequence of steady-state processes in very short time intervals considering the effects of vaporization and the chemical kinetics of the propellant reaction. The model does not account for varying injector flow rates that occur during the start transient as a result of flashing of such highly volatile propellants as N_2O_4, which appears to play an important role in the actual start characteristics.

After the start transient is completed, the engine achieves a steady-state operating condition. The chamber pressure and temperature during this phase of operation remain approximately constant as governed by flow rates, mixture ratio, and geometric factors. The fourth and final portion of the pulse that must be modeled is the pressure decay or tailoff. Most analytical models describe the shutdown sequence as an instantaneous stopping of the burned gas generation followed by an immediate decay in chamber pressure. Two examples of these models assume isentropic and isothermal decay rates inside the combustion chamber [13, 14]. As is shown later, these idealizations again fail to give an accurate representation of the transient behavior. Furthermore, the pressure response of the engine during both startup and shutdown does not occur instantaneously upon electrical command to the engine valves. Examination of rocket engine flow data reveals lags in the flow rate response. All of these factors will tend to reduce the accuracy of any theoretical type performance prediction model such that, for short pulses of less than 100-ms duration, theoretical results may be grossly inaccurate. These areas are explored herein to a somewhat greater extent in order to determine their significance and to establish a more accurate prediction model based on empirically derived information.

EXPERIMENTAL INVESTIGATION

Both monopropellant and hypergolic bipropellant engines of separate thrust levels [5 to 445 N (1 to 100 lb)] were tested. Although various engine configurations were tested, the test data presented and those data that were used as the basis for the empirical model were obtained from tests of bipropellant engines using N_2O_4-MMH propellants. The basic features of the test engines are summarized in Table 1. Engine A was selected as the primary data source based on engine configuration, quality of the test data, and the type of instrumentation used during

TABLE 1. DESCRIPTION OF TEST ENGINES

Test Configuration	Engine A	Engine B
Propellants	N_2O_4/MMH	N_2O_4/MMH
Thrust, N (lbf) (vacuum)	445 (100)	98 (22)
Chamber Pressure, N/cm^2 (psia)	98 (142)	66 (95)
Mixture Ratio, O/F	1.6	1.6
Nozzle Expansion Ratio, A_e/A_t	60:1	40:1
Throat Area, cm^2 ($in.^2$)	2.561 (0.397)	0.8562 (0.1327)
Injector Configuration	Multiple element unlike impinging doublet	Single element impinging doublet
Characteristic Length, L^*, cm (in.)	27.9 (11.0)	17.8 (7.0)
Cooling Technique	Film and Radiation	Radiation
Boundary Layer Coolant, $\%\dot{m}_f$	40.0	0

the test. Tests on engine B were not conducted for the specific purpose of analysis of pulse performance, but sufficient information was obtained to provide a reasonable basis of comparison with engine A. In certain instances, test data from a second engine (B-1) identical to B are included for additional analysis purposes. Engines A and B are considered to be very representative of the current state-of-the-art for attitude control engines both in terms of hardware design and performance.

The propellant valve for engine A was torque-motor operated with mechanically linked oxidizer and fuel valves. The valve poppets were held in the closed position by permanent magnet biasing forces on the torque motor. Two welded flexure tubes provided redundant seals to prevent the propellants from intermixing and to isolate the torque motor from the propellant. The design was of all-welded, corrosion-resistant steel construction with a soft-seat teflon seal at each nozzle orifice to minimize leakage. Solenoid valves were used for propellant control for engine B.

A steam ejector system with diffuser was used to maintain near vacuum conditions in the vacuum test chamber. The ejector system was capable of simulating an altitude of 25 000 m (82 000 ft) at propellant flow rates of 0.18 kg/s (0.40 lb/s) [approximately 445 N (100 lbf) thrust] and 35 100 m (115 000 ft) at 0.05 kg/s (0.10 lb/s) [approximately 111 N (25 lbf)]. When the engine was not firing, the pressure inside the vacuum chamber was maintained at 0.041 N/cm^2 (0.059 psia) or 38 100 m (125 000 ft). The vacuum chamber was approximately 0.9 m (3 ft) in diameter and 0.9 m (3 ft) long. The engines were mounted horizontally on a thrust measuring test bed which utilized a Flexcell consisting of a load cell and a parallelogram flexure. The primary instrumentation used for the performance analysis consisted of propellant flow rates and temperatures, engine chamber pressure, and valve current. Redundant (series-mounted) flowmeters were used in each propellant line to obtain accurate flow measurements. Both a turbine type flowmeter and a Ramapo flow transducer were used.

Pre-test and post-test calibrations indicated that the Ramapo transducer was the more accurate of the two, and it was also found to be more responsive to pulse flow measurements than the turbine type, which had greater inertia to overcome during flow transients. The turbine flowmeter was primarily used to validate steady-state readings. The Ramapo flow transducer

senses the dynamic force of fluid flow as a drag force on a specially contoured body of revolution suspended in the flow stream. This force is transmitted by a lever rod and modified coaxial torque tube to an externally bonded, four-active-arm strain gage bridge. The absence of bearings, linkages, and moving parts provides high frequency response with inherently low hysteresis.

The combustion chamber pressure was measured by a close-coupled strain gage pressure transducer capable of a rise time of 1.0 ms or less from 10 to 90 percent of any pressure step input with an overshoot of less than 10 percent of the pressure step. For most test runs the transducer was mounted approximately 15 cm (6 in.) from the chamber and connected by 0.318-cm (0.125-in.) tubing to the chamber wall. This resulted in a fill volume of 0.9637 cm^3 (0.0588 $in.^3$), which produced negligible effect on pressure response time. Immersion type thermocouples and pressure transducers were used to measure propellant conditions just upstream of the engine valves. Thermocouples on the chamber and nozzle walls were used to determine external skin temperatures.

All data signals were recorded on strip chart recorders with propellant feed pressure, chamber pressure, valve current, and flow rates also being recorded on oscillograph recorders and analog magnetic tape. Steady-state specific impulse and characteristic exhaust velocity were calculated from strip chart recorder data obtained during the steady-state portions of the test run. This proved to be the most accurate method for calculating steady-state performance. Pulse performance calculations were based on the oscillograph and analog tape data.

The same test duty cycle was used for each engine in order to provide a common base for performance comparison and to characterize the engine performance over a range of operating conditions. The duty cycle (Table 2) was considered representative of ACS missions under consideration at the time the test program was conducted.

Typical test results as recorded by oscillograph are shown in Figure 3. The thrust trace was very erratic throughout the test and therefore values of thrust calculated from the chamber pressure were substituted for performance analysis. The difficulty was attributed to overheating of the strain gages attached to the Flexcell. The transient response characteristics of other engines are illustrated in Figure 4. The data presented were obtained from tests which for the most part were not instrumented for pulse performance analysis. The slow rise and decay in propellant flow rates is indicative of the data obtained from a turbine-type flowmeter with a slow response. The oscillograph traces show the erratic nature of the flow transients during pulsing operation. Such behavior is caused by pressure pulses in the engine feed lines produced by rapid opening and closing of engine valves and is influenced by feed line size, volume between valve and injector, and propellant temperature. These unstable flows make it extremely difficult to either model or to accurately measure pulse performance of the engine.

For operation at high altitudes or in near vacuum conditions, once choked flow is achieved in the nozzle, the thrust coefficient c_f remains essentially constant. For very low ambient pressure conditions the flow will be choked almost instantaneously with the first measurable amount of chamber pressure. The thrust, then, depends only on chamber pressure variation with time, and engine specific impulse for a single pulse can be determined from

$$I_{sp} = A_t c_f \int P_c dt / \int \dot{m}_p dt \quad . \qquad (4)$$

Specific impulse for each step (Table 2) was calculated from the recorded data using equation (4). The results for engine A are those given in Figure 2. The values plotted are the averages for two pulses only, because the pulse-to-pulse variations are quite small.

DATA ANALYSIS

The feasibility of adopting a semiempirical approach was investigated by analyzing the test data obtained from engine A. The pressure and flow transients (buildup and decay) appeared to be quite repetitive regardless of duty cycle. The assumption was therefore made that propellant flow rates and chamber pressure are relatively insensitive to duty cycle and depend primarily on a pulse time reference. This assumption is not valid for cases where the time between pulses is of such a short duration that the chamber pressure and flow rates have not had time to completely decay prior to the next pulse. In these instances, allowances must be made for the non-zero start conditions in addition to the possibility of differences in the start transient behavior. This

TABLE 2. ENGINE TEST DUTY CYCLE[a]

Step	Number of Cycles	On-Time (s)	Off-Time (s)
1	10	0.03	100.0
2	10	0.10	100.0
3	10	0.30	100.0
4	10	3.0	100.0
5	10	0.03	10.0
6	10	0.10	10.0
7	10	0.30	10.0
8	10	3.0	10.0
9	20	0.03	1.0
10	20	0.10	1.0
11	20	0.30	1.0
12	20	3.0	1.0
13	20	0.03	0.10
14	20	0.10	0.10
15	20	0.30	0.10
16	20	3.0	0.10
17	5-min steady state run		

a. Total engine on-time = 505.8 s.

is best illustrated in Figure 5, where the oxidizer flow transient is entirely different from that of other pulses presented in Figures 3 and 4. The present analysis is restricted to duty cycles where the off-time is sufficient to allow the pressure and flow rates to decay completely.

Figures 6 and 7 show more clearly the variation of pressure with pulse on-time for A and B respectively. A delay of the order of 10 ms is noted before any pressure rise occurs. These delays are attributed to the electromechanical characteristics of the valve, the hydraulic response characteristics of the propellants, and the ignition initiation delay. Similar lags are notable at cutoff and affect mass flow rate responses as well as the pressure changes. The largest portion of the lags may be traced to the valve response which has been measured at 6 ms for opening and closing, respectively. For the purpose of this analysis, it is assumed that the rise and decay lags are known or can be reasonably estimated.

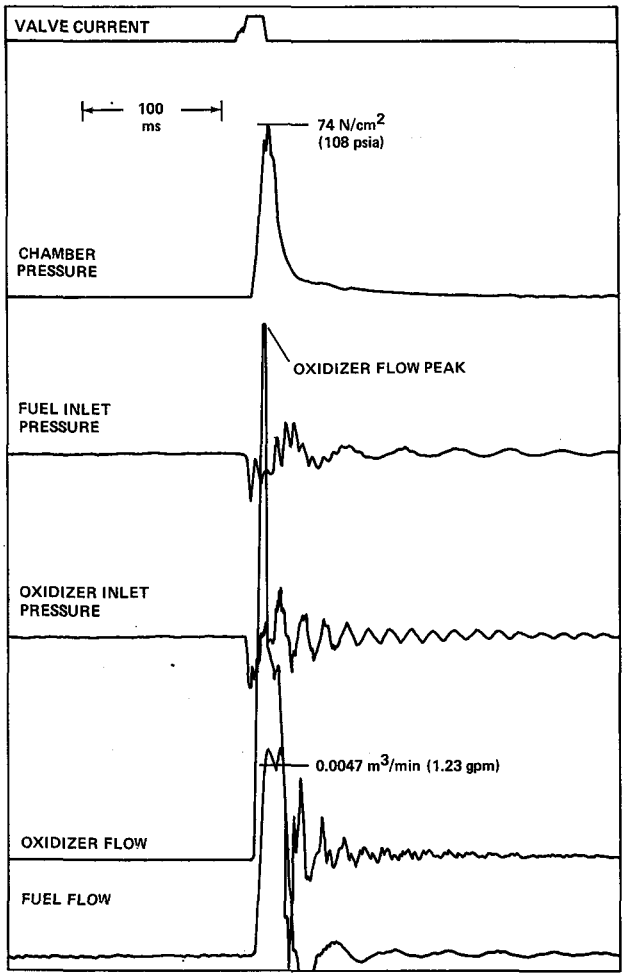

Figure 3. Oscillograph recording of 30-ms pulse for engine A.

As a first approach toward establishing a mathematical model of the start transient, it is further assumed that the propellant burns at a constant rate equal to the steady-state propellant injection rate. The continuity equation establishes a balance between the mass flow rate of propellant $\dot{m}_p$, the mass discharge rate through the nozzle $\dot{m}_d$, and the rate of change of gaseous mass within the combustion chamber

$$\dot{m}_p = \dot{m}_d + d\left(\rho_c V_c\right)/dt \qquad (5)$$

For small engines, it may be assumed that $\dot{m}_d$ is given by the steady-state nozzle discharge equation [14],

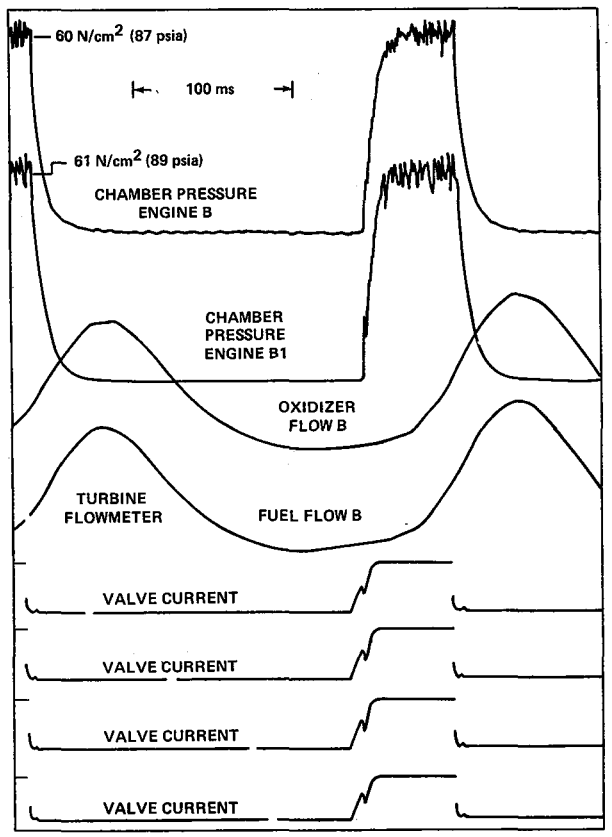

Figure 4. Oscillograph recording of 65-ms pulse for engines B and B1.

$$\dot{m}_d = P_c A_t / c^* \qquad (6)$$

It is next assumed that the gases are perfect ($\rho_c = P_c/RT_c$) and that T_c is constant during pressurization. Equations (5) and (6) then yield

$$dt = dP_c \Big/ \left[c^* \Gamma^2 \left(\dot{m}_p c^* - P_c A_t\right)/V_c\right] \quad , \qquad (7)$$

which when integrated gives

$$P_c = P_{cs}\left[1 - e^{(c^* \Gamma^2/L^*)t}\right] \qquad (8)$$

The result is superimposed on the plot of the test data in Figures 6 and 7. Although substantial differences exist between the theoretical and actual

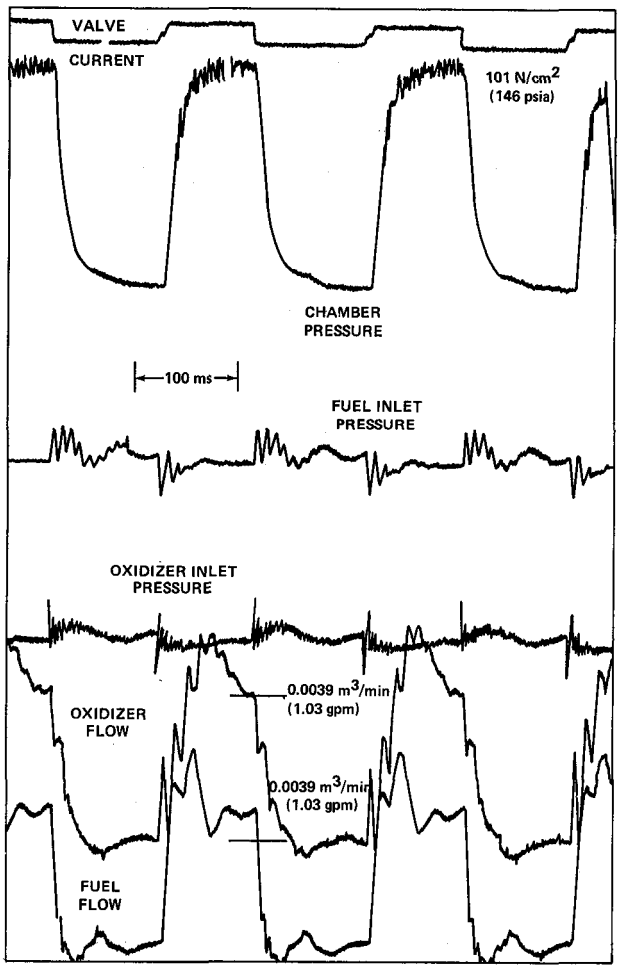

Figure 5. Oscillograph recording of 100-ms pulse for engine A, short off-time.

performance, equation (8) establishes a plausible basic form for the pressure transient.

The solid lines in Figures 6 and 7 are the results of fitting an equation of the basic form of equation (8) to the test data and modifying the equation by the addition of a constant, k, in the exponential term. A k value of 0.036 yields good correlation with the test data for both engines A and B. A deviation was found to exist between the empirically derived values and the experimental data during the latter part of the pressure rise transient for engine A (Fig. 6). This was not true for engine B and would appear to be caused by differences in the thermal response characteristics of the two engines; the case for engine B is discussed later.

Most theoretical models of the pressure decay transient describe the shutdown sequence as an instantaneous stopping of the gas generator followed by either isentropic or isothermal depressurization. For the isentropic case, the continuity equation gives for the time after cutoff [13]

$$t = (L^* / \Gamma^2 c^*)\,[2/(\gamma - 1)] \left[\left(P_{cs}/P_c \right)^{\frac{\gamma-1}{\gamma}} - 1 \right]^{1/2} ; \tag{9}$$

for the isothermal case, the result is

$$P_c = P_{cs} \left[e^{-(\Gamma^2 c^* / L^*)\, t} \right] \tag{10}$$

Both isentropic and isothermal rates of decay give numerical results showing a chamber pressure of 1.38 N/cm^2 (2 psi) in less than 4 ms. The actual test results illustrated in Figures 8 and 9 indicate substantially longer decay rates. The exponential form of the decay transient equation is adopted to describe the shutdown transient, again using the constant k in the exponential term. Curve fitting of the test data again revealed that a k value of 0.036 best described the shutdown transient for both engines as noted by the solid lines in Figures 8 and 9. Thus, a large degree of similarity is seen to exist in both the form of the start and shutdown transient equations and also in the k factor for both engines A and B. For engines B and B1 the decay transient appears to be independent of the duty cycle, whereas for engine A the longer pulse on-times tend to produce longer decay transients (Fig. 8).

A possible explanation for the decrease in decay rates with an increase in pulse width is that the engine chamber wall temperature increases as the pulse duration increases. As the gas remaining inside the chamber starts to expand after the propellant flow ceases, the rate at which heat is transferred from the gas to the hot chamber wall is reduced, thus causing the pressure decay to be slower than for the cooler wall cases. A lack of test data over a wide range of duty cycles would appear to explain why engine B did not exhibit a similar behavior during the decay transient.

As was true of the start transient, a lag time exists before the chamber pressure starts to decay.

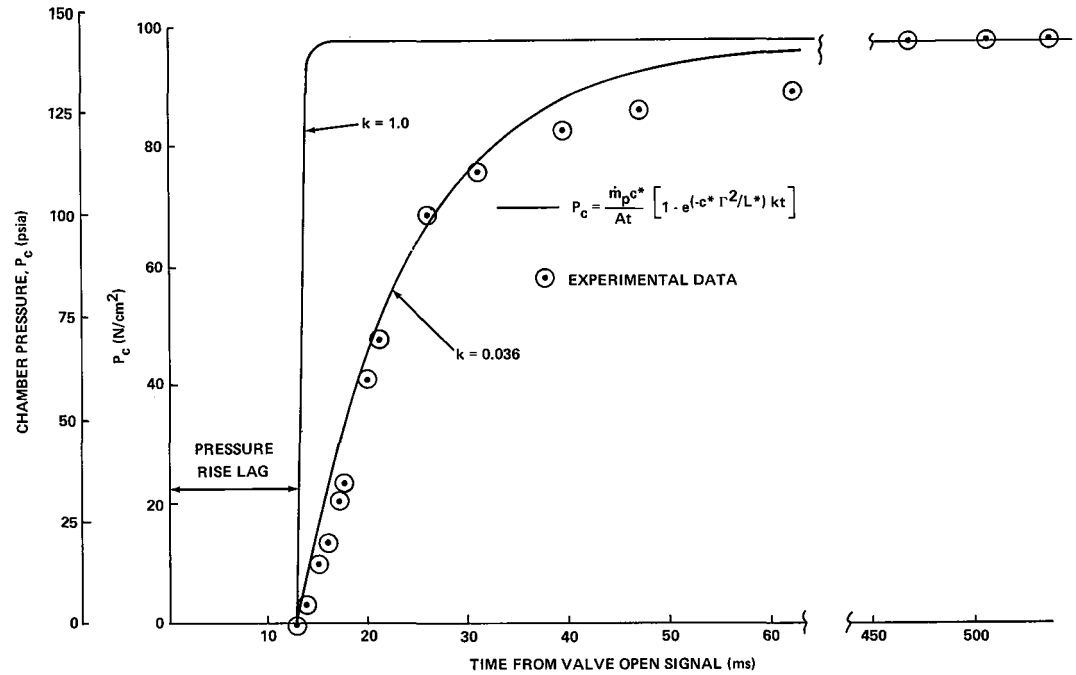

Figure 6. Chamber pressure start transient, engine A.

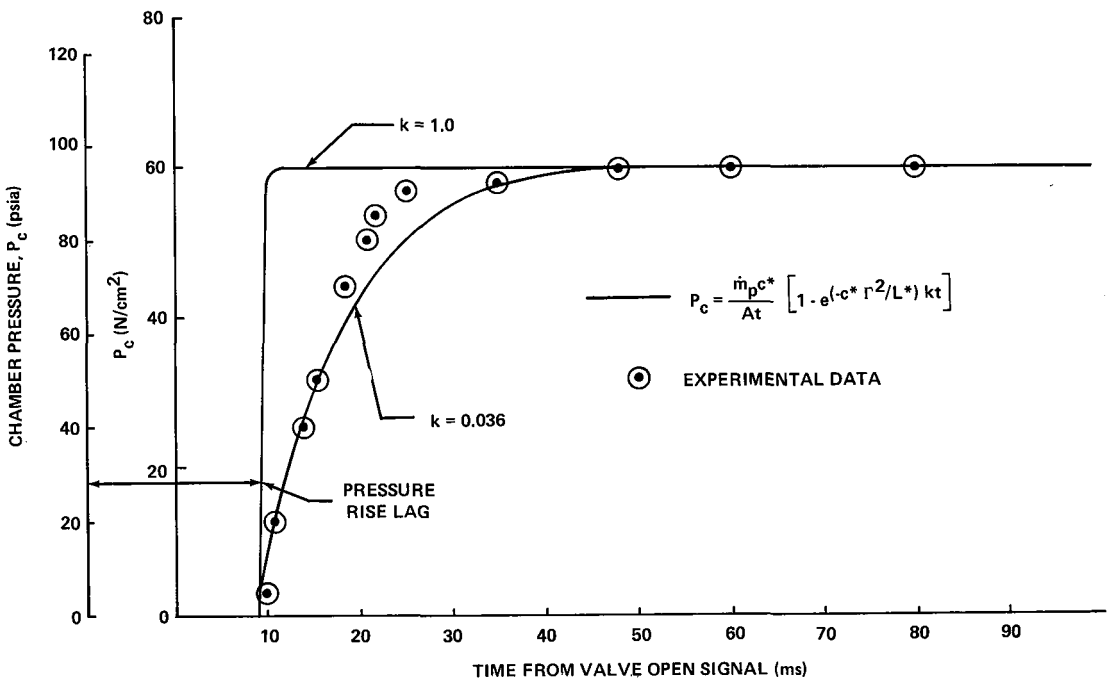

Figure 7. Chamber pressure start transient, engines B and B1.

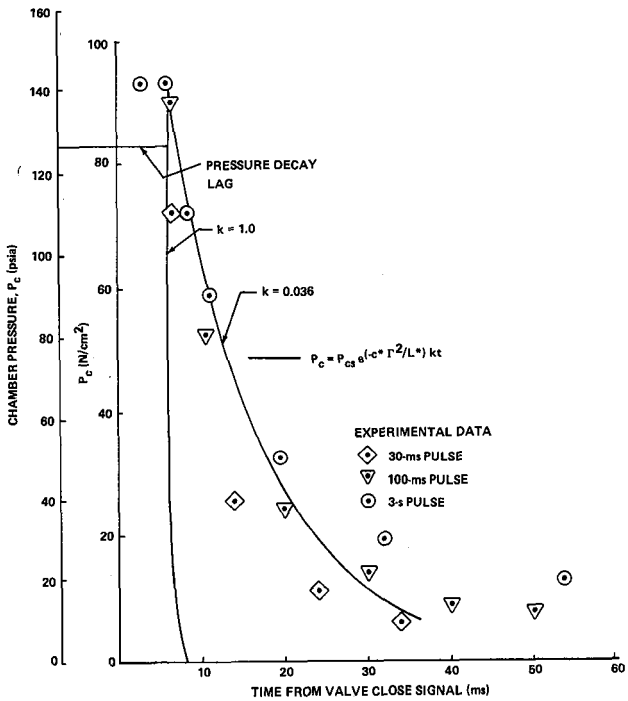

Figure 8. Pressure decay transient, engine A.

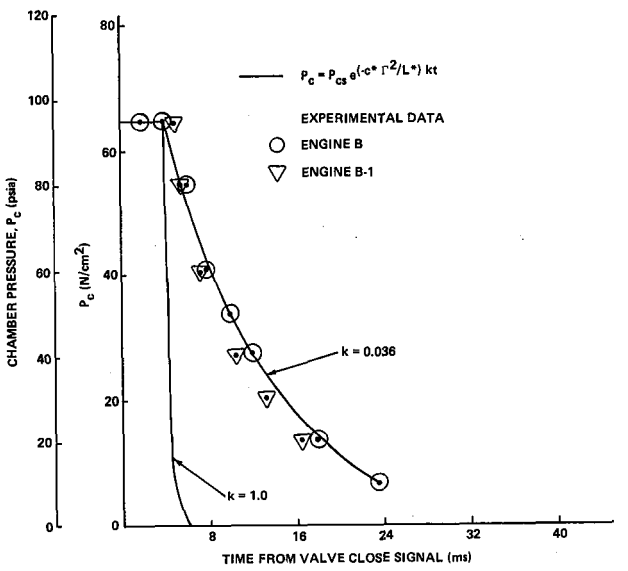

Figure 9. Pressure decay transient, engine B.

For engine A, this lag time is 6 ms. Since the pressure pulse is delayed 13 ms in the starting transient and 6 ms in the decay transient, for a 100-ms electrical pulse width, an active pressure response (greater than 10-percent steady-state pressure) will occur for a period of 93 ms before the pressure decay is initiated.

In an attempt to better understand the differences in the transient behavior of engines A and B, the thermal histories of the engines during the start and shutdown transients were reviewed. Although only limited data were available for analysis, it was notable that engine B achieved thermal equilibrium in a fraction of the time required for engine A. There are several factors which could contribute to this: (1) engine A is film and radiation cooled, whereas B is only radiation cooled; (2) the dribble volume between the valve and injector is much larger for engine A than for B thus producing longer transients; and (3) the larger chamber volume does not have a proportionally larger surface area which reduces the effect of heat transfer from the gas to the chamber wall. A detailed thermal analysis using additional instrumentation would be required to obtain a quantitative evaluation of the engine thermal characteristics.

To complete the mathematical model, expressions for the propellant flow rates must be obtained. The oxidizer flow start transient is shown in Figure 10, which illustrates the characteristic overshoot common to all engines of this type for both fuel and oxidizer. Several attempts were made to curve-fit the transient by means of exponential expressions, but these failed to provide a reasonable degree of correlation with the test data. Furthermore, tailoring of equations to fit the unique characteristics of the propellant flow rates by use of a high degree polynomial results in a mathematical model applicable only to a specific engine configuration and is of little value in the performance prediction of other engines. A study of the test data indicated, however, that the assumption of a step flow rate at the steady-state level beginning with the first evidence of flow would provide a reasonable estimate of the gross response, which is all that is needed for calculation of specific impulse. The flow lag for engine A was consistently 7 to 8 ms after the valve open and close signal for both propellants and was found to be independent of duty cycle. Flow rate data for engine B are not included since high response flow transducers were not used with the engine.

Finally, the flow decay rates were analyzed and are presented in Figure 11. Straight-line approximations of the flow decay provided excellent correlation with the test data.

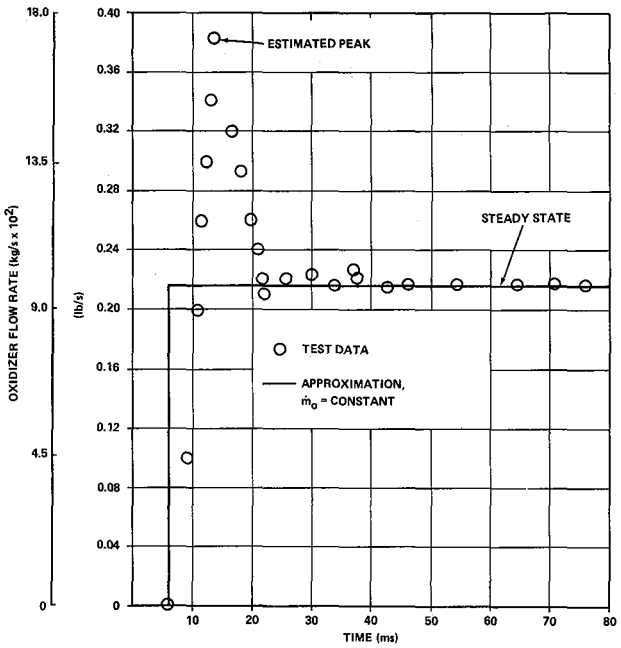

Figure 10. Oxidizer flow start transient, engine A.

RESULTS AND CONCLUSIONS

Integration of the various equations for engine A gives the predicted performance shown by the solid line in Figure 2. A prediction based directly on idealized theoretical start and decay transients (Figs. 6 and 8) using experimental values for pressure and flow rate lag times is indicated by the dashed line on the figure. The use of theoretical expressions alone, without consideration for these lag times, would tend to shift the dashed line upward increasing the error between the predicted and experimental values for specific impulse. As expected, the empirical model agrees more closely with the test data throughout the entire duty cycle range. For pulse on-times greater than 100 ms, the deviation between the model predicted value and the average test value at each pulse on-time increment (Fig. 2) is less than 10 percent. For the very short pulses, propellant overshoot characteristics in both the fuel and oxidizer, which are not accounted for in the model, become significant causing the model results to be somewhat higher than the actual test data. The higher performance for the shorter off-times with fixed pulse duration

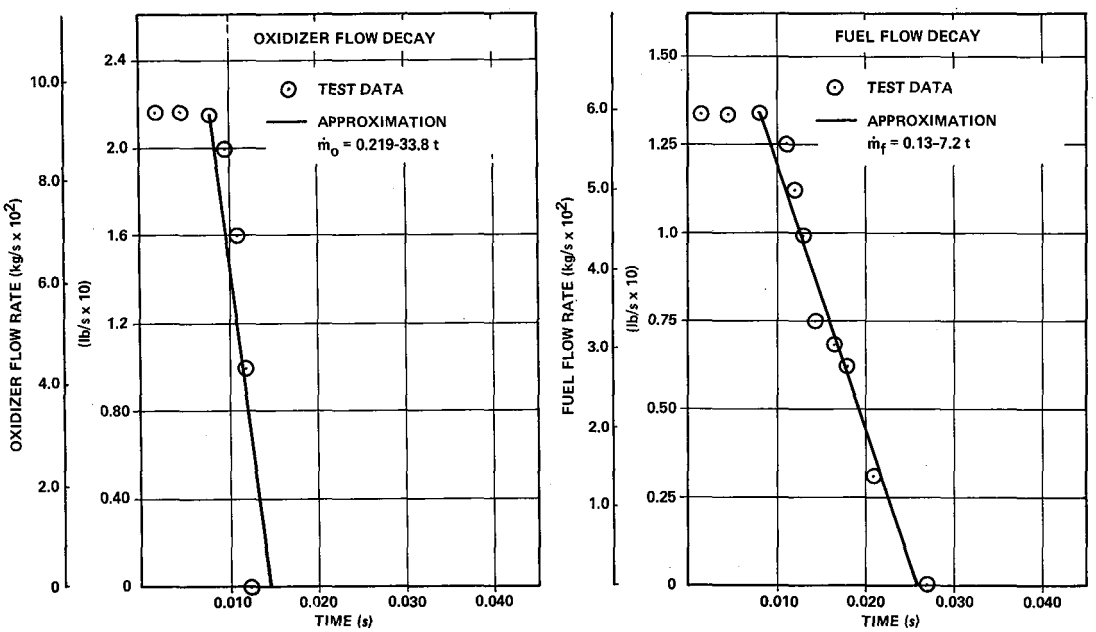

Figure 11. Oxidizer and fuel flow decay, engine A.

appear to be attributable to a combination of higher average pressure during the pulse and a reduced total propellant flow rate. It appears that the model could be further refined by the use of another term to account for effects of off-time; however, without additional tests, the generality of the results could not be properly assessed.

The equations which describe the engine pressure and flow rate behavior were derived based on test data obtained from tests of 98-N (22-lbf) and 445-N (100-lbf) engines representative of current auxiliary propulsion system engines. A large degree of similarity was found to exist in the equations describing the pulse transients and between the two engine configurations studied. This similarity in behavior indicates that an empirical model can be used to predict the performance of a varying range of engine sizes and configurations within reasonable accuracy limits.

The empirical model results were compared to several theoretical prediction techniques and were found to provide a much greater degree of correlation than the ideal equations. To adopt the empirical model without the benefit of additional test data, several characteristics of the engine should be established:

1. The valve opening and closing response times are required and can be determined by component tests. Usually, for ACS size engines, this time will vary between 3 and 8 ms and will be constant for a given valve configuration. This factor determines the time lag for both the propellant flow rates and the pressure transients.

2. The size of the fill volume between the engine valve seat and the injector must be known, since it affects the length of time required for propellants to enter the chamber and thus influences the ignition lag time. The reaction time for the subject hypergolic propellants is so rapid that its effect on ignition delay is negligible.

3. The steady-state operating point can be determined using the characteristic exhaust velocity and the thrust coefficient (c_f) and efficienty factors based on past experience with similar designs. The propellant flow rates can be calculated with standard analytical procedures.

4. An assessment of the engine thermal characteristics should be made based upon analysis of the particular heat transfer case or past test experience of the type described in the article.

The use of the above information in conjunction with the empirical model equations should result in performance prediction values which have a greater degree of accuracy than idealized theoretical prediction techniques and should provide accuracy levels within the ranges required for preliminary design.

The model described herein is based on limited test data. Data analysis of test results from engines of different sizes and configurations might tend to alter the model equations or even further validate the conclusions presented. In any event, a relatively simplified semiempirical model has been demonstrated to be reasonably accurate for two very different engine configurations operating over a considerable range of pulse-on and pulse-off times.

REFERENCES

1. Duncan, A. F.; Kelly, T. L.; and Moberg, D. A.: A Study of Hypergolic Mass Expulsion for Attitude Control of Spacecraft. The Marquardt Corporation, Technical Documentary Report No. AST-TR-62-1065, August 1964, pp. 545-551, 602-603.

2. Lewis, J. D.: Combustion and Propulsion. Fifth AGARD Colloquium, Braunschweig, April 6-13, 1962 pp. 144, 167.

3. Ingebo, R. D.: Relation of Atomization and Rocket Combustion Performance. Chemical Engineering Progress, vol. 58, no. 4, April 1962, pp. 74-76.

4. Miesse, C. C.: On the Combustion of a Liquid Fuel Spray. Sixth Symposium (International) on Combustion, Yale University, New Haven, Connecticut, August 19-24, pp. 732-738.

5. Priem, R. J.: Propellant Vaporization as a Criterion for Rocket-Engine Design; Calculations using Various Log-Probability Distributions of Heptane Droplets. Lewis Flight Propulsion Laboratory, NACA TN 4098, October 1957.

REFERENCES (Concluded)

6. Priem, R. J.: Propellant Vaporization as a Criterion for Rocket-Engine Design; Calculations of Chamber Length to Vaporize Various Propellants. Lewis Flight Propulsion Laboratory, NACA TN 3883, September 1958.

7. Penner, S. S.: Chemical Rocket Propulsion and Combustion Research. Gordon and Breach, New York, 1962, pp. 45-97.

8. Wasko, R. A.: Reaction of Hydrazine and Nitrogen Tetroxide in a Low-Pressure Environment. AIAA Journal, vol. 5, no. 1, August 1963, pp. 1919-1920.

9. Simmons, J. A.; Gift, R. D.; and Spurlock, J. M.: Reactions and Expansion of Hypergolic Propellants in a Vacuum. AIAA Journal, vol. 6, no. 5, May 1968, pp. 887-893.

10. Agosta, V. D.; and Kraus, G.: An Investigation of The Impulse Bit Developed by a Pulsed Liquid Propellant Rocket Engine. Chemical Engineering Progress Symposium Series, vol. 60, no. 52, AIEC, New York, N. Y., 1964, pp. 8-16.

11. Kilpatrick, Baker: A Study of Fast Reactions in Fuel-Oxidant Systems. Williams and Wilkens, p. 196.

12. Seamans, T. F.; Vanpee, M.; and Agosta, V. D.: Development of a Fundamental Model of Hypergolic Ignition in Space Ambient Engines. AIAA Journal, vol. 5, no. 9, September 1967, pp. 1616-1624.

13. Rodean, H. C.: Rocket Thrust Termination Transients. ARS Journal, vol. 29, no. 6, June 1959, pp. 406-409.

14. Barrère, M.; Jaumotte, A.; De Veubeke, B. F.; and Vanderkerchove, J.: Rocket Propulsion. Elsevier Publishing Company, 1960, pp. 244, 404, 622.

ENGINEERING ADVANCES IN AEROSPIKE ROCKET ENGINES

By

Rex Bailey

INTRODUCTION

In a conventional bell nozzle engine, thrust is produced by the expansion of combustion gases within the confines of the nozzle wall. The magnitude of the thrust varies in accordance with the equation shown in Figure 1. For high altitude engine operation, it is generally desirable to maximize nozzle exit velocity, which requires that large nozzle area ratios be used. Operation of high area ratio nozzles at low altitudes, however, typically produces a nozzle exit pressure lower than ambient pressure, which results in a reduction of thrust. Maximum thrust generation at both low and high altitudes can result only if the effective nozzle area ratio varies with altitude such that nozzle exit pressure remains equal to ambient pressure, a characteristic called altitude compensation. The advantages of an altitude compensating nozzle in comparison to a high area ratio bell nozzle are qualitatively shown in Figure 1.

The spike nozzle concept shown in Figure 2 was conceived as a means of achieving altitude compensation. Combustion gases are generated within a toroidal chamber, exhausted through an annular throat, then expanded against a spike nozzle. Since the outer free-jet boundary of the combustion gases is controlled by ambient pressure, overexpansion of the gases cannot occur and the nozzle is altitude compensating to the area ratio limit of the particular design. An aerospike nozzle, also shown in Figure 2, operates in a similar manner except that the lower part of the spike nozzle is removed and an aerodynamic spike formed by a flow of gases through the nozzle base is substituted.

The aerospike nozzle concept had, in addition to altitude compensation, other desirable features when compared to an equivalent bell nozzle: it had the potential of requiring a thrust chamber length only 15 to 20 percent as long; it could be gimballed within a much smaller envelope; and larger area ratios and

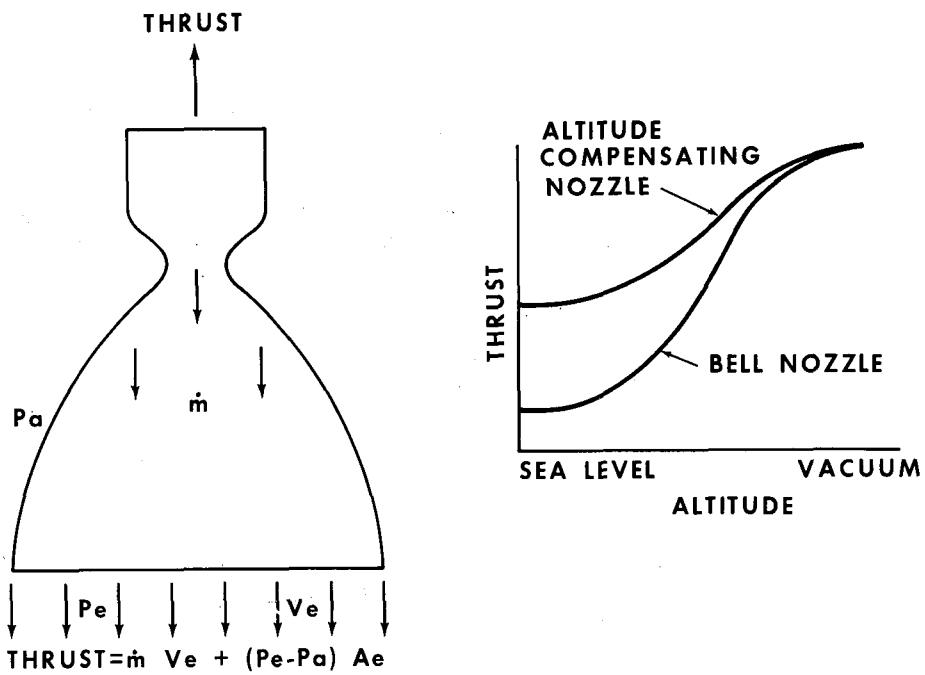

Figure 1. Rocket nozzle characteristics.

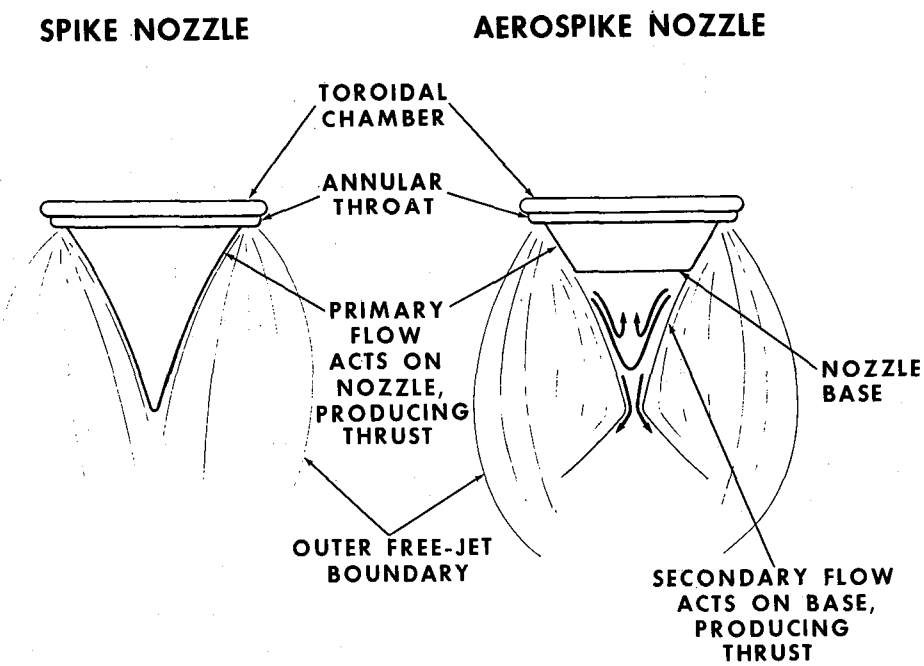

Figure 2. Altitude compensating nozzles.

higher vacuum performance could be achieved by using the entire base area of a stage. Several potential problem areas were also identified as being unique to the aerospike nozzle. Obtaining complete combustion within a short toroidal chamber was a new requirement to be demonstrated. Combustion stability was uncertain from the standpoint of both acoustic stability and feed system dynamics. Thrust chamber cooling was considered more difficult because of larger surface area requirements and the associated complexity of regenerative heat exchangers. To investigate these potential advantages and disadvantages, the Advanced Engine Aerospike (AEA) program was initiated.

ADVANCED ENGINE AEROSPIKE PROGRAM

The Advanced Engine Aerospike program was undertaken to satisfy the following objectives:

1. To demonstrate combustion efficiency.

2. To demonstrate aerospike nozzle performance.

3. To evaluate steady-state and dynamic operation of a full size thrust chamber.

4. To evaluate combustion stability.

5. To demonstrate regenerative cooling of combustor and nozzle walls.

The baseline engine cycle concept used for study purposes is shown in Figure 3. In this cycle, hot gases are extracted from the main combustion chamber and used to drive the fuel and oxidizer turbines. The gases are then expelled through the base of the nozzle to enhance nozzle performance.

The basic thrust chamber design used for the Advanced Engine Aerospike program is shown in Figure 4. The chamber was rated at 1.1 MN (250 000 lb) thrust at a chamber pressure of 10.34 MN/m^2 (1500 psia) using liquid oxygen and liquid hydrogen as propellants. The thrust chamber diameter was 254 cm (100 in.). The injector elements were unlike triplets having two fuel streams impinging on one oxygen stream. Three combustion chambers were fabricated. The first chamber was a solid-wall, uncooled configuration that was used

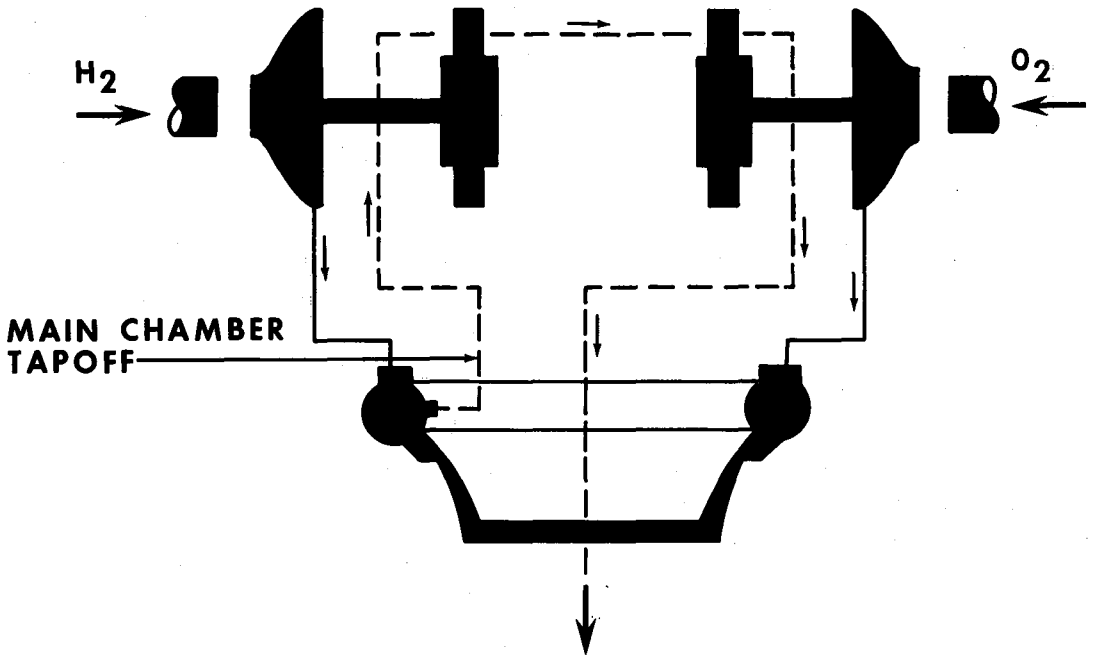

Figure 3. Aero-tapoff engine cycle.

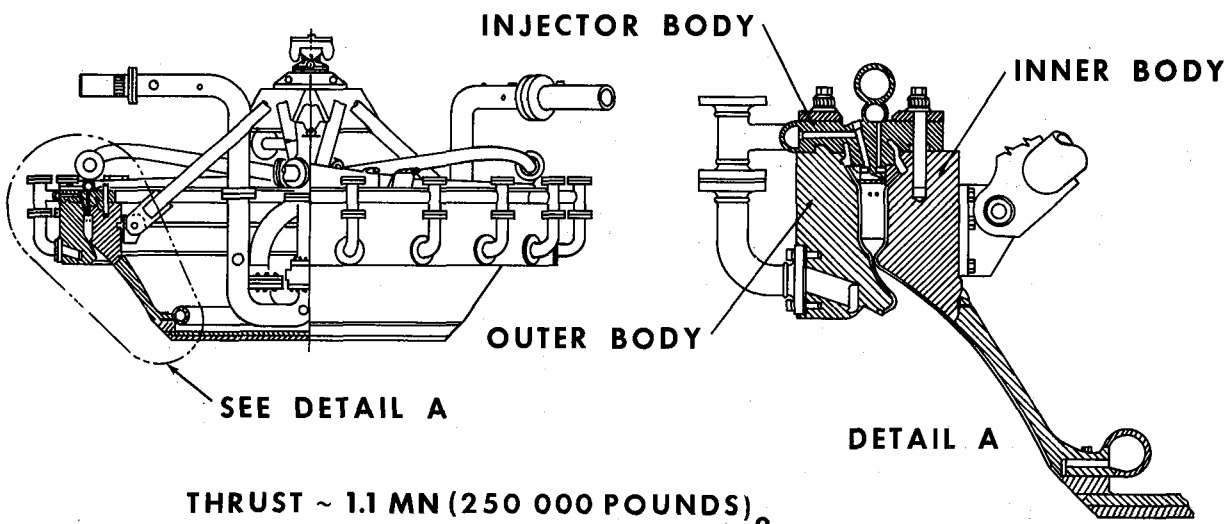

Figure 4. Aerospike tube wall thrust chamber.

for injector checkout. The two additional thrust chambers were fuel regeneratively cooled by using tube bundle heat exchangers. Stainless steel tubes were used for one chamber and nickel tubes for the other. Each assembly required approximately 6000 tubes which were tapered to a diameter of approximately 2.0 mm (0.078 in.) at the nozzle throat. Because of the large number of very small tubes, fabrication of the cooled chambers proved to be difficult. Both solid and porous base plates were used to control base bleed flows.

Testing was initiated using the solid-wall chamber in a system-and-dynamics investigation. This effort was conducted to determine the thrust chamber transient and low frequency stability characteristics. As shown in Figure 5, servocontrol throttle valves and dump valves were used for the simulation of various turbopump and start configurations. By properly sequencing these valves, an indication of turbopump stall margin was obtained.

Testing of the cooled chambers was conducted at both sea level and simulated altitude to obtain performance data. A sea level test firing photograph is shown in Figure 6. A total of 34 firings was conducted, yielding 74 test data points with a total accumulated test duration of 133 s. Chamber pressures ranged from 1.4 to 7.3 MN/m^2 (200 to 1055 psia) with propellant mixture ratios from 2.0 to 5.0. Base bleed hydrogen flow rates were 0, 0.4, and 2.2 percent of total propellant flow rate.

A comparison of test data with predicted performance is shown in Figure 7. It can be seen that the agreement was generally very good. The achieved altitude compensation as compared to the equivalent bell nozzle predicted performance is also evident. The conclusions were reached that high performance was achievable with aerospike nozzles and that the performance achieved through altitude compensation was predictable. Because of difficulties encountered during the fabrication and test efforts, it was also concluded that combustion chamber compartmenting rather than injector baffles should be used for combustion stability, and that nontubular thrust chambers should be investigated to simplify the fabrication processes.

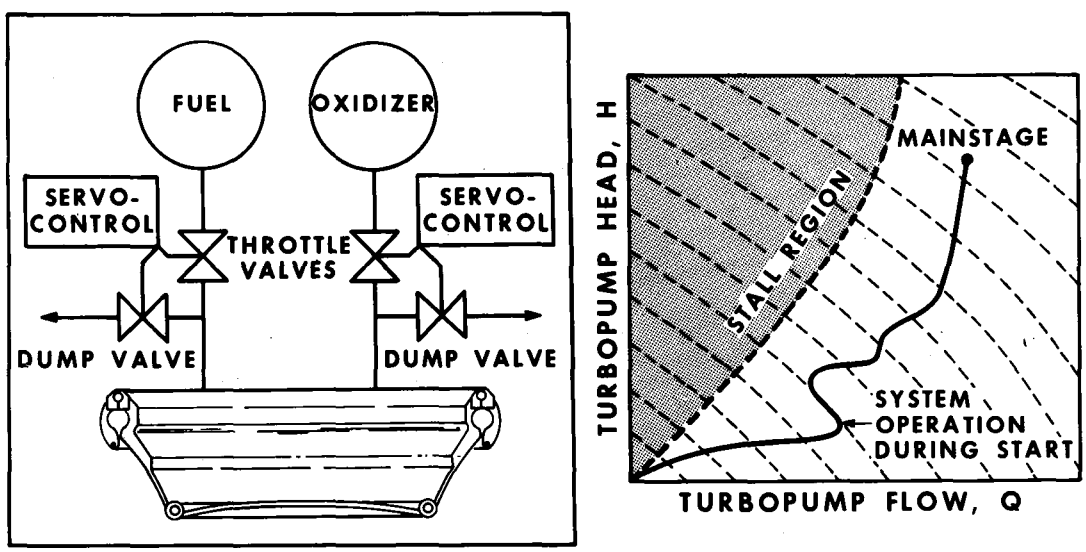

- SIMULATION OF VARIOUS START CONFIGURATIONS (TANK HEAD, GAS-SPIN, TAP-OFF, WARM ENGINE, ETC)
- SIMULATION OF VARIOUS TURBOPUMP CONFIGURATIONS (CENTRIFUGAL, AXIAL, HYBRID, ETC)

Figure 5. Aerospike system-and-dynamics investigation — simulated system transients.

COMPONENT TECHNOLOGY

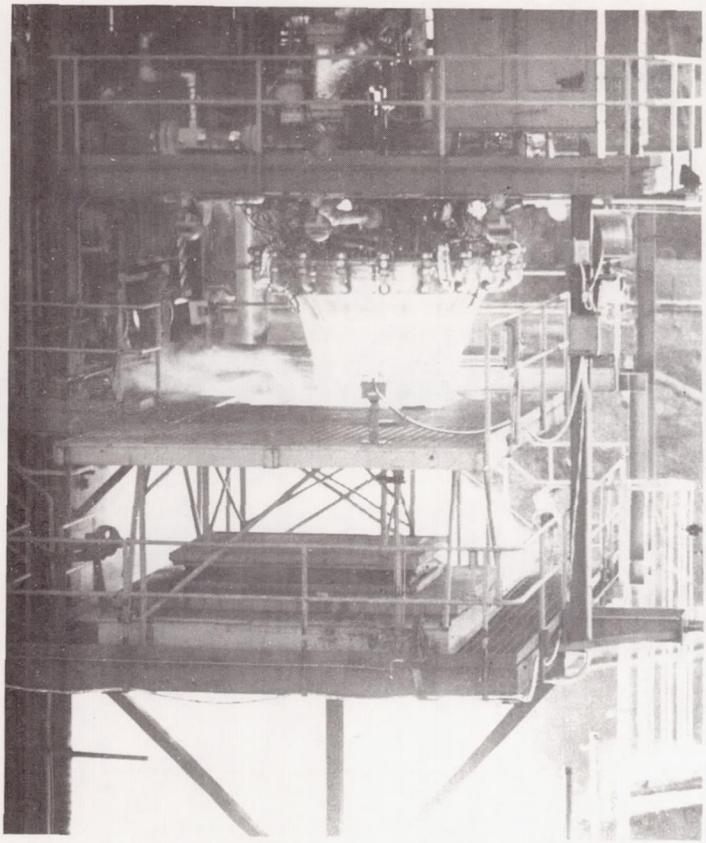

Figure 6. Aerospike thrust chamber firing.

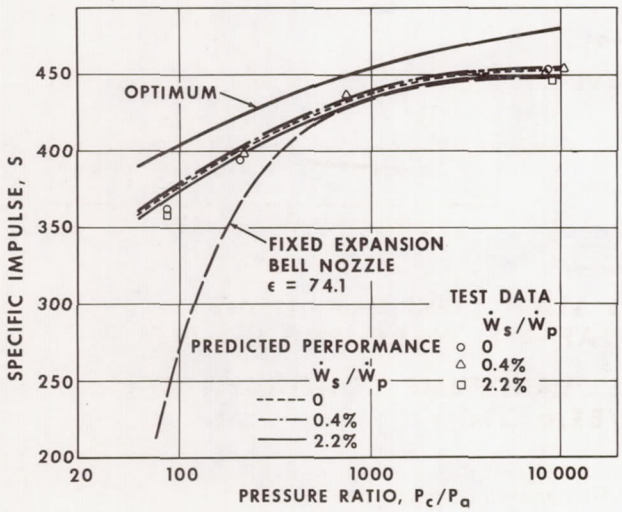

Figure 7. Specific impulse versus pressure ratio for MR = 5.0 .

Segment testing was conducted using hardware of the type shown in Figures 8 and 9. Copper combustion chamber side panels were machined to form variable depth cooling channels in the outer sides. Thin sheets of stainless steel were brazed to the copper lands to close out the channels and form the coolant passages. The panels were then stamped to the desired chamber contour. Copper end plates having drilled coolant passages closed the ends of the combustion chambers, and installation of the injector completed the assembly. Segments of this type were tested at chamber pressures ranging from 2.35 to 14.2 MN/m^2 (340 to 2045 psia) and propellant mixture ratios from 5.7 to 6.3. These tests indicated the feasibility of milled channel construction as a means of chamber segment fabrication. Additional efforts were conducted to establish injector and combustor geometry effects on combustion performance. Combustor lengths ranging from 5.0 to 14.5 cm (2.0 to 6.0 in.) and widths from 2.54 to 5.08 cm (1.0 to 2.0 in.) were tested using both impinging jet and concentric orifice injectors. Data from these tests are summarized in Figure 10 and indicate that impinging jet injectors produce higher combustion performance for chamber lengths less than 13 cm (5.2 in.). For chamber lengths greater than this, both types of injectors performed at nearly 100 percent efficiency. Combustor length rather than characteristic length, L^*, was found to be the primary geometric parameter affecting performance.

In support of the original goal to use thrust chamber tapoff gases for turbine drive, an effort was conducted to determine the feasibility of extracting tapoff gases through the main injector face. One of the two injector configurations tested is shown in Figure 11. The main injector was a standard concentric tube design with a single tapoff port placed in the center of the face. Several main injector elements in the area surrounding the tapoff port operated at a fuel-rich mixture bias to provide the desired temperature for the tapoff gases. A test series of 24 firings was conducted, and it was determined that injector face tapoff is a satisfactory method of providing turbine drive gases.

As the aerospike technology efforts continued to progress, it became increasingly evident that a building block approach to aerospike engine development and fabrication was desirable. This concept is outlined in Figure 12. By segmenting the combustion

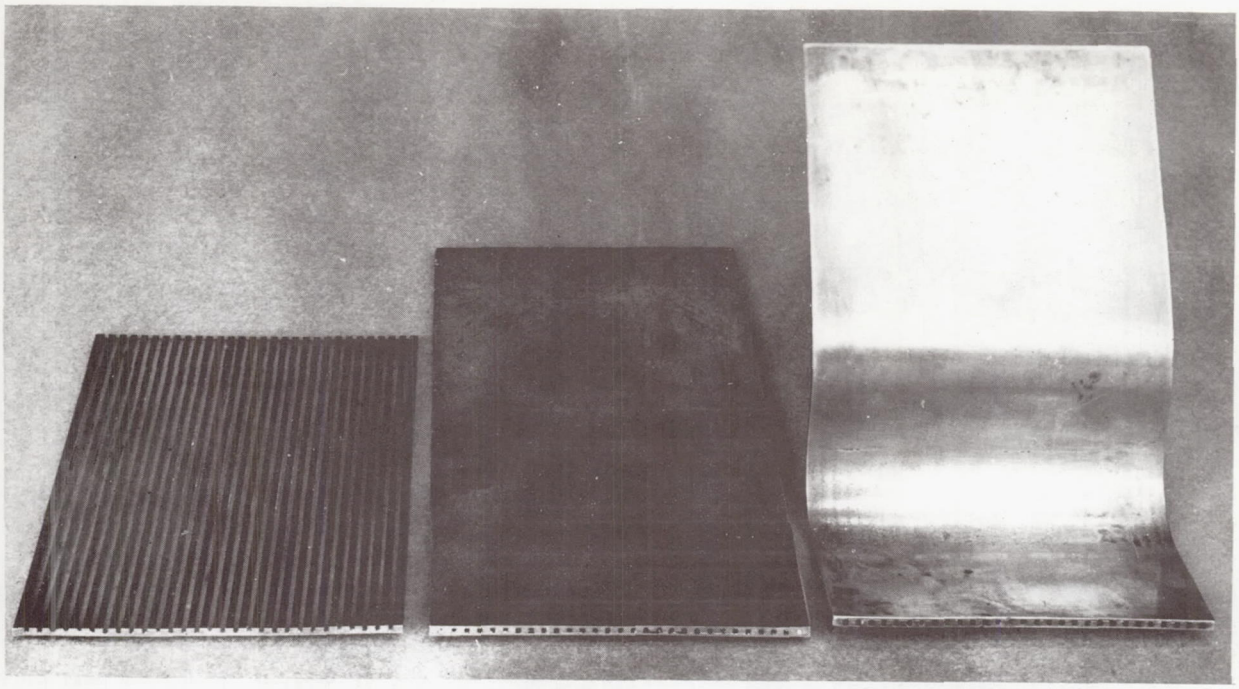

Figure 8. Milled slot chamber panels.

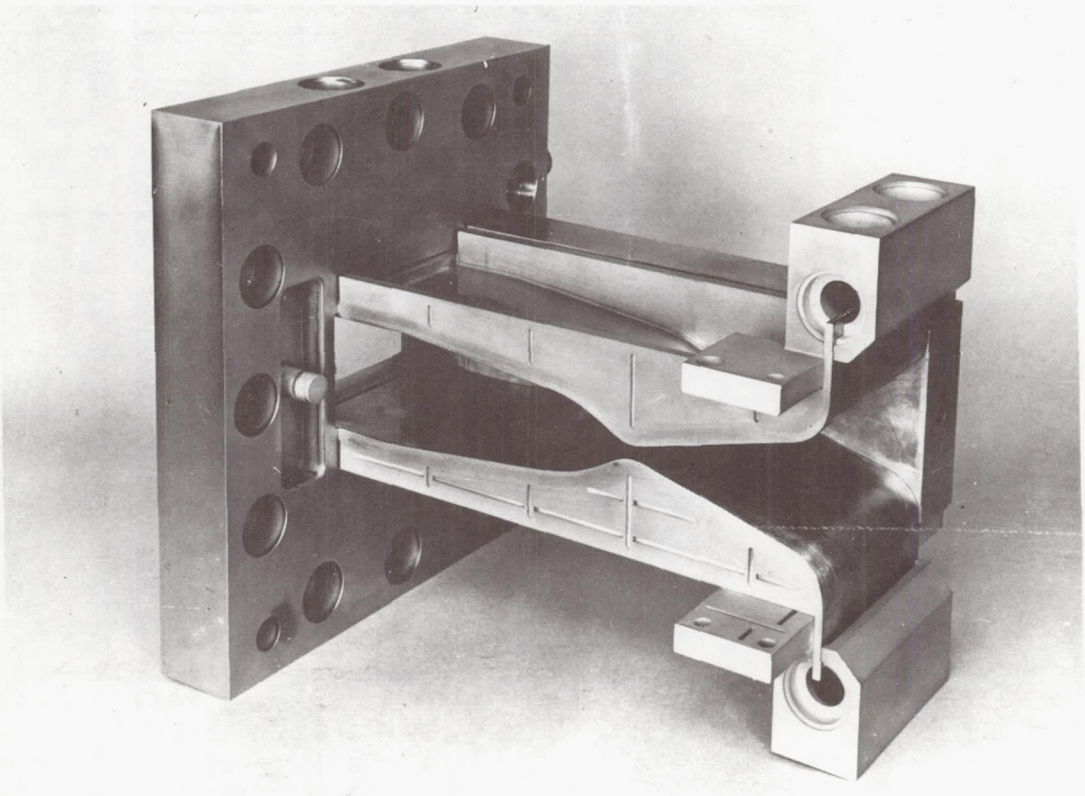

Figure 9. Milled slot chamber segment.

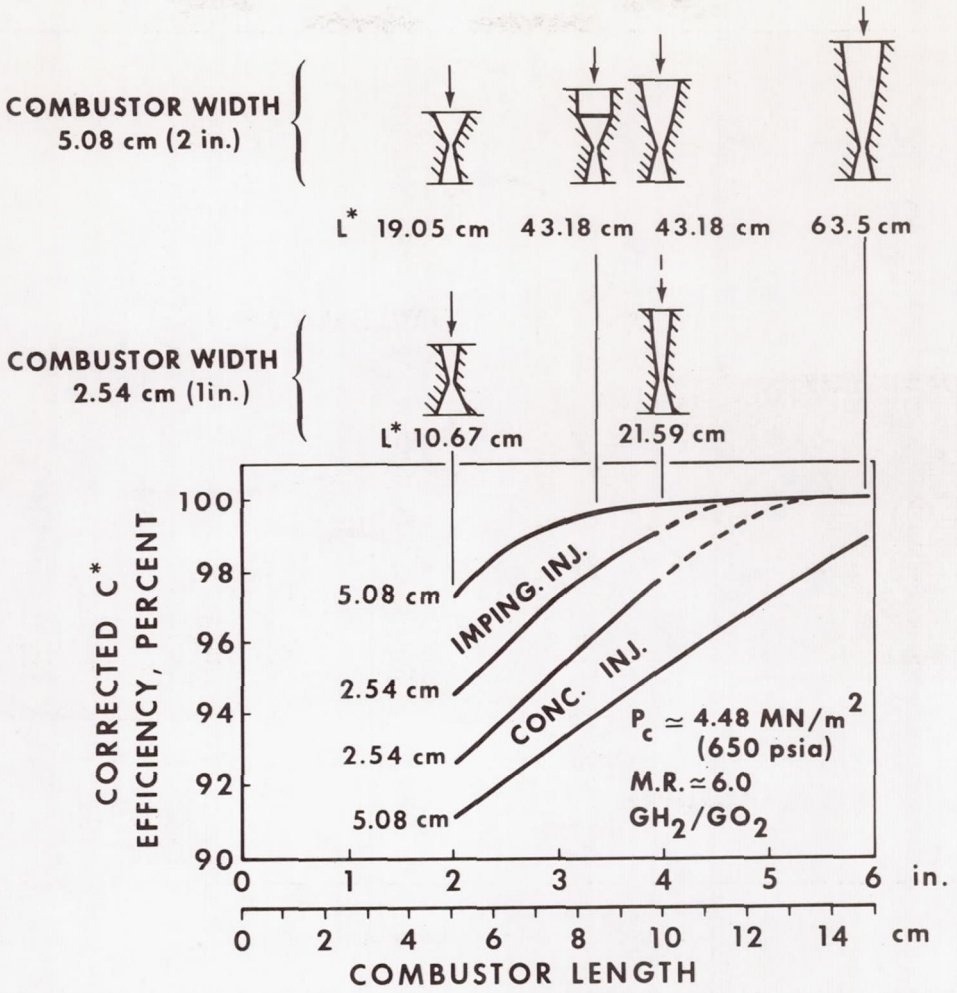

Figure 10. Combustor geometry effects.

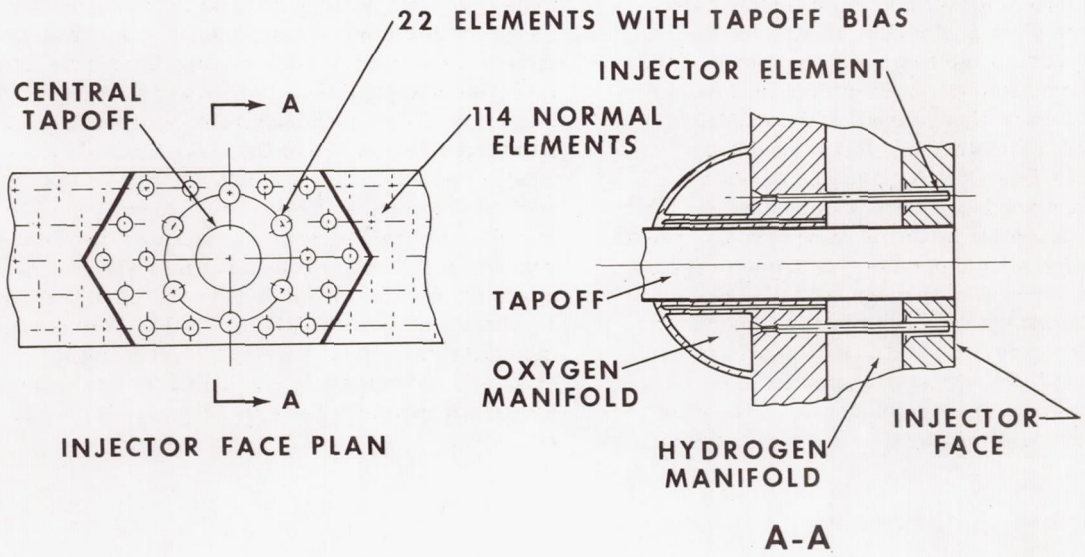

Figure 11. Tapoff injector.

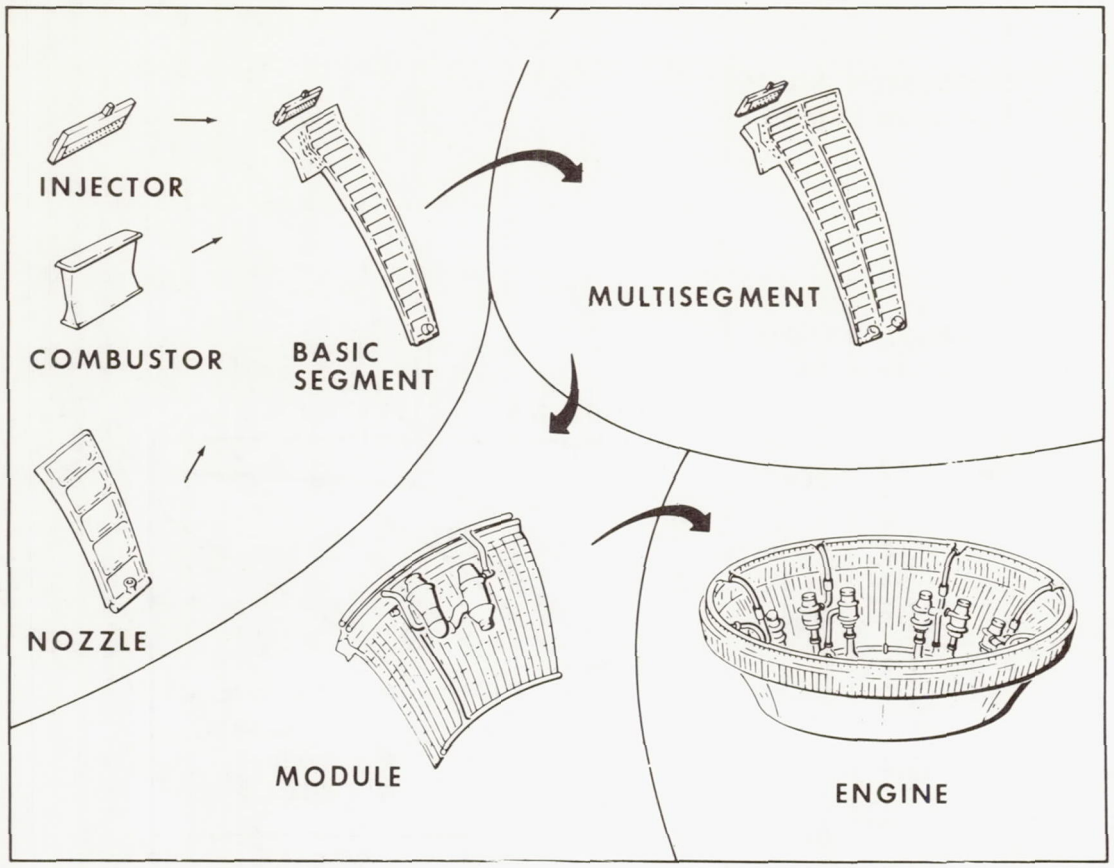

Figure 12. Aerospike building blocks.

chamber, it was possible to optimize the basic design using small, relatively inexpensive hardware. Several segments could then be joined and tested as multi-segments or modules, and finally assembled and tested as a complete engine. In an attempt to minimize the cost of the basic building block of the concept, the combustor, an effort was initiated to determine the feasibility of casting the combustor chamber liner. The design criteria used are summarized in Table 1. An investment casting process summarized in Figure 13 was used for liner fabrication. Machined patterns were used to prepare the waxes which were dipped in a ceramic to form a shell. After removal of the wax from the shell, the copper alloy castings were poured in a vacuum chamber. The ceramic shell was then broken from the casting and the liner was readied for electro-forming the coolant passage closeouts. The case liner at this stage of fabrication is shown in Figure 14.

Completing the cast chamber segment as shown in Figure 15 required electroforming the closeouts and attaching the injector assembly and hydrogen manifolds. The single segment was then readied for test, as shown in Figure 16, by installing the chamber structural members and attaching the nozzle extension. Four complete segments were fabricated in this effort. One of the segments was thoroughly tested in a series of 110 firings. Chamber pressures ranged from 4.14 to 7.72 MN/m^2 (600 to 1120 psia), and mixture ratios varied from 5.6 to 7.9. The remaining three segments were assembled in a multi-segment test configuration shown in Figure 17. This assembly was test fired 22 times at chamber pressures of 2.07 to 8.69 MN/m^2 (300 to 1200 psia) and mixture ratios of 1.5 to 7.6. The post-test hardware condition was good, and the design was judged acceptable for use in a breadboard thrust chamber.

TABLE 1. CAST SEGMENT DESIGN CRITERIA

• Thrust	53.3 kN (12 000 lb)
• Chamber Pressure	8.27 MN/m^2 (1200 psia)
• Mixture Ratio	6.0
• Fuel Inlet Pressure	12.8 MN/m^2 (1850 psia) Maximum[a]
• Oxidizer Inlet Pressure	13.1 MN/m^2 (1900 psia) Maximum[a]
• Cooling Method	Fuel Regenerative
• Chamber Wall Thickness	0.102 to 0.114 cm (0.040 to 0.045 in.)
• Chamber Rib Thickness	0.102 cm (0.040 in.)
• Rib Depth/Rib Width	Up to 3

a. J-25 Turbomachinery Maximum Pressure

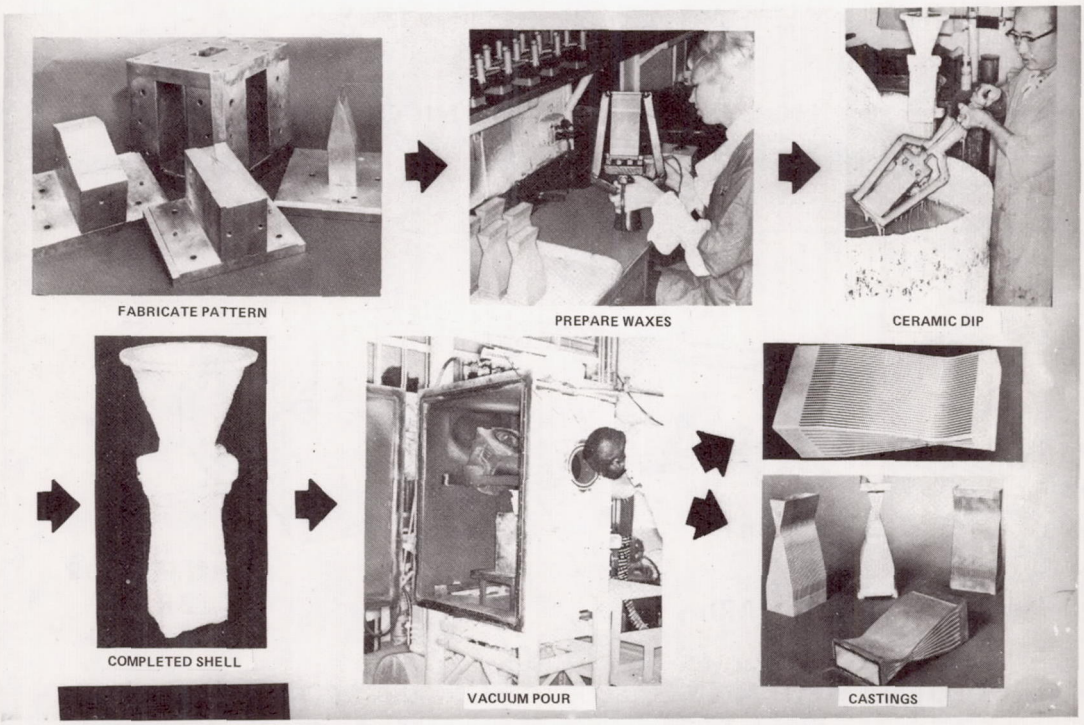

Figure 13. Copper alloy segment — investment casting process.

BREADBOARD THRUST CHAMBER

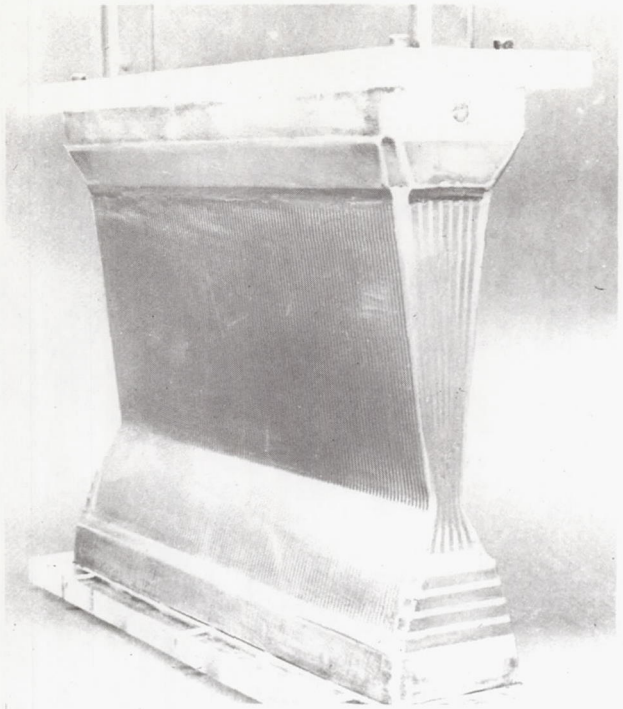

Figure 14. Cast chamber segment.

The breadboard thrust chamber program was initiated to obtain engine system data for an aerospike engine sufficiently large to be representative of a flight system. The selected system, shown in Figure 18, uses 20 of the cast combustion chamber segments developed in the previous segment efforts. A two-dimensional chamber design having 10 segments on each side was selected instead of a round or oval-shaped engine to simplify fabrication and allow the basic segment to be used. J-25 fuel and oxidizer turbopumps are mounted in the center of the engine between the two rows of combustors. Testing of this engine system will provide ignition, transient, and stability data applicable to any future consideration of aerospike engine selection.

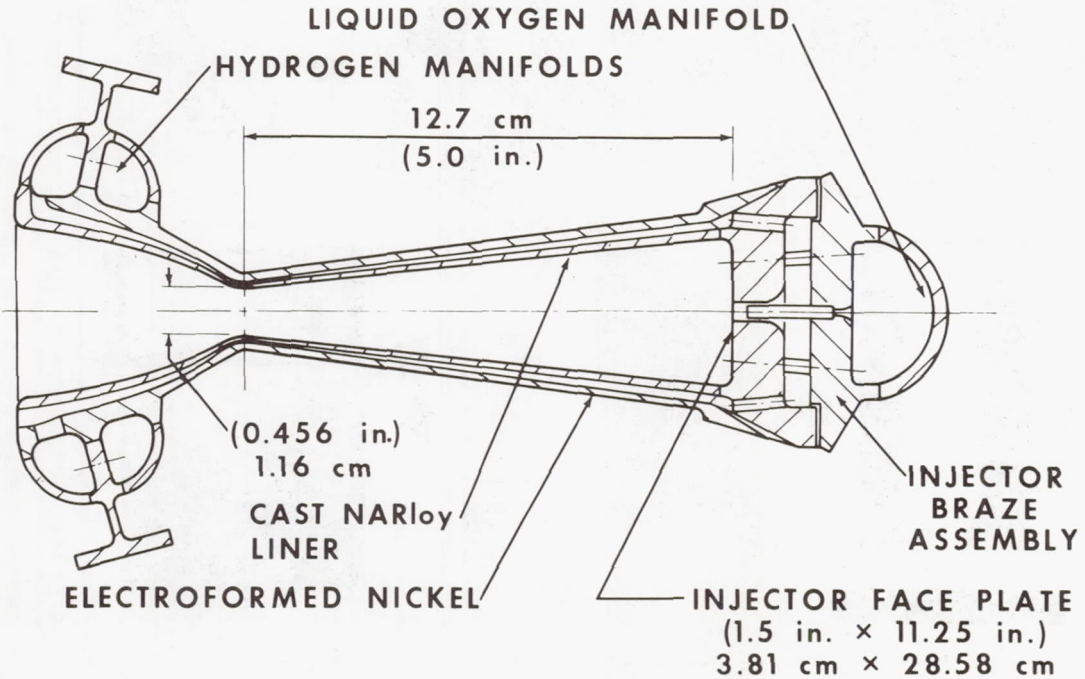

Figure 15. Cast chamber segment.

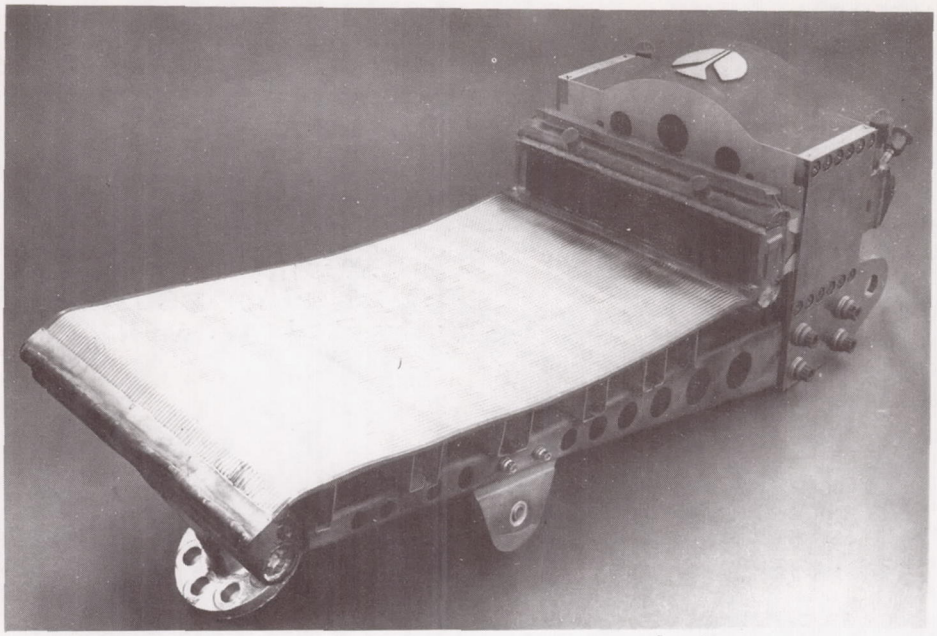

Figure 16. Aerospike single element.

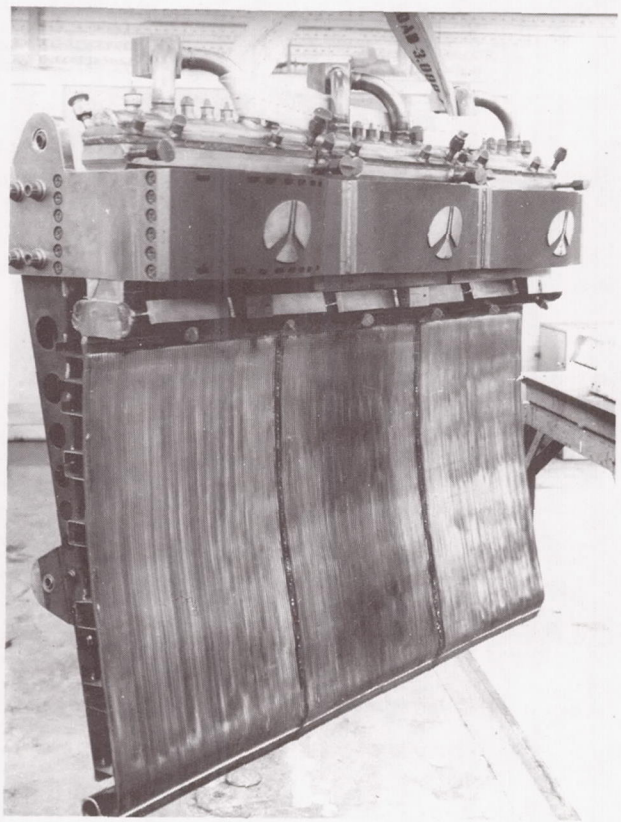

Figure 17. Aerospike multisegment.

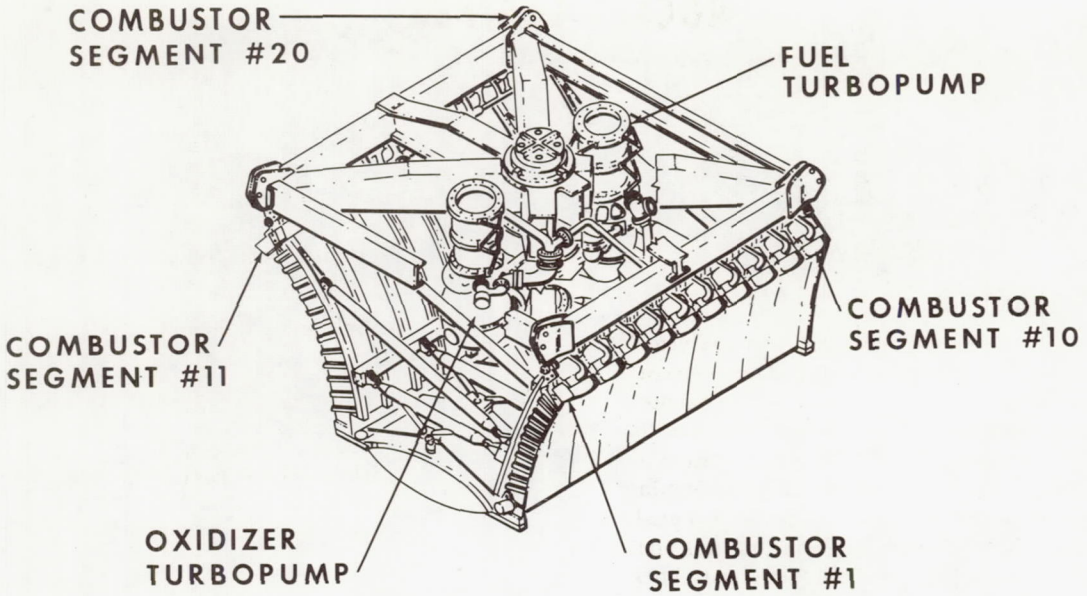

Figure 18. Breadboard thrust chamber.

PERFORMANCE ANALYSIS OF AEROSPIKE ROCKET ENGINES

By

Klaus W. Gross

SUMMARY

The results of an experimental and analytical investigation of the characteristics of the separated flow region for an aerospike nozzle are presented. The primary objective of the investigation was to predict base pressure in the flow recirculation area for open- and closed-wake operation to determine overall engine performance. The developed analytical method and the results of parametric studies including the effects of sonic line shape, internal shock, ambient pressure, base bleed, nozzle area ratio, turbulence effects, plug length, and aerodynamic slipstream are described. A high area ratio, truncated aerospike nozzle as considered by Chrysler Corporation in their single-stage, earth-orbital, reusable vehicle study is discussed, and the performance for various operating conditions is presented.

LIST OF SYMBOLS

Symbol	Definition
A_{ne}	nozzle exit area
A_{nt}	nozzle throat area
C_t	thrust coefficient efficiency
d, j	dividing streamline
L	plug length
L_{max}	ideal plug length
P_{o1}	chamber pressure
P_{amb}	ambient pressure
P_b	base pressure
P_{ne}	nozzle exit pressure
P_{ws}	static-side wall pressure
PR	ratio of ambient and chamber pressure
r	radius normal to nozzle axis
r_3	base radius upstream of recompression shock
r_b	base radius
r_w	trailing wake radius
R, - R	boundary lines separating the mixing free shear layer from the inviscid and base recirculation flow fields
S_L	ordinate of internal shock normal to nozzle centerline
T_{o1}	inviscid flow stagnation temperature
T_b	base flow temperature
u	local velocity in free shear layer
u_a	inviscid flow velocity
x, X	abscissa of coordinate system
y, Y	ordinate of coordinate system
y_m	ordinate of free shear layer
γ	specific heat ratio
ϵ	area ratio

θ	flow angle
$\mathcal{K}$	nondimensional bleed number

INTRODUCTION

In the past, primarily classical rocket engines of the bell type have been used for the propulsion of launch and space vehicles. In the future, advanced rocket propulsion systems will require exhaust nozzles that perform efficiently over a wide range of ambient operating conditions. Furthermore, these exhaust nozzles should be short, lightweight, and relatively easy to cool. Analyses and tests have demonstrated that a group of nozzles referred to as altitude compensating nozzles satisfy these requirements. The expansion-deflection and aerospike nozzles are included in this group (Fig. 1). Altitude compensation in these nozzles is obtained by the flow of the combustion products in the supersonic range. Unlike the bell nozzle, in which the entire flow is contained within a fixed contour, the flow of an aerospike nozzle is guided along the plug only. The outer shroud ends shortly after the nozzle throat and forces the flow to establish its own external contour which must be in pressure balance with the ambient condition. This document will discuss only those aspects relating to the performance analysis of the aerospike nozzle.

AEROSPIKE ENGINE PERFORMANCE

The performance of an aerospike nozzle is composed of two portions; namely, thrust produced by pressure forces acting on (1) the solid wall surfaces guiding the flow and (2) the base area. The latter item primarily will be discussed in this report since it affects performance significantly.

OPEN-CLOSED WAKE OPERATION

Dependent on the chamber-to-ambient-pressure ratio, two significant nozzle operation modes can be identified. At a low pressure ratio, the separated base flow region is open and is sensitive to ambient conditions through the trailing wake corridor. For a high pressure ratio, the base flow field becomes closed preventing any influence of the ambient environment. Experiments have shown that during the open-wake condition the base pressure varies in accordance with the ambient pressure. After the

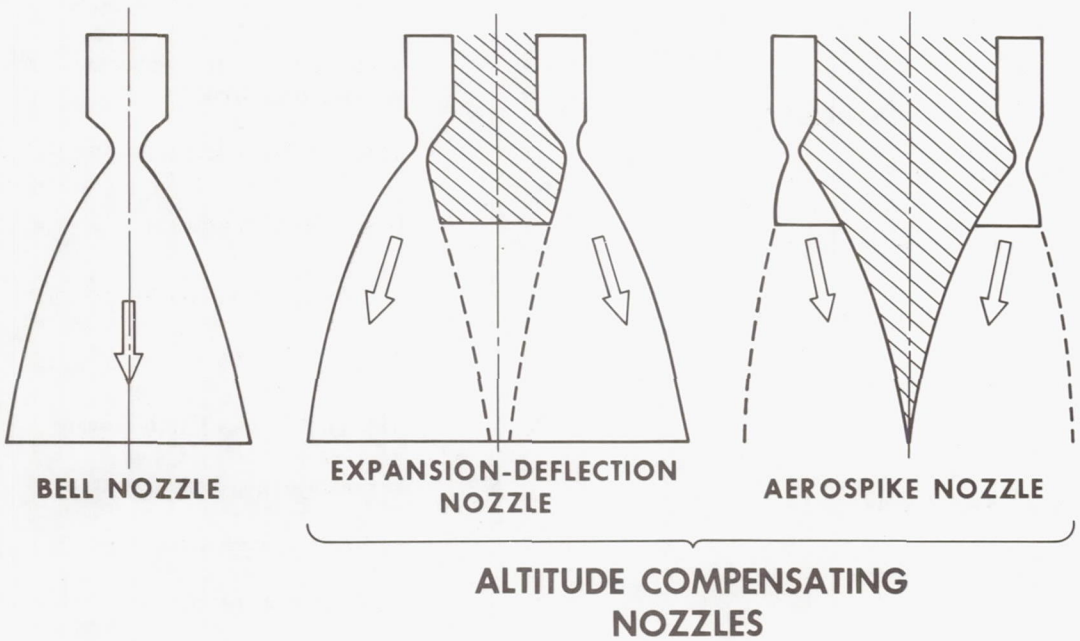

Figure 1. Nozzle types.

wake closes, the base pressure remains constant (Fig. 2).

ANALYTICAL FLOW TREATMENT

The total flow field beginning at the injector can be subdivided into the realms where viscous forces are either negligible or dominant. Viscous effects are insignificant in the core portion of the subsonic, transonic, and supersonic flow fields; whereas strong viscous effects, generated by the interaction of the core flow with the ambient environment and the base recirculation region, must be considered in the boundary layer along the solid surfaces and in the free shear layers (Fig. 3). However, there exist phenomena caused by the boundary and free shear layer which affect the inviscid flow field significantly. Because of the viscous behavior, the boundary layers do not separate from the wall contour at the end of the outer shroud and plug truncation corner, rather they bend around these wall discontinuities and then separate. This effect produces a local overexpansion of the inviscid core flow, represented by an expansion fan. Afterwards, the flow balances itself by changing direction resulting in the generation of internal, lip, and recompression shocks (Fig. 4).

After determination of the chamber and nozzle geometry, the theoretical analysis of the inviscid flow field begins with the calculation of the combustion reaction in the chamber based upon propellant combination, chamber pressure, and mixture ratio. The results are used in a transonic model to generate a sonic start line that, in turn, will be used to calculate the supersonic flow field by the rotational method of characteristics. Solutions of the free jet boundary, internal shock, and recompression shock are included.

The performance of the nozzle down to the plug truncation corner is then determined from the inviscid flow analysis reduced by the losses from the boundary layer. The performance contribution from the base pressure depends upon whether an open- or closed-wake condition exists. For

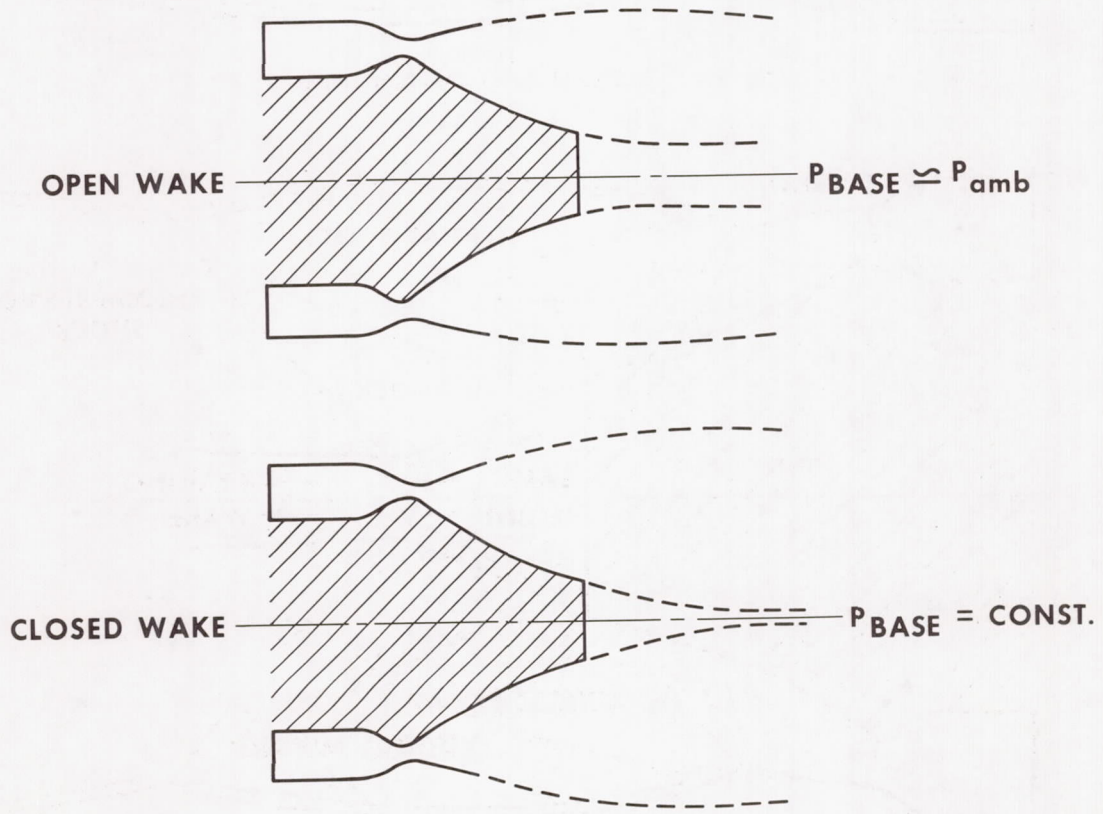

Figure 2. Truncated plug nozzle operation mode.

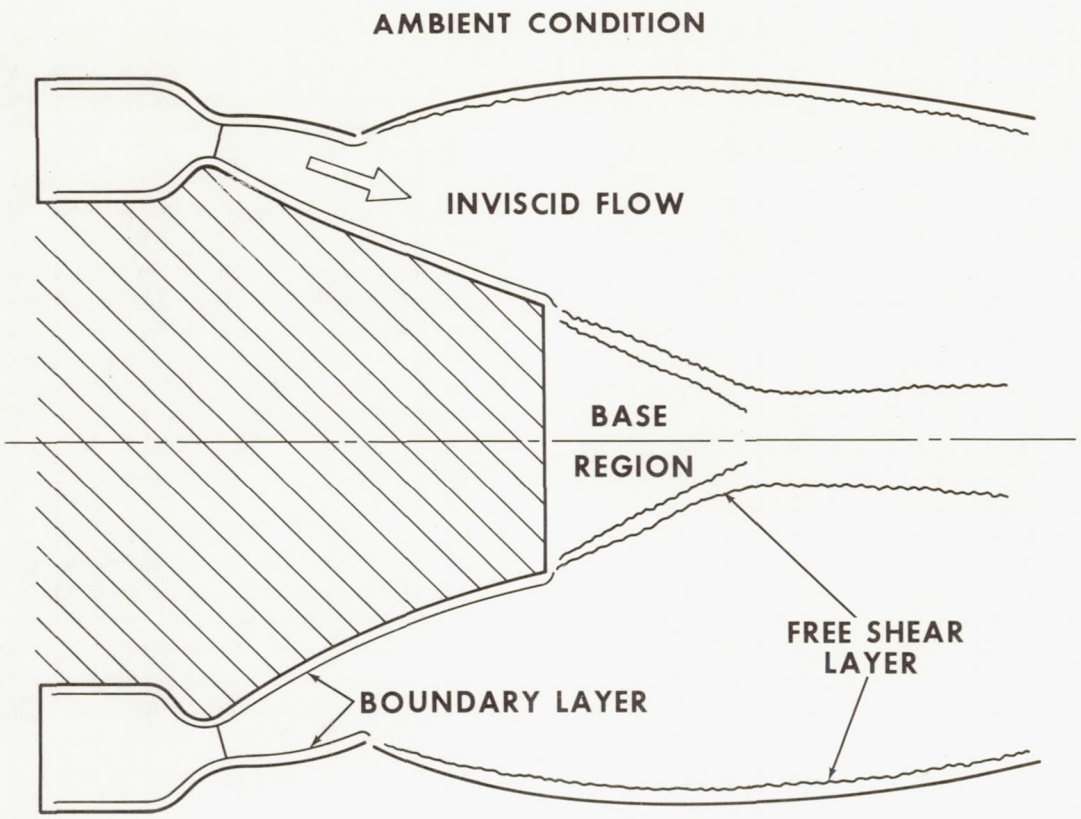

Figure 3. Analytical flow field treatment.

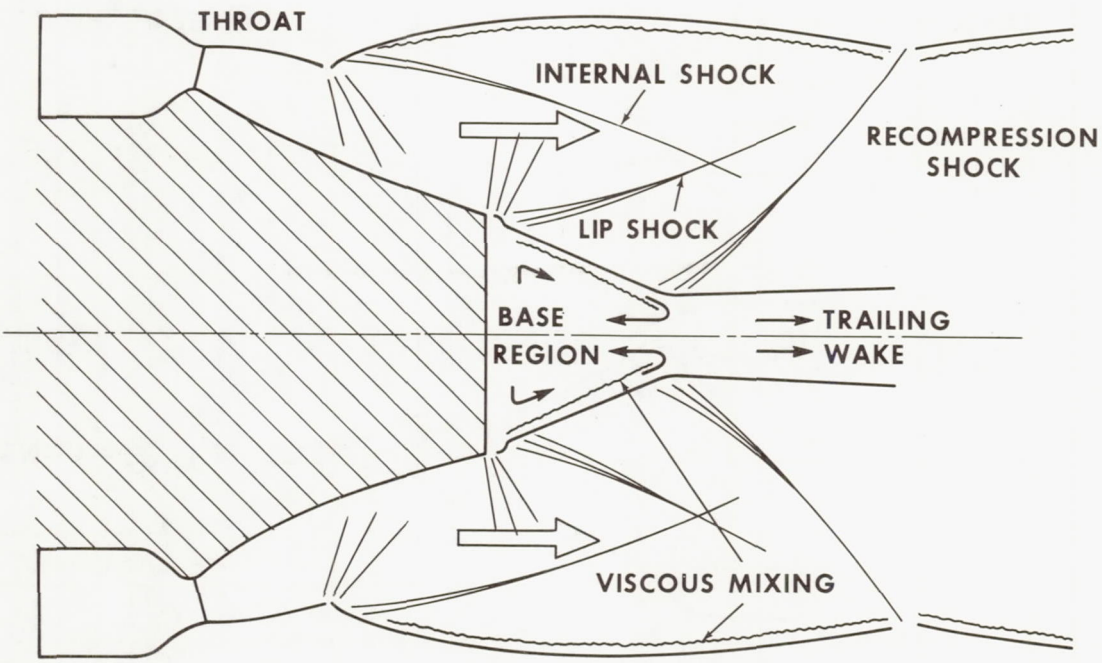

Figure 4. Plug nozzle flow field (closed wake).

open-wake flow the base pressure is slightly lower than the ambient pressure and is approximately constant across the whole base area. Under a closed-wake condition, the base pressure is determined as discussed in the following (Fig. 5).

Downstream of the plug corner a domain, bordered by the lines R and -R, exists in which the mixing free shear layer develops. Within this domain lies one streamline that separates the base recirculation flow from the remainder of the flow field. From the previous analysis the flow conditions just upstream of the corner at location (1) are known. Now, an assumption of the base pressure P_b is made. This base pressure value is assumed to exist at location (2), since a pressure gradient across the shear layer is very small. With the two known pressures, a Prandtl-Meyer expansion can be performed, resulting in the flow angle θ_{1-2} reflecting a conical surface. This cone serves as a geometrical boundary condition and allows one to proceed with the method of characteristics calculation until the trailing wake radius r_w is reached. Simultaneously, the flow condition at location (3) is specified. At this point the flow outside the recirculation area is turned in an axial direction by an angle θ_{3-4}, which is equal to θ_{1-2}, and this results in the generation of a recompression shock. Application of the method of characteristics simulates this occurrence and leads to the flow condition at location (4). Within the shear layer dynamic energy is lost because of the viscous effects, thereby lowering the total pressure continuously. For the correct base pressure solution, the following criterion must be satisfied: the static pressure at location (4) is equal to the total pressure of the streamline dividing the recirculation base flow from the external flow. This means that all particles within the recirculation flow field have a lower total pressure and cannot flow further downstream but will be recirculated instead. If the criterion at the wake radius location is not satisfied, a new base pressure P_b must be assumed and the calculation must be repeated until convergence is obtained.

At present a theory does not exist that determines the location of the recompression shock. Therefore, an empirical relationship relating the wake radius to the Mach number of the inviscid flow at location (1)

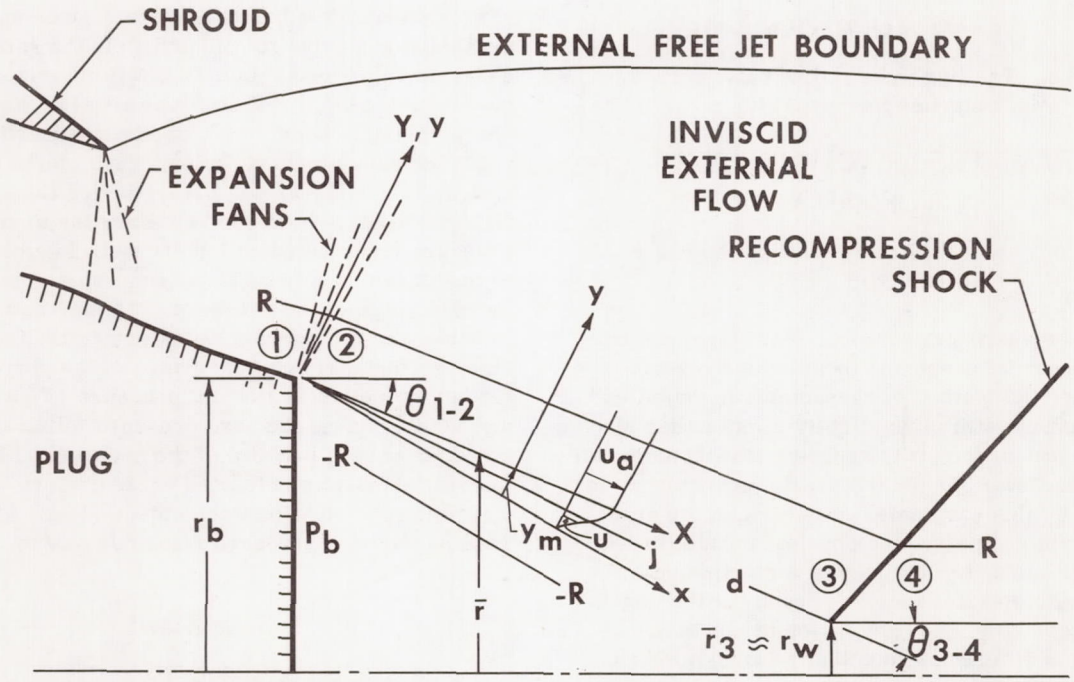

Figure 5. Flow model for the determination of the turbulent base pressure for an axisymmetric plug nozzle.

has been generated (Fig. 6). From this graph a wake radius is obtained for a given approach Mach number, and it is used in the base pressure solution procedure.

It should be mentioned that a base pressure solution for an expansion-deflection nozzle is determined by the same analogy.

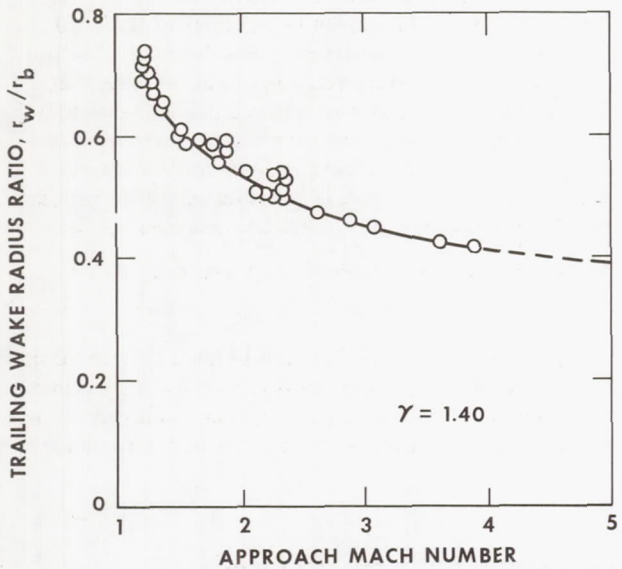

Figure 6. Trailing wake radius ratio versus Mach number for $\gamma = 1.40$

PARAMETERS AFFECTING NOZZLE PERFORMANCE

Sonic Line Shape

For the analytical solution, it is important to know the correct shape and location of the sonic line. Since the method of characteristics solution is based upon a start line slightly greater than Mach number equal to one, it is apparent that the complete supersonic flow field and the nozzle performance is governed by this parameter. Because of the aerospike nozzle geometry, the physical nozzle throat area is not normal to the engine centerline but is inclined by a specific angle. Because of the nozzle contour geometry, the combustion products are accelerated differently such that an axisymmetric sonic line shape, even with regard to the nozzle throat centerline, is not formed. In Figure 7 measurement location, static pressures converted to Mach number, and the interpolated sonic line are presented. To obtain the effect of various sonic line shapes on the base pressure, four different start lines symmetric to the geometric throat were selected. The analytical results presented in Figure 8 indicate that the closed recirculation area and the location of the recompression shock do not change. The base pressure, however, is affected by the start line profile.

Ambient Pressure

In Figure 9 the flow fields of a planar truncated plug nozzle for various ambient-to-chamber-pressure ratios are presented covering the open- and closed-wake operation mode. The respective base pressure measurements, nondimensionalized by the chamber pressure, are shown in Figure 10 as a function of the external or ambient pressure. During open-wake operation [Figs. 9(a), 9(b), 9(c), and 9(d)], the base pressure follows the ambient pressure very closely. As soon as the closed-wake condition is reached [Figs. 9(e) and 9(f)], the base pressure remains constant.

In contrast to the planar nozzle, Schlieren photographs of an axisymmetric truncated plug nozzle for various ambient pressures are shown in Figure 11 with corresponding base pressure measurements presented in Figure 12. In principle the same characteristics occur in both flow field pictures; however, for the three-dimensional case the characteristics seem to be more pronounced. Here again the base pressure follows the ambient pressure closely [Figs. 11(a) and 11(b)] during the open-wake condition. However, lowering the ambient pressure from the condition shown in Figure 11(b) to that shown in Figure 11(c) generates a sudden increase in the base pressure. This pressure rise is caused by the internal shock emanating from the outer shroud striking the surface of the plug. A further reduction in ambient pressure [Figs. 11(c) and 11(d)] makes the base pressure follow the same trend, however, because of the presence of the internal shock at an elevated pressure level. Finally, when the recirculation wake closes [Figs. 11(e) and 11(f)], the base pressure remains constant.

Base Bleed

Introduction of base bleed flow into the base recirculation area may be used to increase the base pressure and consequently raises the nozzle

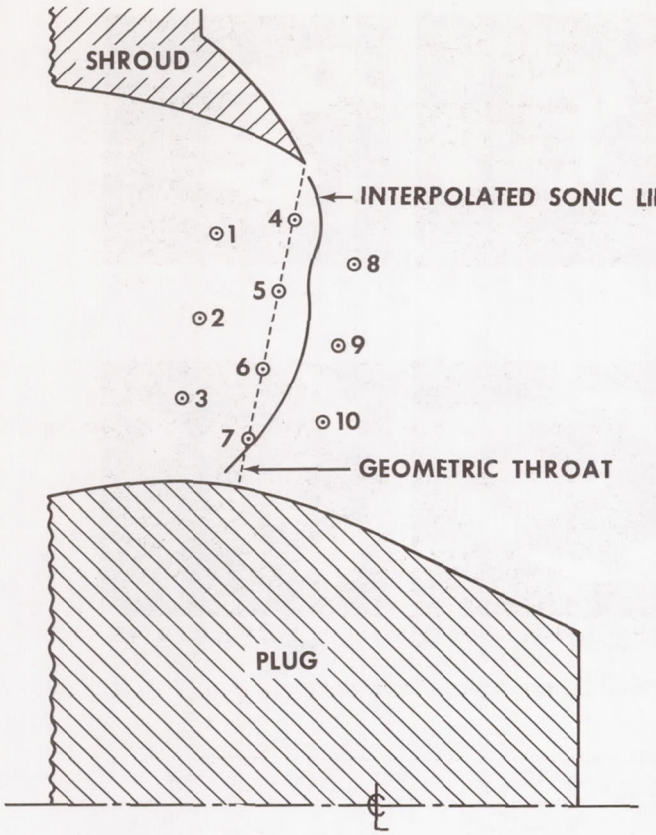

PRESSURE TAP	MACH NO.
1	0.66
2	0.72
3	0.81
4	0.88
5	0.90
6	0.91
7	0.99
8	1.18
9	1.10
10	1.12

Figure 7. Location of interpolated sonic line with respect to geometric throat.

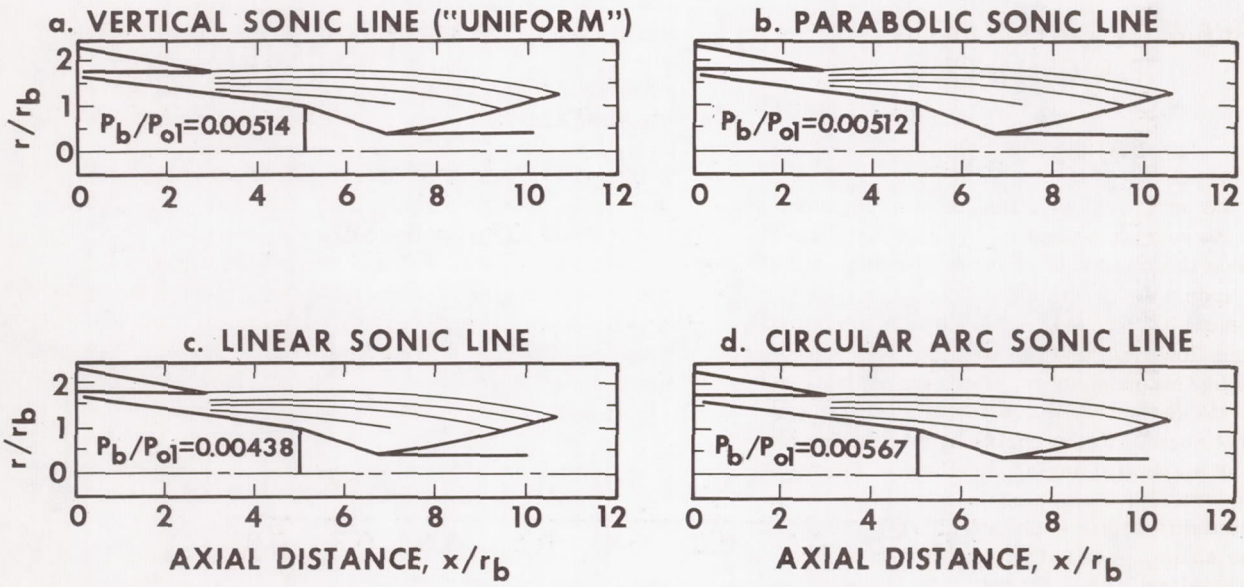

Figure 8. The influence of sonic line shapes for an axisymmetric internal-external-expansion truncated plug nozzle.

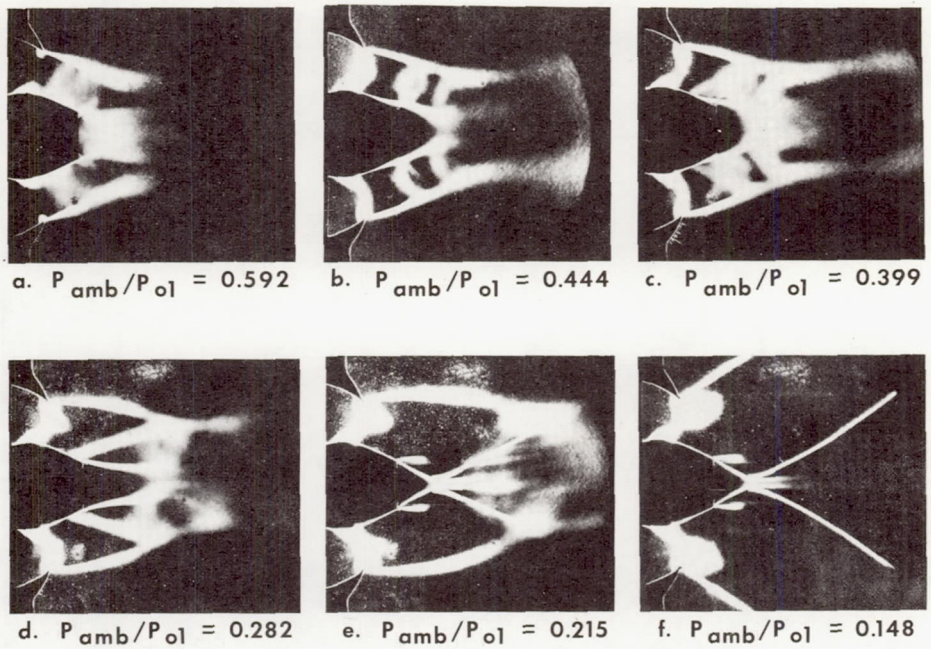

Figure 9. Truncated plug nozzle flow development.

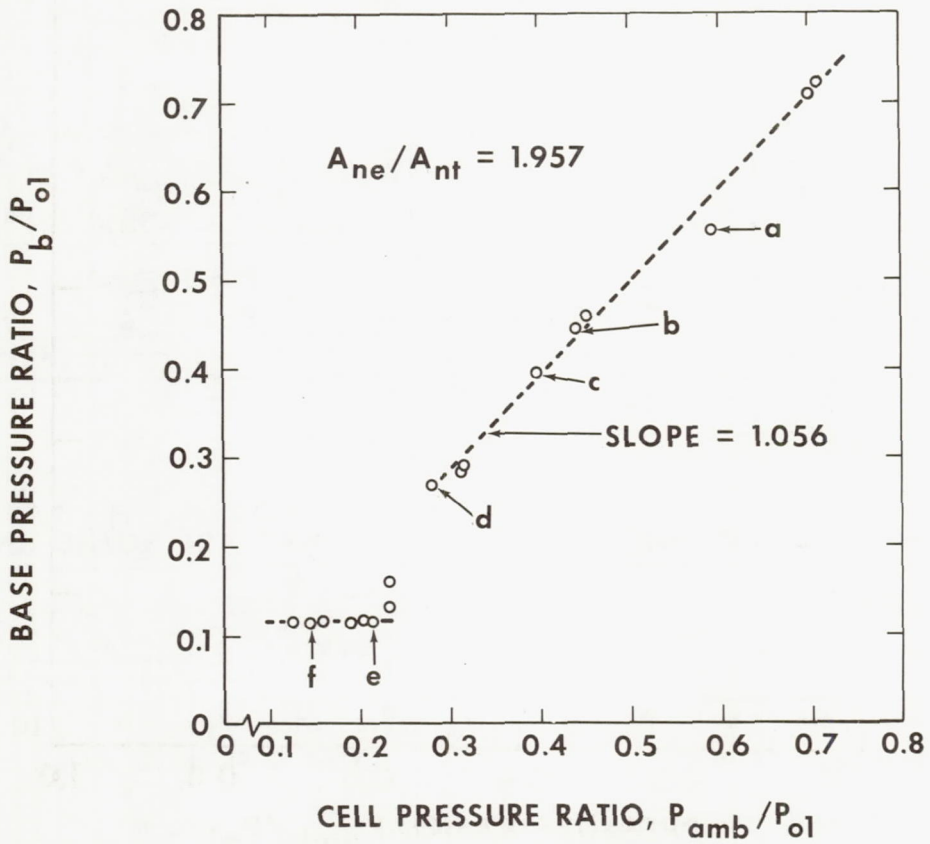

Figure 10. Variation of planar truncated plug nozzle base pressure ratio with ambient pressure ratio.

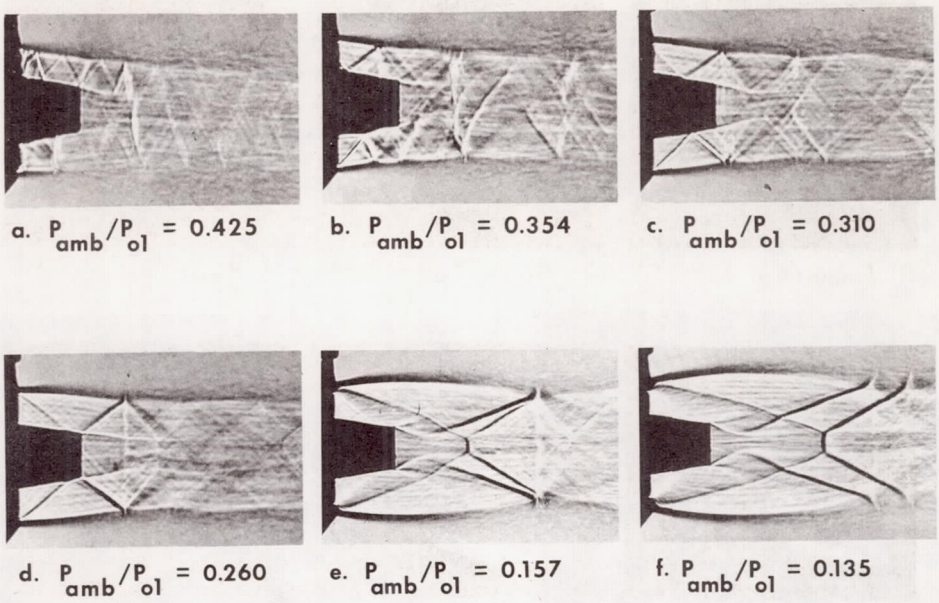

Figure 11. Axisymmetric truncated plug nozzle flow development.

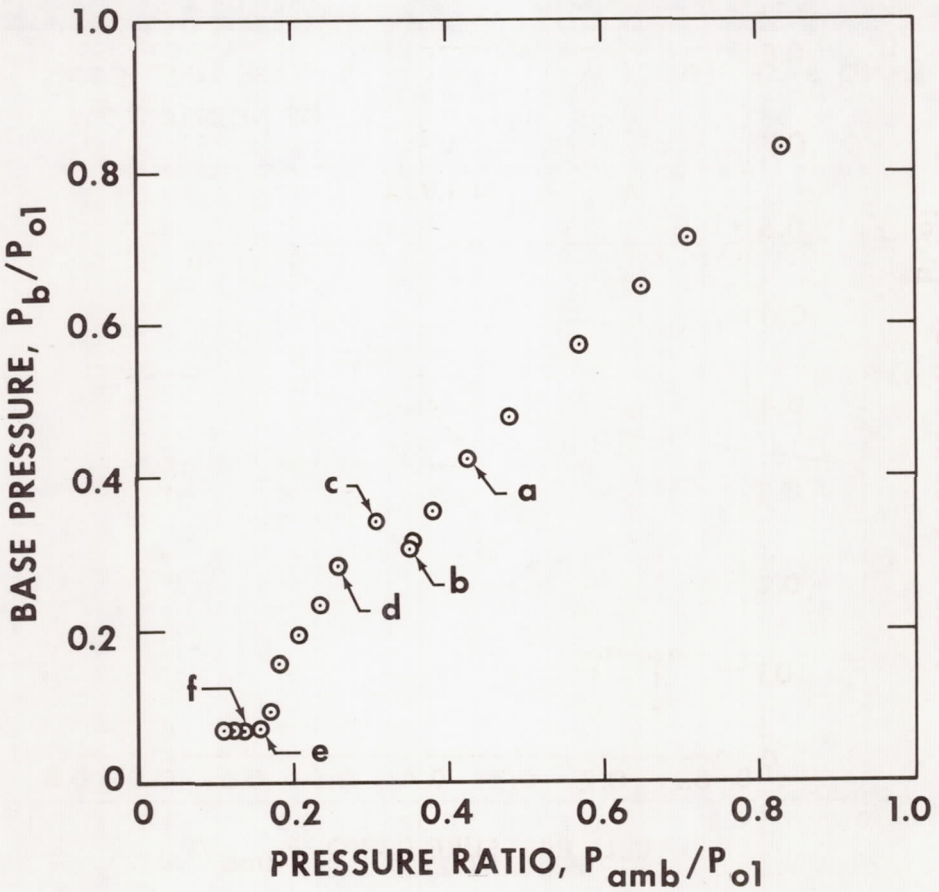

Figure 12. Axisymmetric truncated plug nozzle operating characteristics.

performance. Also, it could be used as a possible means of cooling the plug. Figure 13 shows Schlieren photographs for a test configuration with 0-percent and approximately 1-percent base bleed flow. It is evident from these photographs that even a small bleed rate produces a marked change in the visual flow pattern. The neck of the wake is noticeably thicker and the wake length appears to be longer. Also, the lip shock, which is barely visible in the no-bleed case, has become clearly defined in the flow field with bleed and has changed its position. The effect of base bleed on the nozzle base pressure is presented in Figure 14. As expected, the base pressure increases linearly with base bleed. At approximately 1-percent base bleed with regard to the total flow, a base pressure ratio increase of 30 percent is possible. For base bleed flow greater than 1 percent, the base pressure rise becomes very small and the concept loses its effectiveness. In case of performance optimization, a base bleed flow

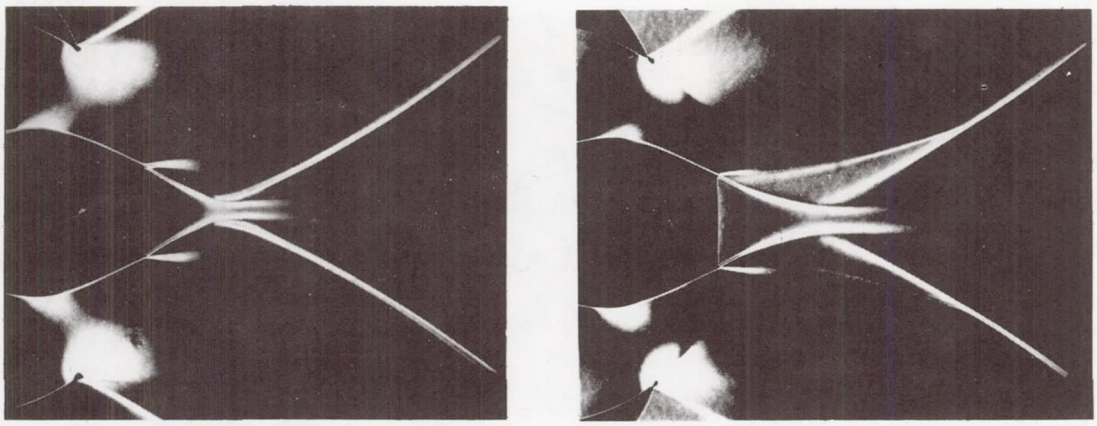

a. NO BASE BLEED

b. BASE BLEED 0.82% OF NOZZLE FLOW

Figure 13. Schlieren photographs of planar truncated plug nozzle.

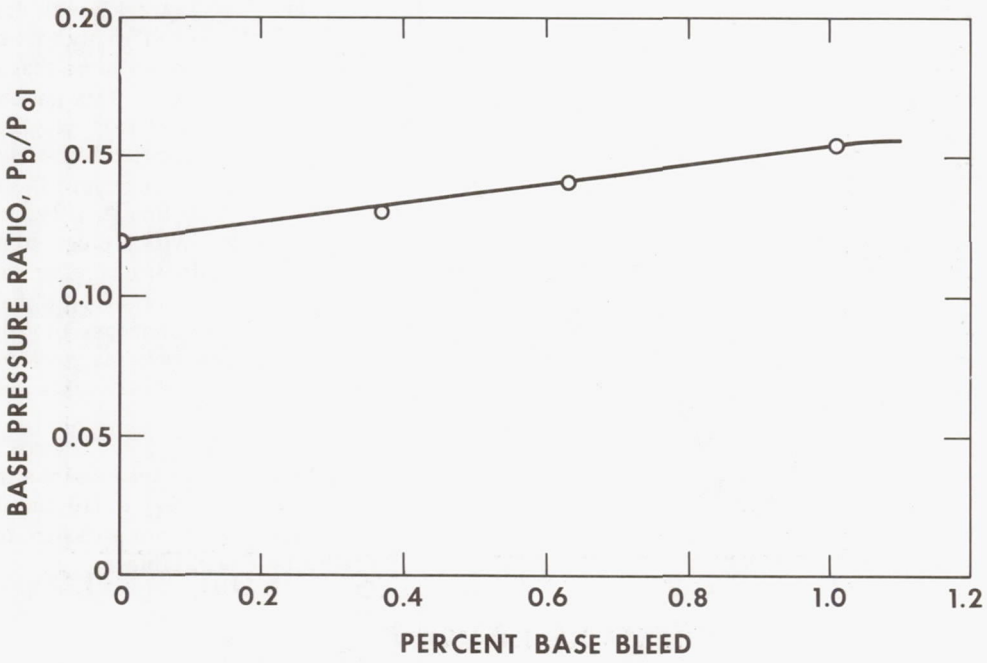

Figure 14. Effect of base bleed on base pressure of truncated plug nozzle.

must be selected such that divergence of this flow from the main chamber flow does not deteriorate the chamber performance significantly, and although the base pressure has been increased, the overall performance is lower.

Nozzle Area Ratio

Increasing the velocity of the combustion products and, therefore, the thrust is possible by varying the overall area ratio A_{ne}/A_{nt} of the nozzle. Results of an analytical investigation are exhibited in Figure 15. Note that an increasing area ratio produces a corresponding decrease in the base pressure. This result is to be expected, since an increasing overall area ratio implies a higher design Mach number of a nozzle.

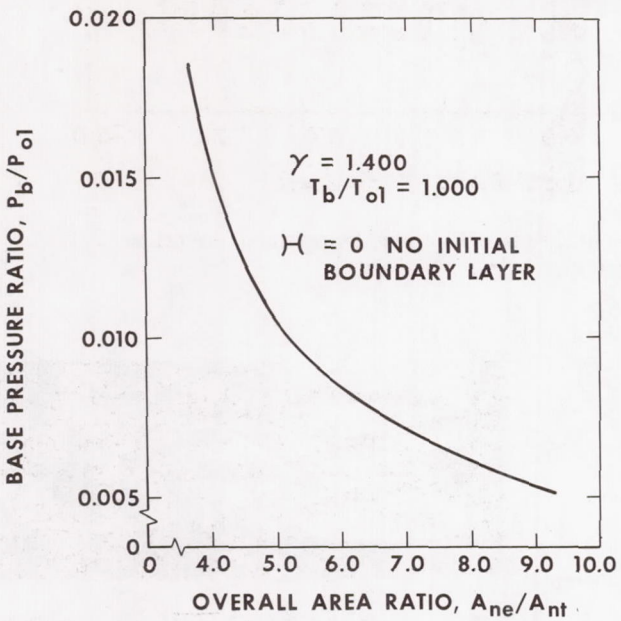

Figure 15. Influence of area ratio on the base pressure ratio of an axisymmetric internal-external-expansion truncated plug nozzle.

Turbulence Effects

Laminar or turbulent flow, especially in the boundary layer, significantly affects the location of the flow where transition from a subsonic to a supersonic condition occurs. The nozzle test configuration, as analytically designed, indicated λ shocks upstream of the geometric throat. Boundary layer trips installed in the subsonic flow area reduced the sequence of λ shocks to a single strong shock which appeared as a slightly curved normal shock. This observation revealed that under normal operating conditions, the boundary layer was laminar and that with the trip, the boundary layer became turbulent. Translating the plug physically downstream by a small amount eliminated the shock formation in the nozzle convergent area. At the same time the effects of turbulence on the nozzle centerline static pressure distribution and the base pressure were investigated. In addition to the boundary layer trip a 0.64-cm (0.25-in.) wire mesh was installed at the inlet to the nozzle section to induce turbulence in the entire flow field. The resulting measurements are shown in Figure 16. The largest deviation in the base recirculation area [from 0 to 2.54 cm (0 to 1.0 in.) distance from the plug base] occurred with the wire mesh and was on the order of 8 percent. The boundary layer trip does not appear to have affected the static pressure distribution in this area. Variation in the base pressure demonstrated the same trends.

Plug Length

In general it is desirable to have as high a closed-wake base pressure as possible to obtain the maximum thrust. Experimental results obtained for the same nozzle configuration with varying plug lengths (Figs. 17 and 18) imply that the most desirable configuration would be that with the plug ending at the shroud exit. This geometry also has the obvious advantages of less weight and a shorter length. However, since the thrust contribution resulting from the base pressure is usually not the major part of the total thrust, other considerations are also important. With a plug extending beyond the shroud exit, the additional plug surface may gather enough thrust to offset both the decrease in base pressure and the increase in weight. Although the base pressure tends to increase for plug lengths greater than $L/L_{max} \approx 0.5$, this extreme of plug length is not practical. As L/L_{max} approaches 1.0, both the plug base area and the increase in plug surface area become very small and the changes in total thrust resulting from pressure forces on these surfaces become negligible.

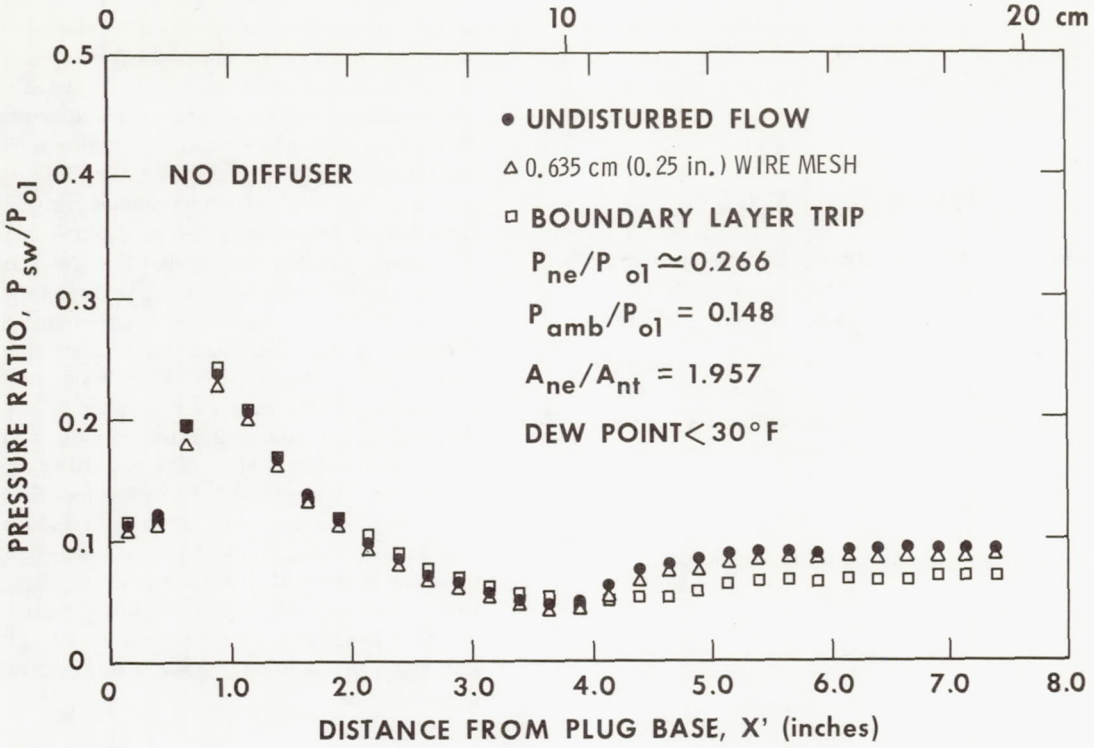

Figure 16. Induced turbulence effects on side-wall centerline static pressure variation of planar truncated plug nozzle.

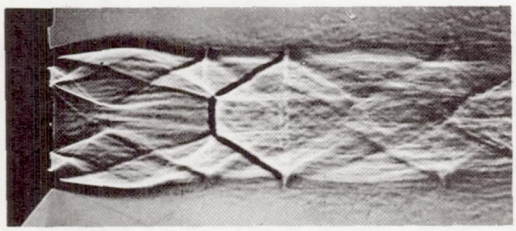

a. $P_{amb}/P_{ol} = 0.135; L/L_{max} = 0.218$

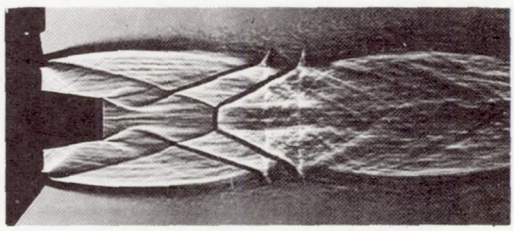

b. $P_{amb}/P_{ol} = 0.135; L/L_{max} = 0.481$

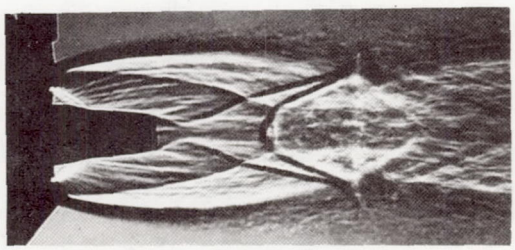

c. $P_{amb}/P_{ol} = 0.104; L/L_{max} = 0.641$

Figure 17. Nozzle flow fields for three different plug lengths.

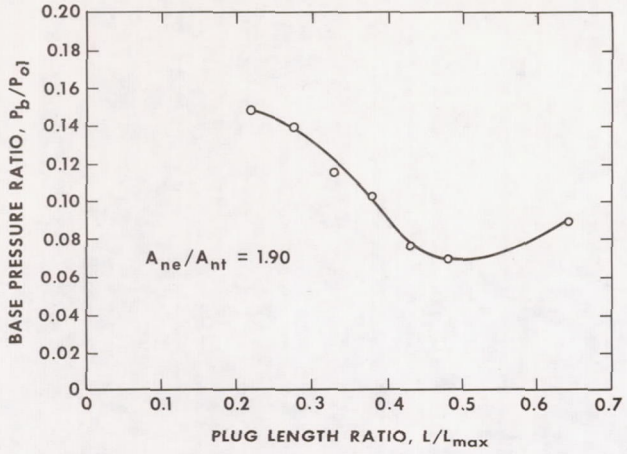

Figure 18. Effect of plug length ratio on the closed-wake base pressure for axisymmetric truncated plug nozzle.

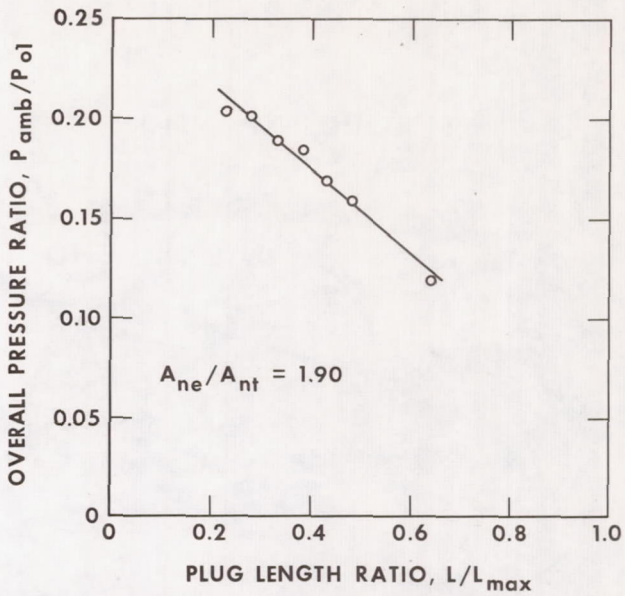

Figure 19. Effect of plug length ratio on overall pressure ratio at wake closure for axisymmetric truncated plug nozzle.

The overall pressure ratio at which the wake closes is important for determining optimum nozzle efficiency. Figure 19 presents this relationship. The increase in overall pressure ratio at wake closure as the plug length ratio is decreased presents further justification for the desirability of shorter plugs. The calculation of total performance for a given mission is greatly facilitated if the base pressure is constant (closed wake) for the longest period possible. Figure 19 indicates that shorter plug lengths lead to the establishment of closed-wake operation at higher values of ambient pressure, i.e., lower altitudes, and therefore increase the percentage of vehicle flying time at the closed-wake condition.

Experimental-Analytical Flow Field Comparison

A flow field Schlieren photograph of an axisymmetric truncated plug nozzle is shown in Figure 20. For performance determination, the subsonic and transonic flow field is of vital importance. However, in the supersonic area, only the flow field bounded by the shroud surface, plug surface, free jet boundary, separated base flow region down to the location of the recompression shock location, and the recompression shock itself is significant.

A comparison between the observed free jet boundary and internal shock location with analytical predictions is presented in Figures 21 and 22. The predicted constant pressure boundary deviates slightly from the observed location downstream of the outer shroud; this deviation was caused by the assumption of flow overexpansion around the shroud lip. In the case of the internal shock location, again a small difference occurs that results from the flow overexpansion assumption and also from the selected shape of the start line governing the supersonic flow field calculation. More accurate input data for the analytical concepts would eliminate these differences.

In Figure 23 the analytical results are superimposed on the Schlieren photograph. In addition to the previously mentioned parameters, the base recirculation area shape, the trailing wake shape, and the recompression shock shape are shown, and they agree well with the observed highly complicated flow field.

Aerodynamic Slipstream

The Chrysler Corporation, Space Division, recently investigated the performance of an aerospike engine in a feasibility study of a single-stage, earth-orbital, reusable vehicle (SERV). The engine is integrated into the base area of the cone-shaped vehicle (Fig. 24). Because of the enormous base area of the aerospike engine, which contributes greatly to the overall propulsion, the performance

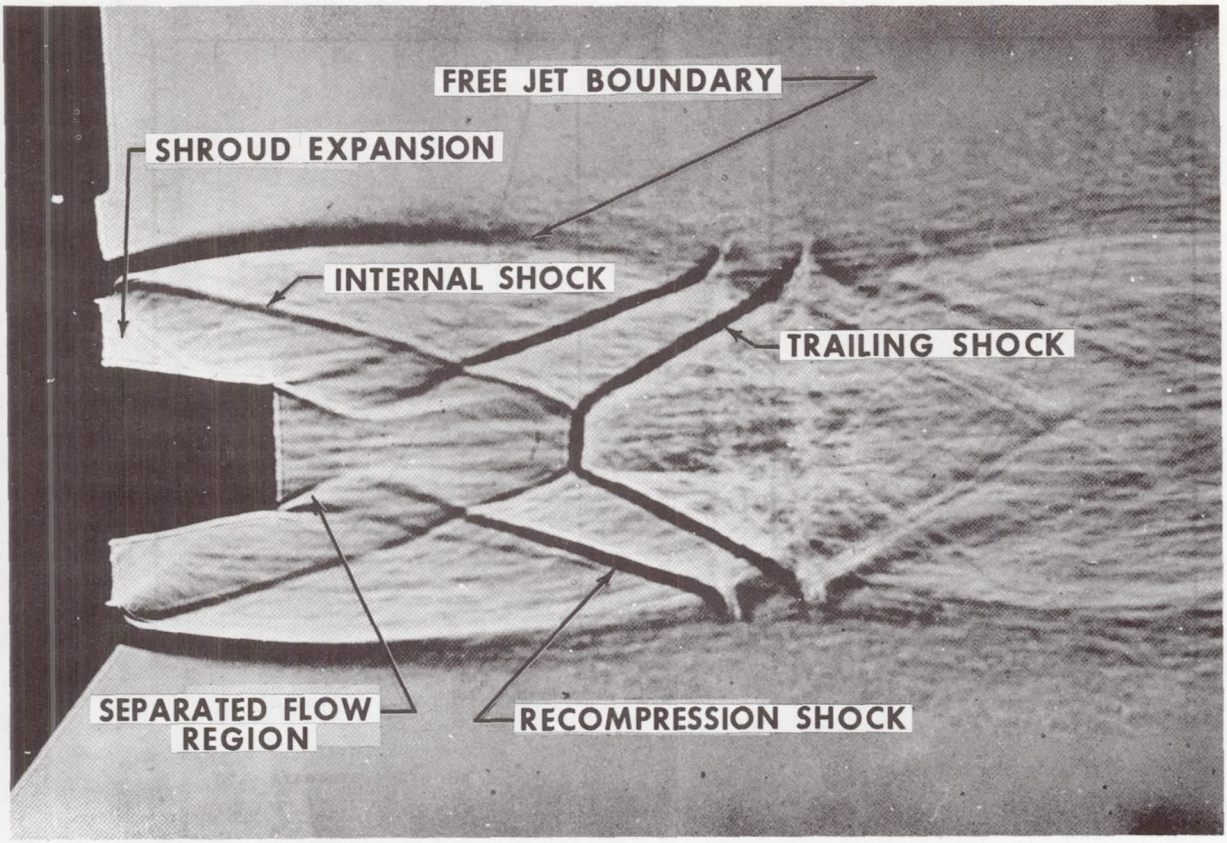

Figure 20. Flow field of the axisymmetric internal-external-expansion nozzle.

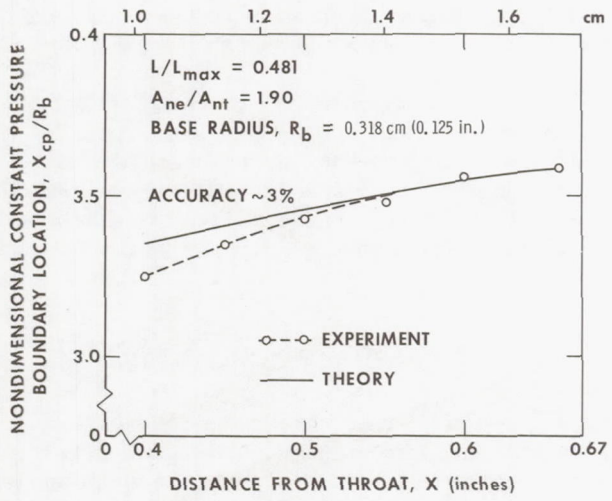

Figure 21. Comparison between analytical and observed constant pressure boundary location for axisymmetric truncated plug nozzle.

during open-wake operation and the condition of wake closure was important. When the vehicle flies through the atmosphere, the body geometry produces a slipstream with conditions in the aerospike engine area that are different from the undisturbed environment. The free jet boundary formed between the nozzle exhaust flow and the ambient air will adapt to the local condition and therefore affect the inviscid nozzle flow field, the base recirculation area, and the base pressure. Since most aerospike nozzle testing has been performed in still air, a wind tunnel test program with a 2.5-percent scaled SERV model using air flowing through the engine was executed to investigate the slipstream or Mach number effect on performance. The results of the test data, modified by scaling laws to account for the full size geometry and hot engine firing, are presented in a so-called carpet plot in Figure 25. This carpet plot does not show any numbers on the abscissa and has been generated by using equal intervals between each 3048-m (10 000-ft) interval for the zero Mach number condition. Such a plot is very convenient for data

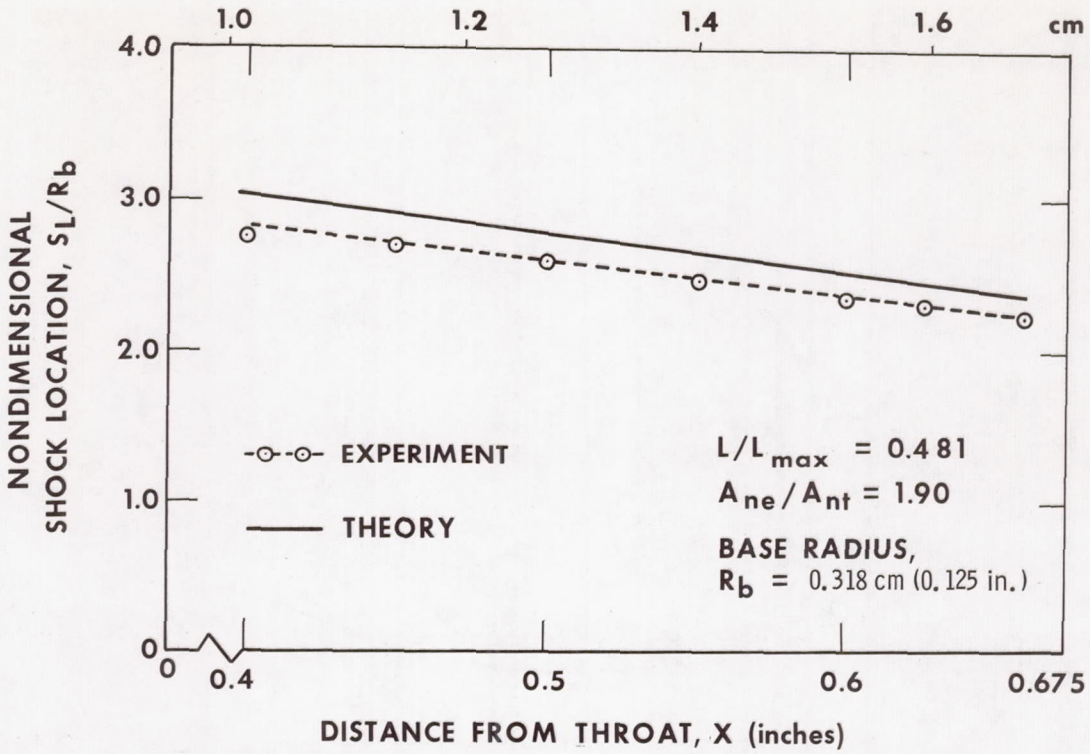

Figure 22. Comparison between analytical and observed internal shock location for axisymmetric truncated plug nozzle.

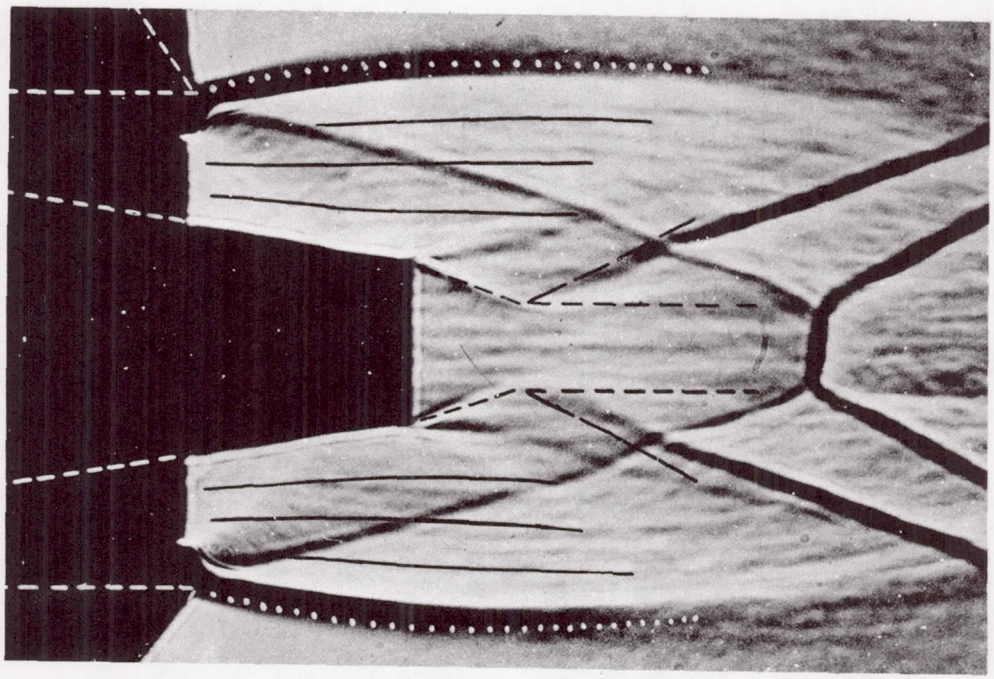

Figure 23. Experimental and analytical comparison of the flow fields of an axisymmetric internal-external-expansion nozzle.

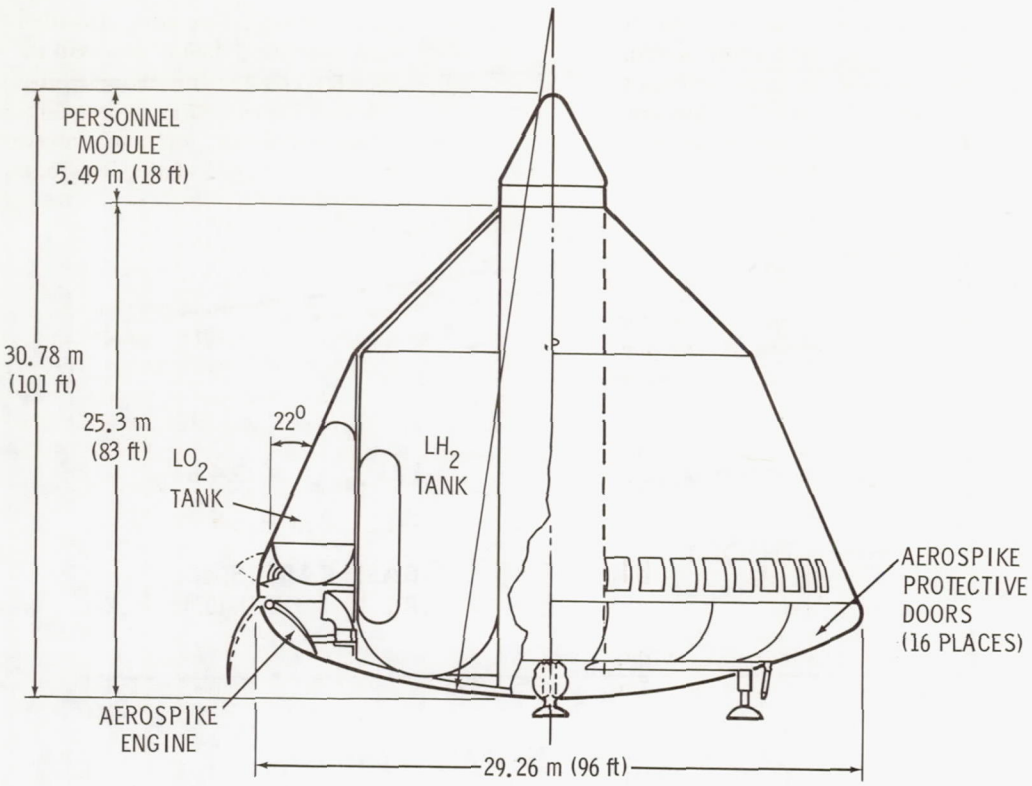

Figure 24. SERV vehicle.

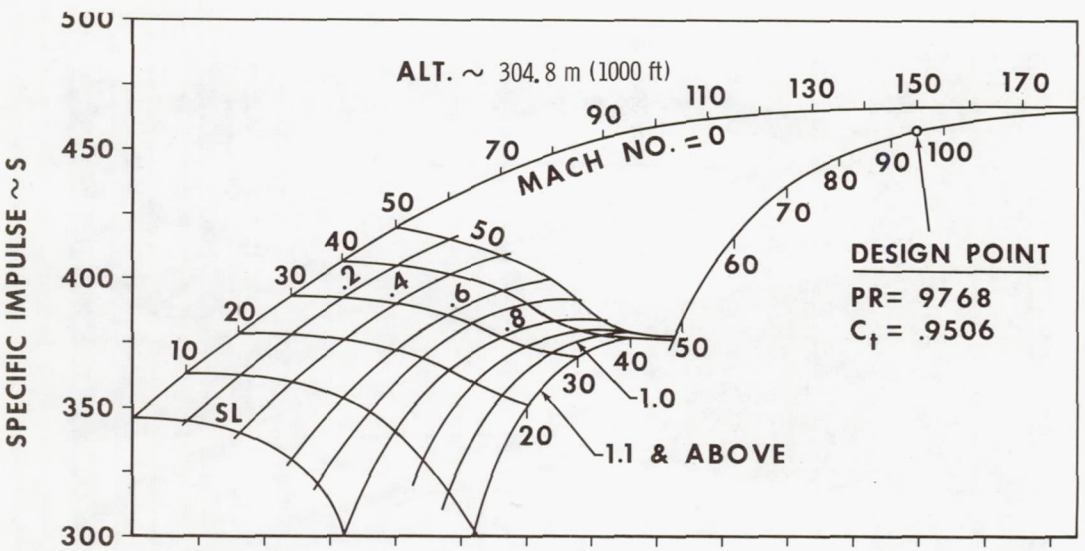

Figure 25. SERV nominal performance of design-point engine ($\epsilon = 433.7$).

interpolation. It is interesting to observe that this engine operates at the point of wake closure with a specific impulse approximately 50 s lower than it would provide in still air. This great difference, however, is caused by the slipstream effect in connection with the tremendous base area.

CONCLUSIONS

An analytical method to determine the performance of an aerospike nozzle, especially the performance contribution from the base area, has been discussed.

Two different types of operation mode exist. The base pressure follows the ambient state just outside the free jet boundary very closely during the open-wake operation mode, whereas the base pressure remains constant for the closed-wake condition. Several parameters such as the sonic line shape, internal shock, ambient pressure, base bleed, nozzle area ratio, turbulence effects, plug length, and aerodynamic slipstream have an effect on the base pressure.

A comparison between experimental and analytical data in connection with visual flow field observance shows good agreement. The parametric presentation of data allows the determination of individual effects and provides a useful tool for aerospike engine performance prediction and optimization.

BIBLIOGRAPHY

Characteristics of Separated Flow Regions Within Altitude Compensating Nozzles. Progress Report No. 4, Report No. 601-PR-4, Contract NAS8-25601, University of Notre Dame, Notre Dame, Indiana, February 1971.

Characteristics of Separated Flow Regions Within Altitude Compensating Nozzles. Progress Report No. 5, Report No. 601-PR-5, Contract NAS8-25601, University of Notre Dame, Notre Dame, Indiana, May 1971.

Mueller, Thomas J.; Sule, Wayne P.; and Hall, Charles R., Jr.: Characteristics of Separated Flow Regions Within Altitude Compensating Nozzles. Final Report UNDAS TN-029-FR-9, Contract NSR15-004-029, University of Notre Dame, Notre Dame, Indiana, January 1971.

Single-Stage Earth-Orbital Reusable Vehicle, Space Shuttle Feasibility Study. Final Report, Contract NAS8-26341, Chrysler Corporation, Space Division, New Orleans, Louisiana, June 30, 1971.

Page intentionally left blank

EXTENDIBLE ROCKET NOZZLE DEVELOPMENT

By

Don Pryor

The extendible rocket nozzle effort at MSFC was an outgrowth of the J-2X experimental engineering program that was active in 1967. The J-2X program investigated a number of improved features for possible incorporation into an advanced version of the Saturn S-IC J-2 engine. The J-2 engine is used as the primary propulsion system for the S-II and S-IVB stages of the S-IC launch vehicle. As depicted in Figure 1, the J-2X program had as a primary objective the evaluation of J-2 engine modifications that would simplify operation and improve reliability. As a secondary objective, the program also investigated methods of increasing thrust without extensively modifying the S-II or S-IVB stages. A thrust increase was achieved by raising engine combustion pressure through a redesign of the engine thrust chamber and propellant feed system.

With the chamber pressure raised to a higher level on an engine that was already operating at an underexpanded nozzle area ratio, the addition of a nozzle extension had obvious thrust improvement possibilities. This concept was, however, restricted in its application to the S-IVB stage of the S-IC launch vehicle. This stage utilizes a single J-2 engine installation, while the S-II stage has five J-2's clustered in such proximity that any additional length-diameter growth is impossible from an engine-to-engine interference standpoint. To accomplish a J-2 engine area ratio increase without violating the interstage confines of the existing S-IVB stage, a movable nozzle extension was required that could be stored about the existing J-2 nozzle before stage separation and translated axially to the full nozzle expansion ratio just prior to S-IVB stage ignition.

Quite early in the evaluation of the J-2X extendible nozzle concepts, the general features listed in Figure 1 were recognized as being worthwhile for application to any upper stage engine. The performance improvement is the most impressive gain realized by adding the additional area ratio for expansion of exhaust gases at vacuum flight conditions. Also, the capability of operating the engine at sea level conditions, with the nozzle extension removed, offers a significant cost reduction feature to an engine development program by removing the requirement of expensive vacuum test facilities

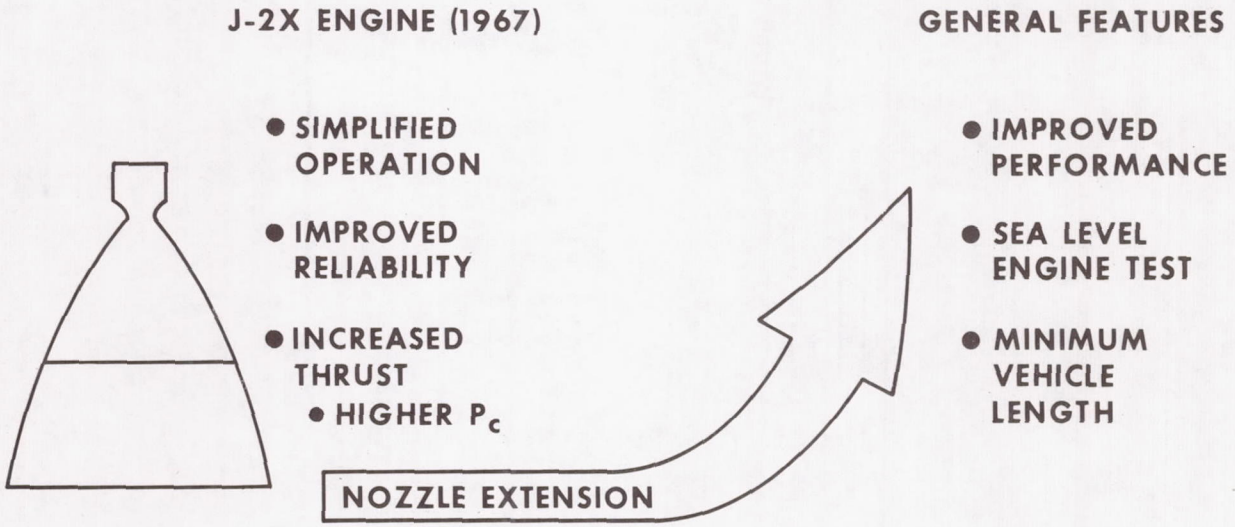

Figure 1. *Extendible nozzle concept evolution.*

during preflight testing. A reduction in vehicle length is realized because of the efficient packaging effect realized by stowing the nozzle around the basic thrust chamber until upper atmosphere engine operation is required.

Figure 2 shows the primary candidate nozzle extension configurations considered by the J-2X program. The design approach to all configurations was limited by several basic constraints, which are listed as ground rules in Figure 2. By far the most influential constraint was the requirement that the extension not violate the basic storage envelope provided for the conventional J-2 installation within the S-IVB engine compartment. This constraint called for ingenious design techniques to stow the additional nozzle length while allowing reliable deployment to the full extension area ratio within a 2-s actuation time.

The Airmat concept shown in Figure 2 is an inflatable extension skirt design that is fabricated from a woven wire structure manufactured by the Goodyear Aerospace Corporation. This concept features a nozzle skirt wall fabricated from two layers of conventionally woven, stainless steel wire yarn with the layers being loosely tied together by a number of interwoven wire yarn strands 10.2 cm (4.0 in.) in length. These strands hold the two wire-cloth layers from expanding outward when pressurizing gas is fed between them. The resulting effect when pressurized is a 10.2-cm (4.0-in.) thick wall that exhibits a high resistance to bending moments when fabricated into the integral cone frustum of the nozzle extension. When unpressurized, the Airmat extension is flexible and can be folded or rolled around the existing J-2 nozzle for storage within the S-IVB interstage. The inflation gas for pressurizing the wall structure comes from

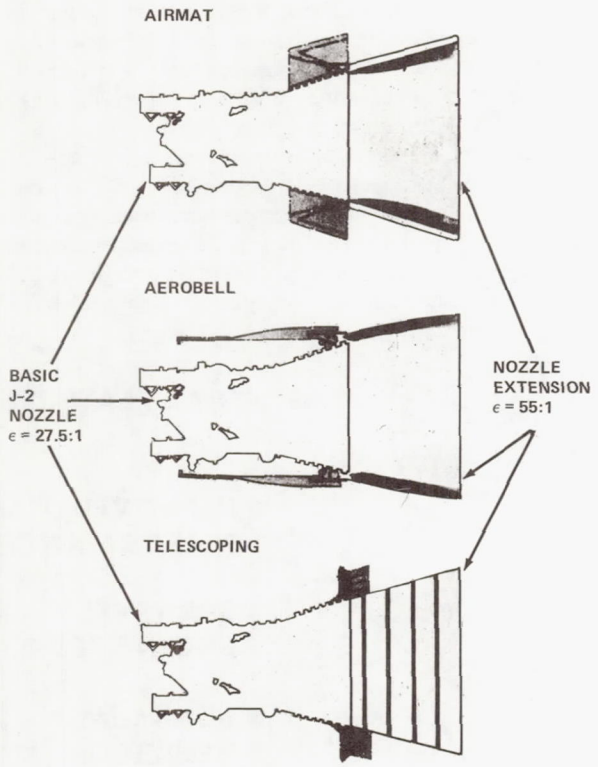

- INFLATABLE SKIRT
- WIRE-WOVEN CONSTRUCTION
- TRANSPIRATION COOLED BY TURBINE EXHAUST

- TRAVERSING SKIRT
- REFRACTORY MATERIALS
- FILM COOLED BY TURBINE EXHAUST

- MULTISECTION TRAVERSING SKIRT
- REFRACTORY MATERIALS
- RADIATION OR TURBINE EXHAUST GAS FILM COOLING

GROUND RULES

- HARDWARE WEIGHT LIMITED TO 340 kg (750 lb)
- PACKAGED WITHIN S-IVB INTERSTAGE
- 2 s ACTUATION TIME

PREDICTED GAINS

- 10 TO 11 s I_{sp}
- 1452 TO 1905 kg (3200 TO 4200 lb) PAYLOAD (MINUS SYSTEM WEIGHT)

Figure 2. J-2X extendible nozzle concepts.

the J-2 turbine exhaust products that are normally dumped into the main exhaust stream through a ring of orifices around the basic J-2 nozzle.

As in any woven product, the Airmat exhibits a matrix of fine openings between the woven yarn filaments that make up the two wire-cloth face layers. This porosity is utilized on the inner nozzle face, next to the hot main chamber combustion flow, to allow the turbine exhaust pressurizing gas to escape from the nozzle extension and perform a transpiration cooling function in the process. The external wall is sealed to prevent escape of the pressurizing gas.

Actuation of the Airmat extension is automatic, with turbine exhaust flow providing the driving force to deploy the folded material to the fully extended position. Overall system weight estimates, including the turbine exhaust ducting and manifold, nozzle attachment fixtures, etc., indicate that the Airmat extension assembly will weight 204.12 kg (450 lb).

The Aerobell nozzle extension concept of Figure 2 required a single piece, truncated cone fabricated from refractory materials. It was to be mechanically actuated from its stowed position about the basic J-2 nozzle cone by eight pneumatic motors driving collapsible struts. These collapsible struts were to be fabricated from flexible steel tubing that would fold into a flat ribbon about a storage drum and expand into a rigid columnar strut upon being unrolled from the drum. Nozzle cooling was to be accomplished by dumping the turbine exhaust flow in at the extension attachment plane through a 360-deg circumferential slot. This flow would provide a protective film coolant boundary layer along the extension wall. This concept was estimated to have total assembly weight of 249.48 to 272.16 kg (550 to 600 lb).

The third configuration shown in Figure 2 was a telescoping extension concept composed of five truncated cone segments that nested one within another in the stowed position about the J-2 basic nozzle. These segments were linked together by six sets of spring-loaded scissor arm mechanisms. The extension was to be stored with the spring-loaded arms compressed so that the deployment command released them to actuate the conical segments to the fully extended position. In reaching the extended position, the scissor arm assemblies moved past center and mechanically locked into a compression-carrying member that was capable of transmitting the extension thrust into the basic nozzle. Cooling would be by radiation or film using the turbine exhaust products in a manner similar to the Aerobell concept. A circumferential seal was required at each of the four joints between the five extension segments, and a total assembly weight of 192.78 kg (425 lb) was predicted

The J-2X program was canceled prematurely, leaving the nozzle extension concepts only partially evaluated. Based on the impressive benefits for engines in general shown in Figure 1, a decision was made to continue the evaluation of at least one of the three concepts of Figure 2 under research technology sponsorship. Since the Aerobell concept with its mechanically driven, single-piece skirt was very similar in concept to the LR-129 research engine already under test by the Air Force, this concept was eliminated from further consideration. The telescoping extension had already been modeled in full scale on a nonoperational J-2 engine to demonstrate the acutation characteristics of the spring-driven scissor arm mechanisms. The results of this modeling effort were encouraging, but the complexity of the multiple-section telescoping assembly was overriding and the evaluation was discontinued. The Airmat extension concept with its competitive light weight and attractive simplicity was therefore selected for further study.

The Airmat extension is fabricated, as mentioned earlier, from a woven wire structure that is woven on looms that are somewhat conventional (Fig. 3). Figure 4 is a cross section of the nozzle wall structure showing the two face plys connected by the interwoven drop cords. The pressurizing/cooling medium is shown to be sealed from ineffectual escape through the outer wall face ply by a silicon rubber coating bonded to the external wall surface. The yarn used to weave the wall material was twisted from filaments of 1.27×10^{-5} m (0.5 mil) stainless steel (type 304) wire, and the finished material has a highly pliable quality quite similar to woven textile products. This flexible nature makes the stowage design for the conical extension about the basic J-2 engine nozzle highly practical. It also improves the likelihood of reliable deployment from the stowed to the extended position solely by the turbine exhaust pressurization transient.

Before these features of stowage and deployment could be investigated, the more basic design considerations of Figure 5 had to be made compatible. These parameters are each interrelated and highly

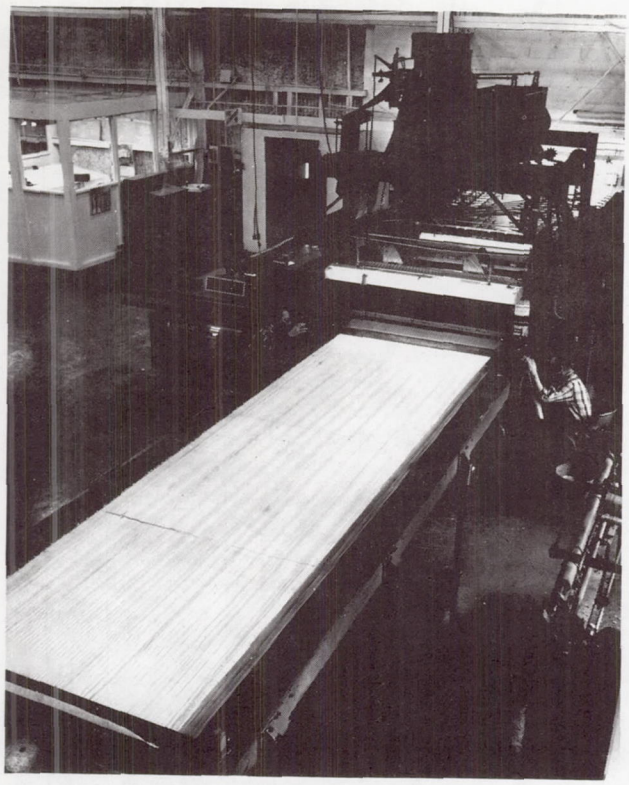

Figure 3. Looms used for weaving wire structure.

dependent on one another, and the design process consisted of a series of compromises aimed at providing the maximum performance improvement available for the given operating conditions.

The two biggest interrelated parameters of the inflatable nozzle design were the coolant gas conditions and nozzle wall inflation pressure. In the subject design application, the coolant gas supply conditions from the turbine exhaust of the J-2 engine were fixed and could not be modified without throwing the engine system operation out of balance. This left the nozzle wall pressure and the parameters influencing it as the design variables.

Of primary consideration to the concept design was just how large an expansion ratio/performance increase could be provided with the given coolant/pressurization gas flows. Figure 6 shows the relationship of internal Airmat wall pressure versus nozzle expansion ratio for various families of wall porosity and structural load carrying capability. The structural load curves indicate the minimum wall pressure required to maintain structural integrity for a nozzle of the desired area ratio. The various factors of structural load (1.0 through 1.5) represent multiples of the basic stress imposed by main engine exhaust gas pressure, friction drag, etc., acting on the nozzle extension.

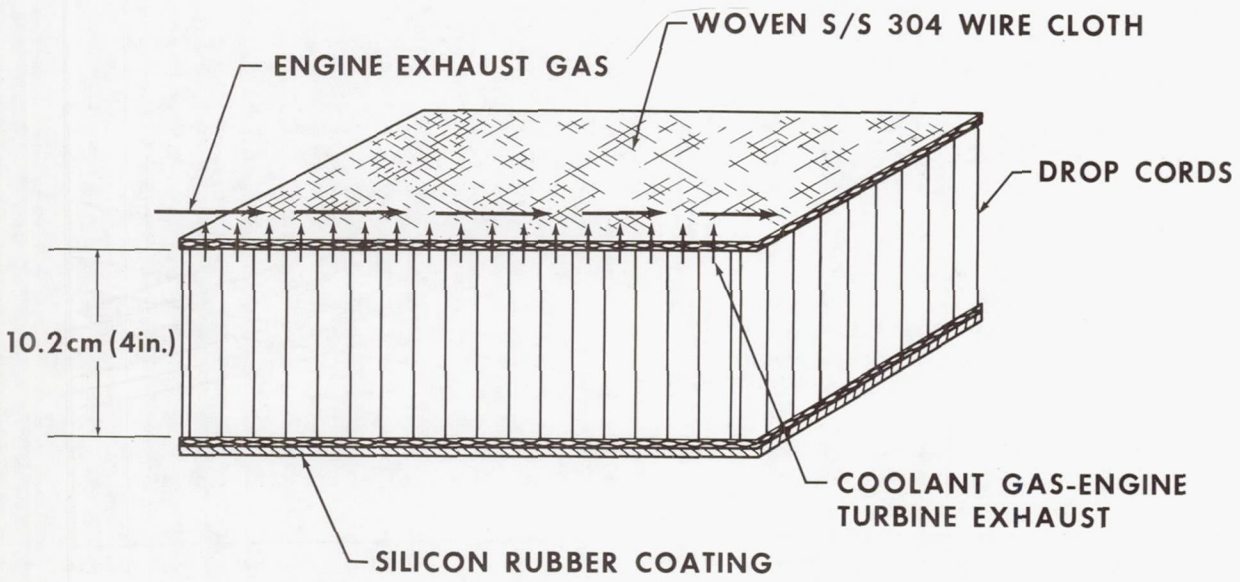

Figure 4. Airmat inflatable nozzle extension wall structure.

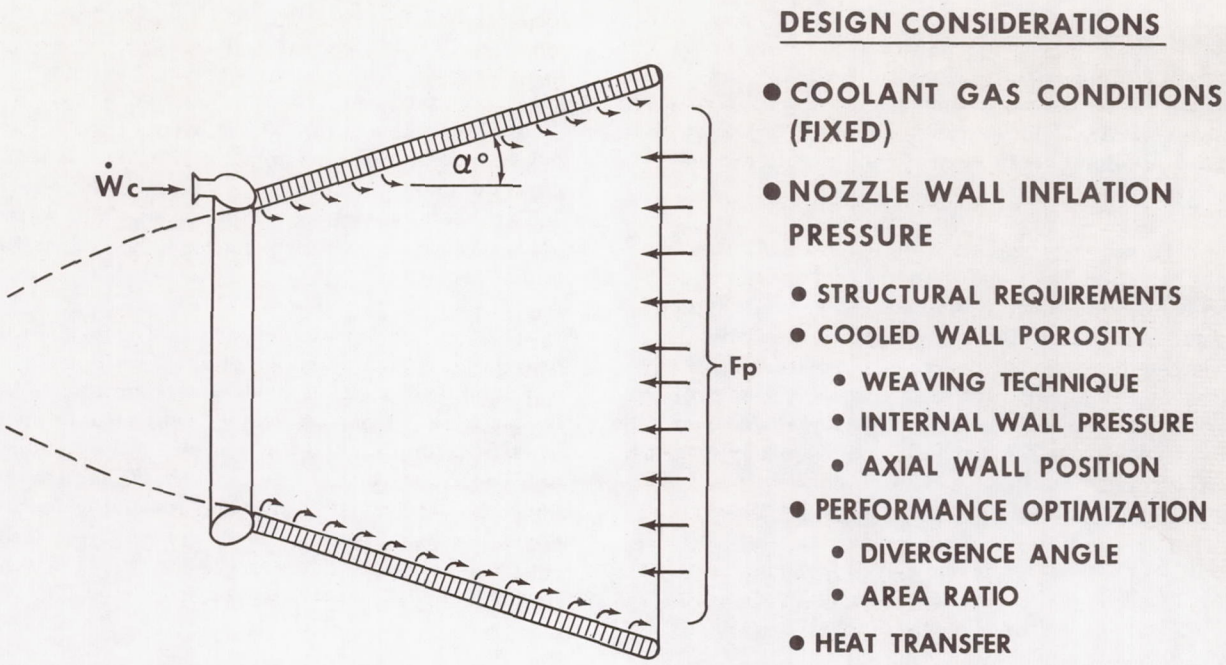

Figure 5. Extendible rocket nozzle development.

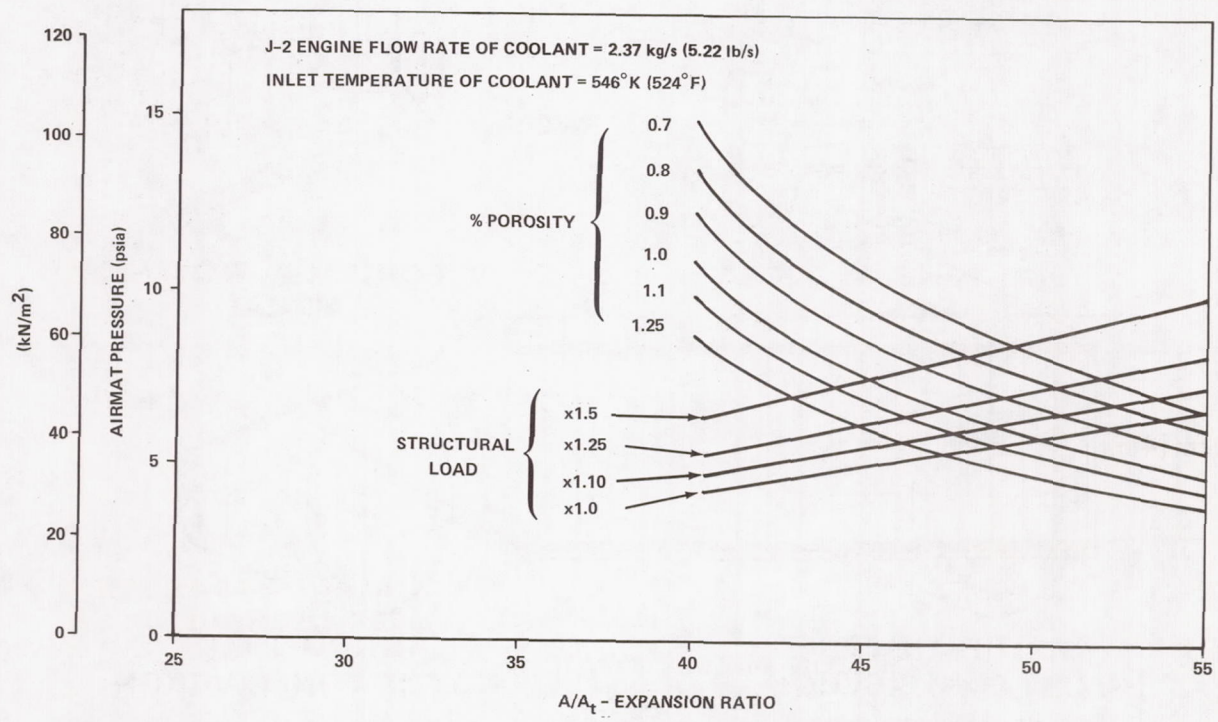

Figure 6. Airmat pressure versus nozzle extension expansion ratio.

The percent porosity curves show a decreasing internal wall pressure, as would be expected to result from increasing the area ratio and consequently the wall surface area/cooling flow openings. Wall porosities ranging from 0.7 to 1.25 were predicted as reasonably achievable for the woven-wire Airmat.

The porosity value of the Airmat wall was dependent on the weaving and nozzle construction technique as shown in Figure 7. The wall material could be woven in flat panels which simplified the weaving process and improved porosity control but greatly complicated the nozzle construction process. With flat panel woven Airmat for a raw material, the conical nozzle form had to be shaped by appropriate cutting, splicing, and seaming operations. A true conical frustum was difficult to control using this construction method. If however, the basic Airmat wall was woven in a manner such that the material advanced from the loom at an unequal rate across its outlet, the resulting effect was a curled panel that could be joined at one seam to produce the desired cone frustum shape. Porosity was affected by the uneven feed rate from the loom such that the slower advancing material achieved a tighter, less porous weave while the higher advance rate material from the loom was less dense and more porous. This porosity variation, while undesirable, was not considered serious with variations only amounting to 0.2 percent.

Other considerations listed in Figure 5 that affect wall porosity are the internal wall pressure and axial wall position at which the porosity is being evaluated. The porous Airmat wall tends to stretch when pressurized, thereby spreading the openings between the woven yarn and increasing the effective porosity. In regard to the axial position of measured porosity, there is likely to be a slight inner wall pressure drop between the end that is attached to the basic J-2 nozzle and the exit end of the

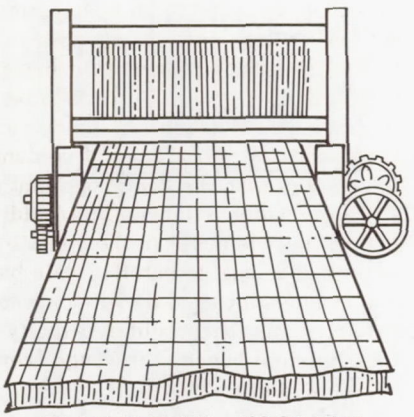

FLAT PANEL WOVEN AIRMAT

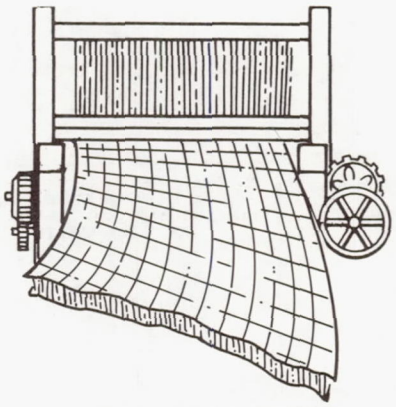

CONICALLY WOVEN AIRMAT

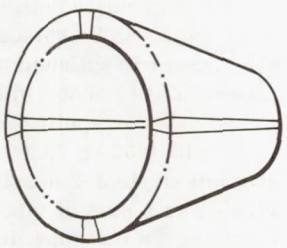

MULTIPANELED NOZZLE CONSTRUCTION

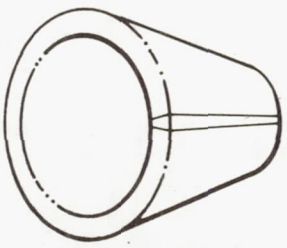

SINGLE PIECE NOZZLE CONSTRUCTION

Figure 7. Airmat woven wall construction techniques.

extension. This internal pressure decay down the nozzle length would tend to close somewhat the effective porosity resulting from the aforementioned stretching phenomena of the Airmat structure under inflation.

The design considerations of Figure 5 included the performance optimization aspects for the nozzle extension. Figure 8 illustrates the gain in engine specific impulse resulting from increasing the area ratio by multiples of some basic expansion ratio (ϵ). For purposes of illustration, this basic expansion ratio (ϵ) was identified as that nozzle exit area which would flow full, without separation, at a sea level back pressure. Figure 8 shows the increase in engine specific impulse above the sea level delivered value (expansion ratio = ϵ) when the nozzle expansion ratio is increased to some new level (ϵ') and operated at vacuum back-pressure conditions. This relation is a function of engine chamber pressure, and three different pressures are plotted in Figure 8. Divergence angle as well as area ratio must be optimized as a part of the performance optimization step of the design process.

The final area of discussion from the design considerations of Figure 5 is heat transfer. Because of the criticality of the transpiration cooling concept for the Airmat nozzle extension, an experimental evaluation was conducted. Figure 9 shows the experimental Airmat extension in place and inflated in a model test engine facility. The model test engine was a 17 792-N (400-lb) thrust, lox/GH_2 engine operating at 586 N/cm^2 (850 psia) chamber pressure.

The Airmat nozzle extension was attached to the existing engine nozzle at an area ratio of 27:1 and extended the expansion ratio to an 80:1 value. To provide the required 80:1 expansion ratio test capability, the nozzle extension was operated in a self-pumping diffuser that was removed in Figure 9 to expose the nozzle. The nozzle extension was inflated and transpiration-cooled with heated hydrogen gas in an attempt to duplicate the turbine exhaust products from the J-2 engine. The major constituent of the J-2 engine exhaust gas is hydrogen at a temperature of nearly 589°K (600°F). This temperature could not be modeled by the hydrogen pressurant used in the test program, since the facility could only provide 422°K (300° F) hydrogen at the required flow rates.

Testing was conducted over a range of inflation/coolant inlet flows and temperatures and the data are plotted over curves of theoretically predicted nozzle extension wall temperature versus coolant flow rate in Figure 10. The major conclusion from the experimental data was that the theoretical predictions of wall temperature versus coolant flow/temperature conditions are conservative. The theory expressed in Figure 10 shows a strong increase in the nozzle wall temperature as the coolant flow is reduced. The test data agreed fairly consistently with the theoretical data except that the reduced coolant flow of tests A and B failed to drive the wall temperature up the theoretical curve for coolant temperatures of 422°K (300°F). A projection of these data to the J-2 application is shown in Figure 11.

Figure 11 plots theoretical J-2 nozzle extension wall temperature adjusted by the test data of Figure 10. The temperature predictions are made for the extension wall at the plane of attachment to the fixed J-2 nozzle exit. This plane of the nozzle extension is under the most severe heating environment, not only from the worst case conditions of the main engine exhaust flow but from the lack of any protective boundary layer from upstream transpiration-coolant flow. Even with these severe conditions, the wall temperature is seen to range from only 533 to 755°K (500 to 900°F) depending on the selected nozzle extension expansion ratio and coolant flow rate. The range of coolant flows is that associated with the J-2 propellant utilization (PU) system which balances fuel/oxidizer flow so that propellant residuals in the vehicle tanks may be minimized at engine cutoff. This balancing process is accomplished by varying the amount of turbine drive gas that would eventually be fed to the nozzle extension; hence, the range from 2.04 to 2.95 kg/s (4.5 to 6.5 lb/s).

The end product of this study is illustrated in Figure 12. The J-2 engine with the nozzle extension is shown in both the retracted and extended positions. As optimized by the previously outlined design process, the area ratio can be raised from 27.5:1 to 48:1. Higher area ratio extensions are limited by the structural capability of the inflated assembly. Payload gains predicted for application to a J-2/S-IVB stage amount to 1452 kg (3200 lb). Figure 13 shows one of two full-scale J-2 nozzle extensions that were fabricated as a part of this effort. One unit was fabricated at the optimum design expansion ratio of 48:1, while the other was fabricated at a more conservative 41.3:1 expansion ratio. It was originally intended to fire the J-2 engine with first the 41.3:1 extension and then the 48:1 unit within the altitude facilities of Arnold Engineering

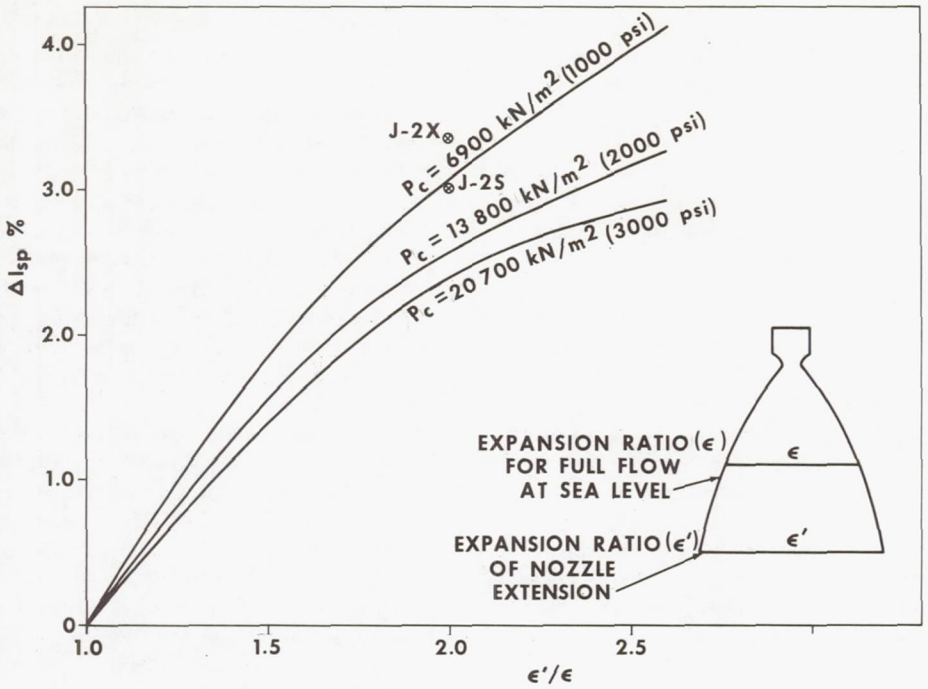

Figure 8. Theoretical performance gain for expansion below sea level pressure.

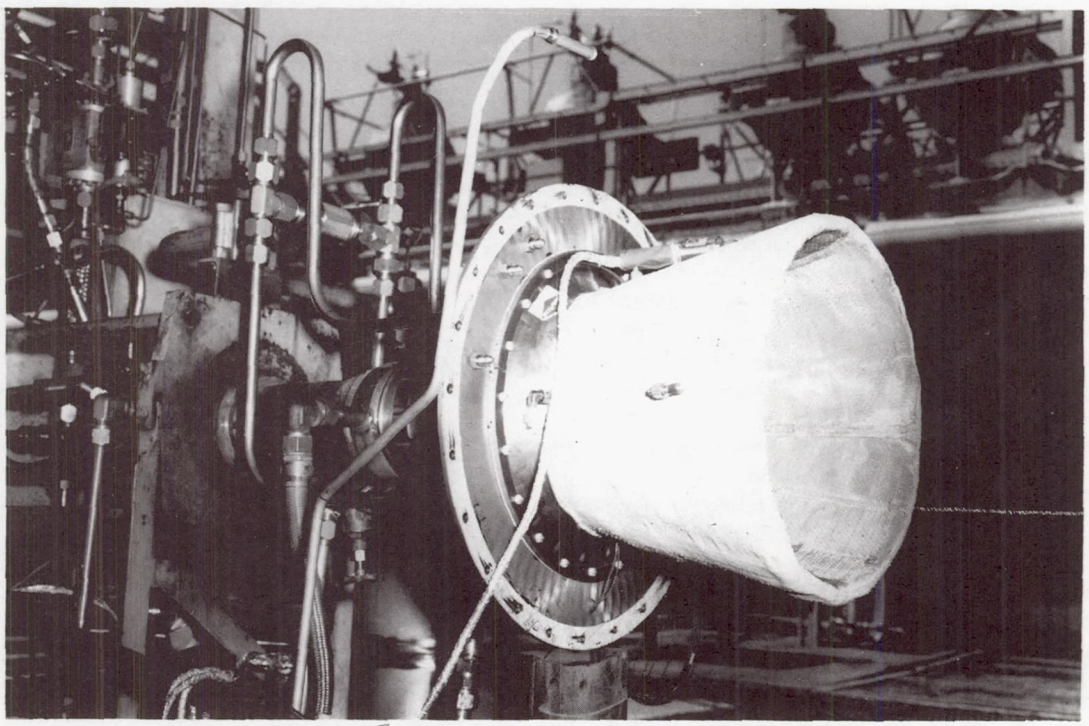

Figure 9. View of Goodyear nozzle setup.

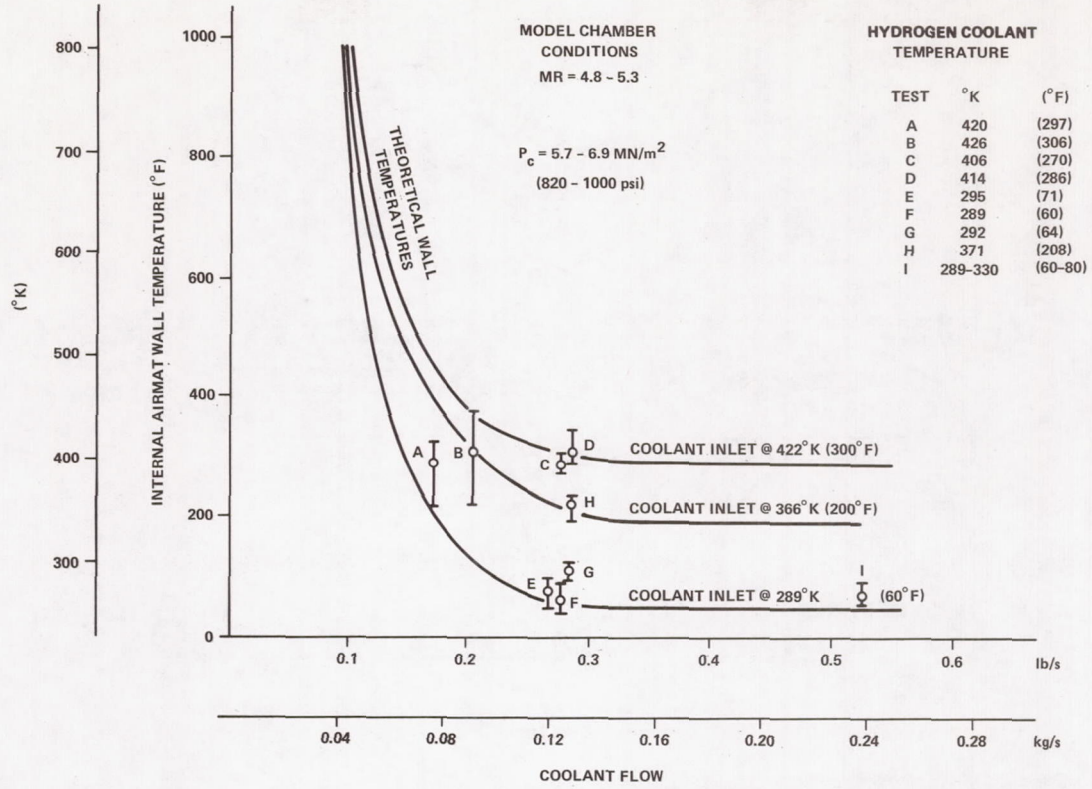

Figure 10. Model extension test data.

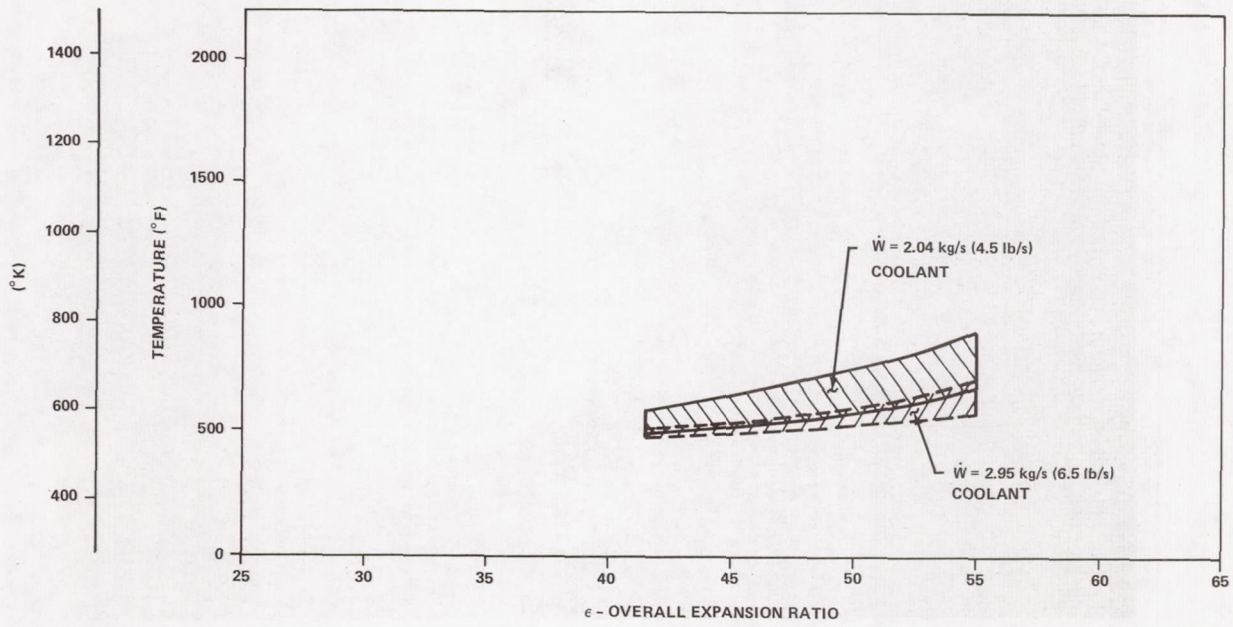

Figure 11. Theoretical nozzle extension surface temperature at attachment point (ϵ = 27.5:1) for varying overall expansion ratios.

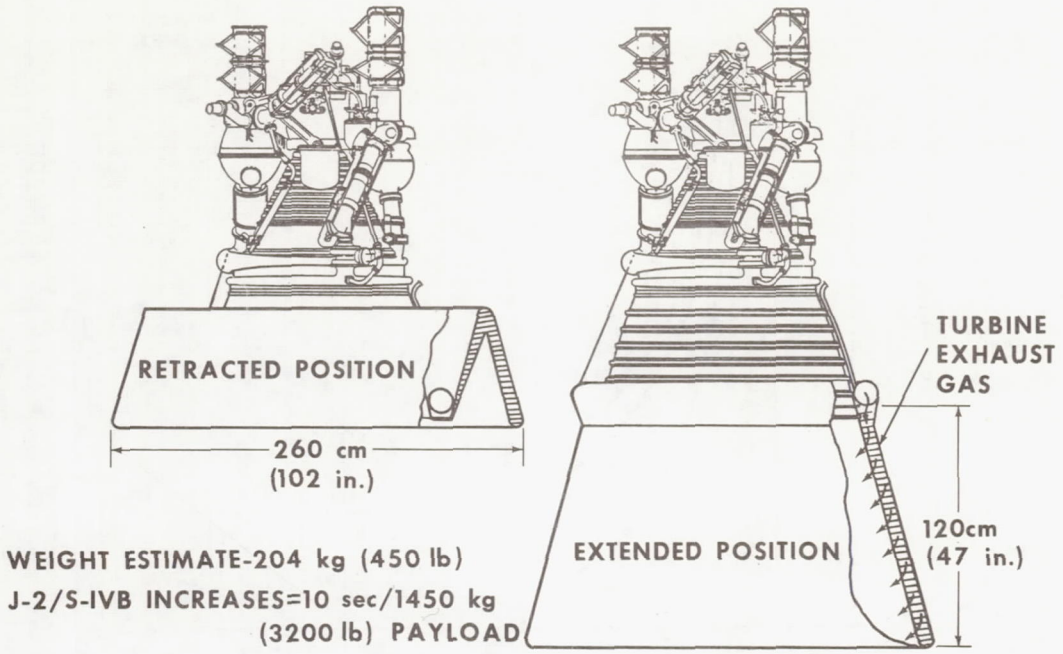

Figure 12. Airmat inflatable nozzle — J-2 application.

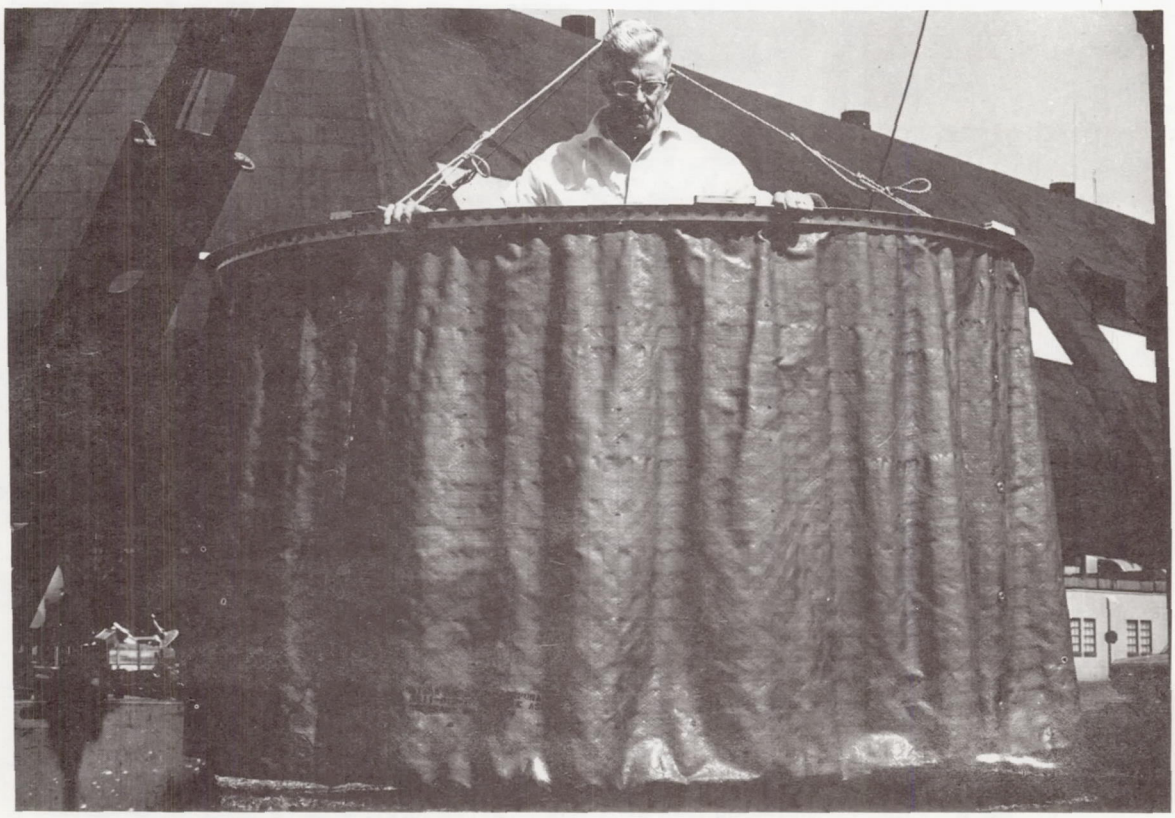

Figure 13. Long nozzle.

Development Center, but the J-2 engine firings at that facility were prematurely canceled before fabrication of the nozzle extensions could be completed. However, the fabrication program was completed in order to gain the valuable weaving and nozzle cone fabrication technology necessary to evaluate the concept for any future application. In addition, an inflation/deployment test series is scheduled to be conducted at MSFC using the full-size nozzle extensions. This test series will subject the extensions to the design inflation pressures and transients predicted for actual J-2 operation but will use a cold gas (GN_2) inflation source on an inoperative J-2; i.e., no main chamber exhaust products passing through the nozzle extension. Also, as a part of the testing, the extension will be stored in its retracted position, similar to the concept of Figure 12, and will be actuated by internal pressurization to the fully extended position. The test series will include appropriate instrumentation and filming to demonstrate the extension deployment process and fully inflated nozzle shape.

Page intentionally left blank

CRYOGEN FLOW CONTROL COMPONENTS FOR ROCKET PROPULSION SYSTEMS

By

J. H. Potter*

INTRODUCTION

The design envelope for Saturn V components far exceeded prior launch vehicle design envelopes and required significant advances in flow control component technology. The systems were assessed and component requirements revealed significant departure from previous requirements in the areas of mass flow rate, temperature, and pressure. The specific example selected is the Saturn V S-IC lox prevalve. The program resulted in new technology for the valve drive mechanism, valve closure scheduling, the main dynamic seals, the cryogenic seal for rotating surfaces, the cryogenic seal for sliding surfaces, and in turbine flowmeter design.

COMPONENT DESIGN ENVELOPE

The Saturn V component design envelope exceeded prior programs in the combined areas of vibration, flow, pressure, and temperature (Fig. 1). The technology derived from the Saturn vehicles is directly applicable to suborbital and orbital vehicles as presently envisioned.

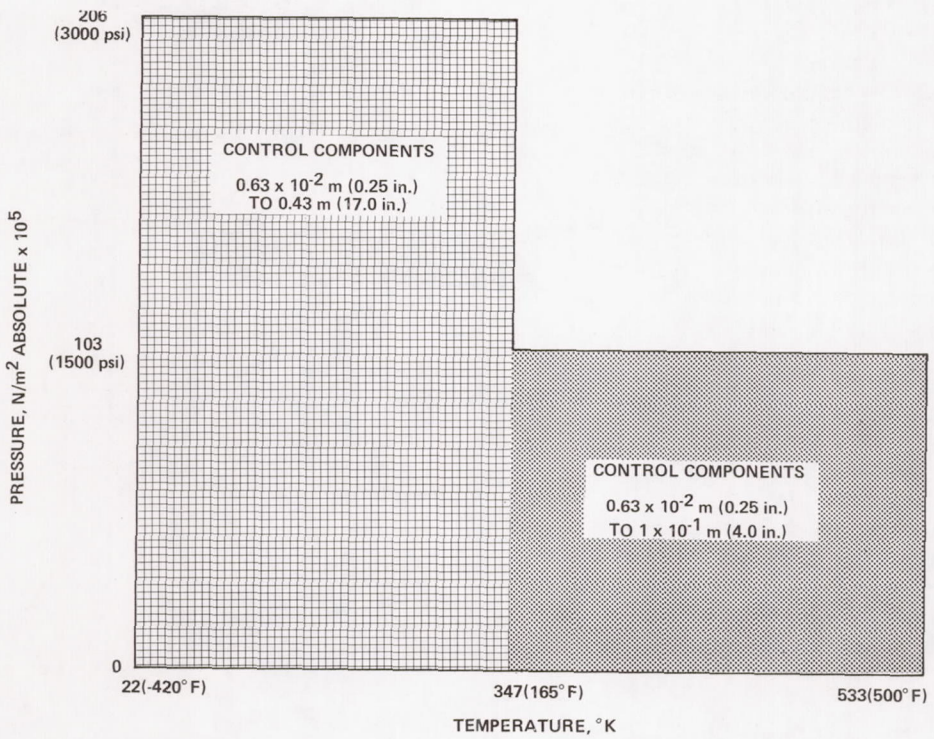

Figure 1. Saturn V component design envelope.

* The author wishes to express his appreciation to Mr. W. Dunaway, Contracting Officer's Representative for contract NAS8-5104, Design, Development, and Qualification of Lox and RP-1 Prevalve and Flowmeter Assemblies, for his assistance in the preparation of this paper.

The S-IC lox prevalve that was selected for discussion required many novel ideas to cope with the combined requirements of flow, vibration, pressure, temperature, life cycle, and closure time (Figs. 2 and 3).

VALVE TECHNOLOGY

The Saturn V S-IC prevalve represents a significant contribution to technology advancement in cryogen flow control components. The areas of significant interest are:

1. The Valve Drive Mechanism — The primary function of the sequencing mechanism is to provide a differential motion to allow retraction of the main seal prior to movement and opening of the valving element (visor). During closure, the reverse is true. The visor is in the full closed position before the seal contacts the visor sealing surface. This sequence is necessary to prevent scuffing and damage to the sealing element during valve operation. The latching function is a redundant provision against inadvertent valve closure.

The actuator output is through rotation of a single spline shaft which is coupled into two concentric shafts through the sequencing mechanism to be described. As shown in Figure 4, condition 1 indicates the valve in the full open position. The mechanical relationship between the pneumatic actuator, valve position, and sequencing mechanism is depicted in four stages. The latching provision is shown schematically in one position only. Latching is accomplished in the full open position by means of two redundant spring-loaded detents, secured in a strcutural ring fixed to the valve body.

The antifriction roller axle pins have extensions beyond the plane of the drive links to engage the detents for positive locking action. Actuation of the valve toward the closed position causes the antifriction rollers to spread apart, thus disengaging the detents and unlocking the mechanism. All other functions of the sequencing mechanism are clearly described by Figure 4.

2. Valve Closure Scheduling Device — The design specification for the 43.18-cm (17-in.)

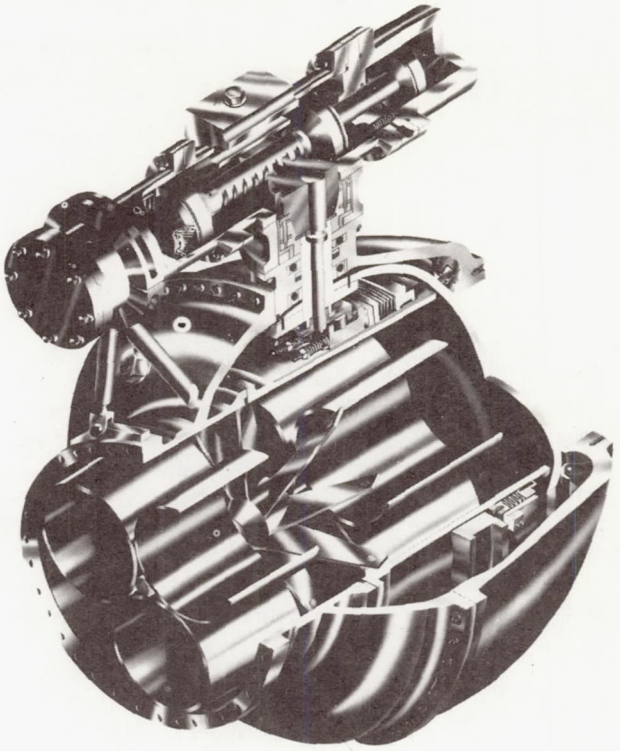

Figure 2. S-IC lox prevalve.

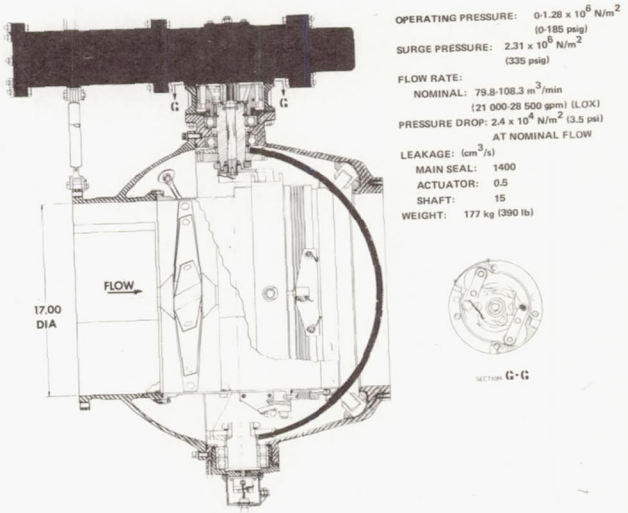

Figure 3. Schematic of S-IC lox prevalve.

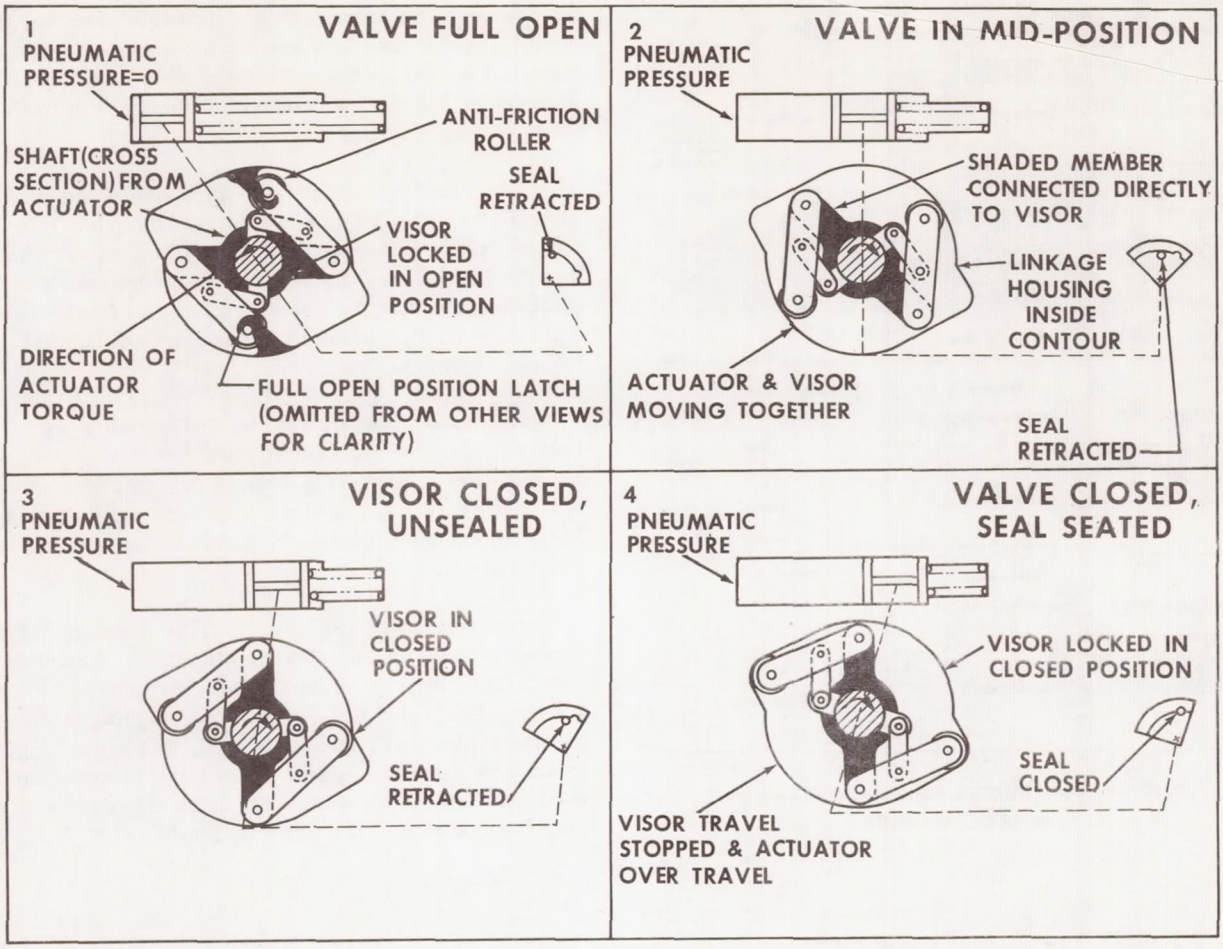

Figure 4. Valve sequencing mechanism.

prevalve limits allowable surge pressures upon closure. The purpose of the snubber circuitry is to schedule valve closure to limit surge pressures. The purpose of the booster circuit is to augment the main piston output at or near the point of complete valve closure where additional input torque is required.

The operation of the snubber and boost circuits is schematically depicted in Figure 5. The operation is shown in four stages, and the actuator position is related to the spherical gate position in the same series of diagrams. The following brief verbal description will assist in the understanding of the diagrams.

The application of closing pressure fills chambers a, b, and c, at essentially equal rates. The fill rates are controlled by fixed orifices in the case of chambers b and c and by a priority valve (variable orifice) in the case of chamber a. Application of pressure starts the closing cycle into force buildup across the actuator piston. The condition is depicted in the diagram labeled "Start."

As the actuator moves and the valve moves toward the closed position, the priority valve no longer contacts the actuator piston, and essentially unrestricted flow takes place into chamber a. The in-flow orifice to chamber b is covered by the boost piston, initiating a compression cycle in chamber b with consequent snubbing of the valve. This condition is depicted in the diagram labeled "Snub."

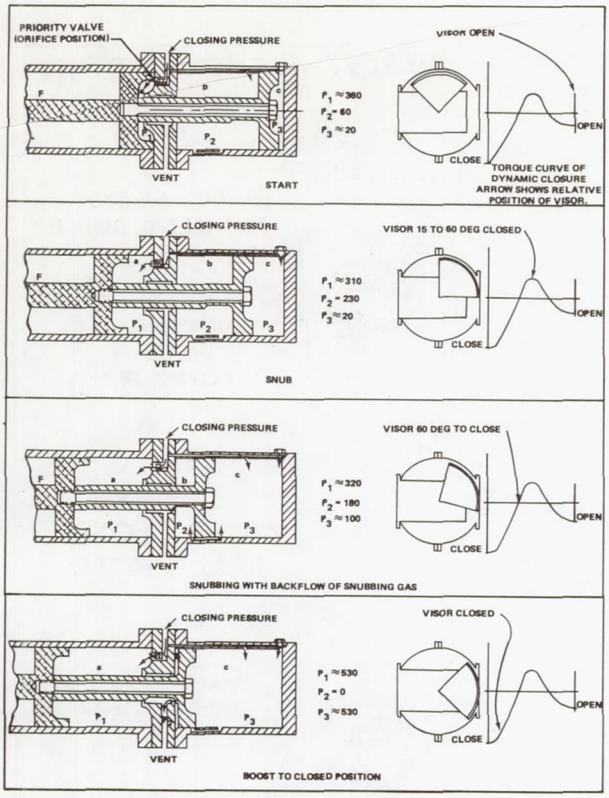

Figure 5. Operational schematic of snubber and boost circuits.

Further travel of the valve toward the closed position causes the boost piston to uncover bypass ports between chamber b and chamber c, thus equalizing the pressure across the booster piston and terminating the snubbing action. This condition is depicted in the diagram titled "Snubbing with Back Flow of Snubbing Gas."

Finally, as the valve approaches the full-closed position, the gas in snubbing chamber b is vented overboard through slots in the actuator shaft and the full area of the booster piston becomes effective to assist the actuator piston in final closure. This condition is depicted in the diagram labeled "Boost to Closed Position."

3. Main Dynamic Seal — The metallic main seal (Fig. 6) forms a liquid tight barrier at cryogenic temperatures, accepting limited deformations of the spherical gate. The seal is pressure-sensitive and functions on the principle of deformation within the elastic limit.

The metal seal seats against a spherically lapped surface on the concave side of the spherical gate. The spherical concave sealing surface is generated on a pad by conventional machining and lapping techniques, hard anodized, and again lapped to achieve a mirror finish. The flexible metal seal is attached to a bellows assembly to allow translation prior to rotation of the spherical gate (Fig. 7). The

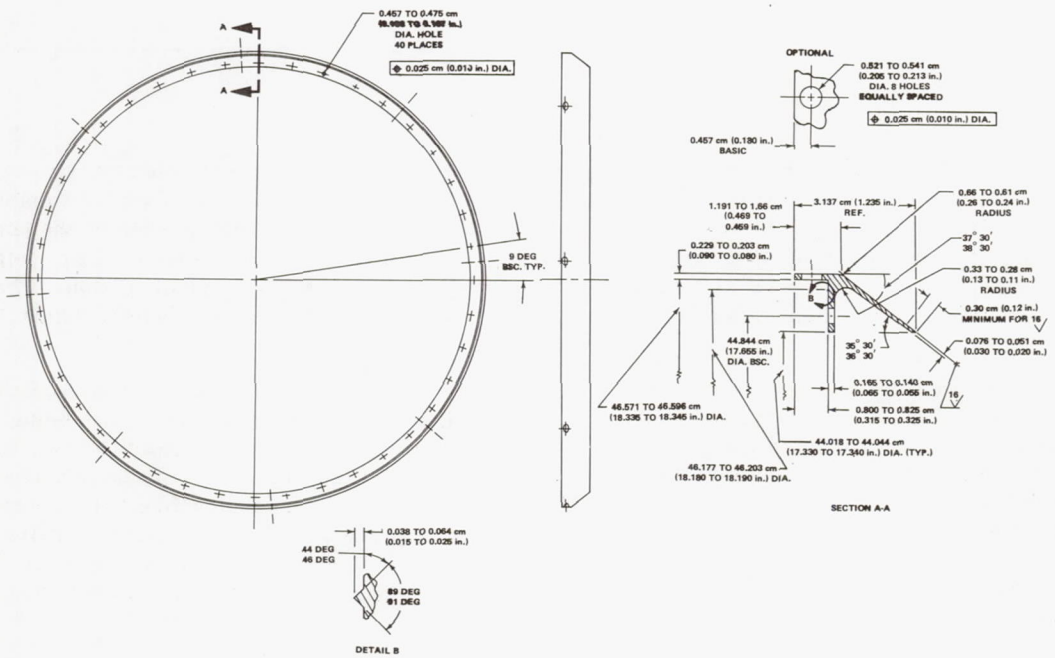

Figure 6. Physical configuration of seal.

seal lip and exterior conical surface of the metal seal are finally finished. Application of load to the metal seal takes place as a result of mechanical spring force on the bellows assembly and from hydrostatic pressure on the upstream face of the seal. These loads cause mechanical deflection and high bearing stress between the surface of the seal and the mating spherical pad.

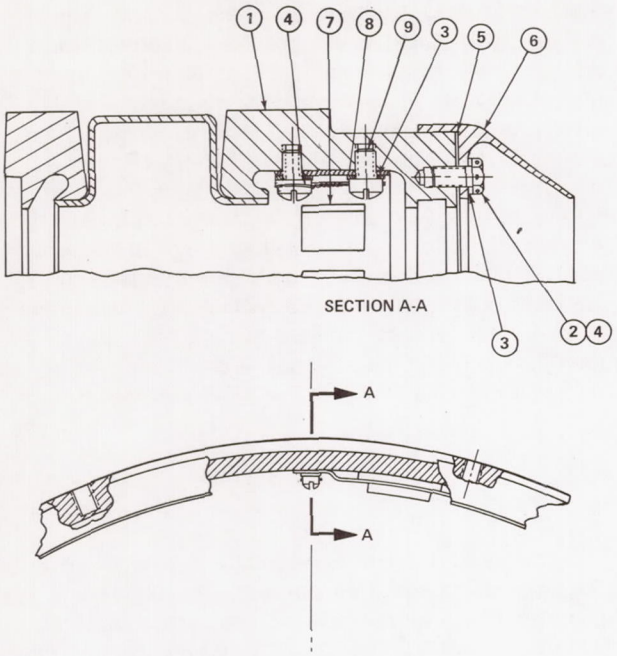

ITEM NO.	PART NUMBER	PART NAME	REQ. QTY.
9	137330	SCREW	16
8	137239	RETAINER	4
7	137328	PAD	12
6	137109	SEAL	1
5	135707	GASKET	1
4	MS2099SC25	LOCKWIRE	A/R
3	NAS620CB	WASHER	56
2	135708	SCREW	40
1	135520	BELLOWS & RING	1

Figure 7. Bellows and seal assembly.

To prevent interference and rubbing action between the thin metal seal and the seating surface, the entire bellows assembly including the seal is translated axially to produce clearance prior to rotation of the spherical gate.

4. Cryogenic Seal for Rotating Surfaces — It is essential to seal against the flow of liquid oxygen along the main actuator shaft under conditions where the spherical gate valve is open and flowing. Under closed conditions, the shaft is exposed to downstream conditions and is normally not subject to leakage of liquid oxygen.

The shaft seal (Fig. 8) consists of a metallic spring similar in configuration to one convolution of a metallic bellows and two Teflon cases closely machined to match the dimensions of the seal cavity and to maintain the required loading essentially constant through a wide temperature range. Sealing is accomplished between a flat-lapped flange on the rotating shaft and a similar flat-lapped surface within the stationary valve housing. The sealing load results from a combination spring load in the metallic convolute and hydrostatic pressure load within the seal envelope.

It has been MSFC's experience that a continuous Teflon envelope is unsatisfactory for seals of this nature because of the relatively high coefficient of expansion of the elastomer with a continuous envelope shrinkage of the elastomer, which effectively decreases the mechanical spring load generated by the seal to the point where leakage is excessive at cryogenic temperature levels. A unique feature of this seal design is the discontinuous Teflon envelope to eliminate shrinkage problems. An additional sealing feature is obtained through careful consideration of the relative coefficients of expansion of the materials of the shaft and housing to those of the metallic convolute of the seal assembly. This can be and is used to advantage in effecting a radial seal between

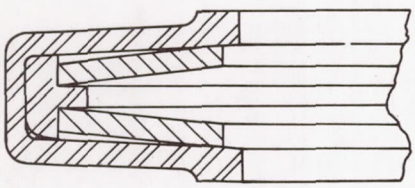

PHASE II

SOLID HEIGHT: 0.5 cm (0.197 in.) NOMINAL

LOAD: 1223-1446 N (275-325 lbf)

MATERIAL: RULON A

Figure 8. Main shaft seal configuration.

the shaft and housing to combine with the axial seal between the shaft flange and housing.

5. Cryogenic Seal for Sliding Surfaces, Actuator Shaft Seal — The cryogenic shaft seal (Fig. 9) prevents excessive leakage of actuator gas at cryogenic temperature levels. The cryogenic shaft seal serves a dual function as a static seal and a pressure loaded and mechanically loaded radial seal between a sliding shaft and a stationary housing. It was developed in cooperation with a commercial supplier specifically for this application.

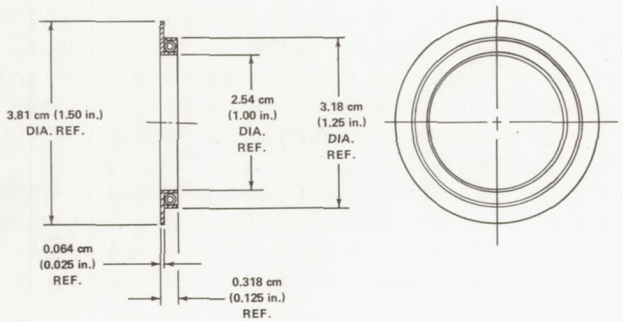

Figure 9. Actuator shaft seal configuration.

The principle of sealing rests in relatively uniform radial loading between the Teflon seal surface and the sliding shaft over a wide temperature range. The seal is mechanically loaded by a garter spring, having low rate and resting within a channel within the Teflon envelope. It is hydrostatically loaded through expansion of the Teflon envelope upon application of pressure to the non-sealing face. The dynamic sealing function was combined with a static seal on the downstream face by making the static seal integral with the Teflon envelope.

6. Turbine Flowmeter Design-Improvement, Method of Attaching Permanent Magnets to Nonferrous Turbine Blades — An improved method of attaching permanent magnets to nonferrous turbine blades consists of encapsulating magnetic slugs in an aluminum housing that is, in turn, shrunk-fit to a recess in the turbine blade. This method was developed as a result of difficulty encountered in retaining magnetic slugs imbedded directly into the aluminum blade. When the slugs were installed in the original manner and the blade was operated in liquid nitrogen, there was a tendency for the liquid to leak into the cavity behind the magnetic slug, gasify, and force the slug out of the blade. This encapsulation method eliminates this problem.

CONCLUSION

The technology derived in the Saturn program in the area of cryogen flow control components will have broad latitude in application to current and future programs such as the Space Shuttle and Space Tug.

BIBLIOGRAPHY

Skei, E.: New Technology Report No. 3113. Contract NAS8-5104, Whittaker Corporation, Controls and Guidance Division, Chatsworth, California, October 27, 1965.

APPROVAL

RESEARCH ACHIEVEMENTS REVIEW
VOLUME IV REPORT NO. 6

The information in these reports has been reviewed for security classification. Review of any information concerning Department of Defense or Atomic Energy Commission programs has been made by the MSFC Security Classification Officer. These reports, in their entirety, have been determined to be unclassified.

These reports have also been reviewed and approved for technical accuracy.

KARL L. HEIMBURG
Director, Astronautics Laboratory

☆ U. S. GOVERNMENT PRINTING OFFICE: 1972 — 746-823 / 4742

1. Report No.	2. Government Accession No.	3. Recipient's Catalog No.
NASA TM X-64690		

4. Title and Subtitle	5. Report Date
RESEARCH ACHIEVEMENTS REVIEW, VOL. IV, REPORT NO. 6 Chemical Propulsion Research at MSFC	August, 1972 6. Performing Organization Code

7. Author(s)	8. Performing Organization Report No.
Hans G. Paul, F. D. Pitsenberger, H. P. Stinson, L. A. Gross, R. J. Richmond, R. H. Counts, Gerald W. Smith, Rex Bailey, Klaus W. Gross, Don Pryor, and J. H. Potter	10. Work Unit No.

9. Performing Organization Name and Address	11. Contract or Grant No.
George C. Marshall Space Flight Center Marshall Space Flight Center, Alabama 35812	13. Type of Report and Period Covered Technical Memorandum

12. Sponsoring Agency Name and Address	14. Sponsoring Agency Code
National Aeronautics and Space Administration Washington, D.C. 20546	

15. Supplementary Notes

Prepared by Astronautics Laboratory,
Science and Engineering

16. Abstract

New and greater demands confront the field of chemical propulsion today. The Space Shuttle and Space Station require an updated technological base to lift propulsion power, efficiency, and reliability to far more challenging levels than those of the Saturn decade. The 10 papers of this review highlight the scope and intensity of work done, and being done, in combustion instability, liquid/gas hydrogen pumping, nozzles, fluid-flow system components, and aerospike engine thrust.

1. Technological highlights and achievements in chemical propulsion during the last 5 years are presented, with emphasis on the work performed by Marshall Space Flight Center.

2. Three optimum concepts, of many analyzed, for the secondary static seal of the turbopump dynamic shaft seal have been tested in a simulated cryogenic environment. These optimum seal-concepts and the test results are discussed.

3. During the past 5 years, two-phase (liquid/gas) pumping of hydrogen has been developed into an operational technique. This operational technique and its advantages are presented.

4. Originally, the pressure-sensitive, time-lag (PSTL) theory of combustion instability allowed only nominal prediction of combustion instability. An improved stability theory that permits prediction of new injector designs without the necessity of building and firing them was developed, and its capabilities are discussed.

Continued

17. Key Words (Suggested by Author(s))		18. Distribution Statement
chemical propulsion	aerospike engines	Unclassified — Unlimited
seal concepts	altitude compensating nozzles	See Document Release Form
two-phase pumping	nozzle extension concept	
combustion instability	fluid flow systems	
rocket thrust chambers		
bipropellant rocket motors		

19. Security Classif. (of this report)	20. Security Classif. (of this page)	21. No. of Pages	22. Price*
Unclassified	Unclassified	138	NTIS

*For sale by the Clearinghouse for Federal Scientific and Technical Information
Springfield, Virginia 22151

5. Rocket thrust chambers have, until recently, shown performance degradation from high frequency combustion instability. However, advances in resonator theory and design procedure have eliminated this problem by the use of tuned resonator cavities. Details and highlights of these advances are presented.

6. Engines operating in a pulsing mode are performance-sensitive to pulse on-and-off time durations. Results of tests performed with small monopropellant and hypergolic bipropellant rocket motors are outlined. Similarities in engine transient behavior that form the basis for an empirically-derived, pulse-performance prediction model are noted.

7. Technology for aerospike engines has been aimed at development of large expendable boosters, and stages requiring engines of high performance, small physical space, and simple thrust-vectoring. Details of these efforts and recent progress are presented.

8. Separated-flow regions within altitude-compensating nozzles have been investigated for improved performance. Background and results of the analytical/experimental work are discussed.

9. A summary of results is given from the design evaluation and experimental verification of a prototype inflatable nozzle extension concept. A unique woven-wire nozzle-wall material is described, including fabrication and operational characteristics.

10. A discussion of fluid flow systems for rocket propulsion is presented. Emphasis is placed on valve elements, valve actuators, separable connectors, and seals. The development of a submerged LH_2 relief valve is also presented.

CALENDAR OF REVIEWS

FIRST SERIES (VOLUME I)

REVIEW	DATE	RESEARCH AREA
1	2/25/65	RADIATION PHYSICS
2	2/25/65	THERMOPHYSICS
3	3/25/65	CRYOGENIC TECHNOLOGY
4*	3/25/65	CHEMICAL PROPULSION
5	4/29/65	ELECTRONICS
6	4/29/65	CONTROL SYSTEMS
7	5/27/65	MATERIALS
8	5/27/65	MANUFACTURING
9	6/24/65	GROUND TESTING
10	6/24/65	QUALITY ASSURANCE AND CHECKOUT
11	9/16/65	TERRESTRIAL AND SPACE ENVIRONMENT
12	9/16/65	AERODYNAMICS
13	9/30/65	INSTRUMENTATION
14	9/30/65	POWER SYSTEMS
15	10/28/65	GUIDANCE CONCEPTS
16	10/28/65	ASTRODYNAMICS
17	1/27/66	ADVANCED TRACKING SYSTEMS
18	1/27/66	COMMUNICATIONS SYSTEMS
19	1/6/66	STRUCTURES
20	1/6/66	MATHEMATICS AND COMPUTATION
21	2/24/66	ADVANCED PROPULSION
22	2/24/66	LUNAR AND METEOROID PHYSICS

SECOND SERIES (VOLUME II)

REVIEW	DATE	RESEARCH AREA
1	3/31/66	RADIATION PHYSICS
2	3/31/66	THERMOPHYSICS
3	5/26/66	ELECTRONICS
4	7/28/66	MATERIALS
5	9/29/66	QUALITY AND RELIABILITY ASSURANCE
6	1/26/67	CHEMICAL PROPULSION
7	3/30/67	CRYOGENIC TECHNOLOGY
8**	5/25/67	COMPUTATION
9	7/27/67	POWER SYSTEMS
10	9/28/67	TERRESTRIAL AND SPACE ENVIRONMENT
11	11/30/67	MANUFACTURING
12	1/25/68	INSTRUMENTATION RESEARCH FOR GROUND TESTING

THIRD SERIES (VOLUME III)

REVIEW	DATE	RESEARCH AREA
1	3/28/68	AIRBORNE INSTRUMENTATION AND DATA TRANSMISSION
2	5/22/68	ASTRODYNAMICS, GUIDANCE AND OPTIMIZATION
3	7/25/68	CONTROL SYSTEMS
4	9/26/68	AEROPHYSICS
5	11/21/68	COMMUNICATION AND TRACKING
6	1/30/69	THERMOPHYSICS
7	3/27/69	RADIATION PHYSICS
8	6/26/69	METEOROID PHYSICS
9	9/25/69	COMPUTATION RESEARCH (PART I)
10	12/18/69	MATERIALS RESEARCH FOR SHUTTLE AND SPACE STATION
11	1/29/70	MICROELECTRONICS RESEARCH FOR SHUTTLE AND SPACE STATION
12	3/26/70	COMPUTATION RESEARCH (PART II)

FOURTH SERIES (VOLUME IV)

REVIEW	DATE	RESEARCH AREA
1	5/28/70	STRUCTURES
2	10/29/70	CRYOGENICS
3	11/19/70	INSTRUMENTATION
4	3/25/71	ELECTRICAL POWER SYSTEMS
5	5/27/71	QUALITY AND RELIABILITY ASSURANCE
6	8/5/71	CHEMICAL PROPULSION

*Classified. Proceedings not published.
**Proceedings summarized only.

Correspondence concerning the Research Achievements Review Series should be addressed to:
Research Planning Office, S&E-R, Marshall Space Flight Center, Alabama 35812